Meriggi, Laura (2015) *Antimonide-based mid-infrared light-emitting diodes for low-power optical gas sensors*. PhD thesis.

UNIVERSITY OF GLASGOW

Antimonide-based mid-infrared light-emitting diodes for low-power optical gas sensors

Laura Meriggi

Submitted in fulfilment of the requirements for the
Degree of Doctor of Philosophy

in the
School of Engineering
College of Science and Engineering

October 2015

Abstract

The 3–5 µm mid-infrared spectral region is of great interest as it contains the fundamental molecular fingerprints of a number of pollutants and toxic gases, which require remote real-time monitoring in a variety of applications. Consequently, the development of efficient optoelectronic devices operating in this wavelength range is a very fascinating and pertinent research. In recent years, there has been a rapid development of optical technologies for the detection of carbon dioxide (CO_2), where the detected optical intensity at the specific gas absorption wavelength of 4.26 µm is a direct indication of the gas concentration, the main applications being in indoor air quality control and ventilation systems. The replacement of conventional infrared thermal components with high performance semiconductor light-emitting diodes (LEDs) and photodiodes in the 3–5 µm range allows to obtain sensors with similar sensitivity, but with an intrinsic wavelength selectivity, reduced power consumption and faster response. Gas Sensing Solutions Ltd. has developed a commercial CO_2 optical gas sensor equipped with an AlInSb-based LED and photodiode pair, which has demonstrated a significant reduction in the energy consumption per measurement.

The aim of this Ph.D. project, supported by an EPSRC Industrial CASE Studentship, was to improve the performance of mid-infrared AlInSb LEDs. This was achieved through the optimisation of the layer structure and the device design, and the application of different techniques to overcome the poor extraction efficiency ($\sim 1\,\%$) which limits the LED performance, as a consequence of total-internal reflection and Fresnel reflection. A key understanding was gained on the electrical and optical properties of AlInSb LEDs through the characterisation of the epi-grown material and the fabrication of prototype devices. Improved LED performance, with a lower series resistance and stronger light emission, was achieved thanks to the analysis of a number of LED design parameters, including the doping concentration of the contact layers, the LED lateral dimensions and the electrode contact geometry. A Resonant-Cavity LED structure was designed, with the integration of an epitaxially-grown distributed Bragg reflector between the substrate and the LED active region. The advantage of this design is twofold, as it both redirects the light emitted towards the substrate in the direction of the top LED surface and adds a resonant effect to the structure, resulting in a three-times higher extraction efficiency at the target wavelength of 4.26 µm, spectral narrowing and improved temperature stability. Finally, 2D-periodic metallic hole array patterns were integrated on AlInSb LEDs, showing potential advantages for spectral filtering and enhanced extraction of light emitted above the critical angle.

Declaration of Authorship

I, LAURA MERIGGI, declare that this thesis titled, *Antimonide-based mid-infrared light-emitting diodes for low-power optical gas sensors* and the work presented in it are my own. I confirm that:

- This work was done wholly or mainly while in candidature for a research degree at this University.
- Where any part of this thesis has previously been submitted for a degree or any other qualification at this University or any other institution, this has been clearly stated.
- Where I have consulted the published work of others, this is always clearly attributed.
- Where I have quoted from the work of others, the source is always given. With the exception of such quotations, this thesis is entirely my own work.
- I have acknowledged all main sources of help.
- Where the thesis is based on work done by myself jointly with others, I have made clear exactly what was done by others and what I have contributed myself.

Signed: ________________________________

Date: ________________________________

Publications

Y Ding, L Meriggi, M J Steer, W Fan, K Bulashevich, I G Thayne, C MacGregor, C N Ironside, M Sorel. Design, simulations and optimisation of mid-infrared multiple quantum well LEDs. *8th International Conference on Materials for Advanced Technologies (ICMAT) of the Material Research Society of Singapore.* Singapore, June 2015.

L Meriggi, M J Steer, Y Ding, A Samarelli, I G Thayne, C MacGregor, C N Ironside, M Sorel. Enhanced performance of plasmon-assisted resonant-cavity mid-IR $\mathrm{Al_xIn_{1-x}Sb}$ LEDs. *Conference on Laser and Electro-Optics CLEO Europe 2015.* Munich, June 2015.

L Meriggi, M J Steer, Y Ding, I G Thayne, C MacGregor, C N Ironside, M Sorel. Development of mid-infrared light-emitting diodes for low-power optical gas sensors. *11th Conference on PhD Research in Microelectronics and Electronics (IEEE PRIME 2015).* Glasgow, June 2015.

L Meriggi, M J Steer, Y Ding, I G Thayne, C MacGregor, C N Ironside, M Sorel. Mid-IR resonant-cavity LEDs with p-contact grid geometry for gas sensing applications. *SU2P Annual Symposium 2015.* St Andrews, March 2015.

L Meriggi, M J Steer, Y Ding, I G Thayne, C MacGregor, C N Ironside, M Sorel. Enhanced emission from mid-infrared AlInSb light-emitting diodes with p-type contact grid geometry. *Journal of Applied Physics* 117 (6), 063101, 2015.

Y Ding, L Meriggi, M J Steer, I G Thayne, C MacGregor, M Sorel, C N Ironside. Investigation of mid-infrared AlInSb LEDs with an nip structure. *Conference on Optoelectronic and Microelectronic Materials and Devices (COMMAD) 2014.* Perth, Western Australia, December 2014.

Y Ding, L Meriggi, M J Steer, K Bulashevich, I G Thayne, C MacGregor, M Sorel, C N Ironside. An investigation of MWIR AlInSb LEDs based on double heterostructures and multiple quantum wells. *Conference on Optoelectronic and Microelectronic Materials and Devices (COMMAD) 2014.* Perth, Western Australia, December 2014.

L Meriggi, M J Steer, Y Ding, I G Thayne, C MacGregor, C N Ironside, M Sorel. Improving efficiency of mid-IR LEDs for gas sensing applications. *European Semiconductor Laser Workshop.* Paris, September 2014.

L Meriggi, M J Steer, Y Ding, I G Thayne, C MacGregor, C N Ironside, M Sorel. Optimisation of p-contact grid geometry for mid-infrared LEDs and photodiodes. *Semiconductor and Integrated OptoElectronnics (SIOE) Conference.* Cardiff, April 2014.

L Meriggi, M J Steer, Y Ding, I G Thayne, C MacGregor, C N Ironside, M Sorel. Efficiency enhancement of mid-wave infrared AlInSb LEDs. *22nd European Workshop on Heterostructure Technology (HETECH) 2013.* Glasgow, September 2013.

L Meriggi, M J Steer, Y Ding, I G Thayne, C MacGregor, C N Ironside, M Sorel. Mid-wave infrared (3-5 µm) AlInSb resonant-cavity LEDs. *Conference on Laser and Electro-Optics CLEO Europe 2013.* Munich, May 2013.

Other Publications

H Li, M J Strain, L Meriggi, L Chen, J Zhu, K Cicek, J Wang, X Cai, M Sorel, M G Thompson, S Yu. Pattern manipulation via on-chip phase modulation between orbital angular momentum beams. *Applied Physics Letters* 107 (5), 051102, 2015.

M J Strain, C Lacava, L Meriggi, I Cristiani, M Sorel. Tunable Q-factor silicon microring resonators for ultra-low power parametric processes. *Optics Letters* 40 (7), 1274-1277, 2015.

A D Simard, M J Strain, L Meriggi, M Sorel, S LaRochelle. Bandpass integrated Bragg gratings in silicon-on-insulator with well-controlled amplitude and phase responses. *Optics Letters* 40 (5), 736-739, 2015.

L Chen, J Zhu, M J Strain, L Meriggi, M L Garcia, K Cicek, H Li, X Cai, M Sorel, S Yu. Measuring the angular emission of optical vortex beams from integrated devices. *IEEE 11th International Conference on Group IV Photonics (GFP) 2014.* Paris, August 2014.

M J Strain, H Li, X Cai, L Meriggi, J Wang, J Zhu, K Cicek, L Chen, M L Garcia, M G Thompson, M Sorel, S Yu. Actively reconfigurable compact vortex beam emitters. *IEEE 11th International Conference on Group IV Photonics (GFP) 2014.* Paris, August 2014.

H Li, M J Strain, L Meriggi, L Chen, J Zhu, K Cicek, X Cai, J Wang, M Sorel, M G Thompson, S Yu. On-chip modulation of phase shift between optical vortices with opposite topological charge. *Conference on Laser and Electro-Optics CLEO 2014.* St Jose, California, June 2014.

H Wang, J Mi, X Zhou, L Meriggi, M J Steer, B Cui, W Chen, J Pan, Y Ding. 1.06 µm InGaAs/GaAs multiple-quantum-well optical thyristor lasers with a PiNiN structure. *Optics Letters* 38 (22) 4868-4871, 2013.

L Meriggi, M Simonetta, M Soldo, G Russo, M Zanola, M J Strain, M Sorel, G Giuliani. Integrated optically isolated laser source via non-reciprocal counter-propagating Four-Wave Mixing. *Conference on Laser and Electro-Optics CLEO Europe 2013.* Munich, May 2013.

"To accomplish great things we must travel along the horizon and upon the tide."

Acknowledgements

I have always thought about how I would feel in this moment and, finally, here I am.
I would like to thank all the people that have been part of my life and the ups and downs of my journey in the last four years.

To my supervisor, Prof. Marc Sorel, for having believed and invested in me from the start, for his great support during my Ph.D. and for his informal and friendly approach.

To Dr. Matt Steer, the best colleague and mentor I could have ever had. For everything that he taught me and the always useful and inspiring discussions, and for being a friend, from the dungeons of the lab to the search of Aurora.

To Prof. Iain Thayne, Calum Macgregor and all the people involved in my Studentship and in the TSB project, for trusting me and my work along the way.

To all the members, present and past, of the Optoelectronic Group who have shared with me the joys and pains of fabrication. Thanks, in order of appearance, to Marco, Vincenzo, Piotr, Antonio, Corrie, Barry, Harris, Alessandro and Emanuele.

To all the staff of the JWNC for making the magic of fabrication possible and for creating the amazing environment of a big family.

To my Captain, for having granted me the permission to get onboard his amazing ship and being with me with a smile every step of the way.

And last but not least, to my family, the funniest and strongest of all, for always trusting and supporting my decisions and for being with me every single day, no matter the distance.

Contents

List of Figures

List of Tables

Abbreviations

CTLM	**C**ircular **T**ransfer **L**ength **M**ethod
CVD	**C**hemical **V**apour **D**eposition
DCV	**D**emand **C**ontrol **V**entilation
DBR	**D**istributed **B**ragg **R**eflector
EL	**E**lectro **L**uminescence
EOT	**E**xtraordinary **O**ptical **T**ransmission
EQE	**E**xternal **Q**uantum **E**fficiency
FDTD	**F**inite **D**ifference **T**ime **D**omain
FSR	**F**ree **S**pectral **R**ange
FTIR	**F**ourier **T**ransform **I**nfra **R**ed
FWHM	**F**ull **W**idth **H**alf **M**aximum
GSS	**G**as **S**ensing **S**olutions
ICP	**I**nductively **C**oupled **P**lasma
IMF	**I**nterfacial **M**is**F**it
IPA	**I**so**P**rophyl **A**lcohol
IR	**I**nfra **R**ed
IQE	**I**nternal **Q**uantum **E**fficiency
IVA	**I**nter **V**alence band **A**bsorption
LED	**L**ight **E**mitting **D**iode
LPE	**L**iquid **P**hase **E**pitaxy
MBE	**M**olecular **B**eam **E**pitaxy
MIBK	**M**ethyl **I**so**B**utyl **K**etone
MOVPE	**M**etal **O**rganic **V**apour **P**hase **E**pitaxy
MQW	**M**ulti **Q**uantum **W**ell
NDIR	**N**on **D**ispersive **I**nfra **R**ed

NEA	**N**oise **E**quivalent **A**bsorbance
NEP	**N**oise **E**quivalent **P**ower
PD	**P**hoto **D**etector
PL	**P**hoto **L**uminescence
PMMA	**P**oly**M**ethyl **M**eth**A**crylate
ppb	**p**arts **p**er **b**illion
ppm	**p**arts **p**er **m**illion
RC	**R**esonant **C**avity
RIE	**R**eactive **I**on **E**tching
SEM	**S**canning **E**lectron **M**icroscope
SMU	**S**ource **M**easurement **U**nit
SPP	**S**urface **P**lasmon **P**olariton
SRH	**S**hockley **R**ead **H**all
TEM	**T**ransmission **E**lectron **M**icroscope
TLM	**T**ransfer **L**ength **M**ethod
WPE	**W**all **P**lug **E**fficiency

Physical Constants

Speed of Light	c	$=$	$2.997 \times 10^{8}\,\mathrm{m/s}$
Elementary Charge	e	$=$	$1.602 \times 10^{-19}\,\mathrm{C}$
Planck Constant	h	$=$	$4.135 \times 10^{-15}\,\mathrm{eV\,s}$
Boltzmann Constant	k	$=$	$1.380 \times 10^{-23}\,\mathrm{J/K} = 8.617 \times 10^{-5}\,\mathrm{eV/K}$
Thermal Energy	kT	$=$	$25.85 \times 10^{-3}\,\mathrm{V}$ at room temperature ($\approx 300\,\mathrm{K}$)
Vacuum Permittivity	ε_0	$=$	$8.854 \times 10^{-12}\,\mathrm{F/m}$

Symbols

α	absorption coefficient	cm^{-1}
δ	penetration depth	m
ε	electrical permittivity	F/m
η	efficiency	
θ	incident angle	$^{\circ}$
λ	wavelength of light	m
μ	electrical mobility	cm^{2}/V s
ν	frequency of light	Hz
ξ	antinode cavity enhancement factor	
ρ	electrical resistivity	Ω m
ρ_c	specific contact resistance	Ω cm^{2}
τ	carrier lifetime	s
ϕ	optical phase	
Φ	optical power flux	Wsr^{-1}
ω	angular frequency of light	rad^{-1}

a	array periodicity	m
A	area	m^{2}
A_{SRH}	Shockley-Read-Hall recombination coefficient	s^{-1}
B_{rad}	radiative recombination coefficient	cm^{3}s^{-1}
C_{Auger}	Auger recombination coefficient	cm^{6}s^{-1}
d_i	contact finger separation	m
D^{*}	specific detectivity	cm Hz$^{1/2}$ W^{-1}
E_g	energy gap	eV
F	cavity finesse	

ff	fill factor	
G	étendue	
G_e	emission rate enhancement	
G_{int}	spectrally integrated emission enhancement	
I	electrical current	A
J	electrical current density	Acm^{-2}
k	optical wavevector	cm^{-1}
l	optical pathlength	m
$\mathcal{L}$	optical intensity	W
L	optical radiance	$\mathrm{Wsr}^{-1}\mathrm{m}^{-2}$
L_{cav}	cavity length	m
L_s	current spreading length	m
L_t	transfer length	m
m_c	cavity order	
n	refractive index	
n_i	intrinsic carrier concentration	cm^{-3}
Q	cavity quality factor	
R	reflectance	
R_0	diode resistance at zero bias	Ω
R_c	contact resistance	Ω
R_s	series resistance	Ω
R_{sh}	sheet resistance	$\Omega/\square$
t	layer thickness	m
T	transmittance	
V	voltage	V
w	mesa width	m
w_c	contact width	m

To my family,
and to my Captain.

Chapter 1

Mid-Infrared Optical Gas Sensing

This Chapter gives an overview on the project background and motivations. A description of the conventional methods for gas detection is given, focusing on the advantages of optical gas detection based on the absorption of mid-infrared radiation. The different types of mid-infrared light sources and detectors are recalled, highlighting the performance of semiconductor-based mid-infrared light-emitting diodes and photodetectors. The driving applications and performance requirements for commercial carbon dioxide gas sensors are described to introduce the motivations for enhanced-efficiency low-power light-emitting diodes, which have been developed throughout this thesis work.

1.1 Introduction

The mid-infrared region of the electromagnetic spectrum can be defined as the wavelength interval between 2 µm and 12 µm, which corresponds to energies between 0.62 eV and 0.1 eV. In the last decades, this spectral region has received increasing interest from research and industrial institutions due to the presence of several transparent windows of the atmosphere (2–2.5 µm, 3–5 µm, 8–12 µm), in which no water vapour absorption is present. These wavelength ranges have been exploited for both civil and defence applications, such as thermal imaging and security countermeasures. Additionally, the mid-infrared region contains the characteristic absorption bands of a number of important molecules and gases that are useful to detect in our environment, and has therefore become particularly attractive for the development of optical sensor instrumentation. In fact, important gases such as methane (3.3 µm), carbon dioxide (4.2 µm), carbon monoxide (4.6 µm) and nitric oxide (5.3 µm) require accurate, real-time and non-invasive detection and monitoring in a wide range of concentrations (from ppb to almost 100 %). Optical sensors in the mid-infrared region find application in a variety of areas, including

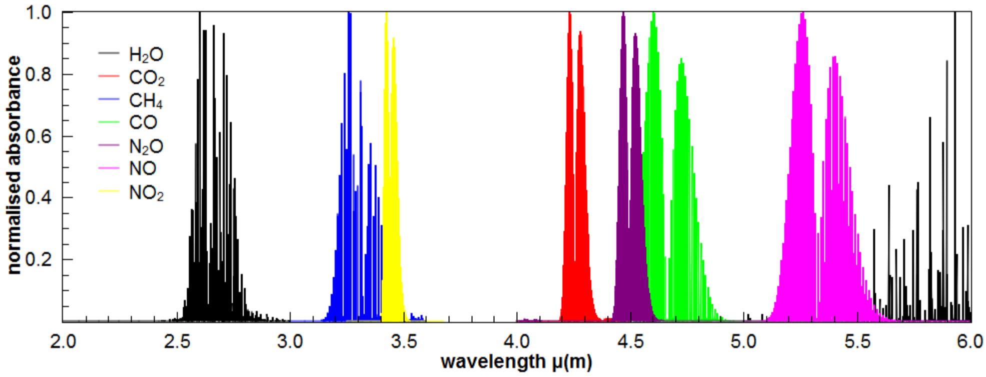

FIGURE 1.1: Absorption bands (normalised intensity) of relevant gas species in the 2–6 µm range (data from SpectralCalc.com based on HITRAN database).

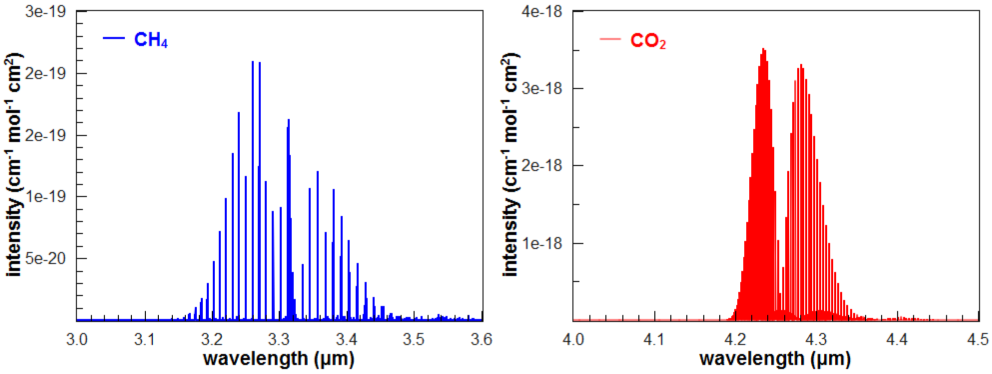

FIGURE 1.2: Zoomed in mid-infrared absorption spectra of CH_4 and CO_2 (data from SpectralCalc.com based on HITRAN database).

environmental pollution monitoring, chemical process control, optical gas sensing and non-invasive medical diagnostics [1, 2].

A typical plot of absorption bands of some relevant gas species in the 2–6 µm range is shown in Figure 1.1. These absorption lines provide a way to detect the presence of a gas and measuring its concentration, as described later in the Chapter.
The absorption of mid-infrared radiation is based on the fundamental transition of a vibrational mode of a molecule [3]. The absorption band is centred at the wavelength corresponding to the vibrational transition of the molecule. Commonly, the absorption band has a 2% bandwidth around the main transition wavelength, due to a fine structure of additional absorption lines given by simultaneous rotational transitions in the molecule. Examples of detailed absorption spectra of methane (CH_4) and carbon dioxide (CO_2) in the mid-infrared range are shown in Figure 1.2.

1.2 Methods for gas detection

A number of detection methods can be used to detect and monitor the presence of gas molecules. These can be summarised in two main categories:

- Chemical detection, such as electrochemical, catalytic and fluorescence sensors [4], and
- Spectroscopic techniques, based on the characteristic optical absorption of the gas species at specific wavelengths.

The electrochemical and catalytic sensors can be inexpensive and sensitive at ppm or ppb levels [5], but they suffer from some disadvantages, including poisoning, shorter lifetimes, and low selectivity. In particular, they can cross-respond to other gas species, including water vapour, causing false alarms or failing to danger. Moreover, they are based on gas sampling, thus precluding real-time data acquisition, which can be important in some applications such as process control.

In contrast, sensors based on optical absorption are immune to poisoning, they offer fast response, minimal drift and high gas specificity, with potentially zero cross-response to other gases. Additionally, the measurements can be made in real time and *in situ* without disturbing the gas sample. However, optical sensors tend to be more expensive than electrochemical sensors, mainly due to the cost of infrared sources, detectors and transfer optics. For this reason, there is an increasing demand for affordable and high performance sources and detectors operating in the mid-infrared wavelength range.

Optical gas detection using absorption spectroscopy is based on the application of the Beer-Lambert law [6]:

$$I = I_0 \cdot \exp(-\alpha l) \tag{1.1}$$

where I is the light transmitted through the gas cell, I_0 is the light incident on the gas cell, α is the absorption coefficient of the sample (in units of cm^{-1}) and l is the cell's optical pathlength (in cm). The absorption coefficient α is the product of the gas concentration and the specific absorptivity of the gas, which strongly depends on wavelength. For low αl, Equation 1.1 is linear with α:

$$\frac{\Delta I}{I_0} \approx \alpha l \tag{1.2}$$

where $\Delta I = I_0 - I$ and $\Delta I / I_0$ is the absorbance. Limits of detection can be quantified as the noise equivalent absorbance (NEA) or the minimum detectable absorption coefficient (α_{min}), allowing instrumental techniques to be compared without reference to the specific gas target.

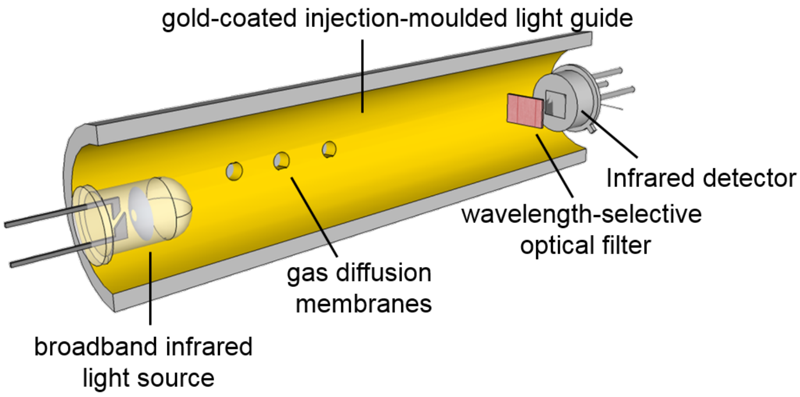

FIGURE 1.3: Schematic configuration of a non-dispersive infrared (NDIR) gas sensor with a gold-coated light guide between the source and the detector.

Depending on the application and its requirements, different light sources can be used in optical gas detector systems. For example, the narrow emission line of a laser source can be tuned to a single absorption line of a gas. Generally, this is the preferred choice for applications requiring high sensitivity and long distance target measurements. They represent the high-cost, low-volume sector of the gas detection market. On the other hand, light sources with a spectrally broad emission, like thermal sources and light-emitting diodes (LEDs), are mainly used in low-cost, high-volume applications. In the following sections, the focus will be on the latter, low-cost high-volume market sector.

1.3 Non-Dispersive Infrared sensors

The non-dispersive infrared (NDIR) gas sensing technique is one of the most widely used, thanks to its quite straightforward implementation. Therefore, it has great commercial significance, as traditional non-dispersive infrared sensors are low cost and can be built in very compact configurations. In a single channel sensor, the infrared radiation emitted from a broadband source is passed through an optical system, a gas sample volume and an optical filter that defines the spectral region of interest. According to Equation 1.2, the amount of radiation that reaches the detector is proportional to the absorption coefficient of the sampled gas and the length of the optical path. Generally, a narrowband optical filter is used to ensure that ideally no other gas species are absorbed in the transmission window. Thanks to the strong optical absorption in the mid-IR, acceptable limits of detection ($\approx 50\,\mathrm{ppm}$) can be achieved with relatively short optical path lengths ($\approx 10\,\mathrm{cm}$) [7]. The measurement is affected not only by the gas concentration, but also by any variation in the emission of the source. To minimise this additional effect, a reference measurement can be done by using a second filter covering a non-absorbed region of the optical spectrum.

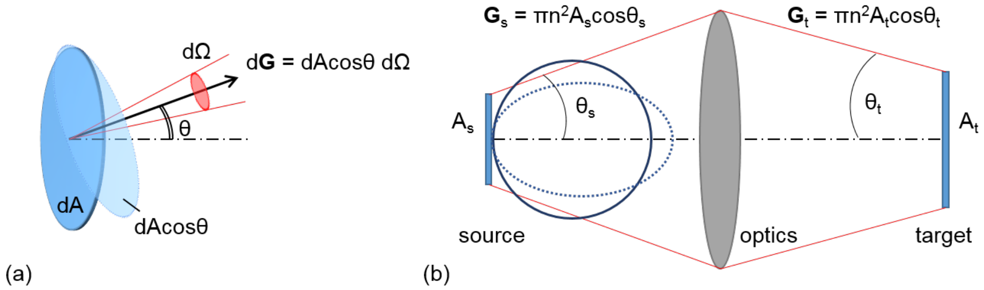

FIGURE 1.4: Schematic illustration of the *étendue* of an axially symmetric optical system.

A NDIR gas sensor can be designed as an optical system with a collimating lens at the source, plus a focusing optic and an optical filter at the detector. However, a simpler and cheaper option is to use a gold-coated light guide with no further optics between the source and detector. A schematic of this configuration is shown in Figure 1.3. Recent research on NDIR sensors has focused mainly on the implementation of small footprint sensors with optimised light coupling between source and detector and maximum optical path length for improved sensitivity [8].

The light collection efficiency of an optical system can be defined using the concept of *étendue*, also known as geometric extent, throughput or acceptance [9, 10]. The étendue G is a geometric quantity that measures the light flux collection capability of an optical system and it is invariant through an optical system with negligible scattering and absorption losses. The total power collected by an ideal optical system is the product of the étendue and the basic radiance of the source, L/n^2 (in $\mathrm{W\,sr^{-1}\,m^{-2}}$), where L is the radiance and n is the refractive index of the medium where the optical system is immersed. From the definition of radiance, the total power flux for a uniform and Lambertian source can be written as:

$$\Phi = L \iint dA\, \cos\theta\, d\Omega = L/n^2 \cdot G \tag{1.3}$$

with the étendue defined as:

$$G = n^2 \iint dA\, \cos\theta\, d\Omega \tag{1.4}$$

where A is the area of the aperture that limits the light beam, θ the angle with respect to the optical axis and Ω the solid angle subtended by the aperture, as shown in Figure 1.4a. In case of an axially symmetric system, as schematically illustrated in Figure 1.4b, the étendue reduces to [11]:

$$G = \pi n^2 A \sin^2\theta \tag{1.5}$$

In a lossless optical system, the element with the smaller étendue defines the overall throughput of the system, therefore geometrical considerations must be applied when coupling light into and from an optical system. Considering the system sketched in Figure 1.4b, if the source emits light outside the optics' acceptance angle ($G_s > G_t$), a portion of the light will be lost. In the same way, if the angle of emission is too small ($G_s < G_t$), the coupled light will be less than in the ideal case when the étendue of the system matches. The optimal coupling is achieved when $G_s = G_t$ and the light emitted from the source fills the acceptance angle of the optical system. Thus, the source area can determined according to:

$$A_s = \frac{G_t}{\pi \sin^2 \theta} \tag{1.6}$$

Once this condition is met, stronger coupling to the target can be achieved only by increasing the light emitted from the same source area and by having a more directional far field, so that a larger fraction of the total light is emitted within the acceptance angle of the optical system.

1.4 Infrared light sources for NDIR sensors

There are two main categories of broadband light sources that can be used in NDIR sensors: thermal sources and semiconductor sources. The requirements for a suitable infrared source vary depending on the application. However, some relevant characteristics can be identified as follows:

- High spectral radiance in the band of interest ($\geq 4\,\%$ bandwidth around the absorption wavelength of the target gas)
- Low electrical driving power (preferably $< 0.5\,\mathrm{W}$);
- Fast modulation ($> 50\,\mathrm{Hz}$);
- Temperature and long-term stability;
- Low manufacturing cost;
- Expected lifetime in normal operation ($>$ 5 years);

1.4.1 Thermal sources

The most common thermal sources used in NDIR sensors are microbulbs. The two main advantages of microbulbs for gas sensors are the relatively high spectral emission (2 mW over a 4% bandwidth at 4.2 µm) and their low cost ($ 1–2) [12].

However, microbulbs are typically operated up to 3000 K, and their emission contains a significant portion of visible and near IR radiation, that is not used in the measurements and therefore wasted [13]. Moreover, the optical transmission of their glass envelope drops to negligible levels at wavelengths longer than 5 µm, thus limiting their application. Additionally, microbulbs have limited electronic modulation frequency, typically up to 10 Hz.

More recent research has focused on the development of sources that are more spectrally efficient and capable of high modulation frequencies. Thin IR emitting membranes based on MEMS technology have been proposed [14, 15]. Their emission spectrum follows the Plank emission curve for a grey body. Their lower temperature operation (870 to 1700 K) gives improved spectral efficiency for the mid-IR region and longer device lifetimes. Microstructured coatings have also been proposed to improve the spectral efficiency at a given wavelength by plasmonic or photonic bandgap approaches [16–18].

1.4.2 Semiconductor sources

The most suitable semiconductor broadband light source for high-volume gas detection applications is a mid-infrared light-emitting diode (LED) [12]. Mid-IR LEDs, based on narrow bandgap III-V semiconductors, can be designed to emit at specific wavelengths, giving an excellent spectral matching between the optical emission and the absorption bands of the target gas, as shown in Figure 1.5. For this reason, they offer superior spectral efficiency compared to thermal sources [19]. Moreover, they can be operated at much higher modulation rates, when used in conjunction with semiconductor photodetectors.

A disadvantage of semiconductor sources is that their emission depends strongly on temperature, due to their energy gap E_g being close to kT at room temperature. The temperature coefficient can be as high as 1% K^{-1} for an LED operated at room temperature compared to the 0.02% K^{-1} for a filament lamp. This requires the LED to be maintained at a constant temperature or, alternatively, this variation can be taken into account with a temperature compensation data processing technique. A second disadvantage is that semiconductor sources are generally more costly than thermal sources, unless a high-volume production is established.

Considerable research work has been invested into the extension of room-temperature LED operation to mid-infrared wavelengths, where thermally activated carriers reduce the radiative efficiency [2, 20, 21]. Moreover, different techniques have been applied to improve the optical coupling efficiency and improve the directionality of the output [22–29]. These aspects are discussed in more detail in Chapter 2.

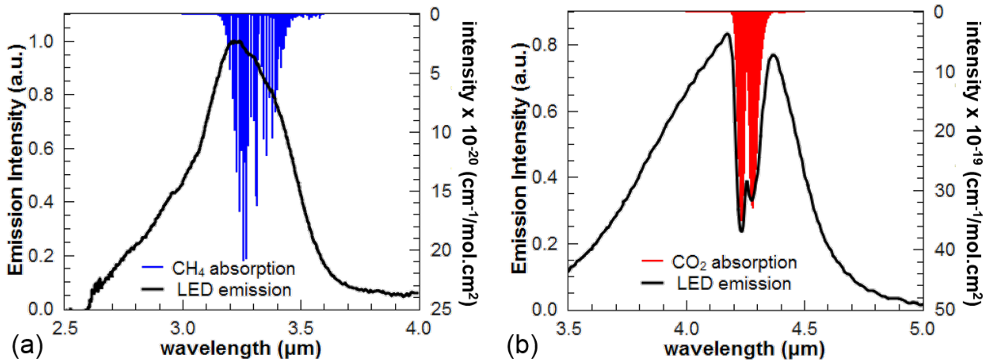

FIGURE 1.5: Emission spectra of mid-infared LEDs designed for the detection of (a) CH_4 and (b) CO_2 . The absorption spectra of the gases are shown to indicate the good spectral matching.

1.5 Infrared detectors for NDIR sensors

The detection limit of the optical sensor system depends on the optical power emitted by the source within a defined spectral range and on the detector noise. Optical detectors are commonly characterised using a normalised figure of merit. The specific detectivity D^* is equal to the signal-to-noise ratio under uniform irradiance, normalised to the detector area A_d and the measurement bandwidth Δf:

$$D^* = \frac{\sqrt{A_d \Delta f}}{\mathrm{NEP}} \quad (\mathrm{cm\,Hz^{1/2}\,W^{-1}}) \tag{1.7}$$

where NEP is the noise equivalent power.

Thermal detectors conventionally used in gas sensors are pyroelectric detectors and thermopiles. Both have been already developed for low-cost, high-volume production. They show a specific detectivity around $10^8\,\mathrm{cm\,Hz^{1/2}\,W^{-1}}$, but both their responsivity and noise performance decrease significantly with increasing frequency above few Hz. For this reason they can only be used in combination with thermal sources modulated at low frequencies.

Photovoltaic and photoconductive detectors can cover the entire mid-infrared region with high detectivity, but in most cases they require cooling to 77 K [30, 31]. This adds unwanted costs and practical inconvenience, especially for portable applications. An improved design for a photodiode operating at room temperature was pioneered by QinetiQ [32–34], providing a specific detectivity D^* around $10^9\,\mathrm{cm\,Hz^{1/2}\,W^{-1}}$ with no additional cooling. This design is described in more detail in Section 2.3 and is used as a reference throughout this work.

1.6 Carbon dioxide sensing: Applications and requirements

The increasing market demand for carbon dioxide (CO_2) gas sensors is mainly driven by their application for control of indoor air quality within buildings and transports systems [35, 36]. As human exhaled air is rich in CO_2 , the monitoring of its concentration gives an accurate measurement of people occupancy in a known air volume. The use of CO_2 sensors, usually integrated with temperature and humidity sensors, has allowed the development of demand control ventilation (DCV) systems. Through these technology, heating, ventilating and air conditioning systems can be controlled and adapted to suit the levels of people occupancy [37]. Buildings with ventilation monitoring and control based on DCV systems have demonstrated up to 25 % of energy savings [37]. As commercial buildings are responsible for at least 40 % of the world's total energy consumption [38], the extensive use of DCV systems with CO_2 sensors can give a significant contribution in achieving global energy savings.

Moreover, the advancement towards autonomous wireless sensors allows the development of sensors networks, which provide low-cost flexible installation and support real-time data acquisition from multiple sensors. Other significant applications in which the use of CO_2 sensors can be exploited are in the horticultural [39], automotive [40] and medical sectors [41].

These markets are creating high-volume demand for low-cost autonomous CO_2 gas sensors. The main requirements for this type of sensors are:

- reduced power consumption for extended battery life operation;
- fast stabilisation time; and
- sensor portability.

As introduced in Section 1.2, commercially available CO_2 sensors are based on two types of technology: solid electrolyte and non-dispersive infrared (NDIR) [1, 42, 43]. Solid electrolyte sensors have cost advantages, but are known to cross-respond to other gas species, including water vapour, and thus are suitable only for the least demanding applications. NDIR sensors, instead, are the most widely used for real-time measurement of CO_2 , thanks to their higher performance in terms of long-term stability and accuracy. The majority of currently available NDIR CO_2 sensors are based on thermal sources and pyroelectric or thermopile detectors. These are associated with long stabilisation times (typically 1 to 10 minutes) and high power consumption (typically $> 200\,\mathrm{mW}$), which requires hard wiring or causes short battery life. An alternative configuration consists of a NDIR CO_2 sensor based on a semiconductor mid-infrared light-emitting diode and photodiode. This configuration has been introduced by QinetiQ [21] and then

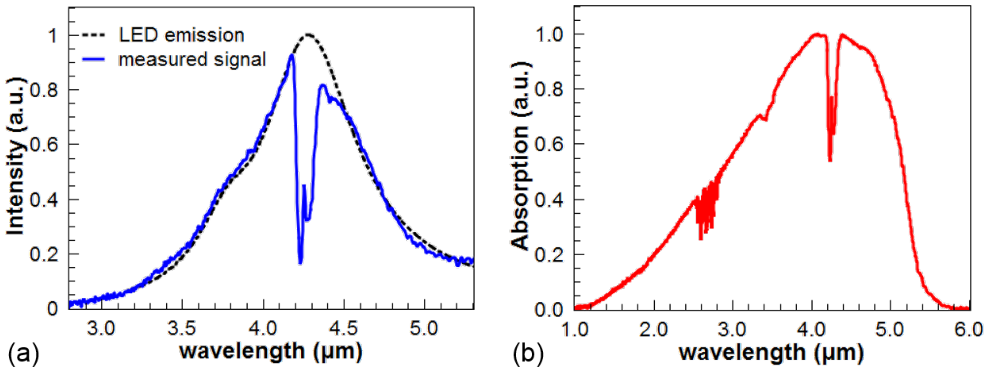

FIGURE 1.6: (a) Emission spectra of an $Al_xIn_{1-x}Sb$ LED with optimised emission around the CO_2 lines at 4.26 µm ($x = 0.05$). (b) Absorption spectra of an $Al_xIn_{1-x}Sb$ photodiode with peak detectivity at 4.26 µm ($x = 0.03$).

successfully commercially exploited by Gas Sensing Solutions Ltd. [44]. Comparing the performance with conventional NDIR sensors based on thermal sources and detectors [12, 45, 46], this solution offers significant advantages:

- intrinsic wavelength selectivity and stability,
- room temperature operation,
- low power consumption (< 3 mW),
- rapid stabilisation time (< 2 s),
- fast modulation rates (tens of kHz).

The sensor comprises a narrow bandgap III-V semiconductor light-emitting diode (LED) and photodetector (PD). As described in Section 1.3, the emitted mid-infrared radiation is launched into an optical path into which the gas can diffuse, causing a reduction in the detected light intensity at the specific gas absorption wavelength. The output parameter is the CO_2 concentration, stabilised over the sensor operating temperature range, and the sensitivity is determined by the optical path length.

The LED and PD are designed to have maximum emission and detection in a relatively narrow spectral region around the target wavelength. Therefore, it is not necessary to use any additional optical filtering, which further reduces the cost and complexity of the optical design. Optical modelling of the sensor sensitivity and noise were performed by GSS Ltd. to identify the suitable optical path length and data processing to comply with the required CO_2 concentration detection range (from ambient up to 100 %) and measurements accuracy (± 5 % of reading) [46]. A 20 mm path length provides the desired accuracy for concentrations from 0.5 % to 100 %, while a 70 mm path length is required

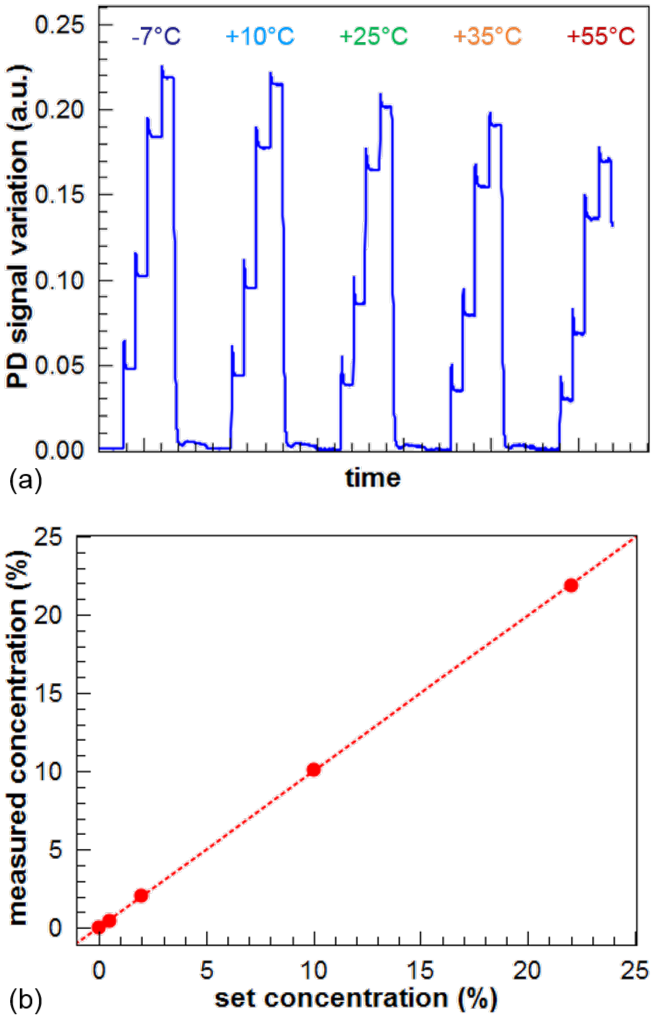

FIGURE 1.7: (a) Photodiode signal variation of a CO_2 sensor from Gas Sensing Solutions. The sensor is stepped through CO_2 concentrations of 0.5%, 2%, 10% and 22% over temperatures of $-7\,°C$, $10\,°C$, $25\,°C$, $35\,°C$ and $55\,°C$ (Courtesy of Calum MacGregor, Gas Sensing Solutions Ltd. [47]). (b) Linearised measured output signal against set CO_2 concentration at $25\,°C$.

for lower concentration levels, from 400 ppm (ambient) to 0.5 %. Depending on the desired accuracy the sensor is built into either a dome geometry or with a folded optic that provides multiple reflections between LED and PD. Both geometries are produced using low cost injection moulded optics, coated with a thin gold layer. Dedicated electronics control the LED drive current and the PD signal processing. Figure 1.7a shows an example of the photodiode raw signal variation when the sensor is stepped through four CO_2 concentration levels (0.5%, 2%, 10%, 22%) and six temperatures ($-7\,°C$, $10\,°C$, $25\,°C$, $35\,°C$ and $55\,°C$). The linearised measured CO_2 concentration is plotted in Figure 1.7b. From these data, the dependence of the sensor performance on temperature can be analysed:

- The amplitude of the output signal decreases with increasing temperature. This

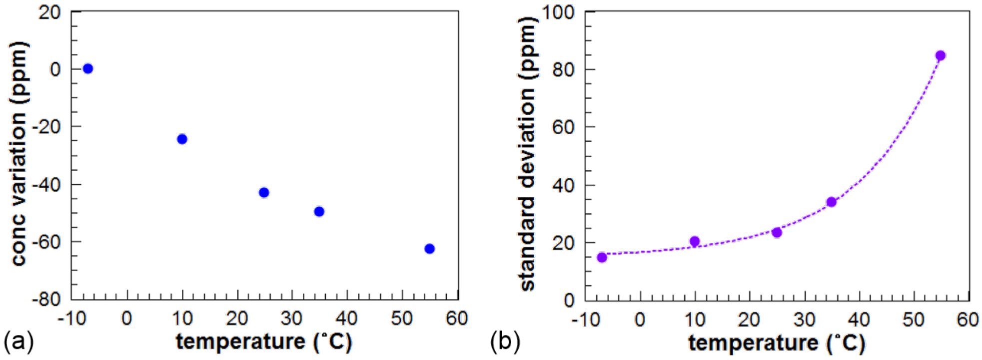

FIGURE 1.8: (a) Variation in the measured CO_2 concentration at a set gas concentration of 0.5% as a function of temperature. (b) Standard deviation at a set gas concentration of 0.5% as a function of temperature.

is due to the shift of the LED emission spectrum with temperature, which results in a poorer alignment of the emission peak with the CO_2 absorption band. The variation in the measured CO_2 concentration at 0.5 % as a function of temperature is shown in Figure 1.8a.

- The noise amplitude increases with temperature, due to the dominant contribution of the photodiode dark current noise for temperature $\geq$ 20 °C. The measured standard deviation at 0.5 % as a function of temperature is shown in Figure 1.8b.

These features together contribute at the reduction of the signal-to-noise ratio (SNR) with increasing temperature. As a consequence, a data compensation technique is required. A factory-based automated calibration procedure is performed by stepping the sensors through the full span of CO_2 concentrations and operating temperature. The calibration data are uploaded into the signal processing electronics and used for real-time compensation.

The sensor power-up/measurement time is typically one second, dominated by electronic initialisation, with operating voltage of 3.3 V, average current of 1.1 mA and power consumption of 3.3 mW in continuous operation [46]. Performance parameters in comparison with other sensors available on the market are summarized in Table 1.1. Thanks to the low energy required for each reading ($\approx$ 12 mJ in pulsed operation), the sensors has more than 10 year battery life when operated at less than 10 measurements per hour, which is within the requirements for building control applications and portable sensors for industrial safety and medical applications. The energy usage can be further reduced by optimising the drive electronics and the signal processing. This allows to break the 10 mJ per measurement limit that enables the use of energy harvesters in self-powering devices. Industrial collaboration with world leaders Schneider Electric and EnOcean Gmbh has allowed the development of a unique technology, which provides

TABLE 1.1: Performance of commercial single channel NDIR CO_2 sensors [46].

Manufacturer	Measurement Range	Accuracy (ppm)	Power Consumption (mW)	Warm-up Time (s)
GSS	ambient-5000 ppm	±50	3.3	1.2
SenseAir	ambient-5000 ppm	±70	315	60
OptoSense AS	ambient-2000 ppm	±50	500	60
GE Telaire	ambient-2000 ppm	±30	165	120

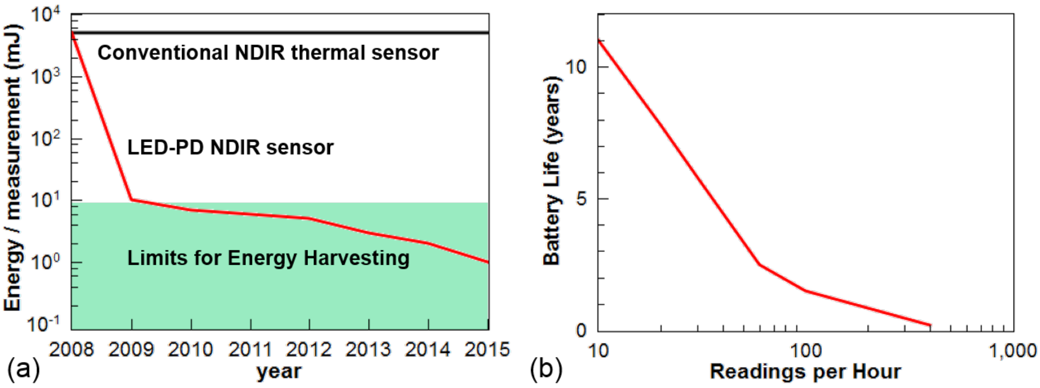

FIGURE 1.9: (a) Evolution of energy per measurement of LED/PD CO_2 sensor in comparison with conventional NDIR sensors and consumption limits compatible with energy harvesting. (b) Battery life as a function of number of measurements per hour (data from GSS Ltd. technical publications [46]).

CO_2 detection from ambient to 3000 ppm, with ± 15 ppm resolution and compatible with solar cell powering [46, 48].

1.7 Motivation and Overview

The work discussed in this thesis was developed as an Industrial CASE studentship, funded by the Engineering and Physical Sciences Research Council (EPSRC). The project was carried out in close collaboration with Gas Sensing Solutions (GSS) Ltd., with the main purpose of improving the overall performance of their commercial CO_2 optical gas sensor.

As discussed in Section 1.6, the low power consumption is an essential requirement for portable and autonomous sensors, which represent the main target market for GSS devices. The current production LEDs show less than 2 % internal quantum efficiency (IQE) and about 2×10^{-4} external quantum efficiency (EQE), as discussed in more detail in Section 2.4. Therefore, improving the LED efficiency is of fundamental importance: while maintaining a low electrical input power, a higher output optical power is achieved. This results in a higher signal-to-noise ratio of the detected signal and, therefore, a higher sensitivity of the overall sensor. Improved sensor performance would allow GSS to consolidate its current market of low power portable CO_2 gas sensors and open up new opportunities to expand to different sectors of the optical sensors' market, in which devices with higher resolution and lower noise would be beneficial.

With these background and performance requirements in mind, this Ph.D. project focussed on the improvement of the electrical and optical performance of AlInSb mid-infrared LEDs, with particular attention to the enhancement of the external efficiency of the devices, by exploring different approaches:

- The improvement of the diode epi-layer structure for enhanced optical emission, while maintaining the electrical characteristics compatible with the sensor's driving electronics.
- The optimisation of the device geometry design for the uniform distribution of the bias current and the efficient use of the device area for light generation and extraction.
- The evaluation of techniques aiming at overcoming the LED's low extraction efficiency, such as the introduction of distributed Bragg reflectors and periodic metallic array patterns.

At first, significant progress had to be made on the understanding of the material system and the existing devices' operational characteristics. In fact, LED devices based on this material system were never fabricated nor characterised at the University of Glasgow before. A strong asset for this work has been the close collaboration with Dr. Matthew Steer, responsible for the growth of the AlInSb material by Molecular Beam Epitaxy (MBE) at the West of Scotland Science Park. This allowed a quick feedback process between the growth and characterisation of LED devices, while varying a number of design parameters. The following aspects of the LED design were evaluated during this work and are discussed in detail in the following chapters:

- The effect of layers' thickness and doping concentration on the current-voltage characteristics and the emitted optical power of the LED;
- The effect of the device size on the coupling efficiency and contribution of the surface leakage current in devices with higher surface-to-area ratio;
- The analysis of the current crowding effect and the development of an improved contact geometry design;
- The introduction of a resonant-cavity structure to redirect a higher fraction of the isotropic emitted light towards the top surface of the device;

- The incorporation of a plasmon-resonant array pattern on the top device surface to enhance the output coupling.

Both the last two approaches introduce an additional filtering effect of the transmitted light around the target resonant wavelength, which can be beneficial for both the LEDs and the photodiodes, by improving their spectral matching with the target gas absorption band.

During this research activity, it has been of fundamental importance to keep into consideration the application and requirements of the LED devices for their commercial exploitation. Beside the initial investigation, it was necessary to consider the devices' reliability and reproducibility, and evaluate any possible fabrication challenge for the technology transfer to mass production. Some optimisation approaches and techniques, developed during this research through device modelling and prototyping, have already been transferred to Gas Sensing Solutions, and its partner Compound Semiconductor Technology (CST) Ltd., for production via UV lithography on 4 inch wafers and for testing in the commercial gas sensor configuration.

The next chapters are organised as follows:

Chapter 2 describes the background theory of LED operation and the performance limitations in terms of light extraction efficiency. A review of the material systems used for mid-infrared LEDs in the literature is reported. The material characteristics and performance advantages of the antimonide-based structure used in this project are discussed.

Chapter 3 reports on the description of the standard process steps used in the fabrication of the devices. Photolithography, mesa etching, passivation and metal deposition processes are briefly described and specific requirements for the fabrication of AlInSb LEDs are discussed. The final fabrication flow developed during this work is presented with schematics and representative images.

Chapter 4 discusses the electrical and optical characterisation of the devices fabricated accordingly to the process described in Chapter 3. The current-voltage characteristic and electroluminescence spectra are analysed as a function of a number of device parameters, including the device layer structure, doping concentration of the contact layers, surface passivation and dimensions of the mesa area. The transfer-length method (TLM) is used to characterise the ohmic contacts to the semiconductor material and to evaluate both the specific contact resistance and the bulk resistivity of the semiconductor material. Reflectance and transmittance measurements are used to confirm the refractive index dispersion of the semiconductor material used for the device modelling.

Chapter 5 focuses on the effect of current spreading and current crowding in mid-infrared LEDs grown on semi-insulating substrates. The background theory is discussed, based on the analysis of the device's equivalent circuit. The theoretical analysis of the current density distribution across the device area is confirmed by the experimental spatial mapping of the photocurrent generated in the device under illumination. Consequently, an improved contact geometry is designed and tested, giving a significant improvement of the LED efficiency.

Chapter 6 describes the design, model and implementation of resonant-cavity LEDs. The background theory of resonant-cavity enhanced optical devices is discussed, together with the design parameters and the Distributed-Bragg Reflector (DBR) modelling by the transfer matrix method. Results and parameters optimisation are discussed to obtain maximum enhancement at the desired wavelengths. The effects of the significantly enhanced and spectrally narrower emission on the overall sensor performance are analysed and the possibility of implementing the resonant-cavity structure in production devices is discussed.

Chapter 7 reports on the research activity developed on plasmon-enhanced mid-infrared optical devices. The background on optical enhancement through excitation and coupling to surface plasmon modes at the interface between a patterned metal film and a dielectric is reviewed. The process optimisation for the fabrication of plasmonic array patterns on mid-infrared devices is discussed. The modelling of the spectral characteristics of patterned metal hole arrays by Finite-Difference Time-Domain (FDTD) numerical simulations is analysed and compared to the measured transmittance of fabricated test samples. Measurement of the spectral response of fully processed LED devices with 2D-periodic metal hole arrays patterned on the top surface are presented and further development work is discussed.

Chapter 8 summarises the significant progress that was achieved during this work on the design of efficient mid-infrared AlInSb LEDs and highlights the improved performance of the devices demonstrated through the implementation of the outcomes of this research.

Chapter 2

Antimonide-based Light-Emitting Diodes

This Chapter outlines the physics and technology challenges associated with the realisation of efficient mid-infrared light-emitting diodes. The processes that limit the device performance are considered, with particular attention to the specific aspects peculiar to light-emitting diodes based on narrow bandgap III-V semiconductor materials.

2.1 Background on mid-infrared LEDs

As discussed in Chapter 1, the development of monochromatic sources in the mid-infrared (3–5 µm) wavelength range has received significant research interest in the recent years. In particular, the extension of mid-infrared LEDs operation to room temperature, without the requirement of additional cooling, has attracted growing attention due to their application in optical gas sensors [1, 2, 12, 23].

A number of semiconductor materials have been investigated by different research groups in order to achieve high efficiency, uncooled LED operation in the mid-infrared spectral region [20, 33, 49, 50]. The first mid-infrared LEDs were grown by liquid phase epitaxy (LPE). The advent of epitaxial growth techniques, such as molecular beam epitaxy (MBE) and metalorganic vapour phase epitaxy (MOVPE), allowed a wider range of available materials and the development of more efficient LEDs based on double heterostructure and quantum structures [51, 52]. Extensive research was carried out on p-n junction devices from II-VI and IV-VI materials, in particular the lead salts (alloys of PbS, PbSe, PbTe and CdS) [53, 54]. Even if these materials have a significant lower Auger recombination rate than III-V narrow bandgap semiconductors, they are

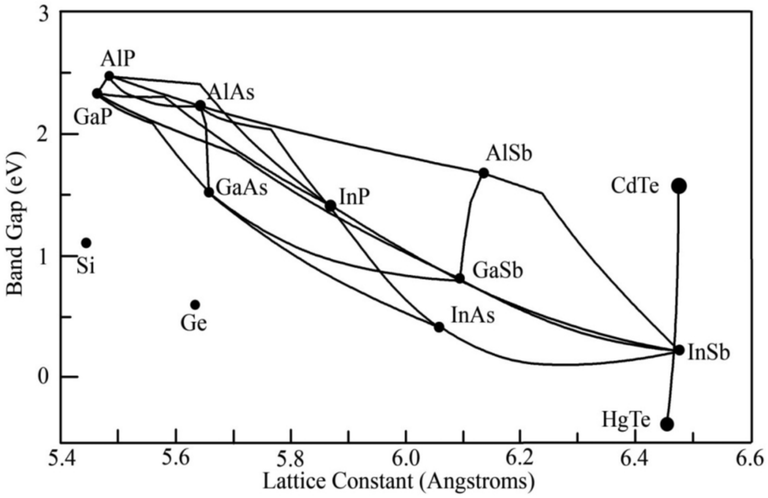

FIGURE 2.1: Bandgap versus lattice constant plot for common semiconductor materials (adapted from [30]).

characterised by low thermal conductivity, poor substrate quality and low immunity to moisture [55]. Despite the massive development of HgCdTe infrared detector, only few reports are available on electroluminescence from this material. The best results were reported from devices grown on CdZnTe substrate, showing 6 % efficiency at 3.5 µm at 300 K thanks to the use of an optical immersion lens [56].

Consequently, structures based on narrow bandgap III-V semiconductors, such as InAs and InSb and their related alloys, were identified as the best candidates for the development of efficient mid-infrared LEDs operating at room temperature. In particular, for the development of optoelectronic devices in the near to mid-infrared wavelengths, much interest has been focused on InAs and GaSb based alloys (for example InAsSb, InGaAsSb and InAsSbP) [20]. A number of LEDs have been successfully developed covering the mid-infrared range up to 3.8 µm [57–59]. Less results are instead available for III-V LEDs operating at room temperature in the 4 µm to 5 µm range, particularly interesting for the detection of carbon dioxide (4.26 µm) and carbon monoxide (4.6 µm). The main technology is based on InAsSb heterostructures, developed by Yakovlev's and Matveev's research groups at the Ioffe Institute in St Petersburg and by Krier's group at the University of Lancaster. Electroluminescence from InAsSb/InAsSbP bulk symmetric double heterostructure LEDs, grown by LPE, have been demonstrated at 300 K up to 4.6 µm [60]. The output power is higher than 1 mW when operated at a peak injection current of 2 A, pulsed at 1 kHz and at 0.2 % duty cycle. This correspond to an external quantum efficiency of 2×10^{-3}. However, when increasing the pulse width to 5 %, the measured output power decreases significantly, suggesting lower internal efficiency as effect of Joule heating and dominant non-radiative recombination mechanisms at higher injected currents. Electroluminescence around 4 µm has also been reported from multi-quantum well (MQW) structures grown by MBE [61]. The measured output power at

Table 2.1: Operating parameters of III-V mid-infrared LEDs at room temperature [62].

Material system	Technology	Peak Power (pulsed)	λ_{peak} (µm)	η_{ext}	Ref.
InAs	LED	560 µW	3.5–3.7		[58]
InAs/GaInSb/InAs/AlGaAsSb	WQW	4 µW	3.3	3×10^{-4}	[57]
InAsSb/InAsSbP	BSDH	> 1 mW	4.6	2×10^{-3}	[60]
InAsSb/InAs	MQW	1.4 µW	3.6–4.0	2×10^{-5}	[61]
InSb/AlInSb	LED (4x4 array)	≈ 17 µW	5.3	4×10^{-4}	[21]

room temperature was 1.4 µW when biased at a peak injection current of 500 mA with 50 % duty cycle, giving an external quantum efficiency of 2×10^{-5}.

The material system and diode heterostructure used in this work follow from the structure proposed by Ashley et al. at QinetiQ Malvern [50]. The LEDs are based on MBE-grown InSb/AlInSb, with a thin barrier of wider bandgap material that provides carrier confinement in the active region and helps reducing the effect of thermally generated carriers, which contribute to leakage currents in narrow bandgao materials. At room temperature, InSb has an energy gap of 0.18 eV, thus potentially allowing emission up to 7 µm. The structure is similar to the one developed for uncooled mid-infrared detector and its behaviour is described in more detail in Section 2.3. Room temperature electroluminescence from this structure has been reported up to 5.3 µm for 2.5 % Aluminium composition with an external quantum efficiency of 4×10^{-4} [21].

A summary of the most significant work discussed in the literature with operating parameters of room temperature mid-infrared LEDs is listed in Table 2.1.

2.2 LEDs performance limitations

An ideal LED would emit a photon into air for each injected electron-hole pair. This means having a unit efficiency, where every injected electron-hole pair generates a photon from the active region and each photon is extracted from the LED chip and emitted into air. This, however, cannot happen because of a number of limiting loss mechanisms. The overall power conversion efficiency, or wall plug efficiency η_{WPE}, of an LED is defined as the ratio of the radiant flux over the electrical input power [22]:

$$\eta_{\mathrm{WPE}} = \frac{\text{emitted flux (W)}}{\text{electrical input power (W)}} = \eta_{\mathrm{el}}\, \eta_{\mathrm{ext}} = \eta_{\mathrm{el}}\, \eta_{\mathrm{int}}\, \eta_{\mathrm{extr}} \tag{2.1}$$

where η_{el} is the electrical efficiency and η_{ext} is the external quantum efficiency, defined as the product of the internal quantum efficiency η_{int} and the extraction efficiency η_{extr}. The electrical efficiency η_{el} is associated with the ohmic losses given by the finite resistance of the contacts and the epitaxial layers. The internal quantum efficiency η_{int} and the extraction efficiency η_{extr} are discussed in more detail in the following sections.

2.2.1 Internal Quantum Efficiency

The internal quantum efficiency is defined as the ratio of the number of photons generated into the active region per second to the number of electron-hole pairs injected into the LED per second [63]. In semiconductors, there are two fundamental mechanisms for electrons and holes recombination:

- *radiative* recombination, when an electron-hole pair recombines with the generation of a photon of energy equal to the bandgap energy of the semiconductor;
- *non-radiative* recombination, when the energy of the electron-hole pair recombination is transferred to a phonon, a vibrational energy of the lattice atoms.

The ratio between radiative and non-radiative recombination defines the LED internal quantum efficiency, which can be expressed as the probability of radiative recombination over all possible recombination processes [22]:

$$\eta_{\text{int}} = \eta_{\text{inj}} \frac{\tau_{\text{rad}}^{-1}}{\tau_{\text{rad}}^{-1} + \tau_{\text{non-rad}}^{-1}}, \tag{2.2}$$

where τ_{rad} and $\tau_{\text{non-rad}}$ are the radiative and non-radiative carrier lifetime, respectively. The probability of non radiative recombination is the sum of the probabilities of the two main non radiative recombination mechanisms, Schockley-Read-Hall and Auger, which are discussed in the following: $\tau_{non-rad}^{-1} = \tau_{SRH}^{-1} + \tau_{Auger}^{-1}$. Additionally, the injection efficiency η_{inj} takes into account the efficiency of the carriers confinement in the active region.

Figure 2.2 schematically illustrates the three main recombination mechanisms in direct bandgap semiconductors that contribute to LEDs internal quantum efficiency.
The non-radiative Shockley-Read-Hall (SRH) recombination is caused by defects in the semiconductor crystal structure [64]. These can be native defects and dislocations, which create one or more energy levels within the bandgap of the semiconductor. SRH recombination through these trap levels is proportional to the carrier concentration and mainly contributes to the internal quantum efficiency at low temperature and low injected current densities.
Radiative recombination occurs when an electron in the conduction band recombines with a hole in the valence band, with emission of a photon. In the limit of a high level of injection, in which the excess carrier concentration generated by the injected current is higher than the equilibrium concentration ($\Delta n \gg (n_0 + p_0)$), the radiative recombination rate is proportional to the square of the carrier concentration [63]:

$$R_{\text{rad}} \approx B \cdot n^2 \tag{2.3}$$

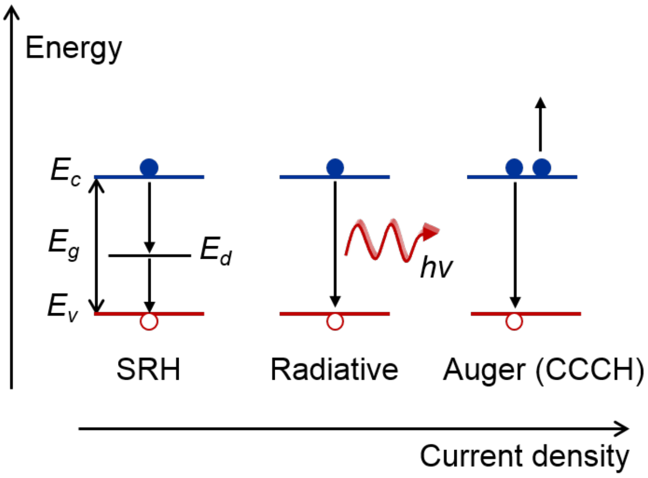

FIGURE 2.2: Schematic illustration of the three main recombination processes in direct gap semiconductors, ordered by the dominant contribution as a function of injected current density. Shockley-Read-Hall (SRH) recombination through deep levels in the bandgap associated with defect and impurities; radiative recombination with emission of a photon with energy equal to the material bandgap; and Auger recombination with excitation of a second electron to a high level within the conduction band (CCCH).

where B is the recombination coefficient and has typical values of 10^{-11}–10^{-9} cm^3/s in direct gap III-V semiconductors. As radiative recombination involves two charge carriers, it is the dominant recombination process at intermediate current densities.

In the non-radiative Auger recombination process, the energy generated by the electron-hole recombination is transferred to a third carrier, which is excited to a higher energy level within the same band and in the end relaxes back to the band edge by transferring its energy to multiple phonons [65, 66]. For high injection levels, the Auger recombination rate reduces to:

$$R_{\text{Auger}} \approx C \cdot n^3 \tag{2.4}$$

where C is the Auger coefficient and has typical values of 10^{-28}–10^{-29} cm^6/s in III-V semiconductors. As the Auger recombination involves the interaction of three charge carriers, it is generally the main non-radiative recombination mechanism at high temperature and high current densities. The two dominant processes in narrow bandgap direct semiconductors are Auger-1 (CCCH) and Auger-7 (CHHL) [65, 67]. The letters in the notation indicate the bands containing the carriers taking part in the Auger process, C is the conduction band, H the heavy holes band and L the light holes band. In the CCCH process, an electron from the conduction band recombines with a hole in the heavy holes band, while a second electron is excited to a higher level within the conduction band. In the CHHL process, instead, the recombination of an electron from the conduction band with a hole from the heavy holes band, is accompanied by the transfer of a high-energy hole from the heavy to the light holes band. CCCH dominates in n-type material, while CHHL prevails in p-type narrow bandgap semiconductors.

Table 2.2: Electronic and optical properties of III-V semiconductors at 300 K. Data from [68].

	GaAs	InAs	InSb
energy gap E_g (eV)	1.42	0.35	0.18
intrinsic carrier concentration n_i (cm^{-3})	2.1×10^6	1.0×10^{15}	2.0×10^{16}
intrinsic resistivity ρ (Ω cm)	3.3×10^8	0.16	4×10^{-3}
effective mass ratio m_e/m_0	0.063	0.023	0.014
electron mobility μ_e (cm^2/V s)	8.5×10^3	$\leq 4.0 \times 10^4$	$\leq 7.7 \times 10^4$
hole mobility μ_h (cm^2/V s)	400	≤ 500	≤ 850
refractive index	3.3	3.51	3.96
radiative coefficient B (cm^3/s)	7.0×10^{-10}	1.1×10^{-10}	5.0×10^{-11}
Auger coefficient C (cm^6/s)	1.0×10^{-30}	2.2×10^{-27}	5.0×10^{-26}

Additionally, significant contribution to the non-radiative recombination can derive from the semiconductor surface. Surfaces represent a strong perturbation of the crystal lattice periodicity and introduce electronic states in the semiconductor bandgap where they act as recombination centres. Surface recombination causes reduced internal quantum efficiency and heating of the semiconductor surface, which can lead to a reduced lifetime of the LED device [63].

Some particular considerations need to be made on the relative contribution of the different non-radiative recombination mechanisms depending on the III-V semiconductor material [20]. Compared to the more conventional and developed GaAs-based compounds, narrow bandgap III-V semiconductors such as InAs and InSb have about an order of magnitude lower radiative recombination coefficient and three to four orders of magnitude higher non-radiative recombination coefficient, as can be seen from data in Table 2.2. Therefore, the internal quantum efficiency of LEDs based on such materials are significantly lower compared to GaAs-based LEDs. Additionally, surface recombination becomes more significant and has to be addressed adequately. SRH recombination through impurities and traps has a significant contribution in the efficiency of InAs devices at room temperature. Auger recombination is instead the dominant non-radiative recombination mechanism in InSb devices due to its high intrinsic carrier concentration at room temperature [62].

With the improvement of the material quality and an accurate design of the LED layer structure and device geometry, aiming at minimizing the non-radiative recombination processes, higher internal quantum efficiency can be obtained.

2.2.2 Extraction Efficiency

The extraction efficiency is defined as the ratio of the number of photons emitted into free space to the number of photons generated in the LED active region. The poor

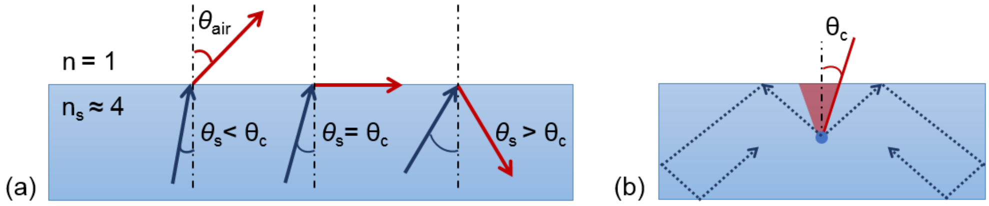

FIGURE 2.3: Schematic illustration of (a) Snell's law and (b) escape cone in case of a small critical angle of 15° for high refractive index semiconductor materials.

extraction efficiency is a common problem for most LEDs due to the high refractive index of the semiconductor material compared to the surrounding medium, which is typically air. This large difference in refractive index results in most of the light being trapped inside the semiconductor material, as a result of total internal reflection (TIR) and Fresnel reflection [22, 69]. This issue is even more pronounced in mid-infrared LEDs due to the even higher refractive index values of narrow bandgap material ($n_{\mathrm{InSb}} \approx 4$).

Snell's law of refraction is used to describe the relation between the incident θ_s and refracted θ_{air} angle of light when incident on a planar semiconductor-to-air interface, as illustrated in Figure 2.3:

$$n_{\mathrm{s}} \sin \theta_{\mathrm{s}} = n_{\mathrm{air}} \sin \theta_{\mathrm{air}} \tag{2.5}$$

For angle of incidence greater than the critical angle $\theta_c = \arcsin(n_{\mathrm{s}}/n_{\mathrm{air}})$, the value of the refracted angle becomes complex and the light is totally internally reflected at the interface. Therefore, the critical angle for TIR defines the so-called *escape cone*: photons emitted at an angle outside the escape cone will be trapped inside the semiconductor material. The extraction efficiency is determined by the fraction of photons emitted into the escape cone. For an isotropic light source emitting from a high-index semiconductor material into air:

$$\eta_{\mathrm{extr}} = \frac{1}{2}\int_0^{\theta_c} T(\theta_{\mathrm{s}}) \sin \theta_{\mathrm{s}} d\theta_{\mathrm{s}} \tag{2.6}$$

where $T(\theta_{\mathrm{s}})$ is the polarisation-averaged Fresnel transmission. The TIR gives a contribution which can be approximated by $1/4n_{\mathrm{s}}^2$. The Fresnel reflection at the interface gives an additional reduction of $4n_{\mathrm{s}}/(n_{\mathrm{s}}+1)^2$. Therefore, the extraction efficiency can be approximated to:

$$\eta_{\mathrm{extr}} \approx \frac{1}{n_{\mathrm{s}}(n_{\mathrm{s}}+1)^2} \tag{2.7}$$

For InSb, the high refractive index results in a small critical angle for total internal reflection of ≈ 14.5°. This translates to an extraction efficiency as low as 1 %, leaving most of the generated light trapped inside the LED device.

Several methods have been proposed in order to maximise the extraction efficiency of LEDs by maximising the number of photons incident on the emission surface within

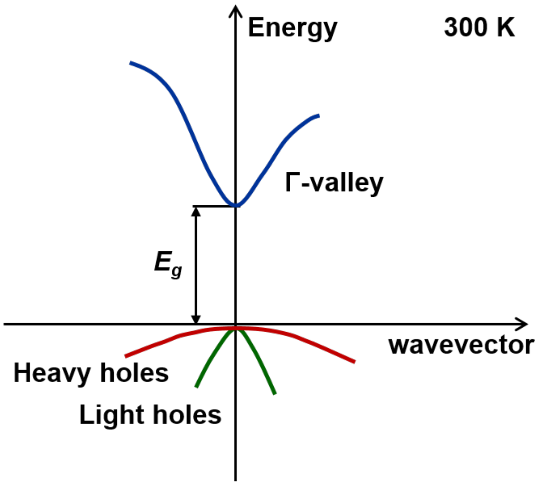

FIGURE 2.4: Bandstructure of InSb at 300 K. The direct energy gap at the Γ-valley is $E_g = 0.18$ eV.

the escape cone. Despite the rapid development of LED technology in the visible and near-infrared spectral region, only few approaches were extended to the mid-infrared. The main adopted techniques for mid-infrared LEDs are the use of immersion lenses and optical concentrators [24], surface patterning [25] and resonant cavity structures [26–28]. These techniques will be discussed in more detail in Chapter 5 to present the advantages of the approach used in this work.

2.3 InSb/AlInSb LEDs

The dispersion relations for the conduction, heavy holes and light holes bands of InSb at room temperature are shown in Figure 2.4, as in Refs. [70–72]. Due to the many interesting properties arising from its band structure, including a small direct energy gap, small electron effective mass and high room temperature electron mobility, InSb and its related compounds have many potential applications in a wide range of electronic and optoelectronic devices. However, for a long time these properties have not been accessible at room temperature. In fact, due to the high intrinsic carrier density and thermal generation rates, InSb-based devices generally require cryogenic cooling (commonly at 77 K), leading to bulky and expensive systems. Table 2.2 reports on the most significant electronic and optical properties on InSb at 300 K compared to InAs and GaAs [68]. These data can be summarised as follows:

- The direct energy gap of InSb at 300 K is only 0.18 eV, which is about eight times smaller than the energy gap of GaAs, and the intrinsic carrier concentration in InSb is ten orders of magnitude higher than in GaAs.

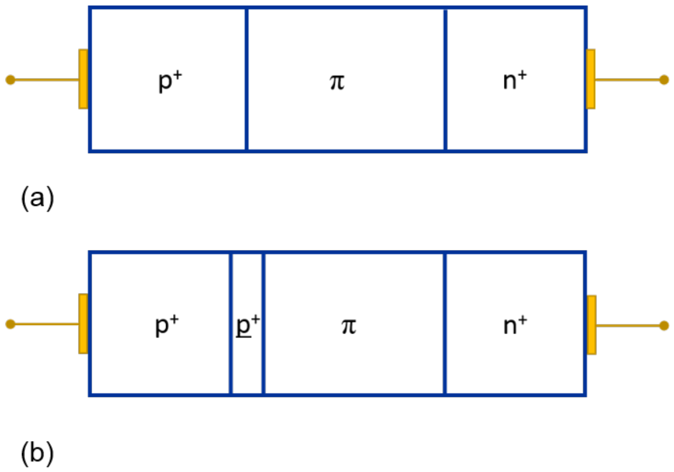

FIGURE 2.5: (a) Three-layer two-terminal homojunction diode structure. (b) Four-layer two-terminal heterojunction diode structure incorporating a wide bandgap barrier layer.

- The electron mass ratio in InSb is about five times lower than in GaAs. Consequently, the electron mobility is up to an order of magnitude higher than in GaAs.
- Thanks to the particularly low intrinsic resistivity, InSb offers a very low contact resistance, which makes it more suitable than InAs for efficient electrically-pumped devices.
- The Auger recombination coefficient is higher than both GaAs and InAs, making it the dominant recombination process in InSb devices.

Non-equilibrium techniques have been used to increase the operating temperature of InSb and MCT detectors [32, 34]. These are based on minority carriers exclusion and extraction configurations, which aim at the reduction of the electron and hole concentrations from their intrinsic values. Additionally, these configurations contribute to the suppression of the dominant Auger generation mechanism, which strongly affects the efficiency of diode devices. As described in Refs. [73, 74], the basic diode structure, schematically illustrated in Figure 2.5a, is a two-terminal homojunction made of three regions: p^+, π and n^+, where the '+' indicates a high-doped material, and 'π' refers to a low-doped material which at room temperature is nearly intrinsic. At room temperature, the dominant generation process in the n^+ region arises from the Auger-1 (CCCH) mechanism. However, due to the low density of states in the conduction band ($4.2 \times 10^{16}\,\mathrm{cm}^{-3}$), the n^+ material becomes degenerate at relatively low doping levels ($\leq 10^{18}\,\mathrm{cm}^{-3}$). Consequently, the leakage current associated with this mechanism can be strongly reduced. In the p^+ region, instead, the dominant generation mechanism is the Auger-7 (CHHL) process. The valence band has a large density of states, therefore

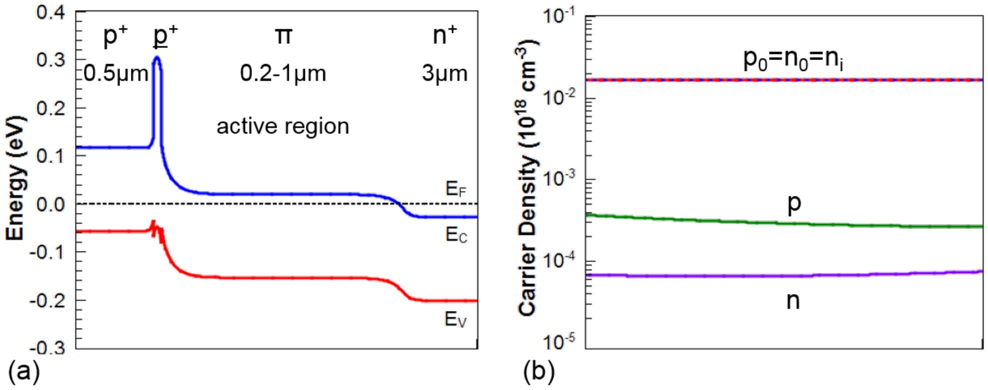

FIGURE 2.6: (a) Energy band diagram of the InSb LED structure under zero bias at 300 K; (b) Equilibrium (n_0, p_0) and reverse bias (n, p) carrier concentrations in the active region. The software *nextnano* was used for the calculations [76].

a significantly higher doping level would be necessary to achieve degeneracy in the p^+ material and reduce the Auger-7 generation. As calculated in Ref. [75], the dominant contribution to the saturation leakage current in such a structure comes from the p^+ region. The proposed solution, illustrated in Figure 2.5b, is to introduce a thin layer of a wider energy gap material $\underline{p}^+$, which forms a barrier in the conduction band to the electron flow from the highly doped p^+ region to the low doped active layer. Therefore, the injection of carriers from the p^+ layer is strongly reduced. As the wider bandgap material of the barrier is not lattice matched, the thickness of the barrier must be kept below the critical thickness for strain relief, but still sufficiently high to avoid electron tunnelling. A suitable thickness of 20 nm has been identified for up to 1 % lattice mismatch between the barrier and bulk material [75]. The energy diagram at zero bias of the $p^+\underline{p}^+\pi n^+$ layer structure was calculated by the software *nextnano* [76] and is illustrated in Figure 2.6a. It is worth noting that, for high doping levels in the barrier, the discontinuities in the valence band are sufficiently abrupt so that hole tunnelling occurs and there is no barrier to the majority carriers flow [75]. Under reverse bias, minority carrier extraction occurs at the diode junction $\pi - n^+$, which results in a substantial reduction of the minority carrier density in the low-doped material. At the same time, the $p^+\underline{p}^+ - \pi$ junction represents an excluding contact, limiting the injection of electrons into the low-doped region. Consequently, the minority carrier density drops substantially in the low doped region and the same happens for the majority carriers in order to maintain the space charge neutrality. The carriers concentrations in the active region under zero bias and reverse bias were calculated with *nextnano* and are plotted in Figure 2.6b.

QinetiQ investigated the use of the same heterostructure with the thin barrier of wider energy gap material as a mid-infrared light-emitting diode when operated in forward bias [21, 50]. The bandstructure at zero bias, plotted in Figure 2.6a, shows how this heterostructure can give a good carrier confinement when forward biased. The electrons are confined in the low-doped active region by the barrier in the conduction band given by the thin layer of wider bandgap material. At the same time, the holes are confined by the step in the valence band, which arises from the degeneracy of the highly-doped n^+ layer.

Based on this structure, mid-infrared light-emitting diodes operating at room temperature were reported [21, 77]. The device epi-layer design consists of a 0.5 µm p^+-$\mathrm{Al_xIn_{1-x}Sb}$ layer, a 20 nm $\underline{p}^+$ $\mathrm{Al_yIn_{1-y}Sb}$ barrier with $y = x + 0.15$, a 1 µm intrinsic $\mathrm{Al_xIn_{1-x}Sb}$ active region and a 3 µm n^+-$\mathrm{Al_xIn_{1-x}Sb}$ layer. The peak emission shifts to shorter wavelengths with increasing aluminium composition in the alloy, according to the wider bandgap of the bulk material. Therefore, as a function of aluminium composition, emission in the whole mid-infrared range, from 3.4 µm to 5.7 µm is achieved. From experimental data, the peak emission wavelengths of electrically-pumped devices are shifted towards shorter wavelengths compared to the ones expected from the intrinsic energy gap. This is due to the Moss-Burnstein effect [78]: the actual energy gap appears wider as a result of the Fermi energy level being well above the conduction band minimum at the applied current injection levels. This effect is more evident at room temperature and for devices with lower aluminium concentration and therefore narrower bandgap [62]. A detailed analysis of the recombination processes in these devices is performed in Ref. [62], based on current-voltage and emittance-current characteristics as a function of aluminium concentration, injected current density and operating temperature. As expected, at low temperatures, non-radiative Schockley-Read Hall recombination occurs through defect states related to carrier trapping. At higher temperatures (300 K) and low current injection levels ($\leq 50\,\mathrm{mA}$), the radiative recombination is the dominant mechanism for all the tested devices. Finally, at high temperature and high injection currents, the contribution from the Auger recombination processes starts to be significant.

The maximum bias current that can be injected into a single element LED device is limited by Joule heating and non-radiative Auger recombination processes. Therefore, a configuration consisting of an array of smaller devices connected in series was proposed [79]. By dividing the LED area into N smaller devices connected in series, the total applied bias current is reduced proportionally, $I'_{max} = I_{max}/N$, and the bias voltage is increased, $V_{series} = N \cdot V_{fw} = N \cdot h\nu/e \approx N \cdot 0.3\,\mathrm{V}$ for an LED emitting around 4.2 µm, where $\nu = c/\lambda$. This eliminates the problems associated with high bias currents and improves the voltage matching with the external drive electronics. When the LED is biased with a current source, the wall plug efficiency can be expressed as:

$$\eta_{\mathrm{WPE}} = \frac{\eta_{ext} \cdot N\,(h\nu/e)}{JA_{tot}R_s/N + N\,(h\nu/e)} \tag{2.8}$$

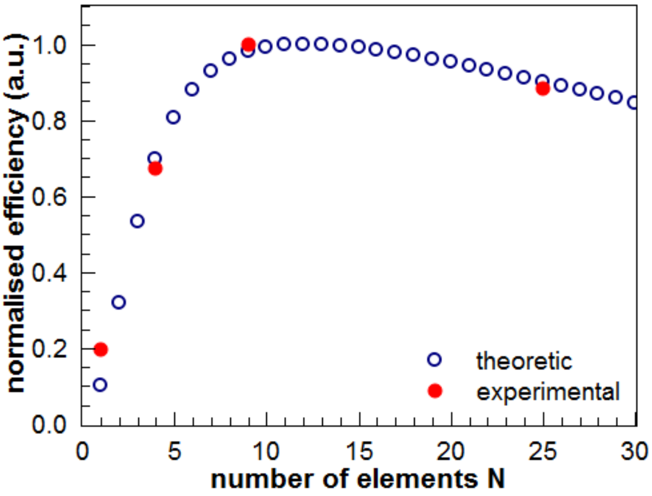

FIGURE 2.7: Normalised efficiency for an LED with increasing number N of individual elements connected in series, emitting around 4.2 µm, and driven by a current source. The effect of the decreasing fill factor due to necessary electrical connections between the individual elements is taken into account.

where η_{ext} is the LED external efficiency, $h\nu/e$ is the forward bias voltage of an individual diode element, J is the bias current density, A_{tot} is the total area of the LED and R_s is the series resistance associated with the metal contacts and bond pads. Therefore, the wall-plug efficiency is improved as the forward bias resistance of the series of individual LED elements increases relative to the series resistance determined by the metal contacts. However, with increasing number N of individual elements, the total brightness of the LED decreases due to the smaller fill factor, as more area is needed to accommodate the electrical contacts to connect all the individual elements. The effective emitting area is given by:

$$A_{eff} = A_{tot}\,(1 - N \cdot A_{metal}) \tag{2.9}$$

where A_{eff} is the effective emitting area of the LED and A_{metal} the area occupied by the electrical contacts for each individual element. The product of the wall-plug efficiency (Equation 2.8) and the effective emitting area of the LED (Equation 2.9) can be used as a figure of merit to identify the optimal number of individual LED elements in the array. An example of the normalised efficiency for an LED emitting around 4.2 µm plotted against N is shown in Figure 2.7. Nine times improvement was demonstrated for a 3-by-3 array configuration, with 2.4×10^{-4} wall-plug efficiency [79]. It is worth noting that the series connection of the individual elements requires the growth and fabrication of the LED structure on a semi-insulating substrate. This is particularly difficult to achieve on lattice-matched narrow bandgap semiconductor substrates due to the particularly high values of intrinsic carriers density. Therefore, the layer structure is epitaxially grown on a semi-insulating GaAs substrate, which has a lattice mismatch with InSb as high as 15 %. This requires the growth of a GaSb intermediate buffer layer

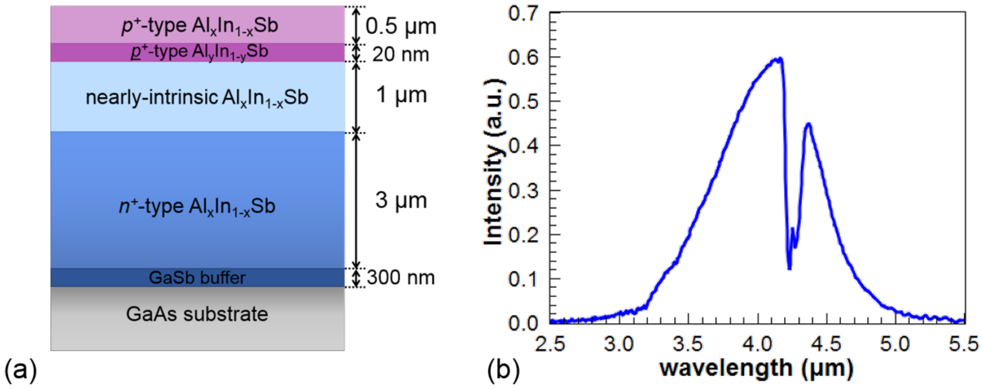

FIGURE 2.8: (a) $Al_xIn_{1-x}Sb$ diode layer structure. The material is epitaxially grown on a GaAs substrate with a 300 nm GaSb buffer layer to partially accommodate the 15 % lattice mismatch. Beryllium and Tellurium are used as dopants for the p-type and n-type contact layers, respectively, at a concentration of $7 \times 10^{17}\,\mathrm{cm}^{-3}$. The thin barrier of wider bandgap material had a composition $y = x + 0.15$ and a thickness of 20 nm. (b) Typical forward bias emission spectrum at room temperature of an $Al_xIn_{1-x}Sb$ LED with aluminium composition $x = 0.05$. The CO_2 absorption bands at 4.2 µm are clearly visible.

to partially accommodate the lattice mismatch are reduce the concentration of threading dislocation, as discussed in more detail in Section 3.1.

2.4 GSS device performance

The light-emitting diode, used as a mid-infrared source in the CO_2 optical gas sensor developed by Gas Sensing Solutions Ltd., is based on the design considerations discussed in the previous section [44, 46, 47]. The epitaxially grown $Al_xIn_{1-x}Sb$ layer structure of a typical LED is shown in Figure 2.8a. The p-type and n-type contact layers are doped with Beryllium and Tellurium, respectively, at a concentration of $7 \times 10^{17}\,\mathrm{cm}^{-3}$. The thin barrier layer has the same doping concentration as the contact layer and an aluminium composition $y = x + 0.15$, where x is the composition of the LED active region and contact layers. A typical forward bias emission spectrum at room temperature is shown in Figure 2.8b, clearly showing the CO_2 absorption bands at 4.2 µm.

The peak emission shifts to longer wavelengths with increasing temperature (−0.37 meV/K), according to the bandgap dependence on temperature [80, 81]:

$$E_g(T) = E_g(0) - \frac{\alpha \cdot T^2}{\beta + T} = 0.24 - \frac{6 \times 10^{-4} \cdot T^2}{500 + T} \quad \text{(eV)} \tag{2.10}$$

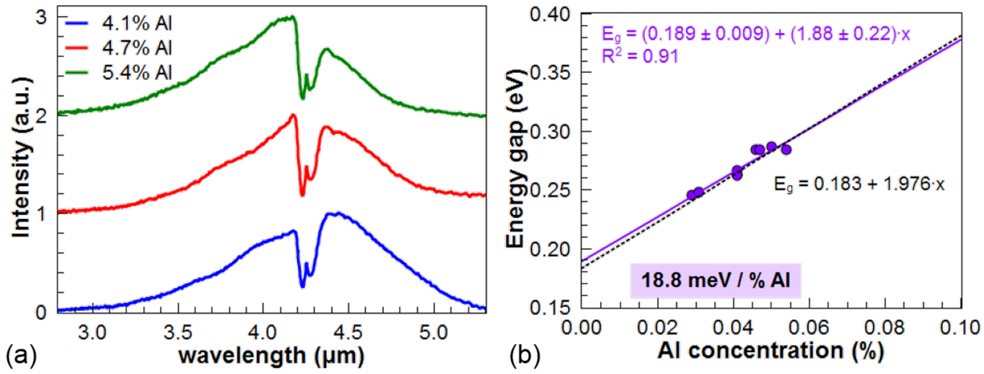

FIGURE 2.9: (a) Measured EL spectra for LEDs with varying aluminium composition, showing the effect on the alignment with the CO_2 absorption lines. (b) Energy gap values as a function of the aluminium composition in the range of interest. The linear fit gives a value of 18.7 meV/% Al. The black dotted line shows the linear dependence according to Ref. [81].

The spectra of emission intensity of devices with different aluminium composition are shown in Figure 2.9a. As expected, the emittance peak shifts towards shorter wavelengths as the aluminium concentration increases [21, 81]. Figure 2.9b shows the variation of the energy gap, calculated as: $E_g = E_{peak} - \frac{1}{2}kT$ [63], with aluminium composition. The linear fit of the experimental data gives a value of 18.8 meV/% Al, which corresponds to 276 nm/% Al at 4.26 µm. These values are in good agreement with the experimental values reported in Ref. [81]:

$$E_g = 0.183 + 1.976 \cdot x \quad (\text{eV}) \quad \text{at} \quad \text{T} = 300\text{K} \tag{2.11}$$

, which are plotted in Figure 2.9b as well for comparison. In conclusion, by tailoring the aluminium composition, it is possible to improve the alignment between the peak emission wavelength and the characteristic absorption of the target gas at the desired temperature of operation. In this case, a composition of $x = 0.05$ aluminium is found to be optimal for emission around the CO_2 absorption line at room temperature.

The LEDs are designed as 3-by-3 arrays of individual elements, giving a total emitting area of about 1 mm^2. The fabrication of the production devices is performed by Compound Semiconductor Technology Ltd. [82] on 3" wafers, giving a yield of about 1500 devices per wafer. Optical images of a single LED and a fully processed wafer are shown in Figure 2.10.

The total emitted power from a standard production device was measured by the group of Professor Anthony Krier at the University of Lancaster. The LED is placed with the top emitting surface in close contact with the collection port of a 4-inch gold-coated integrating sphere and the radiation is measured with a 77 K-cooled InSb detector placed at the detection port. In this configuration, light emitted at all angles is collected with

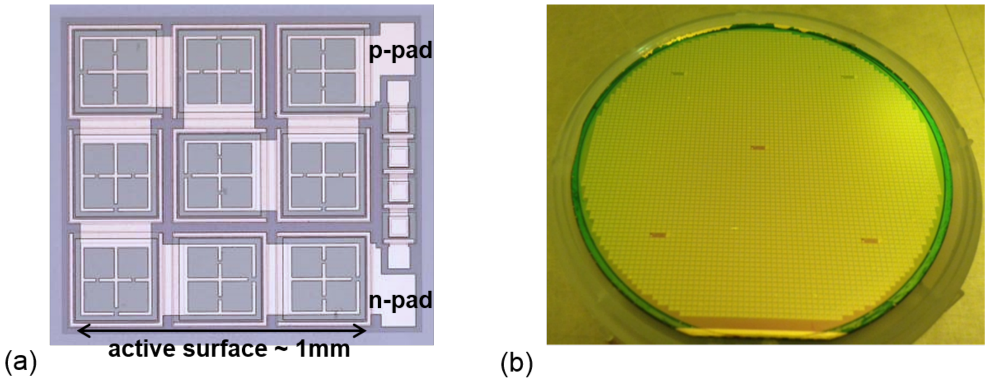

FIGURE 2.10: (a) Production LED device with a 3-by-3 array configuration. The individual elements are electrically isolated by the etching of mesa structures and connected in series. The active surface is of about 1 mm^2. (b) Fully processed 3" wafer with about 1500 $\mathrm{Al_xIn_{1-x}Sb}$ LED devices. (Courtesy of Dr. Stewart McDougall, Compound Semiconductor Technologies Ltd. [82])

the same efficiency and the total emitted power is evaluated by comparison with a known source. The measurement resulted in a total emitted power of 6 µW for the production LEDs, when biased at 100 mA, 1 kHz, 50 % duty cycle. This value will be used as a reference for the improvement to the device output power discussed in the following chapters. From the measured total emitted power, values for the external and internal quantum efficiency can be extracted. The external quantum efficiency can be calculated by dividing the measured output power by the photon energy and by J/e, where J is the peak injected current density and e is the electronic charge. In these operating conditions, $\eta_{\mathrm{ext}} = 2 \times 10^{-4}$. From here, the internal quantum efficiency can be calculated by multiplying for a factor $n(n+1)^2 \approx 94$, where n is the refractive index of the active layer ($n \approx 3.9$ for $\mathrm{Al_xIn_{1-x}Sb}$ with $x = 0.05$). Therefore, the production devices show an approximated internal quantum efficiency of 1.9 %.

2.5 Conclusions

In this Chapter, the challenges and limiting mechanisms for the realisation of efficient room-temperature mid-infrared light-emitting diodes were reviewed and discussed, with the main focus on the InSb material system. In particular, it was shown how the competing non-radiative recombination mechanisms have a more dominant effect in narrow bandgap materials, therefore requiring accurate design of the LED layer structure. Additionally, the particularly high value of the refractive index in narrow bandgap materials makes the common issue of low extraction efficiency even more pronounced than in visible and near-infrared LEDs, reducing the fraction of light emitted into air to less than 1 %. The InSb/AlInSb based heterostructure proposed by QinetiQ is presented: this includes a thin barrier of wider bandgap material to confine the carriers in the active region and to reduce the effect of the thermally generated carriers, which contribute to the device leakage current. $\mathrm{Al_xIn_{1-x}Sb}$ LEDs based on this design with peak emission around 4.26 µm ($x = 0.05$) are used as a mid-infrared light source in Gas Sensing Solutions' commercial CO_2 gas sensor. The production LEDs have a total emitted power of $\sim 6\,\mu W$ when operated in pulsed bias at room temperature, showing an external quantum efficiency of 3×10^{-5}.

As discussed in Section 1.7, the aim of this research work is to improve the performance of $\mathrm{Al_xIn_{1-x}Sb}$ LEDs emitting around the CO_2 absorption line at 4.26 µm. The epi-layer structures grown for production devices were used for the fabrication and initial characterisation of test LED devices. The fabrication process performed in the James Watt Nanofabrication Centre (JWNC) at the University of Glasgow is described in Chapter 3. Electrical and optical characterisations were performed as a function of a number of design parameters in order to achieve an optimised epi-layer structure and device geometry, as discussed in Chapter 4 and Chapter 5. In addition, two different techniques to enhance the LEDs' extraction efficiency were tested and will be analysed in Chapter 6 and Chapter 7.

Chapter 3

Devices Fabrication

In this Chapter, the challenges associated with the growth of $\mathrm{Al_xIn_{1-x}Sb}$ on GaAs substrates are briefly discussed. The main fabrication techniques used in the processing of prototype LED devices are described in detail. Particular focus is given to the development of processes specific to the $\mathrm{Al_xIn_{1-x}Sb}$ material and to the main challenges that had to be addressed.

3.1 Background on $\mathrm{Al_xIn_{1-x}Sb}$ growth on GaAs

Antimonide-based infrared detectors are traditionally grown on GaSb or InSb substrates. However, these substates suffer from high free-carrier absorption losses at infrared wavelengths due to the high intrinsic carrier density (10^{15} to $10^{17}\mathrm{cm^{-3}}$) of narrow bandgap materials at room temperature. Additionally, high quality wafers, with a defect density of less than 10^3 defect/cm^2, are relative expensive and not yet abundantly available in diameters larger than 3 inches. These limitations were circumvented by the development of Sb-related compounds growth technologies on the very well established GaAs platform. GaAs substrates are electrically semi-insulating and optically transparent at infrared wavelengths thanks to the wider bandgap. Moreover, this technology provides an effective solution for manufacturing, thanks to the availability of high quality, larger diameter (up to 6 inches) and relatively cheaper substrates.

The lattice mismatch between an epitaxially grown InSb thin film (lattice constant 6.479 Å) and the GaAs substrate (lattice constant 5.653 Å) is as high as 14.6 %. For this reason, the direct growth of InSb and its related compounds on GaAs results in a high density of threading dislocations, which significantly degrades the electrical and optical properties of the material, unless particularly thick layers of InSb are grown [83, 84]. In fact, a high density of threading dislocations was proved to be the primary cause of low

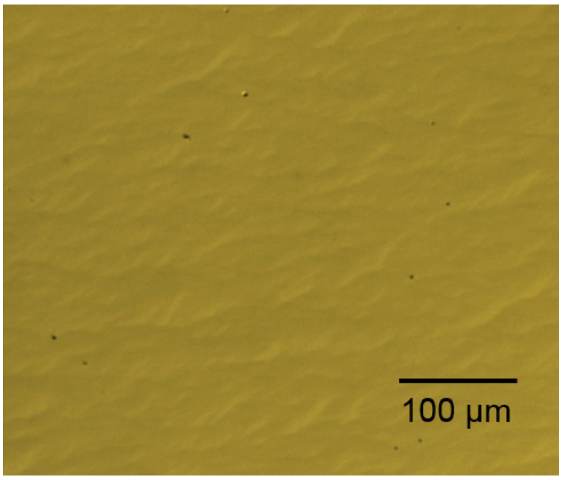

FIGURE 3.1: Optical microscope image, under Nomarski interference contrast illumination, of the typical surface morphology of $Al_xIn_{1-x}Sb$ grown on GaAs under optimised growth conditions.

room temperature electron mobilities in highly mismatched InSb films [85]. Therefore, to guarantee high quality thin films, it is necessary to use a dislocation-filtering buffer layer between the film and the substrate, in order to controllably relax the strain due to the lattice mismatch. Different approaches were proposed for the interposition of highly mismatched resistive buffers to improve the electron mobility of epitaxially grown InSb layers on GaAs substrate, including $In_{0.88}Al_{0.12}Sb$ layers [83] and 1 µm-thick AlSb layers followed by a 1 µm-thick $In_xAl_{1-x}Sb$ ($x = 0.1$–0.9) step-graded buffer [84].

Another suitable material to be interposed between InSb and GaAs as buffer layer is GaSb [85]. In fact, GaSb has a lattice parameter (6.096 Å) intermediate between InSb and GaAs and is highly resistive, with an intrinsic resistivity of 10^5 times that of InSb at 300 K [68]. Recently, a new technique has been reported for the growth of buffer GaSb on GaAs, based on interfacial misfit (IMF) dislocations [86, 87]. With this technique, the 7.8 % lattice mismatch between GaSb and GaAs is accommodated by the formation of a two-dimensional array of highly-periodic, 90° misfit dislocations. In contrast to metamorphic buffers, where thick layers are required to suppress the threading dislocations, in this approach the excess strain is rapidly relieved at the heteroepitaxial interface.

The growth conditions of $Al_xIn_{1-x}Sb$ on GaAs substrates by Molecular Beam Epitaxy (MBE) have been optimised for growth rate and temperature to obtain a high quality planar surface morphology. First, a 250 nm GaAs layer is grown at 590 °C to guarantee a flat substrate surface. Then, the temperature is lowered to 500 °C and the As flux is turned off, leaving the background to pump away for about 20 to 30 minutes. After that, the Sb flux is turned on and the 200 nm-thick GaSb buffer layer is grown at about 0.7 ML/s. Finally, the temperature is reduced further to 450 °C and the $Al_xIn_{1-x}Sb$ layers are grown at about 1 ML/s with a V-III flux ratio of 1.8 : 1.

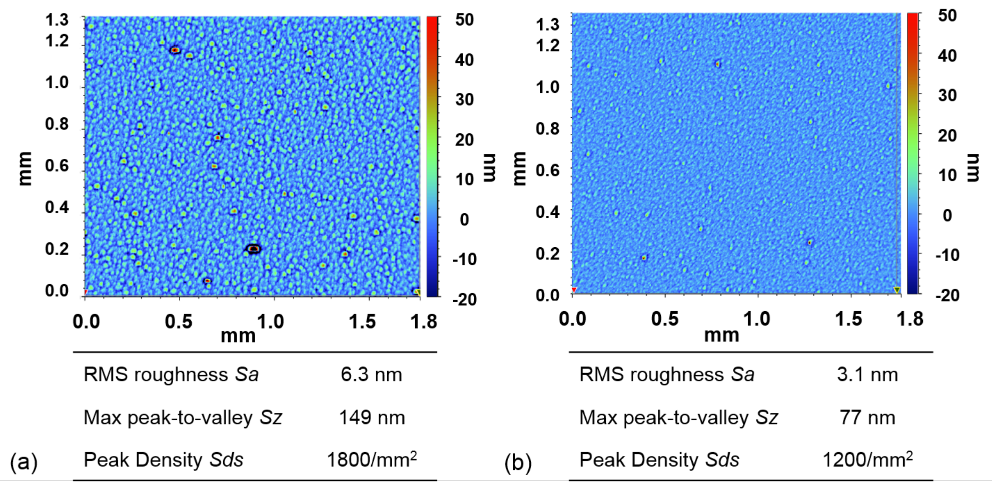

(a)

RMS roughness *Sa*	6.3 nm
Max peak-to-valley *Sz*	149 nm
Peak Density *Sds*	1800/mm^2

(b)

RMS roughness *Sa*	3.1 nm
Max peak-to-valley *Sz*	77 nm
Peak Density *Sds*	1200/mm^2

FIGURE 3.2: Surface roughness analysis of $\mathrm{Al_xIn_{1-x}Sb}$ structures grown on GaAs under (a) unoptimised and (b) optimised growth conditions. The values of Root Mean Square (RMS) roughness Sq, maximum peak-to-valley magnitude Sz and peaks density Sds are reported for comparison. The images and analysis are performed with a Bruker Contour GT Optical Profiler.

Figure 3.1 shows an optical image, acquired in Nomarski mode, of the typical surface morphology of the grown $\mathrm{Al_xIn_{1-x}Sb}$ wafers grown with these parameters, in good agreement with the optimised growth conditions presented in [88], which reports a typical defects concentration lower than $1 \times 10^9\,\mathrm{cm^{-2}}$ close to the buffer interface. Figure 3.2 illustrates the surface roughness analysis, performed with a Bruker Contour GT Optical Profiler, of two different wafers grown under unoptimised and optimised growth conditions, showing an improved surface roughness and defect density. Square pyramidal defects, associated with residual dislocations, are still observed in isolated areas on the wafer surface; however, their presence has not showed any correlation with the electrical or optical performance of the material. An electron mobility of $32\,000\,\mathrm{cm^2/V\,s}$ was measured on a 3 µm-thick undoped $\mathrm{Al_xIn_{1-x}Sb}$ layer with Al composition $x = 0.05$.

A standard wafer, grown with the optimised parameters listed above, was analysed with a transmission electron microscope (TEM) by Dr. Ian MacLaren at the Kelvin Nanocharacterisation Centre, Department of Physics and Astronomy of University of Glasgow. Figure 3.3 shows the cross-sectional TEM image of the epitaxially-grown $\mathrm{Al_xIn_{1-x}Sb}$ on a 200 nm-thick GaSb buffer layer. It can be observed that the GaSb buffer layer has relaxed with the formation of an array of misfit dislocations, which run on the interface plane and do not propagate through the material above. The interface between GaSb and $\mathrm{Al_xIn_{1-x}Sb}$, instead, appears less flat and regular, with threading dislocations forming where island coalescence occurs. However, the higher density of defects is confined to the first few hundreds nm of $\mathrm{Al_xIn_{1-x}Sb}$. As a consequence, a 2–3 µm n-doped $\mathrm{Al_xIn_{1-x}Sb}$ layer is grown in order to achieve a higher crystallographic

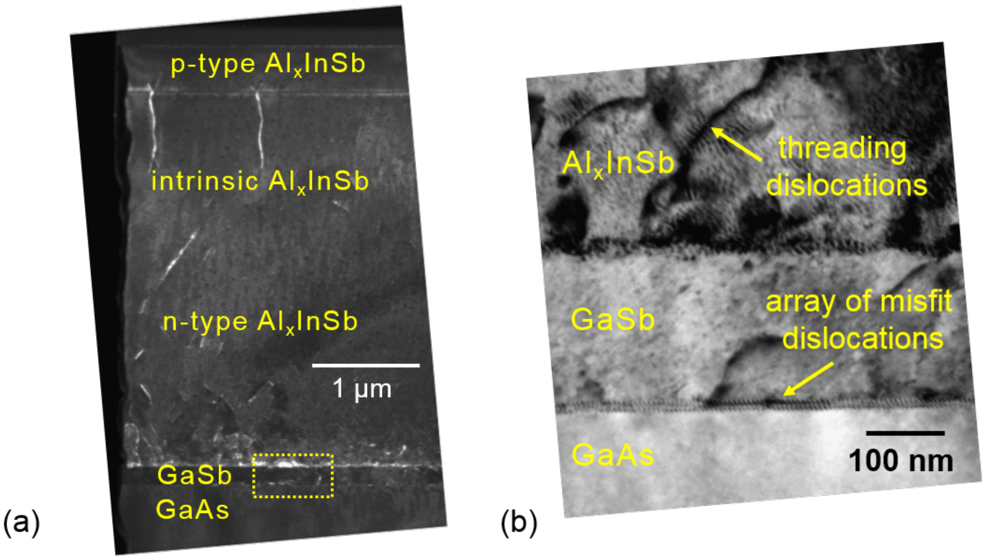

FIGURE 3.3: (a) Low magnification and (b) high magnification bright-field cross-sectional TEM images of the $Al_xIn_{1-x}Sb$ structure grown on a 200 nm-thick GaSb buffer layer on a GaAs substrate. The high magnification image in (b) is a zoom-in of the GaSb buffer layer region. An in-plane array of misfit dislocations releases most of the excess strain at the GaSb/GaAs interface. Threading dislocations are observed in the first few hundreds nm above the $Al_xIn_{1-x}Sb$ /GaSb interface.

material quality and avoid the introduction of non-radiative recombination centres via defects and dislocations close to the active region of the device.

The grown wafers are cleaved in square samples of typically 15 × 15 mm for the fabrication of test LED devices. All the fabrication process is performed in the *James Watt Nanofabrication Centre* (JWNC) [89] at the University of Glasgow. The fabrication steps, described in the following sections, are schematically illustrated in Figure 3.4.

3.2 Lithography

Optical lithography is the process that allows the transfer of a pattern to an optically sensitive polymer, called photoresist. The resulting binary resist pattern is used as a mask to perform a subsequent fabrication step, such as etching or metal deposition. After resist exposure and development, the originally designed pattern is transferred onto the sample material. An important aspect of the lithography process is the accurate alignment of each step to the patterns already present on the substrate. The standard sequence of processing steps for a typical optical lithography process is briefly described below:

- **Substrate preparation:** Substrate preparation is intended to remove any particle or organic impurity that may be present on the sample surface and to improve

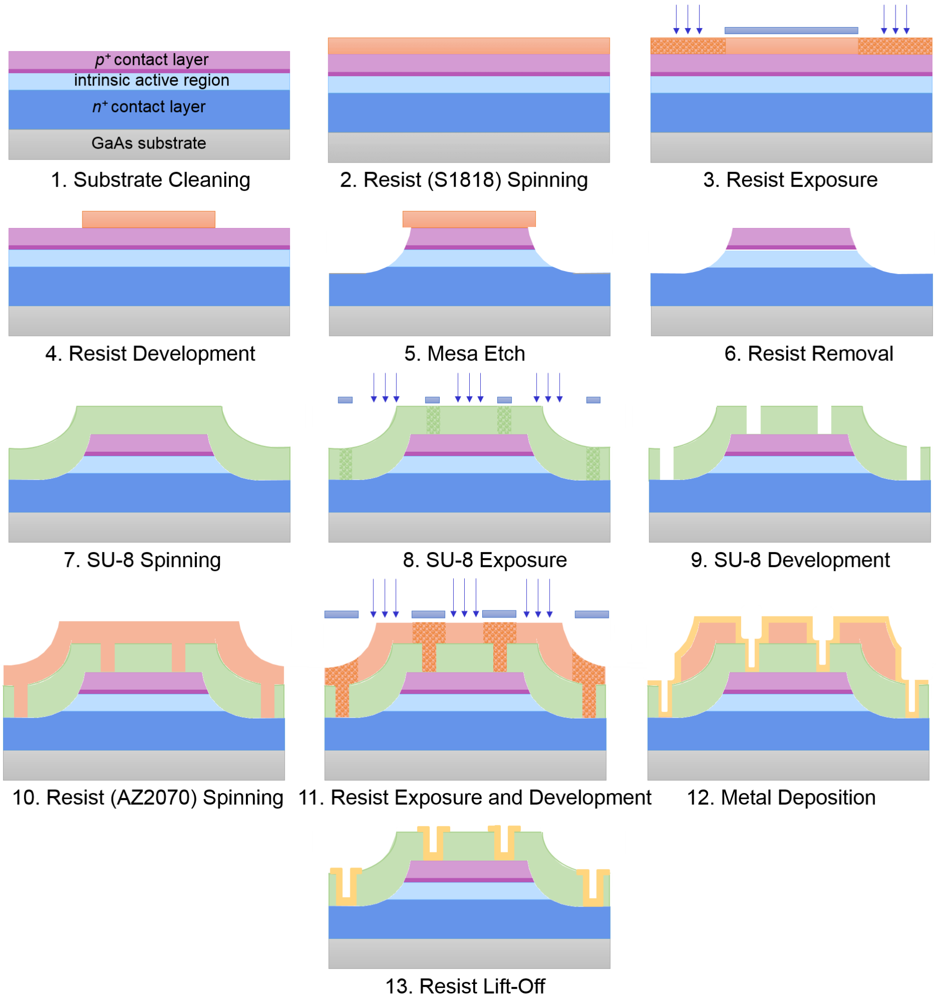

FIGURE 3.4: Schematic illustration of the fabrication steps for the definition of LEDs.

the adhesion of the photoresist to the substrate. Samples are immersed in opticlear, acetone, methanol and isopropyl alcohol (IPA) for 3 minutes each. An additional rinsing in deionised (DI) water can be used. After the last soak, the remaining liquid is dried from the sample surface with a nitrogen gun. A dehydration bake on a hot plate at 115 °C removes adsorbed water, which may decrease resist adhesion. The substrate is then allowed to cool in a dry environment and coated as soon as possible.

- **Photoresist coating:** Spin coating is the process that allows to obtain a thin, uniform coating of photoresist with a specific thickness on the substrate surface. A small amount of photoresist, dissolved in a solvent, is distributed onto the substrate with a clean pipette, and is then spun at high speed. Spin speed, time and acceleration are crucial parameters that determine the thickness of the resist film. Additionally, resist viscosity, substrate material and sample topography must be taken into account when determining the optimal conditions to obtain the desired resist thickness and uniformity.

- **Softbake:** After spin coating, the resist is baked on a hot plate for a few minutes. This process helps to stabilise the resist by removing the excess solvent and improves its adhesion to the substrate.

- **Exposure:** Resists are radiation sensitive polymers, whose chemical properties can be varied upon exposure to UV light in the spectral range of 350 nm to 450 nm. The spatial variation in light energy incident on the photoresist, through the photomask pattern, causes a photochemical reaction which determines a spatial variation in solubility of the resist in the developer. Photoresist are generally classified in two groups, depending on their response at radiation exposure:

  - *Positive* resists become more soluble in the developer after exposure to light. The pattern formed on the substrate is the same as on the mask.
  - *Negative* resists become less soluble in the developer after exposure to light. The pattern formed on the substrate is the reverse as on the mask.

  The optical lithography mask aligner tool available in the JWNC is a *Süss* MA6 [90] with a 350 W mercury lamp. The light source gives an exposure dose of 25 mW/cm^2 for the emission line at 365 nm.

- **Post-exposure bake:** An additional baking can be performed just after exposure and before development. In case of negative resists, this is normally used to activate additional chemical reactions initiated during exposure, such as cross-linking, which are essential to create the solubility differential between exposed and unexposed areas of the resist.

- **Development:** The resist is selectively removed, depending on the areas that have been exposed. Most commonly used resists use aqueous bases as developers. The characteristic of the resist-developer interactions determines to a large extent the shape of the resist profile and the minimum feature size.

The two main limitations of our optical lithography process are related to the minimum feature size that can be patterned and the alignment that can be achieved with previously defined patterns on the substrate. Depending on the resist, minimum features of 1 ± 0.5 µm and minimum alignment of 1 µm can be achieved.

A photolithography mask was designed for the fabrication of test LED configurations. The minimum features size is in the order of 5 µm. Therefore, the performance of the our optical lithography process are sufficient to achieve the desired feature shape and

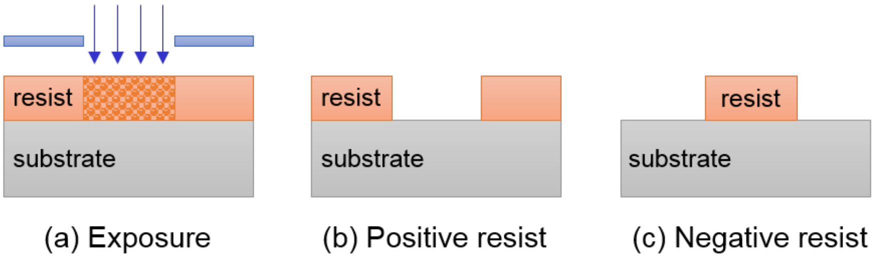

(a) Exposure (b) Positive resist (c) Negative resist

Figure 3.5: Schematic illustration of the exposure and development process for *positive* and *negative* tone resist.

alignment.

However, due to the small throughput requirements and the need of flexible pattern design during the device prototyping, e-beam lithography was also used for some fabrication steps, such as the metal contacts definition and sub-wavelength hole array patterns. E-beam lithography is briefly discussed in Section 7.3.

3.3 Mesa Etching

Mesa etching is the process that defines table-top elevated features by removing the surrounding material. In this case, it is used to create isolated p-n junctions on the substrate. The mesa are defined by a positive resist mask and formed by etching the p-type and intrinsic material, until the n-type contact layer is exposed. The etching process determines the step profile of the mesa sidewalls. For the definition of the mesa pattern, Shipley Microposit S1818 positive photoresist [91] is used, accordingly to the process described below:

- Sample clean in acetone and IPA, 3 minutes dehydration bake at 115 °C.
- Spin S1818 for 30 seconds at 4000 rpm, which gives a film thickness of about 1.8 µm.
- Pre-bake on a hotplate for 2 minutes at 115 °C.
- Expose for 7 seconds through mesa pattern mask using MA6.
- Develop in neat MF-319 developer for 75 seconds.

Dry etch processes generally produce accurate geometric control over designed geometries, especially over small device structures. However, the sidewall damage caused by the physical sputtering of ions and unwanted deposition of etch by-products may result in electrical degradation of devices, especially for narrow bandgap semiconductor materials. Wet etch processes are generally limited by their typical isotropic nature resulting in concave sidewall profiles and unavoidable undercut of the etch mask. However, wet etch is presently the technique of choice for InSb-based compounds because it is simple, cost-effective and limits the additional electronic damage to the semiconductor surface. Section 3.3.1 discusses the citric acid-based wet etch used for the fabrication of the LEDs throughout this work. A dry etch process based on a CH_4/H_2 plasma in an Inductively-Coupled Plasma Reactive Ion Etching (ICP-RIE) tool was also developed and is described in Section 3.3.2.

3.3.1 Wet Etch

Citric acid/hydrogen peroxide ($C_6H_8O_7 : H_2O_2$) solutions have been studied intensively in processing GaAs-based materials [92, 93], and detailed for InSb etching by Chang *et al.* [94]. Chemical etching proceeds by an oxidation-reduction reaction at the semiconductor surface by the hydrogen peroxide, with the dissolution of the oxide products by the citric acid. In Chang's experiment, the super-linear etch rate dependence on time, exponential etch rate dependence on temperature and trench-free behaviour indicate that the InSb mesa etching in citric acid/hydrogen peroxide solution is dominantly controlled by surface reaction rate-limited mechanism [92, 94]. Chang *et al.* suggested that the increase of etch rate with time is caused by the slow decomposition of H_2O_2, and subsequent increase in citric:H_2O_2 ratio.

A reliable citric acid based wet etch process was developed in collaboration with Kelvin Nanotechnology Ltd. (KNT) [95] for the fabrication of AlInSb LEDs and used throughout this work. The desirable features that characterised the wet etch process are:

- positive sloping sidewall angles, suitable for subsequent fabrication steps, such as thin-film coating, without discontinuities;
- smooth etch surfaces, without defect delineation;
- repeatable etch rate;
- minimum selectivity to layers with different Aluminium compositions, avoiding re-entrant profiles at the wider bandgap barrier.

The literature on etching of antimonides and arsenide-based compounds using citric:H_2O_2 solutions highlights the importance of conditioning the semiconductor surface prior to etching. In particular, the native surface oxide should be minimised before etching to allow repeatable control of the step height of the mesa. Therefore, an initial deoxidation sequence is used as follows:

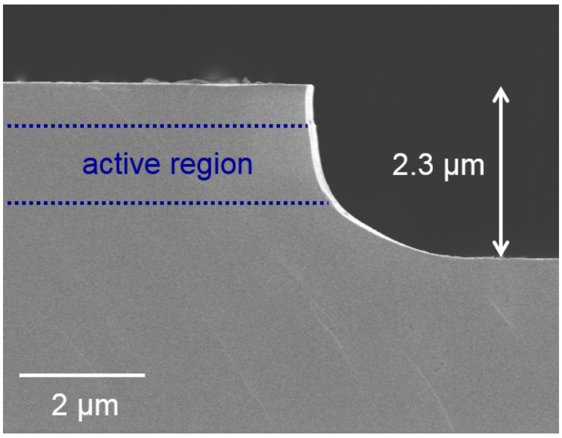

FIGURE 3.6: SEM cross-sectional image of an $Al_{0.05}In_{0.95}Sb$ etched profile in citric acid:H_2O_2:H_2O solution at 20.5 °C.

- 1 minute soak in 5:1 BHF (buffered hydrofluoric acid, 5 parts 40 % NH_4F:1 part 49 % HF), 3 minutes rinse in DI water;
- 1 minute soak in 1:1 HCl (37 % hydrochloric acid):H_2O, 3 minutes rinse in DI water;

The sample is directly transferred from one solution to the next, without exposing the surface to air, and immersed straight after into the citric acid-based solution,. This consists of a 11:1:7 citric:H_2O_2:H_2O solution, which gives a uniform reaction-rate limited etching with an etch rate of ≈ 20 nm/min. The etching is performed in a temperature controlled (T ≈ 20.5 °C) stirring bath to avoid localised depletion/accumulation or reactants/products in solution that could lead to big variations in etch rate due to oxidation/reduction imbalances. A scanning electron microscope (SEM) image of a typical etched profile is shown in Figure 3.6.

3.3.2 Dry Etch

Reactive Ion Etching (RIE) is the most common dry etch method, based on the chemical and physical interaction of plasma ions and radicals with the target material. During a dry etch process, the plasma ions and radicals not only chemically react with the target material, but physically bombard and remove it due to the accelerating bias voltage. This combination of chemical and physical etching process result in a controllable anisotropic etching profile. In conventional RIE, only one RF source is used to generate and accelerated the plasma at the same time, thus limiting the control on density plasma and energy [96]. An additional RF source is present in the Inductively-Coupled Plasma RIE (ICP-RIE) configuration, which allows to separately control the plasma density and energy [97]. A schematic illustration of an ICP-RIE machine is shown in

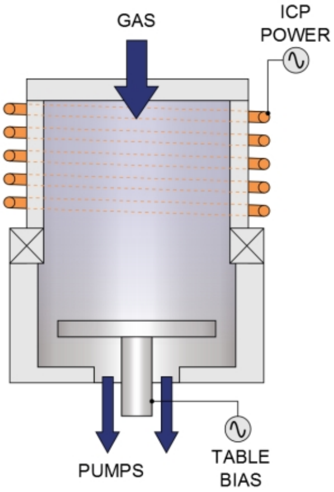

FIGURE 3.7: Schematic diagram of an Inductively Couple Plasma (ICP) Etching tool (from Oxford Instruments [99]).

Figure 3.7. The ICP source generates the plasma and controls its density. The RF bias source, instead, provides a voltage potential that accelerates the plasma in the main chamber. The ICP-RIE machine available in the JWNC and used in this work is an Oxford Instruments ICP-180 [98].

Chlorine-based dry etch chemistries are widely used for the etching of GaSb and related compounds. Cl_2/Ar plasma was used for GaSb etching with high etch rates ($> 1\,\mu m/min$) and mirror-like etched surfaces [100]. However, when applied to InSb, Cl_2 based recipes still provide high etch rates but result in rough surfaces, due to the low volatility of indium chloride ($InCl_x$) compounds depositing on the etched surfaces [101]. Increasing the process temperature can help increasing the $InCl_x$ desorption process. Both $Cl_2/CH_4/H_2$ and $BCl_3/Cl_2/Ar$ plasma recipes were tested on $Al_{0.05}In_{0.95}Sb$ material, resulting in high etch rates (between 500 and 1000 nm/min) but unacceptable surface roughness and high temperatures ($T > 150\,°C$) registered on the sample surface during the etching process. An alternative plasma chemistry for the dry etch of antimonides is based on CH_4/H_2. After ionisation, the methyl radicals tend to bond with the metal elements (In or Ga), while H-radicals capture the antimony and form a volatile hydride (SbH_3). The reported etch rates are lower (< 250 nm/min) than for chlorine-based plasma recipes, but with smooth etched surfaces and sidewalls [102]. The main advantage of CH_4/H_2 plasma is the formation of carbon polymers that deposit on the etched sidewalls, preventing them from being overetched and avoiding the formation of undercut profiles. In the JWNC, $CH_4/H_2/O_2$ is already a mature recipe for the dry etch of InP, providing smooth surfaces and slightly positive sidewalls with an etch rate of 65 nm/min.

Therefore, the etching of $Al_{0.05}In_{0.95}Sb$ in ICP180 with a $CH_4/H_2/O_2$ plasma was tested

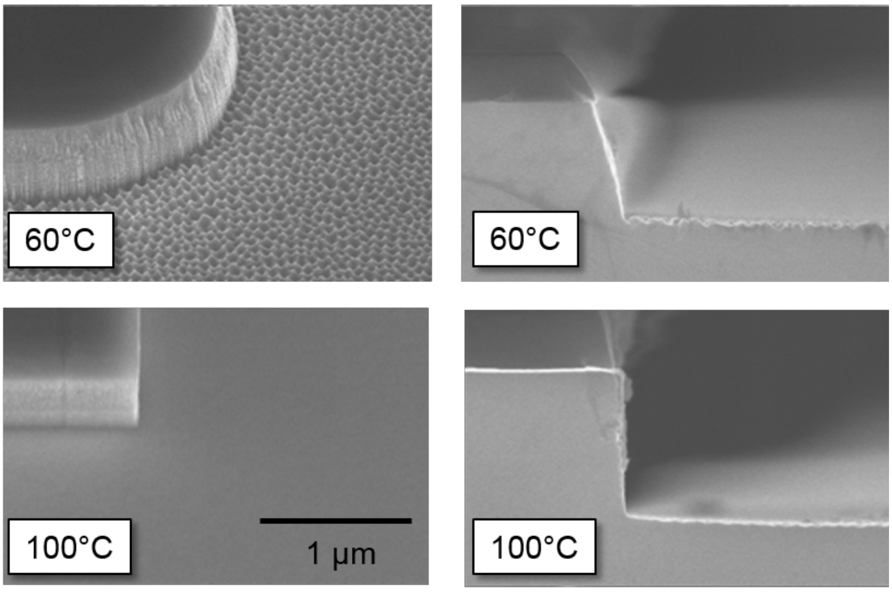

Figure 3.8: SEM images showing the surface morphology (left) and sidewalls cross-sectional profile (right) of $Al_{0.05}In_{0.95}Sb$ etched by $CH_4/H_2/O_2$ plasma in ICP180. The process parameters are: gas flow $CH_4/H_2/O_2$ = 6/50/0.2 sccm, ICP power = 350 W, RF power = 150 W, pressure = 15 mTorr. The effect of the set table temperature is shown.

in the JWNC as a function of a number of process parameters. An etch test pattern was defined on the samples using standard photolithography to pattern a 200 nm-thick layer of silicon nitride, then used as an hard mask for the dry etch process. An O_2 ash and HCl deoxidation steps are added to the standard sample cleaning procedure to ensure that no surface oxides are present before the etching process. In the etch tests, the $CH_4/H_2/O_2$ gas flow is kept constant at 6/50/0.2 sccm, while ICP power (200–600 W), RF bias power (100–200 W), chamber pressure (10–30 mTorr), table temperature (20–200 °C) are varied one by one to evaluate their effect on etch rate, sidewall profile and surface morphology. The observed features are discussed in the following:

- With increasing ICP power from 200 W to 600 W, the etch rate increases from 30 nm/min to 70 nm/min. The sidewalls profile goes from positive to slightly undercut, due to the more isotropic etching of high density plasma.
- Higher RF power results in higher acceleration voltage across the chamber. The physical reaction is enhanced and the bombardment of the target material by high energy ions improves the desorption process of the dry etch by-products, resulting in smooth surface morphology.
- The chamber pressure is kept between 10 and 20 mTorr, which guarantees smooth surface due to the fact that the chemical by-product of the dry etch process are

Table 3.1: Parameters chosen for the ICP180 $CH_4/H_2/O_2$ process for the etching of $Al_{0.05}In_{0.95}Sb$.

Parameter	Value
Gas	$CH_4/H_2/O_2$
Flow	6/50/0.2 sccm
ICP Power	350 W
RF Power	150 W
Chamber Pressure	15 mTorr
Table Temperature	100 °C

generated at a slow rate and can be completely removed by the physical ion bombardment.

- Increasing the table temperature increases the desorption process of the dry etch by-products, therefore increasing the etch rate and improving the surface morphology. Beyond 100 °C, the carbon polymers deposited on the etched sidewalls are also removed, resulting in more pronounced undercut profiles.

The parameters chosen for the final ICP-RIE dry etch process of $Al_{0.05}In_{0.95}Sb$ are listed in Table 3.1. The process has an etch rate of about 50 nm/min, giving a smooth surface morphology and vertical sidewalls, while limiting the sample temperature to about 100 °C.

Despite the achieved suitable dry etch process, there was no evidence of improved performance from processed devices. Therefore, the wet etch process was chosen for the final fabrication process of the LEDs.

3.4 Passivation

The surface condition of an etched mesa diode is important to ensure low surface leakage current, especially in narrow bandgap semiconductors such as InSb. Combined with a suitable etch process, an appropriate surface passivation is an important step to prevent surface degradation and high leakage currents. As narrow bandgap semiconductor materials are more susceptible to the formation of conductive channels along the sidewalls, native fixed charges in the passivation layer may cause the deterioration of the device electrical performance [103, 104]. Passivation with standard dielectrics, such as silicon nitride (SiN_x) and silicon dioxide (SiO_2), was proved effective, but requires high quality dielectric deposition at room temperature. More recently, passivation with SU-8 was demonstrated particularly successful in reducing the leakage current of InAs/GaSb type-II strained layer superlattice detectors [103] and InAs avalanche photodiodes [105, 106].

SU-8 is a high-contrast epoxy-based negative photoresist, which is designed to give uniform thick films for high aspect ratio devices [107]. A high cross-link density is caused in the film during exposure to UV radiation, giving the resist a high chemical resistance to the developer. The resulting SU-8 film has good chemical and mechanical stability [103, 108]. SU-8 is transparent at wavelengths $> 350\,\text{nm}$ and is easy to integrate in the fabrication process as it requires only a standard spin-coat and photolithography process at room temperature, which is important to avoid surface degradation of narrow bandgap materials. For these reasons, SU-8 has been chosen as the passivation material for the devices fabricated in this work. The results of passivation on the current-voltage characteristic and the leakage current of AlInSb LEDs are discussed in Section 4.1.1.

The fabrication steps for the SU-8 passivation are listed below:

- Sample clean in acetone and IPA, 3 minutes dehydration bake at 115 °C, 2 minutes oxygen ash at 80 W.
- Prepare a dilution 2:1 by volume of SU-8 3005 : Cyclopentanone to reduce resist thickness to about 2–2.5 µm.
- Spin using a ramp step to spread the resist uniformly : 5 seconds at 1000 rpm, then 30 seconds at 4000 rpm.
- Pre-bake the sample on a hotplate for 1 minute at 65 °C, then 3 minutes at 95 °C, then again 1 minute at 65 °C.
- Exposure to UV light using MA6 for 15 seconds. A slight overexposure is recommended to improve curing and avoid resist cracking.
- Post-exposure bake for 1 minute at 65 °C, then 3 minutes at 95 °C, then again 1 minute at 65 °C. This step is crucial for resist cross-linking.
- Develop the exposed pattern in neat EC solvent for 1 minute and rinse with IPA.

Note that SU-8 hard-bake and curing is not performed as it requires high temperature ($> 150\,^{\circ}\text{C}$), which can cause significant surface degradation of the narrow bandgap diode material.

3.5 Metal deposition and lift-off

Metal deposition is used to define the electrical ohmic contacts and bond pads of the LED devices. Moreover, it is used to deposit the thin metal layer used in plasmonic-enhanced devices, as discussed in Section 7.3.

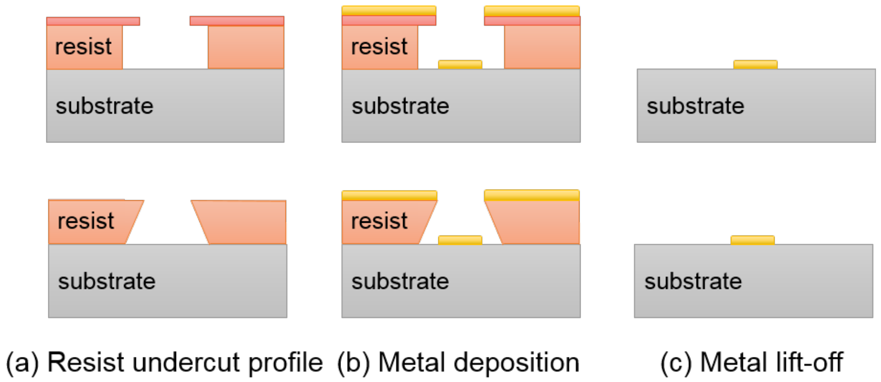

FIGURE 3.9: Schematic illustration of the lift-off process using either a double layer of positive resist (top) and a negative resist (bottom).

The metal deposition is carried out using a Plassys (MEB 400s or 550s) electron-beam evaporator [109]. A target of the source metal is bombarded with an electron beam, generated by a tungsten filament under high vacuum (pressure $< 5 \times 10^{-7}$ mbar). The atoms of the source metal evaporate into the gaseous phase and then precipitate into solid form only when they reach the surface of the substrate, coating it with a uniform thin film. The main advantages of this deposition technique are the coating uniformity and the precise thickness monitoring, thanks to the low deposition rate (0.3 nm/s).

Lift-off is the patterning technique used to define the metal film, as described in Figure 3.9. The metal is deposited on top of the sample, covering all the areas with and without resist. After the deposition, the sample is soaked in acetone at 50 °C for a time varying from under 1 hour to a few hours, depending on the pattern shape and minimum feature size. The acetone dissolves the resist mask, lifting off the metal that was deposited on top of the resist and leaving only the metal that was in contact with the substrate. The thickness of the resist should be at least 3 times larger than the thickness of the metal to assure a successful lift-off. An undercut profile of the resist is also essential for the lift-off release process.
Positive resists are generally not suited for lift-off processes as they only allow positive or at best vertical sidewalls. This promotes the coverage of the sidewalls during metal evaporation, making lift-off problematic. However, a process consisting of a double layer of positive resist with different exposure doses can be used to obtain an undercut profile, which favours a successful lift-off. A lift-off process using a double layer of AZ4562 resist [110] was developed in collaboration with Dr. Corrie Farmer (at KNT [95]). The processe steps are listed below:

- Sample clean in acetone and IPA, 3 minutes dehydration bake at 115 °C, 2 minutes oxygen ash at 80 W.
- Spin AZ4562 for 30 seconds at 3000 rpm.

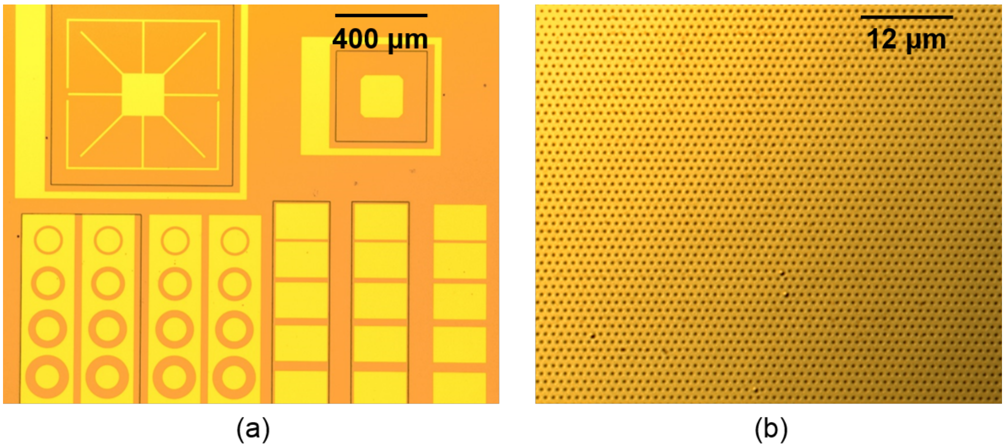

FIGURE 3.10: Optical microscope image of different structures fabricated by metal deposition and lift-off: (a) LEDs with different mesa dimensions and contact geometry and test structure for the characterisation of the contact resistance; (b) 1 μm-periodic array of holes in a 50 nm-thick gold film.

- Oven bake for 1 hour at 90 °C.
- Flood exposure of first layer for 30 seconds using MA6.
- Spin second layer of AZ4562 for 30 seconds at 4000 rpm.
- Oven bake for 1 hour at 90 °C.
- Expose for 25 seconds through pattern mask.
- Develop in 1:4 AZ400K:H_2O for 3 minutes.

Negative resists are generally the best choice for lift-off processes because the exposure dose strongly impacts the resist profile. In fact, low exposure doses keep the resist close to the substrate surface almost unexposed, thus allowing to achieve a pronounced undercut. The post-exposure bake step is essential as it cross-links the exposed resist areas which become insoluble in the developer. With the availability of the AZ2070 [111] thick negative resist, a lift-off process was developed in collaboration with Dr. Antonio Samarelli and colleagues at the University of Glasgow. The process steps are as follows:

- Sample clean in acetone and IPA, 3 minutes dehydration bake at 115 °C, 2 minutes oxygen ash at 80 W.
- Spin AZ2070 for 60 seconds at 3000 rpm.
- Bake on hotplate for 1 minute and 30 seconds at 113 °C.
- Expose for 20 seconds through pattern mask.

- Post-bake on hotplate for a minute at 113 °C. This step is very important for the cross-linking of the negative resist.
- Develop in MF319 for 1 minute and 20 seconds.

The ohmic contacts on both the p-type and n-type layers consist of Ti/Au 50 nm/250 nm. The titanium is used to guarantee a good adhesion onto the semiconductor surface. Gold layers thinner than 200 nm proved to be too fragile and resulted in bond pads pealing off during the wire bonding process. To obtain a better ohmic contact with lower resistance, thermal annealing of the metal contacts is usually performed. However, due to the narrow bandgap, AlInSb gives a low resistance even without annealing. Moreover, baking the devices at temperature higher than 120–150 °C can degrade the performance of the diodes. Thus, to prevent any surface degradation and avoid unnecessary metal diffusion from the contact into the semiconductor, thermal annealing of contacts was not carried out in the final fabrication process. The performance of the ohmic contacts are discussed in Section 4.1.2.

3.6 Summary of fabrication process for $\mathrm{Al_xIn_{1-x}Sb}$ LEDs

After few test runs to optimise the different fabrication steps, a final process was identified for the fabrication of AlInSb LEDs. The most significant constraints in the fabrication of $\mathrm{Al_xIn_{1-x}Sb}$ LEDs are as follows:

- Ultrasonic agitation is never used in the fabrication process to avoid damaging the brittle material.
- A temperature budget of 120 °C is set for all the processes to prevent any surface degradation. Steps that may require higher temperature are performed prior to the mesa etching to avoid exposure of the device active region.

According to standard fabrication techniques for III-V semiconductors, the most significant process steps developed specifically for $\mathrm{Al_xIn_{1-x}Sb}$ LEDs are summarised below:

- Sample cleaning is performed before every step using acetone and isopropyl alcohol, followed by 3 minutes dehydration bake at 115 °C and 2 minutes oxygen plasma ash at 80 W.
- The mesa pattern is defined using S1818 positive resist and photolithography. A deoxidation cleaning is done with 5:1 BHF and 1:1 HCl:H_2O, followed by wet

etch in 11:1:7 citric:H_2O_2:H_2O solution. The etching is performed at a constant temperature of 20.5 °C and with constant stirring at 100 rpm. The etch profile is isotropic with an etch rate of about 20 nm/min. As H_2O_2 degrades with time, it is recommended to use it from a freshly opened bottle.

- Surface passivation is achieved with a 2 µm-thick SU-8 layer. SU-8 was chosen as the preferred passivation material thanks to its stability performance and ease of integration in the fabrication process. The improvement of the LED leakage current obtained with surface passivation are presented in Section 4.1.1.
- The metal contact pattern is defined using the AZ2070 negative resist process described in Section 3.5. Ti/Au ohmic contacts are deposited by e-beam evaporation to both p-type and n-type layers.

The optical and SEM image of a completed device are shown in Figure 3.11.

The designed photolithography mask is shown in Figure 3.12a. It comprises four 5 × 5 mm patterns including about twenty devices with different mesa widths (w = 200 µm, 400 µm and 800 µm) and top contact geometries. This design allows to investigate the contribution of design parameters on LEDs electrical and optical performance, which is discussed in Chapter 4. Once ready, each pattern is cleaved separately, mounted on a chip carrier with a thermal conductive paste and wire bonded for electrical and optical characterisation. The final device, ready to be measured, is shown in Figure 3.12b.

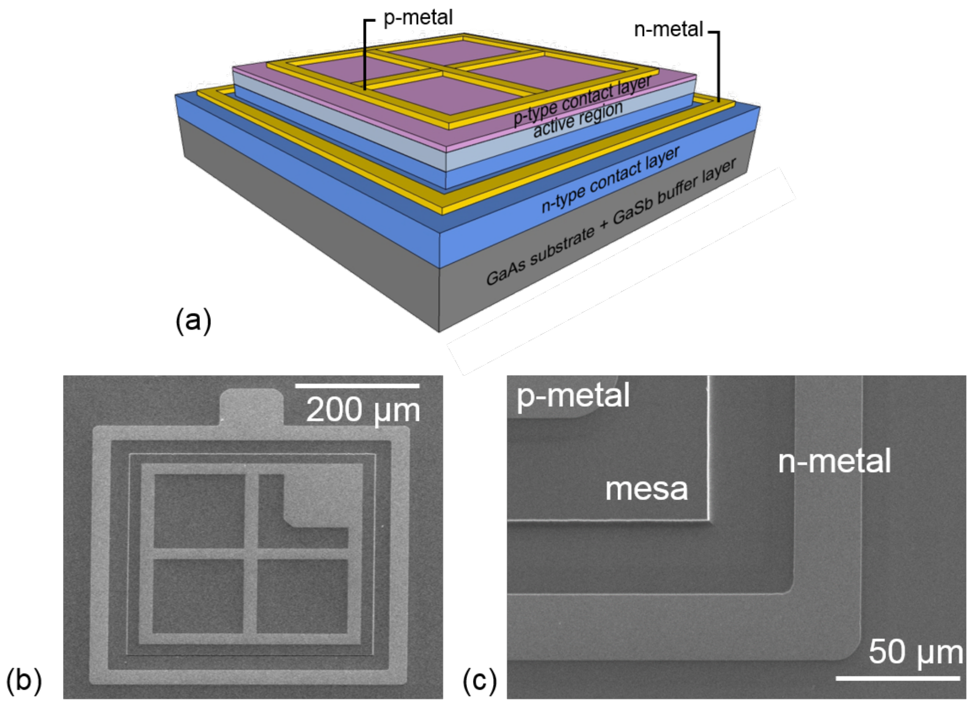

FIGURE 3.11: (a) Schematic illustration and (b) SEM image of a complete fabricated device with cross-shaped top contact geometry; (c) detail of a corner of the mesa structure with n-type and p-type metallisations.

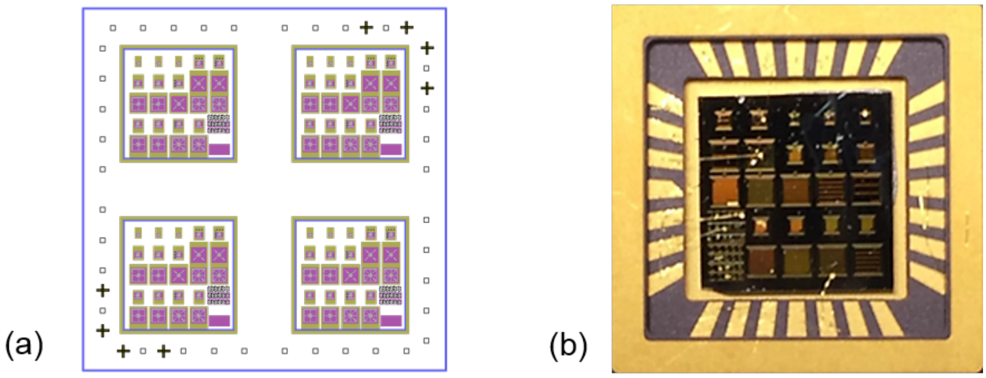

FIGURE 3.12: (a) Photolithography mask design with LED patterns of varying mesa dimensions and top contact geometries. (b) Optical image of a wire bonded chip carrier.

Chapter 4

Devices Characterisation

In this Chapter the main characterisation techniques are reviewed and described in detail. These techniques are tailored and applied to the characterisation of the fabricated LEDs. Both electrical and optical characterisation were performed to assess the performance of devices with different mesa dimensions, surface passivation, doping concentration, ohmic contacts and bias conditions.

4.1 Electrical Characterisation

4.1.1 Current-voltage measurement

The most basic characterisation measurement for an LED is the current-voltage (I-V) curve, which can provide significant information about the characteristics of the fabricated diode. This measurement is performed using a HP 4155A semiconductor parameter analyser and a source-measurement unit (SMU). A bias voltage is applied across the diode and the corresponding value of current is recorded.

A number of device parameters, such as the quality of the material, the formation of the junction and the quality of the contacts, can be retrieved from the forward voltage characteristic. At small current, the forward I-V can be fitted using an empirical diode model [63]:

$$I_F = I_0 \left(\exp \left(\frac{qV}{nkT} \right) - 1 \right), \tag{4.1}$$

where I_0 is the saturation current, n the ideality factor, k the Boltzmann's constant and T the absolute temperature. An ideality factor close to 1 indicates that the current flow is mainly dominated by diffusion, while an ideality factor close to 2 indicates that there is a significant contribution from generation and recombination of carriers. At

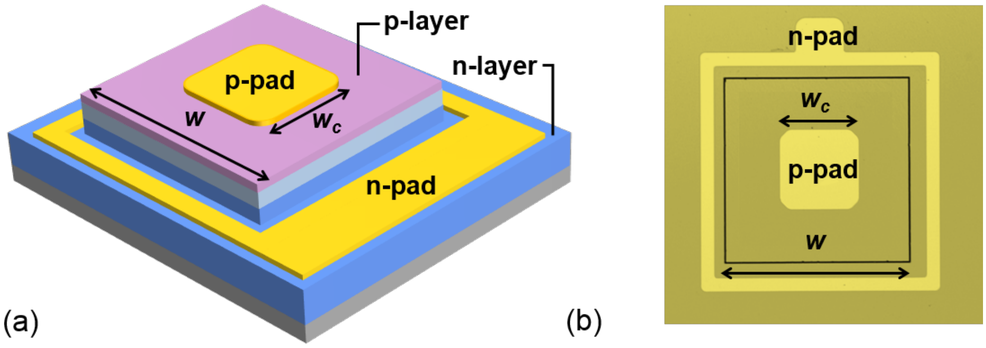

FIGURE 4.1: (a) Schematic illustration of the square mesa geometry with a square top contact pad placed in the centre of the mesa. (b) Optical image of a fabricated device with $w = 400\,\mu\text{m}$ and $w_c = 180\,\mu\text{m}$.

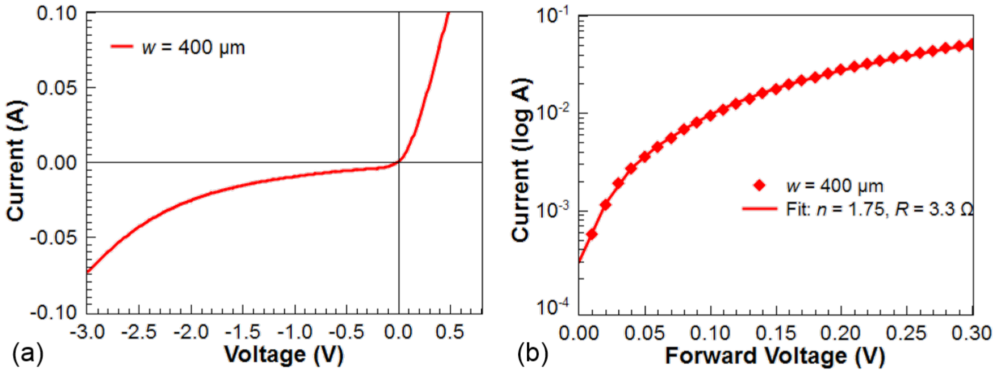

FIGURE 4.2: (a) Measured full I-V characteristic of the the device illustrated in Figure 4.1. (b) Measured and fitted I-V curve under forward bias. The fitting of the measured data according to Equation 4.2 result in an ideality factor of 1.8 and a series resistance of about 3.3 Ω.

higher forward voltage, the diode I-V curve deviates from the theoretical one, due to device heating from the series resistance. For this reason, an equivalent series resistance is added to the equation:

$$I_F = I_0 \left(\exp\left(\frac{q(V - IR)}{nkT} \right) - 1 \right). \tag{4.2}$$

The value of the series resistance can be determined by fitting the experimental I-V data to Equation 4.2.

The schematic illustration and optical image of an AlInSb p-i-n diode with a mesa width $w = 400\,\mu\text{m}$ and a square top contact pad of width $w_c = 180\,\mu\text{m}$ are shown in Figure 4.1. The dimensions of the contact pad were chosen in order to minimise the area covered by the opaque metal ($\sim 20\,\%$) to allow the measurement of the optical emission from the same device and at the same time guarantee a minimum size of the contact pad suitable for wire bonding. Additionally, the distance between the edge of the contact pad and the edge of the mesa is larger than a current spreading length, therefore minimising the

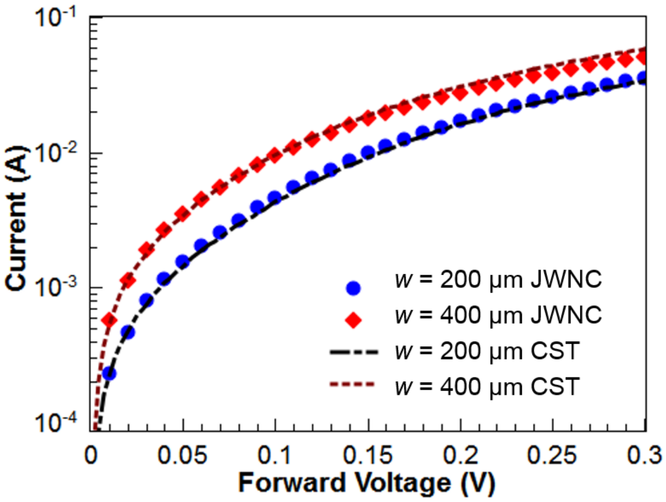

Figure 4.3: Measured forward I-V curves for devices fabricated in the JWNC and by CST. The good agreement of data confirms the repeatability of the fabrication process.

contribution of surface recombination.

The measured I-V characteristic and the fitted curve according to Equation 4.2 are plotted in Figure 4.2. The fitted value of the ideality factor n is close to 2, possibly due to higher recombination current at the heterojunction with the wider bandgap $\mathrm{Al_{x+0.15}In_{1-(x+0.15)}Sb}$ barrier layer. The series resistance is dominated by the contact resistance between the metal and the semiconductor, which scales with contact area according to Ohm's law: $R_c = \rho_c \cdot (t_c/A_c)$.

The contact resistance can be reduced by choosing contact metals with an appropriate work function and by increasing the doping concentration of the semiconductor contact layer. According to the Schottky model [112], the barrier height at the contact depends on the metal work function ϕ_M and the semiconductor electron affinity χ: $\phi_B = \phi_M - \chi$, while the barrier width is proportional to the doping concentration: $W \sim N_D^{-1/2}$. In the case of narrow bandgap materials, as AlInSb, ohmic contacts with metals can be easily achieved thanks to the high values of electron affinity ($\chi_{\mathrm{InSb}} = 4.59\,\mathrm{eV}$), which give low barrier heights at the contact. As a result, the measured diodes show a low series resistance even for relatively low doping concentrations and without any thermal annealing of the contacts. The detailed measurements of the contact resistance for p-type and n-type AlInSb layers is discussed in Section 4.1.2.

The I-V curves of devices with similar mesa area and contact pattern fabricated using the process discussed in Chapter 3 and the production process by Compound Semiconductor Technologies Ltd. [82] are compared for reference. Figure 4.3 shows the forward I-V curves for devices with two different mesa widths. The good agreement in the measured data indicates the high quality and repeatability of the fabrication process.

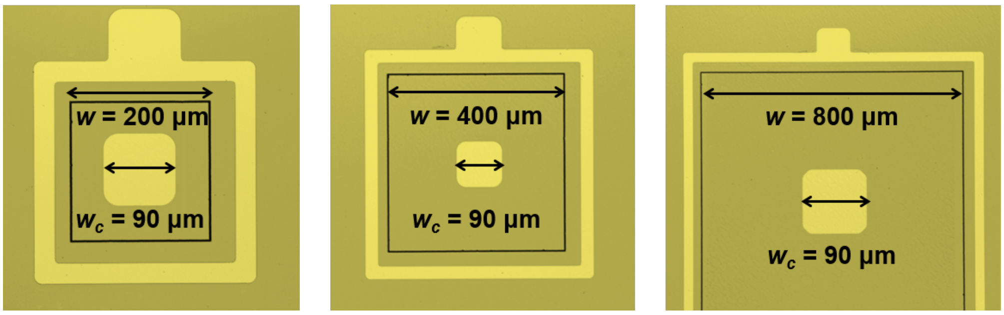

FIGURE 4.4: Optical images of fabricated devices of mesa width $w = 200\,\mu\text{m}$, $400\,\mu\text{m}$ and $800\,\mu\text{m}$ and same contact pad area ($w_c = 90\,\mu\text{m}$).

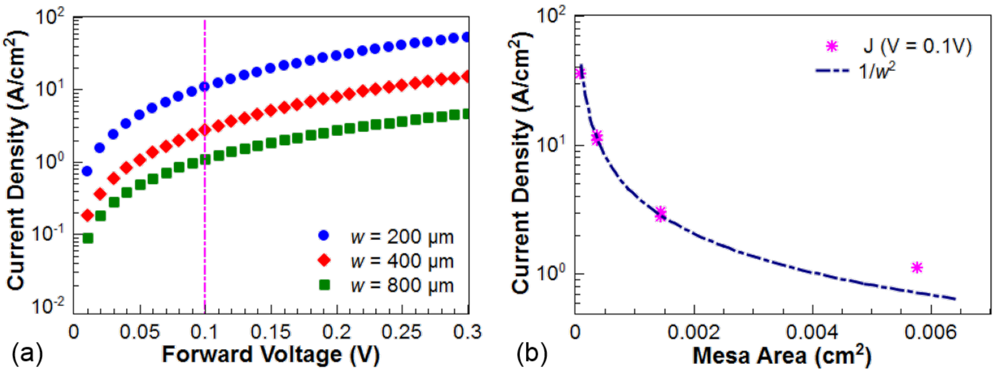

FIGURE 4.5: (a) Measured forward J-V characteristics for devices with different mesa width w and same contact area. The current was normalised to the mesa area. (b) The current density values at $V_{\text{bias}} = 0.1\,\text{V}$ are extracted and plotted against the mesa area. An inverse dependence over the mesa area is shown for comparison.

The effect of the mesa width on the current diffusion was evaluated by comparing devices with the same contact area. In this case, the central contact pad has a width $w_c = 90\,\mu\text{m}$ for all devices, covering 20 %, 5 % and 1.3 % of the area for devices with $w = 200\,\mu\text{m}$, $400\,\mu\text{m}$ and $800\,\mu\text{m}$, respectively, as illustrated in Figure 4.4. Therefore, all devices have the same contact resistance and the same injected current density under the contact pad. The forward I-V curves, plotted in Figure 4.5a, were normalised to the mesa area and the values of current density at a constant bias voltage of 0.1 V were extracted from the J-V curves. As shown in Figure 4.5b, the extracted values of current density still exhibit an inverse dependence on the mesa area (w^2) and deviate from it for the larger devices. This has been attributed to the current crowding effect, which is a consequence of the higher sheet resistance of the p-type top contact layer. The current does not spread uniformly across the device area and the current density shows an exponential decay away from the central contact pad. From the data in Figure 4.5b, it can be calculated that only about 60 % of the total device area is effectively biased in case of a device with $w = 800\,\mu\text{m}$ and $w_c = 90\,\mu\text{m}$. The current crowding effect will be discussed in detail in Chapter 5.

In the reverse bias region, different mechanisms contribute to the leakage current. This is particularly relevant when devices are used as photodetectors, as the leakage current translates into shot noise that will affect the signal-to-noise ratio (SNR) of the device. The two main contributions are the bulk and surface leakage currents.

The former is due to diffusion or generation-recombination currents. Its contribution scales with the junction area and reduces proportionally with decreasing intrinsic carrier concentration as a function of temperature.

The surface leakage current is determined by the abrupt termination of the periodic crystalline lattice at the air-semiconductor interface, causing the formation of dangling bonds. As a consequence, a non-zero surface potential builds up at the sidewall interface, resulting in conductive leakage channels parallel to the surface of the etched mesa [103]. Additionally, native oxides and contaminants create interfacial states which contribute to the leakage current. Therefore, the surface leakage current is expected to be more significant for small devices, which have a larger surface-to-volume ratio.

For a square mesa diode, the leakage current density can be expressed as the sum of its bulk and surface components. By plotting the resistance-area product at zero bias for variable area diodes, it is possible to evaluate the surface dependence of the leakage current. This relation can be written as:

$$\frac{1}{R_0A} = \frac{1}{(R_0A)_{bulk}} + \frac{1}{r_{surf}}\frac{P}{A} \tag{4.3}$$

where $(R_0A)_{bulk}$ is the bulk contribution ($\Omega\,\mathrm{cm}^2$), r_{surf} the surface resistivity ($\Omega\,\mathrm{cm}$), P the diode perimeter and A the diode area [103]. If the leakage current is dominated by the bulk component, the curve has a slope close to zero. Otherwise, if the surface leakage component is significant, the smaller devices will show a higher current density.

The reverse I-V characteristics for AlInSb p-i-n diodes with variable mesa width are shown in Figure 4.6. The data are normalised to the mesa area to factor out the contribution of the bulk leakage current. However, the scaling of the current densities with mesa width (and therefore with perimeter) indicates that there is still a contribution of the surface leakage component at room temperature. This could be reduced with improved etching and passivation processes.

As discussed in Section 3.4, SU-8 was chosen as a suitable material for the mesa sidewalls passivation. Previously reported experimental data for SU-8 passivation of InAs/-GaSb superlattice detectors show a similar level of leakage current density at room temperature, but a significant reduction at lower temperature, with up to four orders of magnitude improvement at 77 K [113]. Figure 4.7 presents the plot of $(R_0A)^{-1}$ as a function of P/A for two different sets of variable area diodes with no passivation and

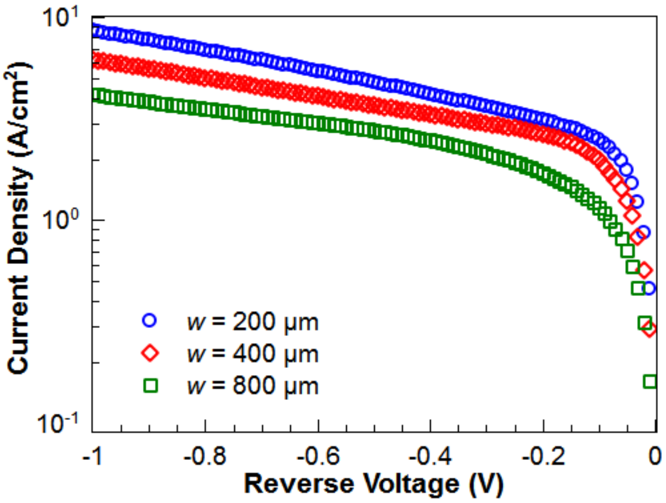

FIGURE 4.6: Measured leakage current densities for devices with different mesa width w. The dependence on the mesa dimension suggests that the contribution of surface leakage current is dominant.

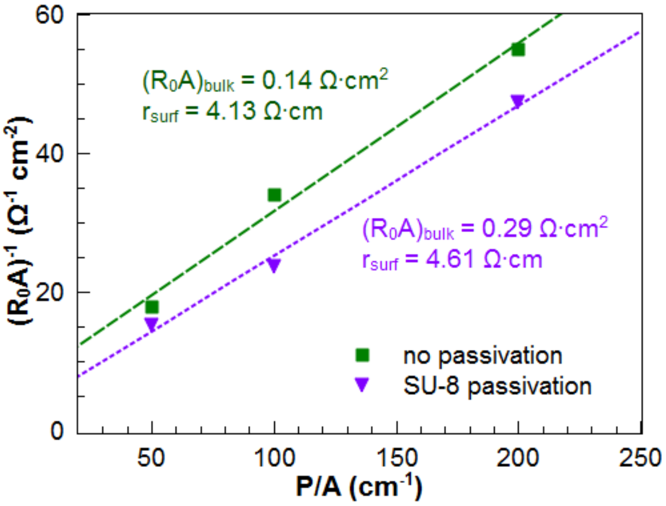

FIGURE 4.7: Dynamic resistance-area product at zero bias $(R_0A)^{-1}$ as a function of the perimeter-to-area ratio P/A for diodes with w between 200 µm and 800 µm at room temperature, showing the effect of SU-8 passivation.

SU-8 passivation according to the process described in Section 3.4. The higher value of surface resistivity (4.6 Ω cm compared to 4.1 Ω cm for the unpassivated device) indicates a slightly weaker dependence of the current density on surface leakage effects at room temperature.

4.1.2 Transfer Length Method (TLM)

The linear Transfer Length Method (TLM) is one of the more common techniques to evaluate the specific contact resistance and therefore the quality of ohmic contacts to semiconductors [112]. The two-terminal test structure consists of a series of identical

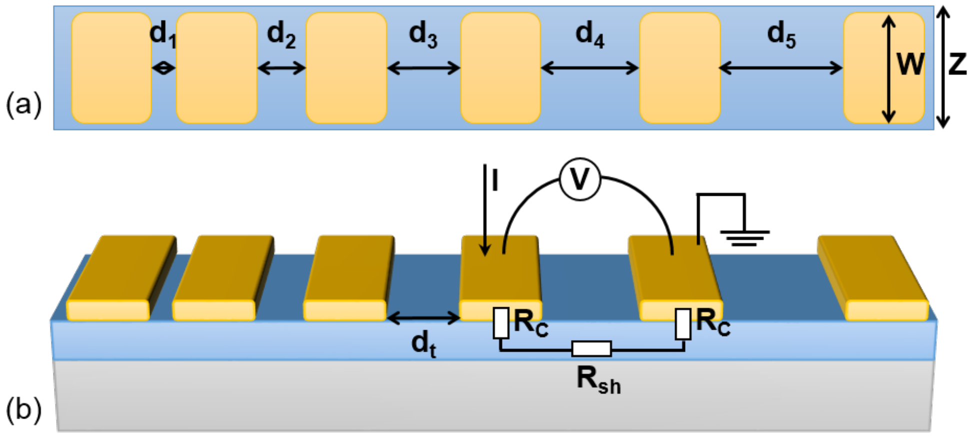

FIGURE 4.8: Schematic illustration of a TLM contact resistance test structure. (a) Top view of the TLM contact pads with increasing gap spacing. (b) Perspective view of the test structure with resistance components.

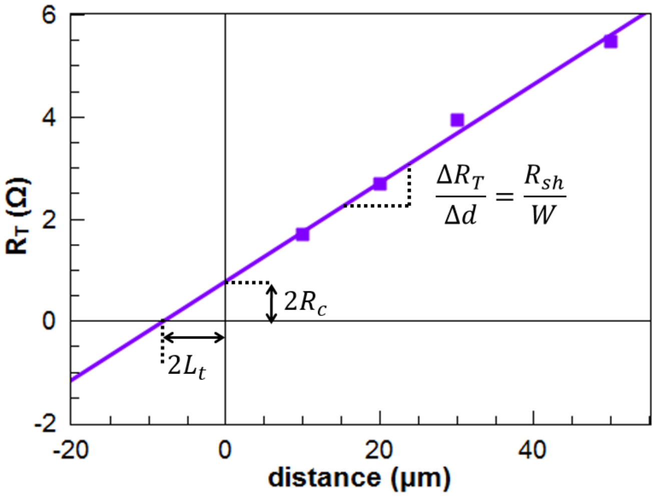

FIGURE 4.9: Example plot of the measured total resistance as a function of the distance between the contact pads of a TLM structure for a Ti/Au p-contact.

contacts pads, with length l and width W, with increasing gap d_t, as illustrated in Figure 4.8. The contact resistance R_c and specific contact resistance ρ_c can be determined from the linear relation between the measured resistance and the increasing gap spacing d_t between the contact pads. Assuming the contact resistance is the same for all pads, the total resistance, measured when applying a current between two consecutive pads, can be written as:

$$R_T = \frac{R_{sh} d_t}{W} + 2R_c \tag{4.4}$$

where R_{sh} is the sheet resistance of the semiconductor thin film.

An example of a plot of R_T as a function of d_t is shown in Figure 4.9. From the slope of this linear relation, the semiconductor sheet resistance R_{sh} (in $\Omega\,\Box^{-1}$) can be

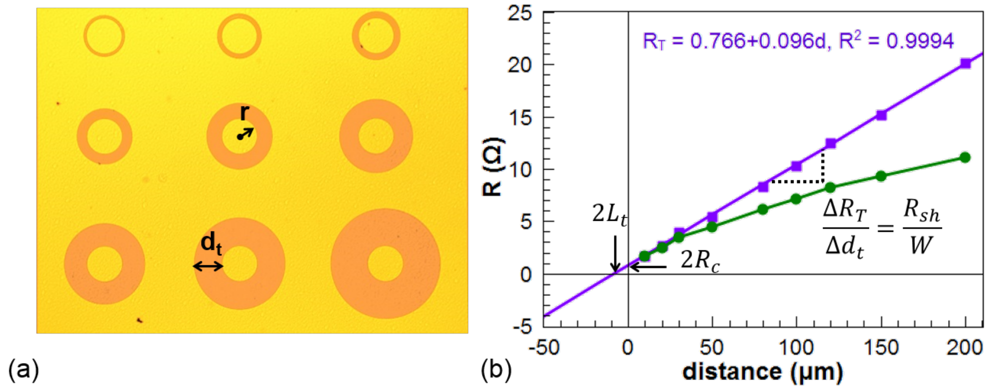

FIGURE 4.10: (a) Optical image of a CTLM test structure defined by photolithography and lift-off. The inner contact pads have a radius r of 100 µm and the gap width d_t varies from 10 µm to 200 µm. (b) Total resistance as a function of gap width, as measured and after correction according to Equation 4.5, for a Ti/Au p-contact. The linear fit of the corrected data allows the retrieval of the significant values: $R_c = 383\,\mathrm{m\Omega}$, $L_t = 3.9\,\mu\mathrm{m}$, $R_{sh} = 60.6\,\Omega/\square$, $\rho_c = 9.6 \times 10^{-6}\,\Omega\,\mathrm{cm}^2$.

extracted. The contact resistance R_c can be obtained from the intercept with the y-axis, which corresponds to $R_T(d_t = 0) = 2R_c$ (in Ω). The intercept with the x-axis gives the transfer length $L_t = \sqrt{\frac{\rho_c}{R_{sh}}}$ (in µm). The transfer length can be considered as the distance over which most of the current transfers from the metal to the semiconductor. For good ohmic contacts, with a specific contact resistance $\rho_c \leq 10^{-6}\,\Omega\,\mathrm{cm}^2$, the transfer length is generally in the order of few µm. From the sheet resistance and the transfer length, the specific contact resistance can be calculated as $\rho_c = R_{sh}L_t$ (in $\Omega\,\mathrm{cm}^2$).

The main drawback of the linear TLM technique is that it requires the etching of a mesa structure of width Z around the TLM pattern, to prevent the current spreading laterally in the thin film material under test. Even so, as $Z \neq W$, the linear TLM suffers from an inhomogeneous distribution of the current density at the edge of the contacts, which results in an underestimation of the contact resistance. An isolation mesa of the same width of the metal pads, $Z = W$, is particularly difficult to achieve by photolithography with the alignment tolerances of the mask aligner available in the JWNC. For this reason, circular TLM (CTLM) test structures were used, as proposed in the literature [112, 114]. These structures consist of circular inner contact pads of radius r, separated from a metallic outer region by a ring-shaped gap of width d_t, as shown in Figure 4.10(a). The circular geometry simplifies the fabrication process by reducing the definition of this test structure to a single lithography exposure and metal lift-off. By forcing a current between the inner and the outer contact pads, the total resistance as a function of the gap width can be measured. The non-linear relation obtained can be reduced to the linear TLM model with a correction factor, which takes into account the

Table 4.1: Measured specific contact resistance ρ_c for p-type and n-type contacts on AlInSb with Ti/Au and Ti/Pt/Au metallisation.

Contact	Metal	Specific Contact Resistance ρ_c ($\Omega\,\mathrm{cm}^2$)
AlInSb p-contact	Ti/Au	5.1×10^{-6}
	Ti/Pt/Au	2.0×10^{-3}
AlInSb n-contact	Ti/Au	1.1×10^{-6}
	Ti/Pt/Au	3.4×10^{-5}

effect of the circular geometry:

$$R_T = \frac{R_{sh}}{2\pi r}(d_t + 2L_t)C \tag{4.5}$$

with C being the correction factor, defined as:

$$C = \frac{r}{d_t} \ln\left(1 + \frac{d_t}{r}\right) \tag{4.6}$$

The measured total resistance as a function of gap spacing before and after the correction is plotted in Figure 4.10(b). From the linear fit of the corrected data, the significant values of semiconductor sheet resistance R_{sh}, contact resistance R_c, transfer length L_t and specific contact resistance ρ_c can be derived as described for the linear TLM.

Two different metallisation, Ti/Au and Ti/Pt/Au, were tested for both p-type and n-type contacts on doped AlInSb. Ti/Pt/Au is known to have superior metallurgical properties, especially at elevated temperatures, as the Pt acts as a barrier metal to the interdiffusion of the contact metal (Au) with low melting point group III elements, such as In [115]. However, as shown in Table 4.1, the measured values of the specific contact resistance for Ti/Pt/Au are significantly higher than for Ti/Au for both p-type and n-type contacts. This can be attributed to the higher work function of Pt, which results in a higher potential barrier at the semiconductor-metal interface. Therefore, Ti/Au was chosen as the metal stack for both p-type and n-type contacts.

As discussed in Section 3.5, narrow bandgap semiconductors like AlInSb form good ohmic contacts with low contact resistance even without performing a thermal annealing process straight after the metal deposition. In fact, an annealing experiment was performed, but did not show a significant improvement in the contact resistance values. Moreover, as discussed in Section 3.5, baking the devices at temperatures higher than 150 °C results in surface degradation of the exposed mesa sidewalls. Therefore, thermal annealing of contacts is not performed in the fabrication of AlInSb LEDs.

Besides the choice of metals, the doping concentration of the p-type and n-type contact layer gives a substantial contribution in defining the contact resistance. In this case, thanks to the narrow bandgap semiconductor material, good ohmic contacts can

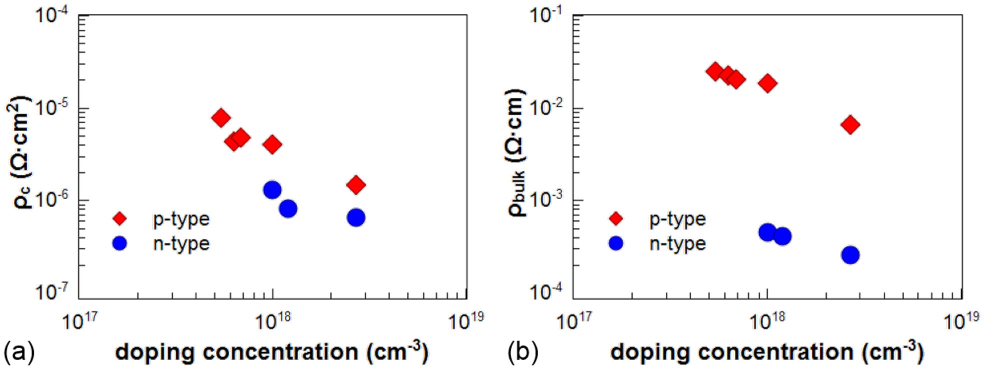

FIGURE 4.11: (a) Specific contact resistance ρ_c for Ti/Au contacts on p-type and n-type AlInSb single layers as a function of doping concentration. (b) Bulk resistivity ρ_{bulk} for p-type and n-type AlInSb single layers as a function of doping concentration.

TABLE 4.2: Extracted values of specific contact resistance ρ_c of Ti/Au contacts and AlInSb bulk resistivity ρ_{bulk} for relevant p-type and n-type doping concentrations.

Contact	Doping Concentration (cm^{-3})	ρ_c (Ω cm^2)	ρ_{bulk} (Ω cm)
AlInSb p-contact	6.9×10^{17}	4.7×10^{-6}	2.0×10^{-2}
	1.0×10^{18}	4.0×10^{-6}	1.8×10^{-2}
	2.7×10^{18}	1.5×10^{-6}	6.6×10^{-3}
AlInSb n-contact	1.0×10^{18}	1.3×10^{-6}	4.4×10^{-4}
	2.7×10^{18}	6.5×10^{-7}	2.6×10^{-4}

be formed with both p-type and n-type AlInSb layers having doping concentration $> 5 \times 10^{17}$ cm^{-3}. To evaluate the effect of the doping concentration on the contact resistance, CTLM test structures were fabricated on 3 µm-thick p-type and n-type AlInSb single layer wafers. The extracted values of specific contact resistance ρ_c and AlInSb bulk resistivity ρ_{bulk} as a function of doping concentration are plotted in Figure 4.11. The more relevant values are listed in Table 4.2 as well. Due to the larger effective mass of the holes in the narrow bandgap material [116], both the specific contact resistance ρ_c and the bulk resistivity ρ_{bulk} are always higher for p-type doped layers than for n-type doped layers. In particular, the difference of about two orders of magnitude in the bulk resistivity has a significant effect on the preferential path followed by the current, when injected into the p-i-n diode structure of a AlInSb LED. This can result in the so called current crowding effect, which will be discussed in detail in Chapter 5.

4.2 Optical Characterisation

Fourier Transform Infrared (FTIR) Spectroscopy is a well-established and developed method for the characterisation of material and devices in both research and application laboratories, with particular relevance to the mid-infrared and far-infrared spectral

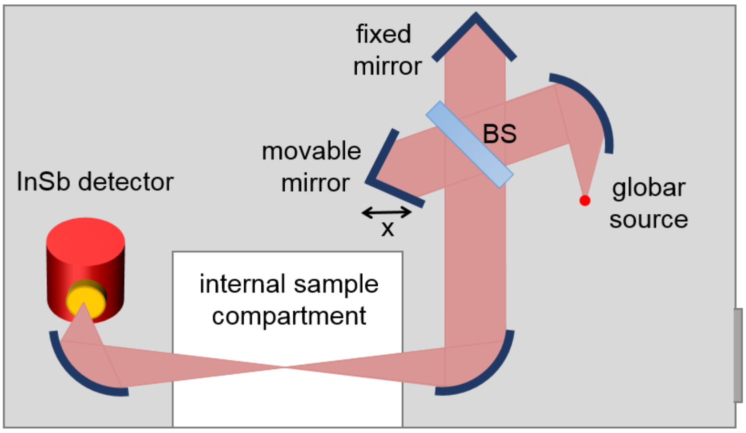

FIGURE 4.12: Schematic illustration of the beam path, including the Michelson interferometer, in a VERTEX 70 FTIR spectrometer.

ranges.

The FTIR spectrometer, of which a schematic illustration is given in Figure 4.12, is based on a Michelson interferometer [112, 117, 118]. Light emitted by an infrared source (generally an internal heated element or Globar source) is collimated and directed onto a beam splitter. This creates two separated optical paths by reflecting half of the incident light and transmitting the other half. In one path, the beam is reflected back to the beam splitter by a mirror at a fixed distance L. In the other path, the beam is returned to the beam splitter after being reflected by a movable mirror, which can be precisely translated back and forth by a distance x around its position starting at L. When the two components recombine at the beam splitter, they are in phase if $x = 0$. Otherwise, if the mirror is moved, an optical path length difference $\delta = 2x$ is introduced. The beam is then focused on a detector, which measures the intensity of the recombined beams as a function of the mirror displacement $I(x)$. The detector gives maximum signal when the two beams interfere constructively, if their optical path difference is an exact multiple of the wavelength: $2x = n \cdot \lambda$, with n being a positive integer. The detector gives a minimum signal when destructive interference occurs, if the optical path difference is an odd multiple of $\lambda/2$. The accuracy of the optical path difference is controlled by using the interference pattern of the monochromatic light of a He-Ne laser. The detector output signal, the interferogram $I(x)$, can be described by the equation:

$$I(x) = \int_0^f S(f)[1 + \cos(2\pi x f)]df \tag{4.7}$$

where $S(f)$ is the source intensity. The interferogram always has its maximum at $x = 0$, when the optical paths are equal and all wavelengths interfere constructively. The height of the central peak can be used as a measure of the average spectral intensity. For $x \neq 0$, the modulation depth of the interference pattern decreases as the difference in the optical path length exceeds the coherence length of the broadband source [119]. The spectral

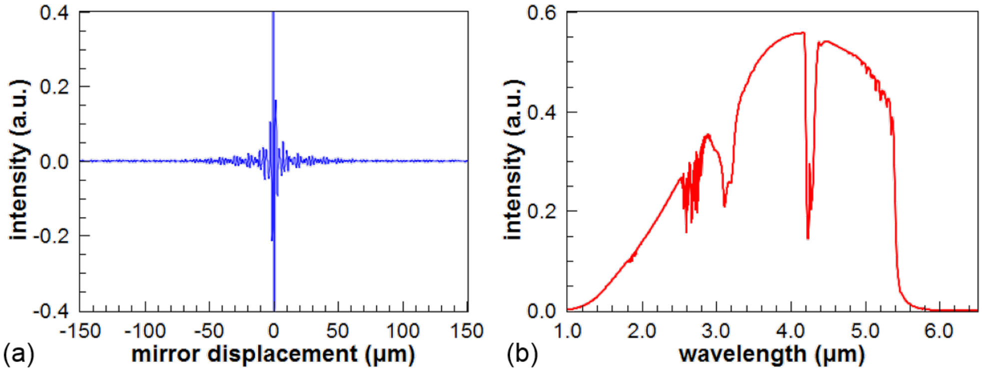

Figure 4.13: Example of (a) the measured interferogram and (b) the corresponding spectrum for the FTIR internal Globar broadband source measured with a 77K-cooled InSb detector.

response is calculated from the interferogram by Fourier transform:

$$S(f) = \int_{-\omega}^{\omega} I(x) \cos(2\pi x f) dx \tag{4.8}$$

$S(f)$ contains the spectral information of the light source, of any sample placed along the optical path and the ambient in which the measurement is performed. One of the main advantages of FTIR spectrometry is that the entire spectrum is measured in a single scan.

In this work, optical measurements were carried out with a VERTEX 70 FTIR spectrometer in the energy range from 0.18 eV to 1.7 eV. The instrument is equipped with a CaF_2 beam splitter and an internal Globar broadband source. The interferograms are detected with a 77K-cooled InSb detector. Figure 4.13 shows an example of the interferogram and corresponding spectrum of the internal broadband source. The very sharp and strong peak corresponds to the broad linewidth of the spectrum, while the wings of the interferogram contain most of the higher resolution spectral information, corresponding to the fine H_2O and CO_2 absorption lines that can be seen in the spectrum at 2.7 µm and 4.2 µm, respectively.

4.2.1 Reflectance and Transmittance Measurement

To obtain a reflectance or transmittance spectrum for a sample under test, a two step measurement has to be performed:

- The background measurement is taken with a gold mirror (in case of reflectance) or without any sample (in case of transmittance) in the optical path.

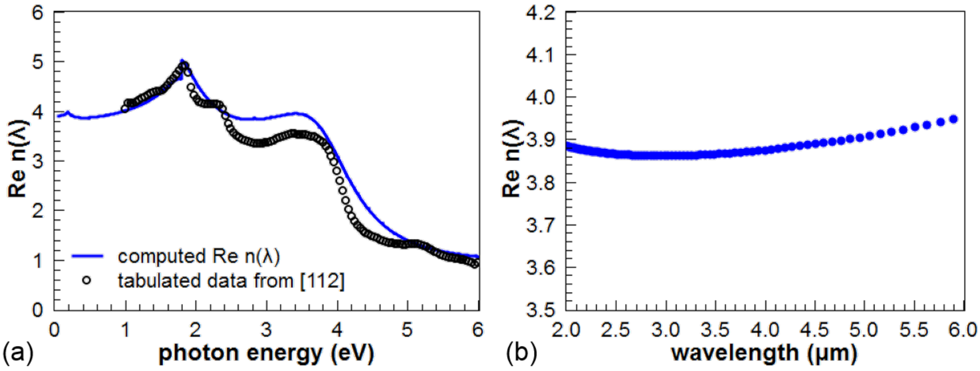

Figure 4.14: Computed refractive index dispersion of AlInSb according to the model reported by Adachi [120, 121]: (a) comparison with numerical values available in the literature [121]; (b) particular of the computed refractive index values in the spectral region of interest (2–6 µm).

- The sample measurement is then performed with the sample to be analysed placed in the optical path.
- The final reflectance and transmittance spectra are obtained by taking the ratio of the sample spectrum and the background spectrum, which eliminates the effect of the source emission spectrum, the detector sensitivity and the surrounding environment.

Both reflectance and transmittance spectra were used to validate the model of the refractive index dispersion $n(\lambda)$ for the epitaxially grown $\mathrm{Al_xIn_{1-x}Sb}$, and extend it over the mid-infrared spectral range. These data were computed from the analytical expressions reported in Adachi's model [120, 121], which takes into account the contribution of the different interband transitions to the dielectric function. The refractive index of $\mathrm{Al_xIn_{1-x}Sb}$ is evaluated as a linear interpolation of the values calculated for InSb and AlSb:

$$n(\mathrm{Al_xIn_{1-x}Sb}) = n(\mathrm{InSb}) - [n(\mathrm{InSb}) - n(\mathrm{AlSb})] \cdot x \tag{4.9}$$

A plot of the real part of the complex refractive index is shown in Figure 4.14. The left panel shows the computed dispersion relation over a wide range of photon energy (eV), compared to the numerical data available in the literature for the near infrared range [121]. The right panel shows the computed real refractive index for the mid-infrared spectral region of interest (2 µm to 6 µm), not previously available in literature.

The refractive index model was used to calculate the theoretical reflectance and transmittance spectra of a $\mathrm{Al_{0.05}In_{0.95}Sb}$ LED wafer. The AlInSb layer is about 4.5 µm-thick, grown on a GaAs substrate with a 300 nm-thick GaSb buffer layer. Figure 4.15 shows both the measured (red) and modelled (blue) reflectance and transmittance spectra in the 3 µm to 6 µm range. With a small adjustment of the layer thickness (4.7 µm), which

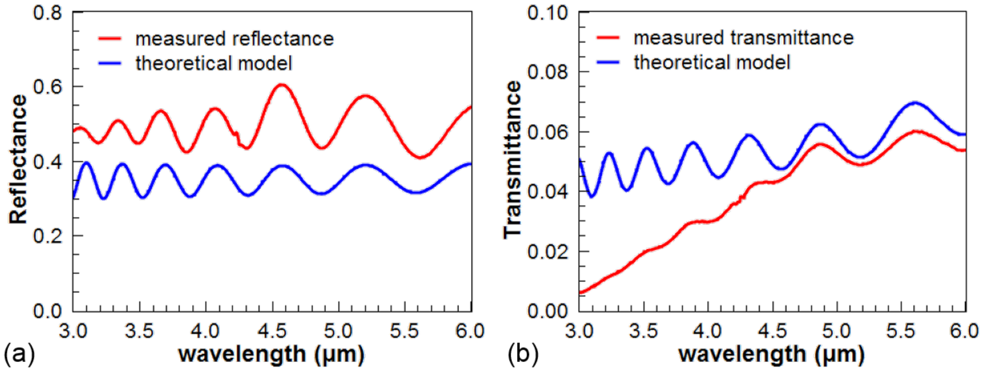

FIGURE 4.15: Measured and modelled (a) reflectance and (b) transmittance spectra of a $Al_{0.05}In_{0.95}Sb$ LED wafer. The discrepancy in the transmittance spectra at short wavelength is related to the strong absorption of the $Al_{0.05}In_{0.95}Sb$ material close to the band edge.

can be attributed to the accuracy of the growth rate, the modelled spectra show a good agreement with the measured curves. The difference of the transmittance curves for shorter wavelengths is due to the strong absorption of the AlInSb material close to the band edge. It is worth noting that the optical properties of the AlInSb narrow bandgap material are more complicated compared to wider gap materials. In particular, the effect of doping is more pronounced due to the contributions from intervalence band absorption (IVA) and Moss-Burnstein shift caused by band filling [72, 122]. Therefore, the accuracy of the refractive index model in the spectral region of interest is of particular importance for the design of the resonant-cavity structure, which will be discussed in Chapter 6.

4.2.2 Electroluminescence

Electroluminescence (EL) is the emission of optical radiation as a result of the application of an electric field or current across the LED p-n junction. Photons generated by spontaneous recombination of electron-hole pairs in the active region are emitted into free space. As described in Chapter 2, this process is quantified by an external quantum efficiency, which is defined as the ratio between the number of photons extracted into air to the number of injected charge particles.

The spectral emission from mid-infrared LEDs was characterised with a VERTEX 70 FTIR spectrometer. The instrument is equipped with an emission port, which allows the use of the LED device under test as an external emission source. The interferogram is measured with a 77K-cooled InSb detector. In the following section, the EL spectra of $Al_xIn_{1-x}Sb$ LEDs are presented and discussed as a function of operating bias conditions, contact layers doping and mesa width. These measurements allow the optimisation of the device design, which is discussed at the end of the Chapter.

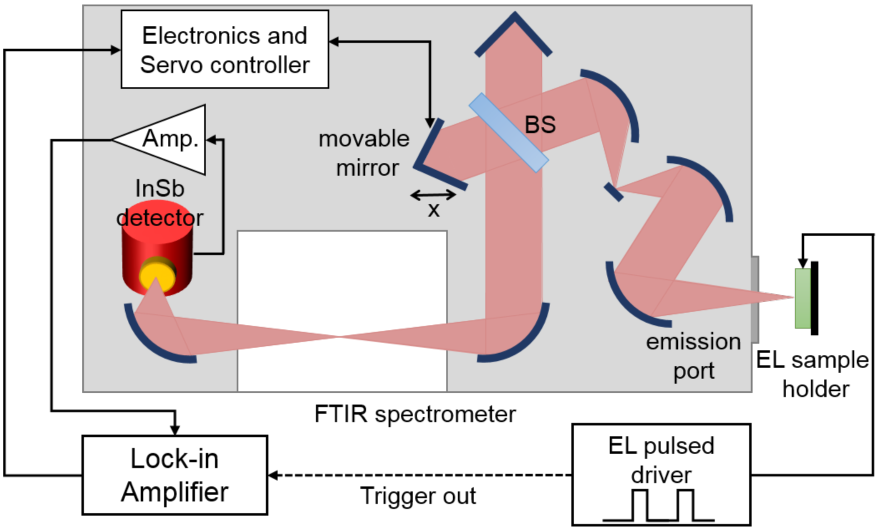

FIGURE 4.16: Schematic diagram of the FTIR spectrometer setup for electroluminescence measurement in step-scan mode.

4.2.2.1 Operating bias conditions

The first aspect that was considered is the bias condition. Mid-infrared LEDs are generally operated at moderate injection current levels, due to their low internal efficiency. However, loss mechanisms such as Joule heating and current crowding prevent continuous-wave (cw) operation [123]. Current crowding can significantly affect the performance of long-wavelength LEDs, since it results in a strong spatial non-uniformity of light emission and flattens out the output power versus bias current characteristic. Additionally, at high injection current levels and high temperatures, the non-radiative recombination process becomes more efficient and indeed the LEDs emit more heat than light. This is confirmed by the measurements of the EL spectra for the same LED operated in cw at 25 mA and 400 mA, shown in Figure 4.17. The spectra are acquired using the conventional rapid scan mode of the FTIR spectrometer. From the normalised spectra, three features can be observed, which confirm the device heating for higher injected bias current:

- Shift of the peak emission wavelength towards longer wavelength (+22 nm),
- Broadening of the emission peak,
- Four times stronger intensity of the thermal blackbody radiation tail.

In order to reduce these effects, the LEDs were characterised in pulsed bias operation. The injected bias current is a modulated square wave with frequency f and variable duty cycle. In this way, the device is switched on only for a limited percentage of the square wave period ($T = 1/f$), so as to reduce the device heating and decrease the overall

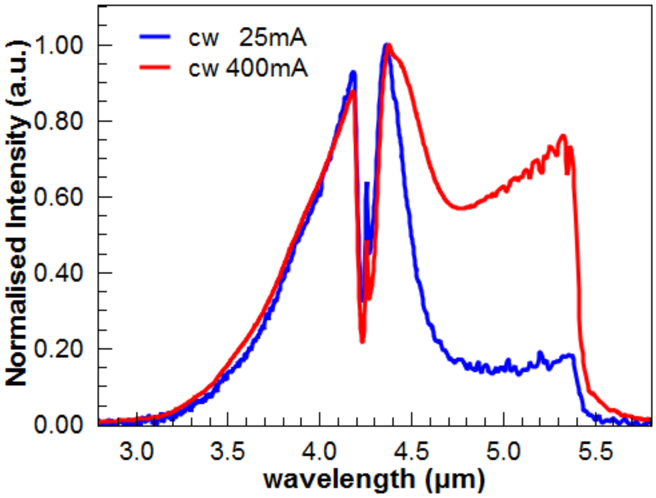

Figure 4.17: Electroluminescence (EL) spectra of an $Al_xIn_{1-x}Sb$ LED operated in continuous wave (cw) at 25 mA and 400 mA. The red-shift of peak emission, spectral broadening and stronger thermal background signal are clearly seen. The spectra were measured by rapid scan FTIR spectroscopy.

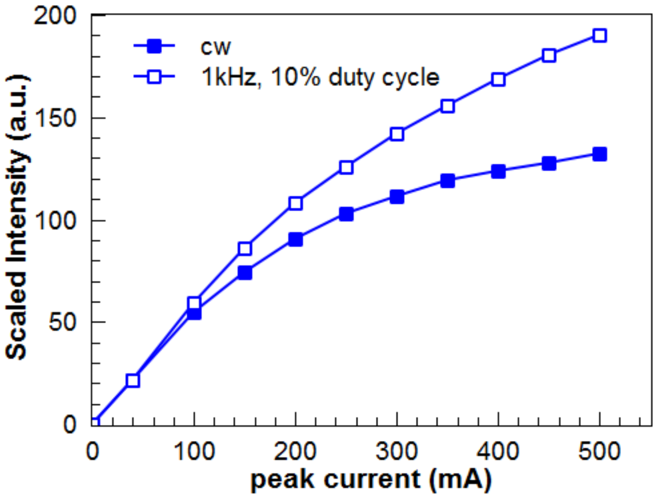

Figure 4.18: Emission intensity versus peak bias current for the same LED device operated in cw and pulsed bias. With a square modulated bias current (1 kHz, 10 % duty cycle), the saturation of the output intensity at high injection currents is significantly reduced.

power consumption. Additionally, the LED modulation allows the use of the step-scan mode of the FTIR spectrometer without restriction on the modulation frequency. In step-scan mode, the moving mirror is moved in discrete steps, and at each step data is collected and averaged. A lock-in amplifier, locked to the LED modulation frequency f and with a suitable time constant ($\tau \geq 3 \cdot 1/f$), is used to amplify the signal before being sent back to the spectrometer. In this way, the modulated EL signal can be extracted, while the unmodulated thermal background radiation can be effectively suppressed. A schematic diagram of the setup for EL measurements is illustrated in Figure 4.16. A modulation frequency of 1 kHz with 10 % duty cycle was chosen for all the subsequent

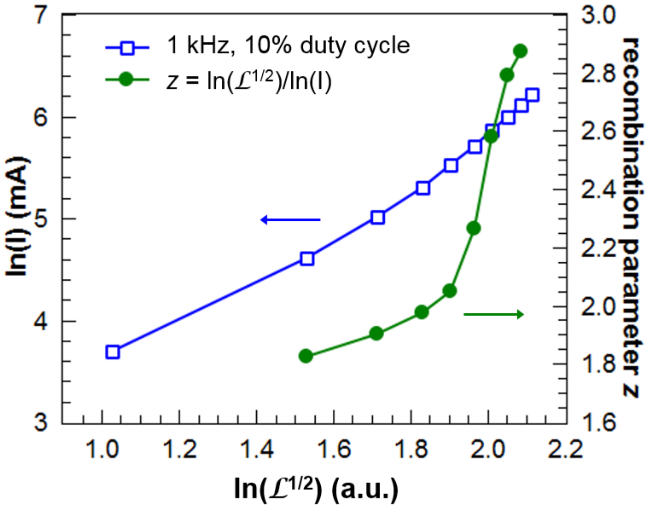

FIGURE 4.19: Plot of $\ln(I)$ versus $\ln(\mathcal{L}^{1/2})$ for an LED operated in pulsed bias at 1 kHz and 10 % duty cycle. The slope of the curve ($1 \leq z \leq 3$) indicates the dominant recombination mechanism under the specific operating conditions.

measurements. For these settings, the time constant of the lock-in amplifier is chosen in the tens of ms range ($\tau \sim$ 10–30 ms), which gives a good signal-to-noise ratio without resulting in excessively long data acquisition times. The LEDs give an output intensity that can be easily measured on the lock-in amplifier in the 1–10 mV range, without showing broadening or red-shifting of the emission spectra at higher injection currents up to 400 mA. The comparison of the output intensity versus peak bias current for cw and pulsed operation is shown in Figure 4.18.

Considering the main recombination mechanisms in an LED, which have been discussed in detail in Section 2.2, the total current through the device can be written as[62, 124]:

$$I = e(A_{\mathrm{SRH}}n + B_{\mathrm{rad}}n^2 + C_{\mathrm{Auger}}n^3)V + I_{\mathrm{leakage}} \tag{4.10}$$

where e is the electronic charge, V the active volume, n the carrier density and A, B, C the temperature dependent recombination parameters for the SRH, radiative and Auger recombination processes, respectively, as described in Section 2.2.1. Equation 4.10 can be approximated by $I \propto n^z$, where z assumes a value between one and three depending on the dominant recombination process. As the emitted intensity $\mathcal{L}$ is proportional to n^2, the same relation can be written as $I \propto (\mathcal{L}^{1/2})^z$. Therefore, the value of z can be obtained as the slope of the $\ln(I)$ versus $\ln(\mathcal{L}^{1/2})$ plot. Figure 4.19 shows the plot of $\ln(I)$ versus $\ln(\mathcal{L}^{1/2})$ for an LED device operated at room temperature, 1 kHz and 10 % duty cycle pulsed bias. The value of z is between 1.8 and 2.1 up to 300 mA peak bias current, suggesting that radiative recombination is the dominant process under these operating conditions, for which a single element LED shows an external quantum efficiency $\eta_{ext} \sim 3 \times 10^{-5}$. For higher peak currents, the value of z increases rapidly

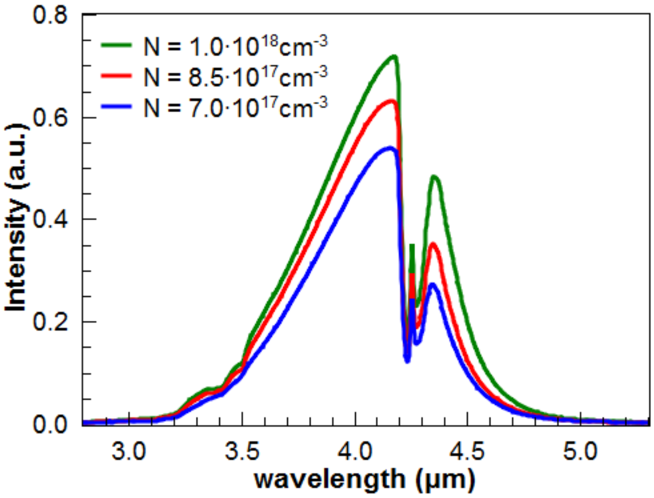

FIGURE 4.20: Measured EL spectra of LEDs with the same nominal aluminium composition and varying doping concentration of both p-type and n-type contact layers. Increasing the doping concentration from $7 \times 10^{17}\,\text{cm}^{-3}$ to $1 \times 10^{18}\,\text{cm}^{-3}$ results in 1.5 times stronger signal at 4.26 µm.

towards 3, confirming that the contribution of Auger recombination becomes more and more significant.

The same analysis was performed with the device operated at 10 Hz, 10 % duty cycle, therefore increasing the length of the bias pulse by two orders of magnitude (from 0.1 ms to 10 ms). In this case, the value of z already exceeds 2 at a peak bias current of 150 mA, suggesting that the higher temperature in the active region makes the Auger recombination dominant at lower injection current levels.

4.2.2.2 Doping Concentration

As discussed in Section 4.1.2, the doping concentration of the p-type and n-type contact layers has a significant contribution in determining the LED series resistance, which is dominated by the contact resistance between the metal and the semiconductor. The measured values of the specific contact resistance ρ_c in Table 4.2 show that the narrow bandgap material form good ohmic contacts with the metal even at moderate doping levels. However, a higher series resistance causes Joule heating and results in increased non-radiative Auger recombination and, thus, reduced internal efficiency of the LED. For this reason, the effect of contact layer doping on the emission intensity is evaluated. Figure 4.20 shows the EL spectra of three LEDs grown with nominally the same aluminium composition, but increasing doping concentration of the contact layers from $7 \times 10^{17}\,\text{cm}^{-3}$ to $1 \times 10^{18}\,\text{cm}^{-3}$. In this case, the aluminium composition is slightly higher than the optimal one, so that all the spectra are shifted towards shorter wavelengths with respect to the CO_2 absorption lines. The devices were operated under the

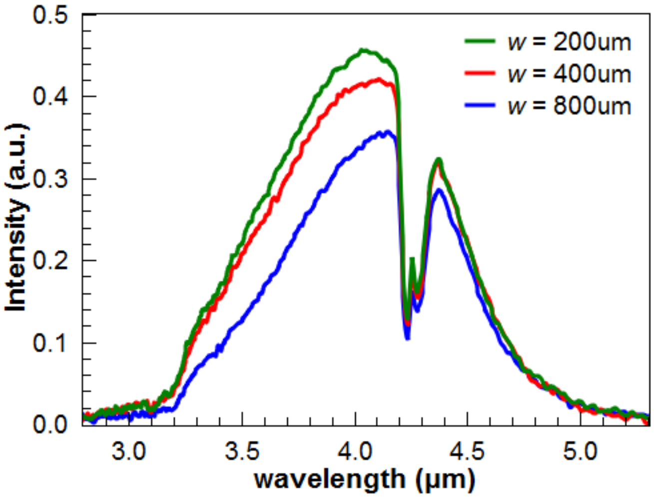

FIGURE 4.21: Measured EL spectra of LEDs with varying mesa width. Under the same electrical bias conditions, the smaller devices give 30 % stronger emission intensity, despite 80 % of the surface being covered by the top contact pad.

same injected current density. The LED with the highest doping concentration shows 1.5 times stronger signal at 4.26 µm thanks to the lower series resistance. Additionally, a lower sheet resistance of the top p-type contact layer has a positive effect on the current spreading, as will be discussed in more detail in Chapter 5.

On the contrary, increasing the doping concentration above $1 \times 10^{18}\,\text{cm}^{-3}$ is expected to cause a stronger absorption ($> 1000\,\text{cm}^{-1}$) in the p-type contact layer due to inter-valence band absorption (IVA) [72]. Therefore, a doping concentration of $1 \times 10^{18}\,\text{cm}^{-3}$ is chosen for both the p-type and n-type contact layers of the LED devices.

4.2.2.3 Mesa Width

Finally, the effect of the mesa width on the emission intensity was considered. Figure 4.21 shows the measured EL spectra of LEDs with 200 µm, 400 µm and 800 µm mesa width, fabricated from the same wafer with $1 \times 10^{18}\,\text{cm}^{-3}$ doping concentration for both the p-type and n-type contact layers. All three devices have a single square top contact pad of width $w_c = 180\,\mu\text{m}$ and are biased with the same square-wave modulated signal, having a peak value of 0.5 V. Having the same contact area, and therefore the same contact resistance, the three devices have almost identical series resistance. As a consequence, all three devices are operated with the same input power. However, the 200 µm device has only $\frac{1}{16}$ of the active area compared to the 800 µm device. Therefore, as shown in Figure 4.5b, the effective current density across the mesa area is ten times higher for the smaller mesa devices, allowing the generation of a stronger optical emission for the same electrical input power. Moreover, it is worth noting that the top contact pad covers a significantly higher portion of the top surface of the smaller area LED (80 % for the 200 µm-wide mesa compared to 5 % for the 800 µm-wide mesa), suggesting that the improvement of the emitted intensity from smaller mesa devices is more substantial than the one measured in this experiment. Additionally, even if operated at the same current density, the smaller area devices will benefit from a more uniform current spreading. In fact, most of the mesa area will fall within a current spreading length from the top contact, thus giving a more uniform distribution of bias current and, therefore, of light emission.

4.3 Conclusions

A series of LEDs were characterised as a function of design parameters, including the surface passivation, the metals for ohmic contacts, the doping concentration of the epitaxially grown $\mathrm{Al_{1-x}In_xSb}$ layers and the mesa dimensions. Significant progress was made in understanding the material properties and the different contributions of the design parameters to the LED electrical and optical performance. These experiments and results were performed in close collaboration with Gas Sensing Solutions Ltd (GSS), industrial partner of the project, and allowed the identification of a series of design guidelines that improve the LEDs electrical performance and emission intensity.

- The measurement of the reverse I-V characteristic and of the dynamic resistance-to-area product at zero bias ($\mathrm{R_0A}$) proved that the surface leakage component has a dominant contribution to the leakage current at room temperature, especially in devices with higher perimeter-to-area ratio. Therefore, a passivation layer is recommended to reduce the surface leakage effect. SU-8 epoxy-based photoresist is proposed as an alternative passivation material to the conventional dielectrics, thanks to the ease of integration within the fabrication process.

- A Ti/Au metallisation was confirmed to be the preferred choice for ohmic contacts on both p-type and n-type $\mathrm{Al_{1-x}In_xSb}$. Specific contact resistance values in the order of $5 \times 10^{-6}\,\Omega\,\mathrm{cm}^2$ were measured for Ti/Au contacts without any additional annealing step and with a relatively low doping concentration ($7 \times 10^{17}\,\mathrm{cm}^{-3}$) of the semiconductor contact layer.

- A higher doping concentration in the p-type and n-type contact layers translates into a lower series resistance of the LED, therefore reducing the Joule heating and the associated non-radiative recombination mechanisms. Additionally, a lower sheet resistance of the contact layers improves the current spreading across the device area, resulting in a more uniform distribution of the injected current and of the light emission. A doping concentration of $1 \times 10^{18}\,\mathrm{cm}^{-3}$ was chosen for both the p-type and n-type contact layers to guarantee a good surface morphology of the material and avoid additional optical losses in the top p-type contact layer due to intervalence band absorption.

- Reducing the LED mesa dimensions resulted in an enhanced efficiency of the device. In fact, thanks to the higher current density and more uniform current spreading associated with the smaller mesa area, the LEDs gave enhanced emission intensity under the same electrical bias conditions.

LED devices with $1 \times 10^{18}\,\mathrm{cm}^{-3}$ doping concentration and 200 µm mesa width have already been implemented by Gas Sensing Solutions Ltd. in production devices with excellent results, giving 2 times stronger emitted power and 50 % improved signal-to-noise ratio across the whole temperature range of operation.

Chapter 5

Current Crowding and Contact Geometry Design

This Chapter focuses on the theoretical analysis and experimental characterisation of the current crowding effect in top-emitting mid-infrared LEDs grown on semi-insulating substrates. The theoretical current spreading well agrees with the experimental spatial photocurrent distribution. These results are then used to design and evaluate the performance of large area AlInSb LEDs with a top contact grid geometry and identify the optimal configuration that leads to a more uniform distribution of the bias current across the device active area.

5.1 Current crowding in mid-IR LEDs on insulating substrates

Light-emitting diodes can be grown on conductive or insulating substrates. In the first case, the applied bias current flows mostly in the vertical direction, normal to the substrate plane. Instead, when LED structures are grown on insulating or semi-insulating substrates, as in the case of AlInSb LEDs on GaAs, the current flow is mostly lateral, parallel to the substrate plane. In both cases, the location and size of the metal contact pads are important to achieve a uniform current distribution across the device area and have a significant contribution on the efficiency of the light extraction [63]. Therefore, an appropriate understanding of the current flow across the diode structure is of fundamental importance for the device design, especially for top-emitting LEDs.

A schematic illustration of the device geometry and an equivalent circuit of the LED p-i-n junction are illustrated in Figure 5.1a nad 5.1b, respectively. In this configuration, the

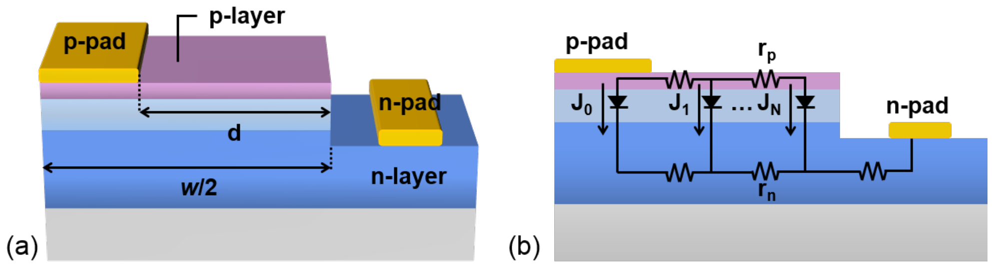

FIGURE 5.1: (a) Lateral current injection geometry and (b) corresponding equivalent circuit.

bias current is injected under the p-type top contact pad and mostly propagates laterally in both the p-type and n-type contacts layers. Ideally, light should be generated in the region between the contacts, so that the metal pads would not block the extraction of light. However, this geometry can easily lead to a non-uniform current spreading, because the p-type sheet resistance ρ_p/t_p is much higher than the n-type sheet resistance ρ_n/t_n (where ρ_i and t_i are the bulk resistivity and layer thickness of the p-type and n-type material, respectively), as discussed in Section 4.1.2 [116]. Additionally, as the applied voltage across the device increases, the non-linear resistance of the p-n junction decreases exponentially. Therefore, the vertical path becomes dominant and the injected current crowds in close proximity to the top contact pad. As a consequence, most of the light is generated under the non-transparent metal pad, which results in a low extraction efficiency.

Considering the equivalent circuit of Figure 5.1(b), with a current density $J(x = 0) = J_0$ at the edge of the p-contact pad and distributed sheet resistances $r_p = \rho_p/t_p$ and $r_n = \rho_n/t_n$, the solution for the current density distribution is exponential with the distance from the contact pad edge [63, 125, 126]:

$$J(x) = J_0 \exp(-x/L_s) \tag{5.1}$$

where

$$L_s = \sqrt{\frac{2V_a}{J_0(\rho_p/t_p + \rho_n/t_n)}}. \tag{5.2}$$

is the current spreading length and V_a is an activation voltage with magnitude of a few kT/e, e.g. $\sim 75\,\text{mV}$ [127]. With typical values of $\rho_p/t_p \sim 400\,\Omega/\square$ and $\rho_n/t_n \sim 2\,\Omega/\square$, the calculated current density distribution is plotted in Figure 5.2 for different values of the injected current density J_0. A long exponential decay length L_s indicates a more uniform current distribution and, therefore, a more uniform light generation across the region between the contacts.

The current crowding effect is even more pronounced in long wavelength emitting LEDs, as demonstrated for InAs-based devices [128]. In fact, the resistance of the p-n junction

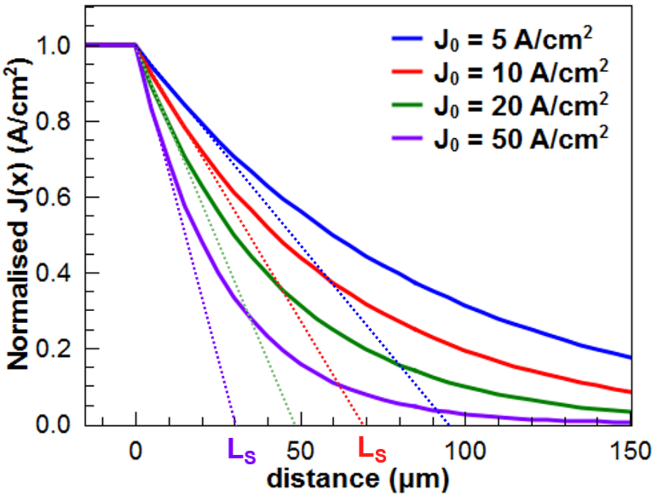

FIGURE 5.2: Calculated current density distribution $J(x)$ normalised to the injected current density J_0. The p-type sheet resistance is assumed to be two orders of magnitude higher than the n-type sheet resistance ($\rho_p/t_p >> \rho_n/t_n$).

is proportional to the saturation current I_0: this is a function of the intrinsic carrier concentration n_i, which in turns depends on the material bandgap ($I_0 \sim n_i^2 \sim \exp(-E_g)$). Therefore, due to the high intrinsic carrier concentration in narrow bandgap materials, the current crowding effect is already significant at lower voltages in mid-infrared LEDs. The main effects of the current crowding are [123, 129–131]:

- The reduction of the effective area of the device, due to the strong spatial non-uniformity of the injected current and, therefore, of the generated light;
- The generation of local heating of the structure in the regions with high current density.

The thermal effect also contributes to the increase of the non-radiative recombination mechanisms in the active region of the LED and, therefore, further reduces its internal quantum efficiency. For these reasons, room temperature mid-infrared LEDs are generally operated at high injection current densities only in pulsed bias mode. Additionally, a number of LED parameters become spatially dependent and the theoretical investigation of the current crowding becomes more complicated, often requiring the experimental verification of the current distribution [123].

The current crowding problem was extensively studied in GaN-based LEDs with both vertical and lateral injection geometries [132–135]. In the majority of high efficiency LEDs emitting in the visible spectral range, the current crowding problem is alleviated by the use of a transparent conductive oxide as a top current spreading layer. In these materials, such as indium tin oxide (ITO), fluorine doped tin oxide (FTO) and doped

zinc oxide, low values of sheet resistance can be obtained by varying their doping concentration. Therefore, optimal conditions for current spreading can be achieved while maintaining high transparency to the emitted radiation. However, these oxides show a reflectivity higher than 80 % at wavelengths longer than 2.5 µm, which limits their application in mid-infrared LEDs [136].
Alternatively, the p-type sheet resistance could be reduced by increasing the p-layer thickness or its doping concentration. However, both these options only marginally contribute to the improvement of current spreading. In fact, due to the much larger effective mass of the holes in the narrow bandgap material [116], the p-type bulk resistivity is always significantly higher than the n-type bulk resistivity, as discussed in Section 4.1.2. Additionally, it is worth noting that the square root dependence of Equation 5.2 translates into a modest $\sqrt{3}$ improvement in the current spreading length when the p-type doping concentration is increased for example from $7 \times 10^{17}\,\mathrm{cm}^{-3}$ to $3 \times 10^{18}\,\mathrm{cm}^{-3}$. On the other hand, a thicker p-layer results in stronger light absorption, due to intervalence band absorption in the p-type material [72], and higher ohmic resistance of the device that increases the Joule heating. Both these effects cause a lower overall efficiency of the device.

An alternative solution, which is the one adopted in this work, is the design of a grid top electrode that uniformly spreads the bias current across the device area. For maximum current spreading, the electrode geometry should be designed taking into account the expected current spreading length, while the electrode area should be minimised to avoid shadowing losses from the opaque metal. Similar grid contact geometries have been widely used in solar cells and visible LEDs [137].

5.2 Characterisation of Current Spreading via Spatially-resolved Photocurrent

In LEDs emitting in the visible spectral range, the current crowding effect can be analysed by means of conventional optical microscopy [138]. Two-dimensional mapping of the emitted power can be measured with standard CCD cameras and suitable contact patterns can be designed accordingly to minimise the current crowding and significantly improve the device performance. Similar techniques are used to characterise and improve the performance of solar cells [139]. However, the characterisation of the spatial current distribution in mid-infrared LEDs is not an obvious task. The two main limiting factors are the following:

- High resolution imaging of the emitted power requires infrared microscopy optimised for the mid-infrared spectral range, which is generally performed with infrared focal plane arrays that are particularly expensive and require cryogenic cooling;

- The total emitted power from mid-infrared LEDs is limited by the low internal quantum efficiency and extraction efficiency, as discussed in Section 2.2. Additionally, due to the current crowding effect, the devices undergo a local heating in the areas with higher current density. Therefore, mid-infrared LEDs operating at room temperature emit more heat than light, which require time resolved measurements to distinguish the emission from radiative recombination of injected carriers from the thermal background radiation.

Previously reported experimental results on InAs-based LEDs are based on time resolved infrared microscopy [123, 129, 130]. The test system consists of an IR camera operating in the 3–5 µm spectral range (HgCdTe cooled detector with $\sim$ 20 µm spatial resolution), that can be synchronised with the pulsed bias current of the LEDs. With this technique, the map of the emitted light can be obtained by subtracting the background radiation from the measured intensity recorded from the biased device. An alternative configuration was proposed in [129], where the device surface is scanned with a 250 µm-core fluoride glass optical fibre which directs the radiation on an InSb cooled detector. The fluoride fibre was modified to have a pointed tip of about 1 µm with lateral gold coated surface, according to the technique described in [140]. The experimental results confirm a strong non-uniformity in the light emission distribution, with the effective emitting area reduced to less than 10 % of the LED surface [128, 129].

The technique proposed in this work to characterise the current crowding in mid-infrared LEDs is a spatially-resolved photocurrent measurement by using the standard instrumentation available at the telecommunications wavelength of 1.55 µm. According to the reciprocity of charge collection [139, 141], the contribution to the total collected current I_{tot} from each point P of the device area is proportional to the current flowing into the point P due to an injected current I_{tot}. Therefore, the detected photocurrent signal, generated in the p-n junction area under illumination, can be related to the spatial current distribution of the device when operated in forward bias and, consequently, to the light emission distribution. As shown in Figure 5.3, the absorption coefficient α for $\mathrm{Al_{0.05}In_{0.95}Sb}$ is almost two times higher in the near-infrared spectral range ($6.5 \times 10^3\,\mathrm{cm^{-1}}$ at 1.55 µm compared to $3.3 \times 10^3\,\mathrm{cm^{-1}}$ at 4.26 µm). This results in a absorption depth of about 1.5 µm and 3 µm at 1.55 µm and 4.26 µm, respectively. Therefore, the devices would be less sensitive to short wavelength radiation because more light is absorbed in the cap layer. However, this absorbed radiation will not be

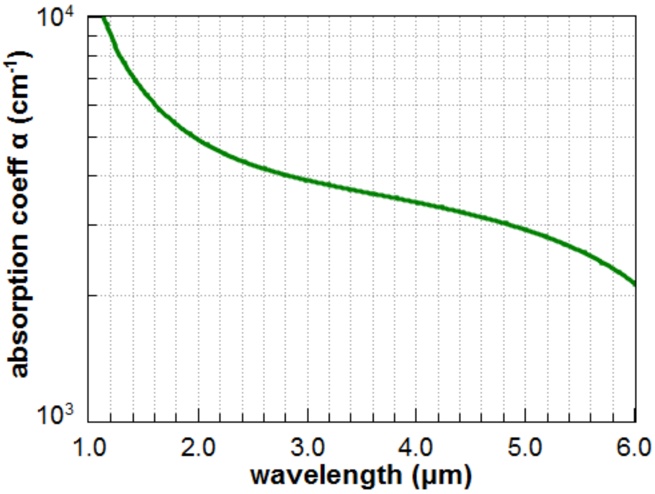

FIGURE 5.3: Absorption coefficient α for $Al_{0.05}In_{0.95}Sb$ across the near- and mid-infrared range. The values of α at 1.55 µm and 4.26 µm are $6.5 \times 10^3\,cm^{-1}$ and $3.3 \times 10^3\,cm^{-1}$, respectively.

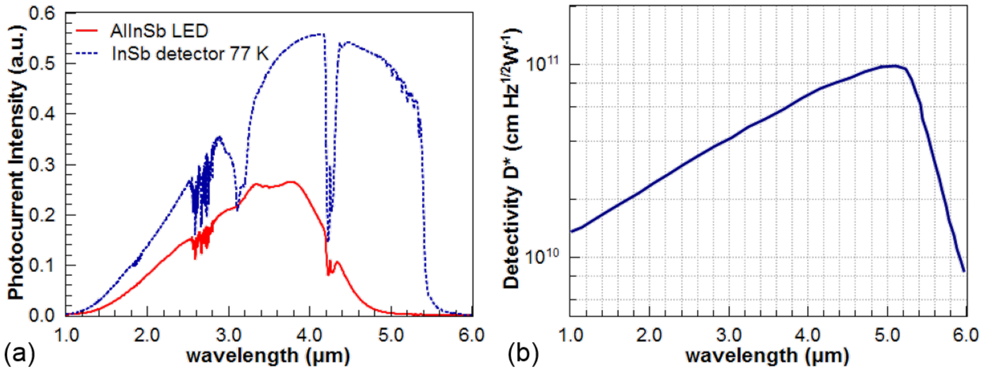

FIGURE 5.4: (a) Measured photocurrent spectra of an $Al_{0.05}In_{0.95}Sb$ LED and a 77 K-cooled InSb detector when illuminated by a mid-infrared Globar source. (b) Typical detectivity D^* response of a 77 K-cooled InSb detector.

detected thanks to the thin wider-bandgap material that forms a barrier to the electrons flow between the p-layer and the active region. Thus, it can be assumed that any light that is detected at 1.55 µm has been absorbed in the active region, so that the generated electron-hole pairs are swept away by the electric field across the depleted region and generate a photocurrent. Consequently, the measurement at this wavelength represent a valid indication of the current distribution in the device. Figure 5.4a shows the absorption spectrum of an $Al_{0.05}In_{0.95}Sb$ LED acquired with a VERTEX 70 FTIR spectrometer by illuminating the device with the internal Globar broadband source. The photocurrent spectrum of the FTIR 77 K-cooled InSb detector is plotted for comparison. Figure 5.4b shows the typical detectivity of a 77 K-cooled InSb detector.

The schematic illustration of the measurement setup is shown in Figure 5.5. A modulated 1.55 µm laser beam is focused onto the device surface by a cone lensed glass optical

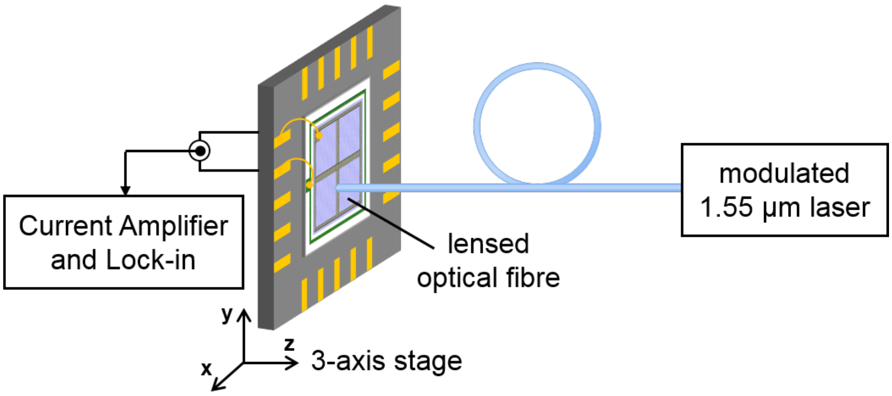

FIGURE 5.5: Schematic illustration of the setup for the spatial photocurrent measurement.

fibre. The working distance is (26 ± 2) µm and the spot diameter is (5.0 ± 0.5) µm. The fibre can be scanned across the device surface thanks to a x-y stage with 5 µm spatial resolution. The device photocurrent is detected with a current pre-amplifier and a lock-in amplifier triggered by the laser modulation signal.

Two LEDs of different mesa width ($w = 400\,\mu m$ and $800\,\mu m$) with a cross-shaped contact geometry were analysed and the two-dimensional spatial maps of the measured photocurrent are shown in Figure 5.6. In device A, with mesa width $w = 400\,\mu m$ and finger separation $d = 130\,\mu m$, the measured photocurrent signal is quite uniform across the area between the contact fingers. This suggests that the contact fingers separation is small enough so that the majority of the points on the device surface are within a current spreading length from the contact, and the generated photocurrent can be effectively collected. On the contrary, device B, with mesa width $w = 800\,\mu m$ and finger separation $d = 320\,\mu m$, shows clearly the effect of current crowding, with a strong signal confined to a small region around the contact edges. By considering the areas where the detected signal is stronger than 50 % and subtracting the area covered by the opaque metal, this result suggests that in large area devices the effective emitting area is only about 5 % of the total LED surface. A single line scan acquired by scanning the beam on device B, across the direction perpendicular to the contact fingers, is shown in Figure 5.7. A fitting of the current distribution using the model described in Equation 5.1 is plotted for comparison. Using the values of the layers thickness and resistivity listed in Table 5.1, a current spreading length of 68 µm is extracted. The results suggest that the optimal spacing between the contact fingers, that leads to a uniform current distribution, should be in the order of the current spreading length.

The measurement was repeated for two different values of laser power, and Figure 5.8 shows the data for the first 100 µm from the edge of the contact. The values extracted for the current spreading lengths are 95 µm and 68 µm, respectively. A decrease in

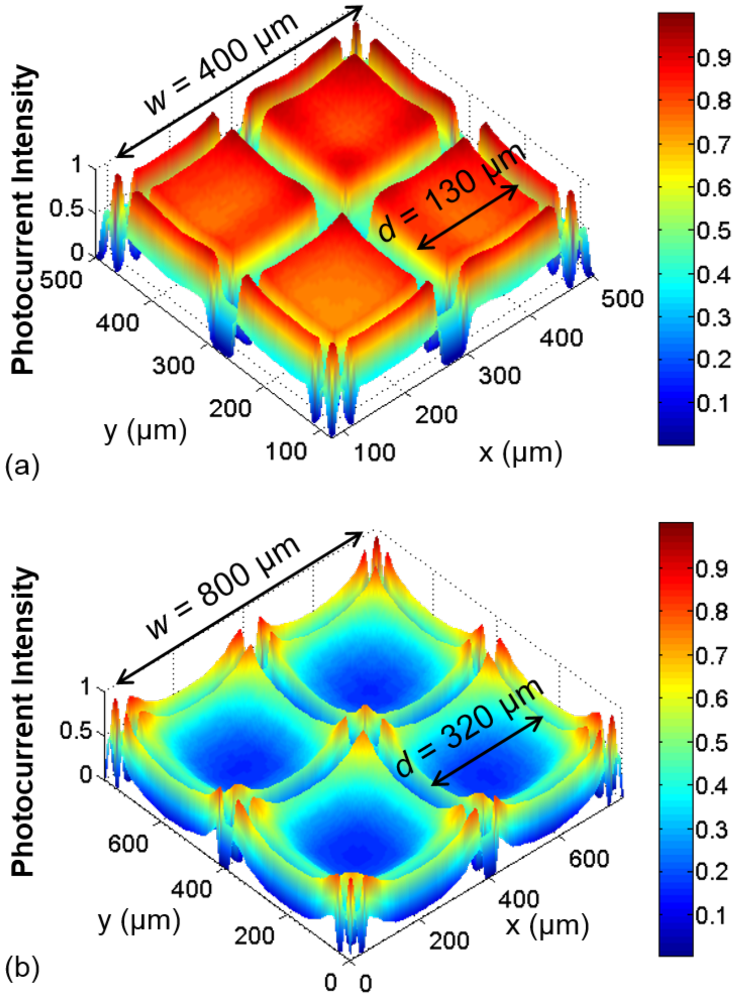

FIGURE 5.6: 3D spatial map of the normalised measured photocurrent while scanning a focused laser beam at 1.55 µm across the device surface. (a) Device A has mesa width $w = 400\,\mu\text{m}$ and finger separation $d = 130\,\mu\text{m}$. The detected signal has good uniformity across the area between the contact fingers. (b) Device B has mesa width $w = 800\,\mu\text{m}$ and finger separation $d = 320\,\mu\text{m}$. The effect of current crowding is evident. The dips in the maps are due to the opaque metal contacts. The colorscale is the same for both plots.

the current spreading length by a factor of $1/\sqrt{2}$ is compatible with a doubling of the applied optical power, according to Equation 5.2. Therefore, even for smaller area devices, it is important to take into account the values of current density at which the LED is operated in forward bias, in order to design a contact geometry that guarantees a uniform current distribution and an efficient use of the whole LED area for light generation and extraction.

Table 5.1: Physical parameters used in Equation 5.1 for the calculation of the lateral current distribution.

	p-layer	n-layer
thickness t_i (µm)	0.5	3.0
bulk resistivity ρ_i (Ω cm)	2.0×10^{-2}	5.7×10^{-4}
sheet resistance ρ_i/t_i ($\Omega/\square$)	404	1.9

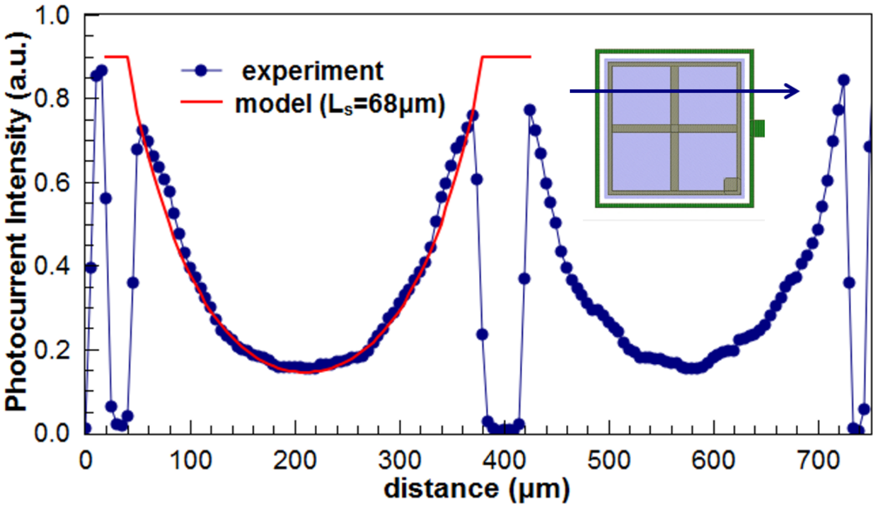

Figure 5.7: Experimental single line scan of the photocurrent intensity across a section perpendicular to the contact fingers of device B. The theoretical exponential current distribution, according to Equation 5.1 with a current spreading length of 68 µm, is plotted for comparison. The device's contact geometry is shown in the inset.

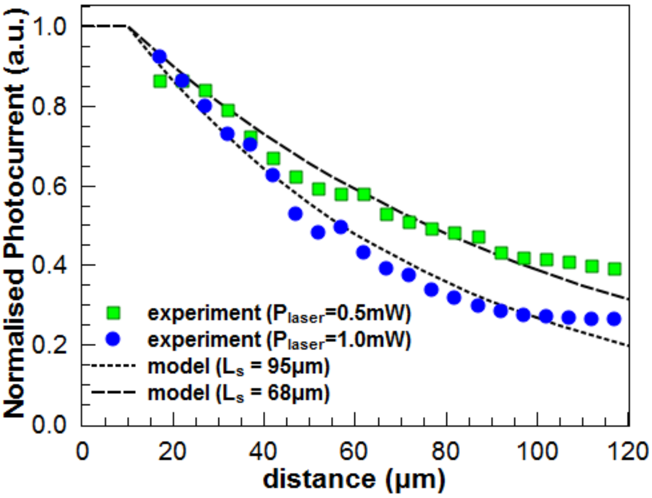

Figure 5.8: Zoom-in of the measured photocurrent intensity on device B for two values of laser power: 0.5 mW (squares) and 1 mW (circles). The fitted theoretical exponential current distributions give current spreading length values of 95 µm (dashed line) and 68 µm (dotted line), respectively.

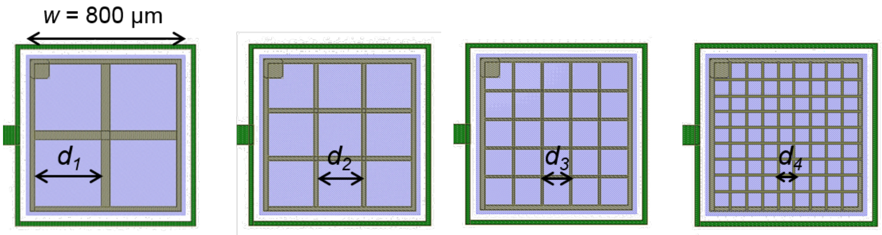

B1: d_1 = 320 μm B2: d_2 = 217 μm B3: d_3 = 130 μm B4: d_4 = 73 μm

Figure 5.9: Schematic illustration of the contact grid geometries for some of the measured devices with increasingly narrower contact fingers separation.

5.3 Contact Geometry Optimisation

A series of large area ($w = 800\,\mu\mathrm{m}$) LEDs with different contact fingers separations was designed and fabricated, in order to determine the optimal configuration for the top p-type contact grid geometry. All devices have the same contact area, to avoid additional shadowing losses from the opaque metal contact. The devices are numbered from 1 to 6 with decreasing contact finger separations of 320 µm, 217 µm, 131 µm, 73 µm, 47 µm and 31 µm. Some of the designed contact geometries are illustrated in Figure 5.9 for clarity.

The test LEDs were fabricated in the JWNC according to the process described in Chapter 3. The light emission at room temperature was measured with a VERTEX 70 FTIR spectrometer and detected with a 77 K-cooled InSb detector, as discussed in Section 4.2.2. All LEDs were tested under the same optical alignment and driving conditions with the bias current being a square wave of frequency 1 kHz and 10 % duty cycle. The total emitted intensity at a peak bias current of 100 mA as a function of the contact fingers separation is plotted in Figure 5.10. The optimal configuration is found to be the one of device B4, that shows about two times stronger EL intensity when compared to device B1, which has a simple cross-shaped contact geometry. The EL intensity seems to decrease for contact fingers separation narrower than the optimal one, i.e. devices B5 and B6. Although the contact area is nominally the same for all devices, 0.5 Ω higher series resistance was measured for device B5 and B6, which was attributed to the narrower fingers width. In case of device B4, the contact fingers separation is 73 µm, which is in the order of two times the expected current spreading length for an injected current density of about $27.7\,\mathrm{A/cm^2}$. This value has been calculated as a mean value of the two extreme possible assumptions about the uniformity of the current spreading across the LED area, i.e. a vertical flow under the metal contact and a uniform current flow across the mesa area.

In order to evaluate the benefit of an optimised contact grid geometry, the emission as a function of the peak bias current was evaluated for two devices (B2 and B4) when operated in quasi-cw bias. Figure 5.11 shows the electroluminescence spectra for the

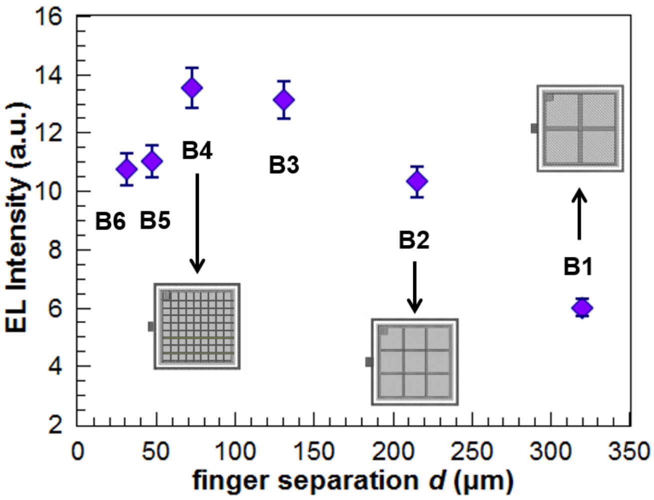

FIGURE 5.10: Measured electroluminescence intensity for LEDs with varying contact fingers separation. The emission is measured at room temperature, with the LEDs operated in pulsed mode (100 mA, 1 kHz, 10 % duty cycle). The stronger signal, indicating the optimal contact geometry, is the one associated with device B4, with a contact finger separation of 73 μm. The contact geometries of relevant devices are shown in the insets for clarity.

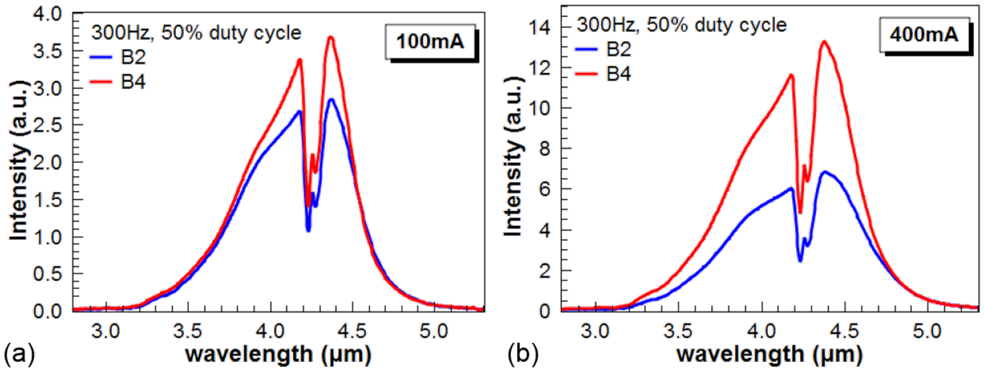

FIGURE 5.11: Electroluminescence spectra for device B2 and device B4 operated in quasi-cw bias (300 Hz, 50 %) at (a) 100 mA and (b) 400 mA.

two devices at 300 Hz, 50 % duty cycle with peak currents of 100 mA and 400 mA. The total emitted intensity as a function of the peak bias current in both pulsed bias (1 kHz, 10 % duty cycle) and quasi-CW bias conditions (10 Hz, 50 % duty cycle) are plotted in Figure 5.12 for the same two devices. While the improvement given by the denser grid contact is limited when the LEDs are pulsed at a low duty-cycle and relatively low currents, the benefit is evident for quasi-CW operation and higher injection current levels, resulting in up to a factor of 3 improvement.

These results confirm how the current crowding can represent a severe limitation to the performance of mid-infrared LEDs operating at room temperature and at high injected current levels. An optimised design of the top p-type contact grid geometry results in a

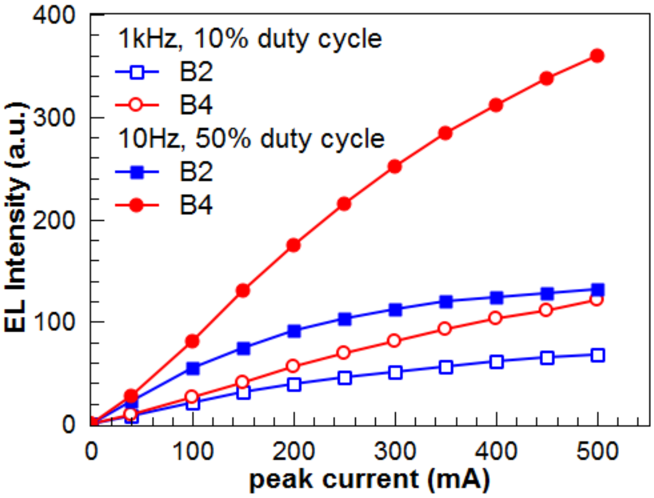

Figure 5.12: Experimental emission intensity for device B2 and device B4 operated in pulsed (1 kHz, 10 %) and quasi-cw bias (10 Hz, 50 %) as a function of the peak bias current. The data highlight how the current crowding effect is more severe in quasi-CW bias and at high injected current levels and how the optimal grid geometry can give up to a factor of 3 stronger emitted intensity in these operating conditions.

more uniform current distribution across the device active region, even at high injected current levels.

In this Chapter, the issues related to the current spreading in top-emitting mid-infrared LEDs on semi-insulating substrates were addressed. It was experimentally confirmed that the current crowding effect is particularly severe for long wavelength emitting devices with large area. In fact, due to the lateral current injection geometry and the high resistivity of the top p-type contact layer, the majority of the light is generated underneath and in close proximity to the contact edge and, thus, shaded by the opaque metal contact. The consequences of current crowding are even more significant at higher injection current levels, because of the non-linear resistance of the p-n junction. Spatial photocurrent measurements were performed to confirm the current density distribution profiles and allowed the design of an improved contact geometry. By introducing a top grid contact with a finger separation of around twice the expected current spreading length at the operating current density, up to a factor of three improvement of the emitted signal can be achieved.

Chapter 6

Resonant-Cavity LEDs

In this Chapter, the motivations and advantages of a Resonant-Cavity LED (RC-LED) design are reviewed. The theory of Fabry-Pérot resonators and DBR designs are recalled, highlighting the parameters that mostly affect the light emission enhancement at resonant wavelengths and the peak emission linewidth. The modelling of the heterostructure reflectivity spectra and the cavity spectral response by transfer matrix method is also discussed. Iterative results of growth and fabrication of RC-LEDs are presented, leading to the design of a RC-LED with improved spectral emission and spectral purity at the target mid-infrared wavelength. Finally, the advantages in terms of sensing performance offered by the RC-LED compared to a non-resonant LED are presented and the challenges for transferring the RC-LED designs to production devices are examined.

6.1 Background on Resonant-Cavity LEDs

As discussed in Section 2.2.2, the high refractive index contrast at the air-semiconductor interface results in a small critical angle ($\sim 15°$) and a narrow escape cone. Therefore, the majority of the generated photons, which are isotropically emitted inside the LED, are subjected to total internal reflection and Fresnel reflection at the air-semiconductor interface, limiting the extraction efficiency to about $1\,\%$, according to Equation 2.7. Therefore, the design of a conventional planar LED has to be modified to increase the probability of light extraction.

The optimisation of the LED structure for improving its light emission has been long studied and several approaches have been investigated. Proposed solutions for the enhancement of extraction efficiency can be divided into two groups.
The first one involves the redistribution of light inside the LED by shaping the semiconductor chip [142], modifying the surface morphology [25, 29], or by introducing a

reflector between the substrate and the LED active layers to redirect the light that is emitted towards the substrate. These approaches aim at increasing the number of reflection and scattering events within the structure, therefore increasing the probability of light meeting the air-semiconductor interface at an incident angle within the escape cone. Another simple technique makes use of immersion lenses, where the devices are encapsulated into a transparent epoxy with an intermediate refractive index between the semiconductor and air, which effectively increases the escape cone. However, this solution is not applicable to mid-infrared LEDs as most of the epoxy resins have strong absorptions in the mid-infrared wavelength range. An alternative is offered by the fabrication of micro lenses and optical concentrators etched into the substrate [20, 24], but with an impractical complication of the fabrication process, not suited for mass production.
The second group of techniques explores the possibility of modifying the distribution of the spontaneous emission of the LED. In particular, resonant cavity structures are obtained by placing the active region of the LED within a Fabry-Pérot cavity, which provides a way to redirect a larger portion of the spontaneous emission towards the escape cone through interference effects [63, 69].

A particularly effective geometry is the Resonant-Cavity LED, since it both redirects the light from the substrate to the top surface and adds a resonance effect to the structure. Resonant-Cavity LEDs (RC-LEDs) were first demonstrated in the early 1990s [143], where electrically-pumped $\mathrm{Al_xGa_{1-x}As}$ devices employed an epitaxially-grown distributed Bragg reflector (DBR) and showed higher emission intensity and narrower linewidth compared to the equivalent planar LED devices. Later, RC-LEDs were exploited in the visible and near-infrared, mainly for plastic optical fibre interconnects, achieving extraction efficiencies as high as 27 %[144]. Mid-infrared RC-LEDs were first reported in CdHgTe-based material [26], followed by InAs/GaAs [27, 28] and InAsSb [145] material systems, demonstrating factors of 2 enhancement of the output power and narrowing of the spectral linewidth, with significant advantages for trace gas detection. However, the development of longer wavelength devices has been slower than their near-infrared counterpart, mainly due to epitaxial growth problems associated with the lattice mismatch between the layers of the DBR mirror and the substrate or active region of the device.

Resonant-cavity structures offer significant advantages over conventional planar LEDs, without having the stringent growth and fabrication requirements of Vertical Cavity Surface Emitting Lasers (VCSELs). Therefore, they are particularly attractive for gas sensing applications, which can significantly benefit for the improved performance in terms of [20, 27, 28, 145, 146]:

- *Spectral emission enhancement.* Thanks to the cavity effect, the light intensity emitted along the axis of the cavity at resonance wavelengths is higher compared to planar LEDs. This translates into an enhancement factor of 2 to 10 times the output power at the designed resonant wavelength.
- *Higher spectral purity.* The emission linewidth is determined by the quality factor of the cavity and not by the spontaneous emission spectrum of the semiconductor active region, proportional to the thermal energy kT ($\Delta E \sim 1.8kT$). A narrower emission linewidth, at a wavelength that matches the absorption line of the target gas, results in a higher wavelength selectivity for gas detection.
- *Improved temperature stability.* The shift of the emission wavelength with temperature is determined by the thermal expansion coefficient dn/dT of the optical cavity and not by the energy gap of the semiconductor.

For these reasons, the design of a resonant-cavity structure was chosen as it offers the most effective approach to enhance the extraction efficiency and improve the spectral properties of the mid-infrared AlInSb LEDs. In the following sections, the theory of Fabry-Pérot cavities and micro-cavity effects on the distribution of the spontaneous emission is briefly reviewed. Then, the design of the DBR mirror is discussed, followed by the design and characterisation of the resonant-cavity LED structures.

6.2 Fabry-Pérot Resonators and Microcavity Effect

An optical Fabry-Pérot cavity consists of two coplanar mirrors of reflectivity R_1 and R_2 separated by a distance L_{cav}, comparable with the wavelength of light propagating inside the cavity, as illustrated in Figure 6.1a [63]. Taking into account the multiple reflections of plane waves inside the cavity, the transmitted light intensity through a Fabry-Pérot cavity can be written as:

$$T = \frac{T_1 T_2}{1 + R_1 R_2 - 2\sqrt{R_1 R_2}\cos(2\phi)} \tag{6.1}$$

where $T_i = 1 - R_i$ and ϕ is the phase change for a single pass between the two mirrors. This is given by:

$$\phi = 2\pi \frac{n L_{cav}}{\lambda} = 2\pi \frac{n L_{cav} c}{\nu} \tag{6.2}$$

where n is the refractive index inside the cavity, λ is the wavelength of light in vacuum and ν the frequency of light. The maxima of transmittance occur when the condition of constructive interference is met: $2\phi = 2k\pi$, with k a positive integer. The cavity order

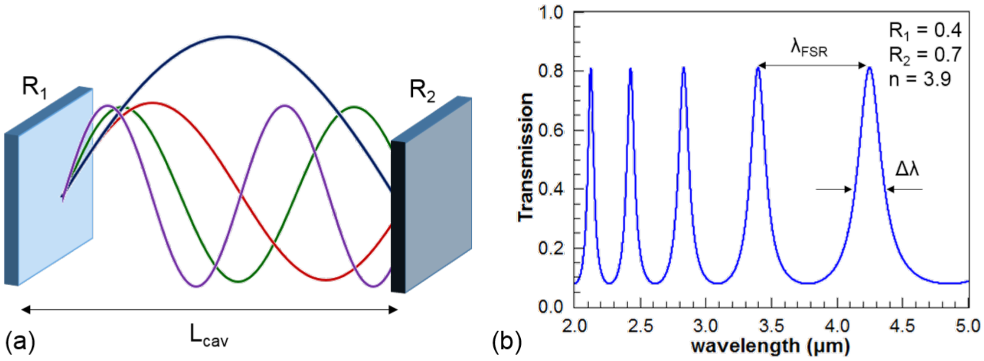

FIGURE 6.1: (a) Schematic illustration of a Fabry-Pérot cavity of length L_{cav} defined by two coplanar reflectors R_1 and R_2. (b) Example of transmission spectrum for a Fabry-Pérot cavity with mirror reflectivity $R_1 = 0.4$, $R_2 = 0.7$, refractive index $n = 3.9$ and cavity length $L_{cav} = 2.2\,\mu\text{m}$.

m_c is defined as the normalised cavity length and represents the number of resonant modes in the cavity at one specific wavelength:

$$m_c = \frac{2nL_{cav}}{\lambda_0} \tag{6.3}$$

An example of a transmittance spectra as a function of wavelength is plotted in Figure 6.1b for $R_1 = 0.4$, $R_2 = 0.7$, $n = 3.9$, $L_{cav} = 2.2\,\mu\text{m}$.

The cavity *finesse* F is defined as the ratio between the peak free spectral range λ_{FSR} and the peak full-width half-maximum (FWHM $\Delta\lambda$), and can be expressed as a function of the mirrors reflectivities:

$$F = \frac{\lambda_{\text{FSR}}}{\Delta\lambda} = \frac{\pi\sqrt[4]{R_1R_2}}{1-\sqrt{R_1R_2}} \tag{6.4}$$

Another important parameter is the cavity *quality factor* Q, which is defined as the ratio of the peak resonance wavelength and the peak FWHM:

$$Q = \frac{\lambda_{peak}}{\Delta\lambda} = \frac{2nL_{cav}}{\lambda}\,\frac{\pi\sqrt[4]{R_1R_2}}{1-\sqrt{R_1R_2}} = m_cF \tag{6.5}$$

For the cavity of Figure 6.1, we obtain $F = 4.85$ and $Q = 19.4$ at $\lambda = 4.26\,\mu\text{m}$.

The resonant-cavity enhancement is achieved by placing the active region of the LED within a Fabry-Pérot cavity. Depending on the required performance, the cavity can be defined by two DBR mirrors, a DBR mirror and a metal mirror, or simply by a DBR mirror and the bare air-semiconductor interface. The interference effects that take place within the cavity strongly modify the spontaneous emission of photons from the active region.

In a one-dimensional homogeneous medium, the density of optical modes per unit length per unit frequency $\rho(\nu)$ is given by [63]: $\rho_0(\nu) = 2n/c$, where n is the medium refractive index. In a planar Fabry-Pérot cavity, the allowed optical modes are discrete and have frequencies which are integer multiple of the fundamental mode at frequency $\nu_0 = c/(2nL_{cav})$. The optical mode density $\rho(\nu)$ of a one-dimensional cavity for emission along the cavity axis can be derived as a function of the transmittance through the cavity $T(\nu)$ [63]:

$$\rho(\nu) = \frac{(R_1 R_2)^{3/4}}{T_1 T_2} \frac{4n}{c} \left(1 - \sqrt{R_1 R_2}\right) T(\nu) \tag{6.6}$$

and allows to calculate the density of optical modes at the maxima and minima of the cavity transmittance. As the mode density is conserved, it can be demonstrated that the mode density is increased at resonant wavelengths at the expense of non-resonant ones. Therefore, the enhancement factor at the resonance wavelength is given by the ratio of the optical mode density in a planar cavity and in a homogeneous medium: $G_e = \rho_{\max}/\rho_0$. The emission rate enhancement at the resonance wavelength for emission in a single direction can be derived as [63]:

$$G_e = \frac{2(1 - R_1)}{2 - R_1 - R_2} \frac{\xi}{2} \frac{\rho_{\max}}{\rho_0} \approx \frac{(1 - R_1)}{1 - \sqrt{R_1 R_2}} \frac{\xi}{2} \frac{2}{\pi} F \approx \xi \frac{(1 - R_1)(R_1 R_2)^{1/4}}{\left(1 - \sqrt{R_1 R_2}\right)^2} \tag{6.7}$$

where the first term takes into account the faction of light emitted from the mirror with lower reflectivity R_1, and ξ is the antinode enhancement factor, which is proportional to the mode intensity at the source position, i.e. active region. Therefore, ξ has a value of 2 if the active region is positioned exactly at the antinode of the standing wave inside the cavity, a value of 1 if the active region is distributed over more than a period of the standing wave, a value of 0 if the active region is placed at a node where no coupling occurs. The emission rate enhancement at resonance has commonly a value between 2 and 10, depending on the finesse of the cavity. For example, the cavity in Figure 6.1, assuming $\xi = 1.5$, gives an enhancement $G_e \approx 2$.

Additionally, as the emission spectrum of the active region can be significantly broader than the cavity resonance peak, the spectrally integrated emission enhancement needs to take into account the ratio between the linewidth of the resonance and that of the active region emission, and is given by [63]:

$$G_{int} = G_e \sqrt{\pi \ln 2} \frac{\Delta\lambda}{\Delta\lambda_s} \tag{6.8}$$

assuming a Gaussian emission spectrum of width $\Delta\lambda_s$. The integrated emission enhancement can be significantly different from the enhancement at the resonant wavelength and even result in a suppression of the overall emission, depending on the spectral matching between the cavity resonance and the emission spectrum of the active region. For example, assuming $G_e = 2$, $\Delta\lambda = 0.2\,\mu\text{m}$ and $\Delta\lambda_s = 0.5\,\mu\text{m}$, the integrated emission enhancement is reduced to only $G_{int} = 1.18$.

From this discussion, some fundamental criteria can be derived for the design of a resonant-cavity structure with maximum enhancement of the spontaneous emission along the axis of the cavity:

- To minimise the re-absorption in the active region, the probability of photon emission through the top mirror must be much higher than the probability of re-absorption in the cavity:

  $$2\xi\alpha L_{cav} < (1 - R_1) \tag{6.9}$$

  This suggests that very high values of cavity finesse are not required as this would reduce the cavity mode emission in the air by increasing the absorption losses.

- To maximise the integrated intensity, the resonant cavity mode needs to overlap as much as possible with the active region emission spectrum. This is achieved with a low cavity order m_c, and therefore a cavity length which is comparable to the wavelength of interest.

As the main objective of this work is to improve the overall performance of $\mathrm{Al_xIn_{1-x}Sb}$ LEDs for CO_2 gas sensing, we have focussed on the design of a resonant-cavity LED (RC-LED) with emission enhancement and reduced spectral linewidth around the CO_2 absorption line. As seen in Chapter 1, CO_2 has a strong absorption band centred at 4.26 µm with a spectral linewidth of about 0.2 µm (Figure 1.2b). As discussed earlier in this Chapter, the emission linewidth of a RC-LED is determined by the quality factor of the cavity. Therefore, in the case of the CO_2 absorption spectrum:

$$Q_{\mathrm{CO_2}} = \frac{\lambda_{peak}}{\Delta\lambda} = \frac{4.26\,\mu\text{m}}{0.2\,\mu\text{m}} = 21.3 \tag{6.10}$$

Considering the definition of the cavity quality factor (Equation 6.5), it is possible to evaluate the effect of the mirror reflectivities R_1 and R_2 and of the cavity length L_{cav} on the emission linewidth. For fixed values of $\lambda = 4.26\,\mu\text{m}$, $n = 3.9$, and $L_{cav} = 2.7\,\mu\text{m}$ ($m_c = 5$), Figure 6.2 shows a contour plot of the quality factor as a function of R_1 and R_2. It can be observed that only moderate values of reflectivity are necessary to achieve the desired quality factor. For example, $Q \sim 20$ can be obtained with $R_1 = 0.35$ and $R_2 = 0.65$. These values of reflectivity can be obtained with a cavity defined by the air-semiconductor interface and a DBR mirror, epitaxially grown between the substrate and the LED active layers. In fact, the reflectivity at the interface between air and a high refractive index semiconductor is given by the Fresnel's equation for normal

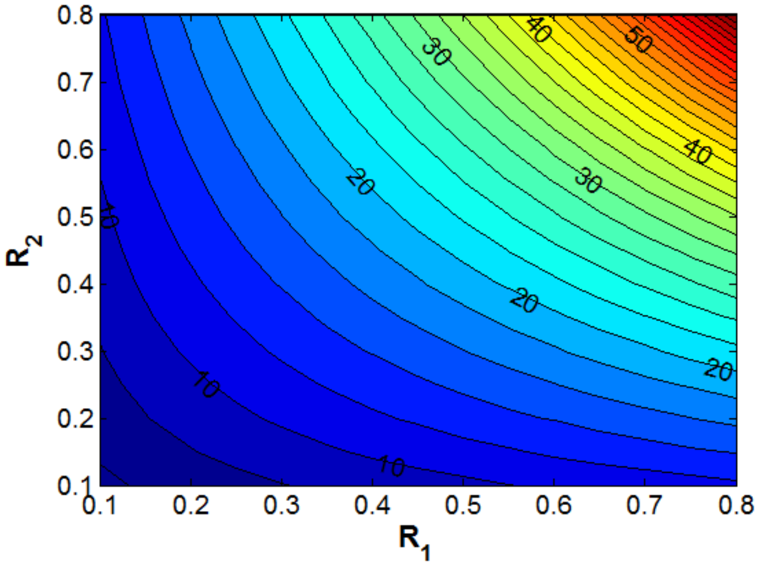

FIGURE 6.2: Contour plot of the Fabry-Pérot cavity quality factor Q as a function of the cavity mirror reflectivities R_1 and R_2. The other cavity parameters are kept constant: λ= 4.26 µm, $n = 3.9$, and $L_{cav} = 2.7$ µm ($m_c = 5$).

incidence:

$$R_1 = \frac{(n-1)^2}{(n+1)^2} \approx 0.35 \quad \text{for} \quad n = 3.9 \tag{6.11}$$

The modelling and design of a DBR mirror are discussed in the next section, followed by the integration of a resonant-cavity on an $\mathrm{Al_xIn_{1-x}Sb}$ LED structure.

6.3 Distributed Bragg Reflector (DBR)

A Distributed Bragg Reflector (DBR) consists of a stack of layer pairs of two materials with different refractive index. As a result of the refractive index step, Fresnel reflection occurs at each interface. The thickness of each layer is designed so that constructive interference occurs at each interface. This condition is fulfilled when each material has a thickness of a quarter wavelength of the light in the material:

$$\begin{aligned} d_L &= \lambda_0/(4n_L\cos\theta_L) \\ d_H &= \lambda_0/(4n_H\cos\theta_H) \end{aligned} \tag{6.12}$$

where λ_0 is the target Bragg wavelength in vacuum, $d_{L,H}$ is the thickness, $n_{L,H}$ is the refractive index and $\theta_{L,H}$ the angle of incidence in the low-index (L) and high-index (H) material, respectively.

The DBR is characterised by a narrow band of high reflectivity, usually referred to as *stopband*. The reflectivity has a maximum at the Bragg wavelength and, for two given materials, is a function of the number N of layer pairs:

$$R_{DBR} = |r_{DBR}|^2 = \left[\frac{1-(n_L/n_H)^{2N}}{1+(n_L/n_H)^{2N}}\right]^2 \tag{6.13}$$

The width of the DBR stopband is instead a function of the refractive index contrast:

$$\Delta\lambda_{DBR} = \frac{2\lambda_0 \Delta n}{2\left(\frac{1}{n_L}+\frac{1}{n_H}\right)^{-1}} \tag{6.14}$$

Among antimonide-based materials, AlSb and GaSb provide a strong refractive index contrast of $\Delta n \sim 0.7$ at 4.26 µm, thus allowing a relative high reflectivity with a limited number of quarter-λ layer pairs.

The DBR reflectance has been calculated with a transfer matrix method code implemented in Matlab. The transfer matrix method [147] is a standard technique used to analyse light propagation in layered media, based on the continuity of the electric field across the interfaces between different materials. The propagation of light of given wavelength λ through a single layer of thickness d can be expressed by a matrix, which represents the electric field exiting the layer as a function of the incident one:

$$M = \begin{pmatrix} \cos(k_q d_q) & \sin(k_q d_q)/k \\ -k_q \sin(k_q d_q) & \cos(k_q d_q) \end{pmatrix} \tag{6.15}$$

where $k_q = 2\pi n_q/\lambda$ is the wave vector of the propagating light in the q-layer of refractive index n_q. The calculation can be extended in case of oblique angle of incidence. The propagation through a layer stack is described by the product of the individual layer matrices:

$$M = \prod_{q=1}^{2N} M_q \tag{6.16}$$

Finally, the amplitude of the transmittance and reflectance can be obtained from the elements of the system matrix:

$$r = \frac{(M_{21} + k_0 k_s M_{12}) + i\,(k_0 M_{22} - k_s M_{11})}{(-M_{21} + k_0 k_s M_{12}) + i\,(k_0 M_{22} + k_s M_{11})} \tag{6.17}$$

$$t = 2ik_0 \exp^{-ik_s L} \frac{M_{11}M_{22} - M_{12}M_{21}}{(-M_{21} + k_0 k_s M_{12}) + i\,(k_0 M_{22} + k_s M_{11})} \tag{6.18}$$

The fraction of light intensity transmitted and reflected by the layer stack are given by $R = |r|^2$ and $T = |t|^2$.

The DBR stack was designed to have a reflectivity stopband centred around 4.26 µm by alternating quarter-wavelength layers of AlSb and $Ga_{0.9}In_{0.1}Sb$. A fraction $x = 0.1$ of

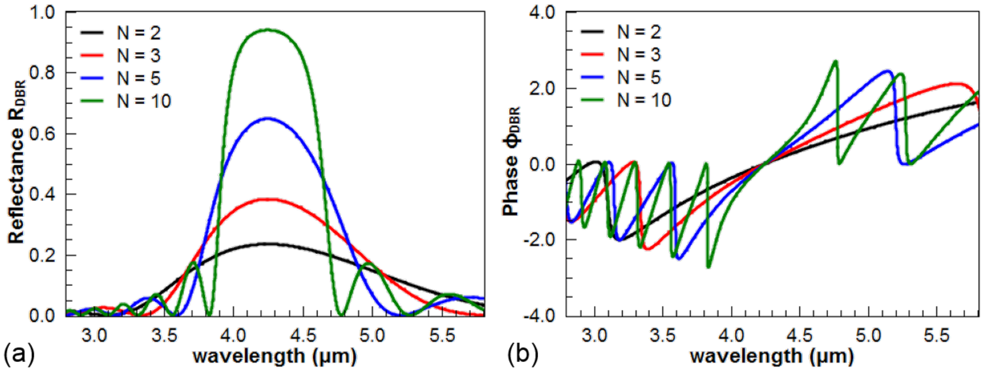

FIGURE 6.3: AlSb/$Ga_{0.9}In_{0.1}Sb$ DBR reflectance intensity (a) and phase (b) centred at 4.26 μm for different numbers of layer pairs. The reflectance was modelled by the transfer matrix method.

indium is used in the $Ga_{1-x}In_xSb$ layers to achieve the lattice matching condition with AlSb. This is of fundamental importance to avoid introducing additional stress to the epitaxially grown structure and the formation of additional misfit dislocations in the mirror and in the $Al_xIn_{1-x}Sb$ LED active layers. The layers have refractive indices of $n_L = 3.12$ (AlSb) and $n_H = 3.79$ ($Ga_{0.9}In_{0.1}Sb$), resulting in $\Delta n = 0.67$. The reflectivity was calculated assuming infinite layers of $Al_{0.05}In_{0.95}Sb$ and GaAs on the two sides of the DBR stack. The amplitude and phase of the reflectivity are plotted in Figure 6.3 for different number of layer pairs. Thanks to the high refractive index contrast, a reflectivity of 65 % is achieved with only N = 5. The spectral width of the stopband is of about 1.6 μm, which guarantees a robust design and a good overlap with the LED spontaneous emission spectrum.

A test wafer (C979) with a DBR stack for maximum reflectivity at 3.3 μm was grown to evaluate the accuracy of the model. The first quarter-wavelength AlSb layer was used as a buffer layer on the GaAs substrate, as described in Section 3.1. Above this, N = 5 pairs of DBR layers were grown, resulting effectively in a N = 5.5 pairs DBR stack. According to Equation 6.12, the layer thicknesses are $d_L = 264$ nm for the AlSb layers and $d_H = 216$ nm for the $Ga_{0.9}In_{0.1}Sb$ layers. The total thickness of the DBR stack is of around 2.4 μm. The growth was terminated with a quarter-wavelength layer of $Al_{0.09}In_{0.91}Sb$, with the same composition of the LED active layers for emission around 3.3 μm. An SEM image of the wafer cross section is shown in Figure 6.4, which shows that the layers are slightly thicker, but within 5 % of the designed value. The wafer reflectivity was modelled by the transfer matrix method, taking into account the quarter-wavelength $Al_{0.09}In_{0.91}Sb$ layer which contributes around 35 % reflectivity at the interface with air. Reflectance and transmittance spectra of wafer C979 were measured by a FTIR spectrometer equipped with a Globar broadband light source, a CaF_2 beam splitter and a liquid-nitrogen-cooled InSb detector, as described in Section 4.2.1. The measured and modelled spectra are

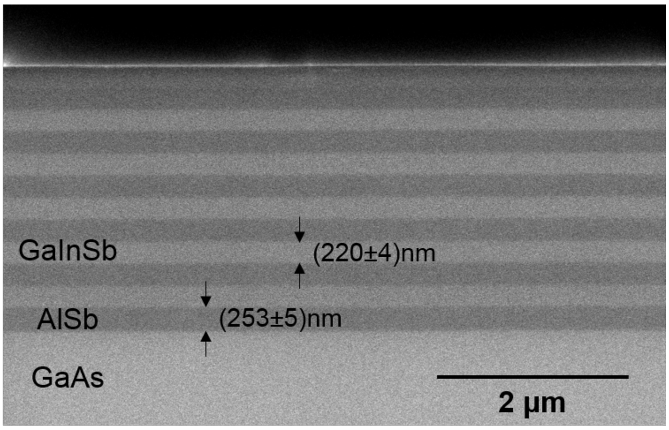

FIGURE 6.4: SEM cross section image of the N = 5.5 AlSb/$Ga_{0.9}In_{0.1}Sb$ stack grown on GaAs substrate.

shown in Figure 6.5 for comparison. The model includes the absorption coefficient in the $Al_xIn_{1-x}Sb$ layer and a 2 % correction factor of the layer thicknesses, which accounts for the variations in the grown structure. Excellent agreement is achieved in terms of central wavelength, peak reflectance, bandwidth and sidelobes positions.

6.4 Resonant-Cavity $Al_xIn_{1-x}Sb$ LED

Following the successful design and growth of the DBR test wafer, a full resonant-cavity $Al_{0.05}In_{0.95}Sb$ LED (wafer C962) was designed and implemented for enhanced emission around the CO_2 absorption lines at 4.26 μm. The standard p-i-n $Al_{0.05}In_{0.95}Sb$ LED structure described in Section 2.4 was grown on top of a DBR structure. This results in the LED active region being placed within a Fabry-Pérot cavity defined by the DBR mirror and the top air-semiconductor interface, as illustrated in Figure 6.6. This first design was chosen in order to evaluate the effect of the DBR mirror and the Fabry-Pérot cavity on a tested and fully characterised LED structure, without the need of modifying different design variables at the same time. Therefore, the cavity thickness is similar to the one of the original structure, only adjusted to be equal to an integer number of half wavelengths:

$$L_{cav} = m_c \frac{\lambda_0}{2n} \approx 4.94\,\mu\text{m} \quad \text{for} \quad m_c = 9 \tag{6.19}$$

The DBR consists of N = 5.5 pairs of AlSb/$Ga_{0.9}In_{0.1}Sb$ designed to have a stopband centred at 4.26 μm. The layer thicknesses are $d_L = 340\,\text{nm}$ and $d_H = 280\,\text{nm}$ for the AlSb and $Ga_{0.9}In_{0.1}Sb$ layers, respectively, according to Equation 6.12. Figure 6.7 reports on the reflectance and transmittance spectra of the full layer structure measured by an FTIR spectrometer, as described in Section 4.2.1. The modelled spectra are calculated by the transfer matrix method, as discussed in Section 6.3, and show an

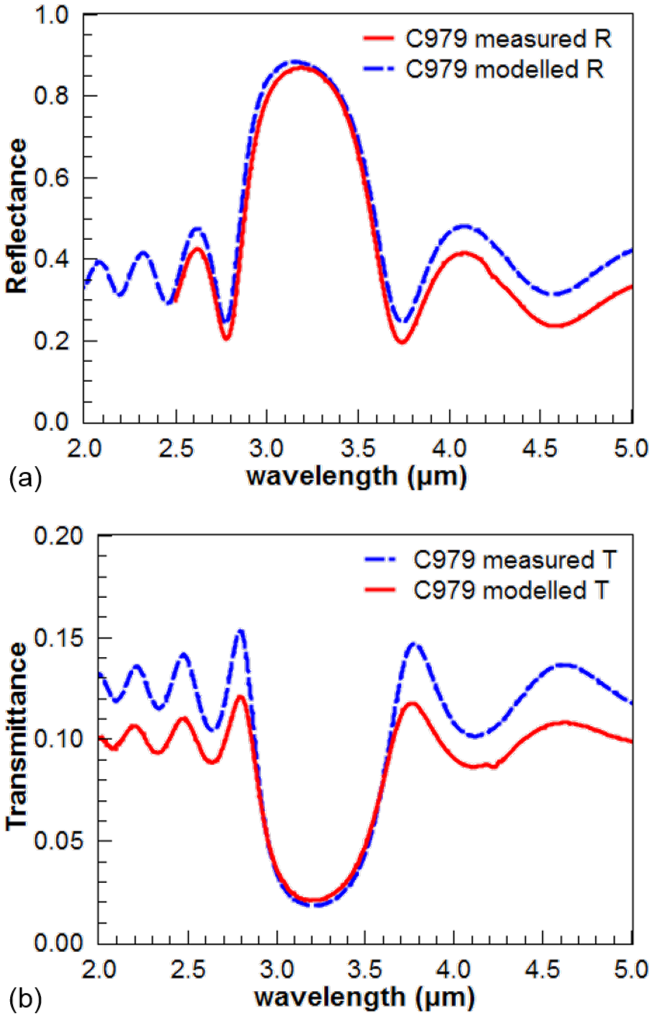

FIGURE 6.5: Measured and modelled reflectance (a) and transmittance (b) spectra for the N = 5.5 AlSb/$Ga_{0.9}In_{0.1}Sb$ DBR stack grown on GaAs substrate and capped with a $\lambda/4$ $Al_{0.09}In_{0.91}Sb$ layer.

excellent agreement with the measured ones for a cavity thickness $L_{cav} = 4.96\,\mu m$. This confirms the accuracy of the refractive index model, discussed in Section 4.2.1 and used in the simulations, and the good control of the growth parameters.

The resonant peaks of the Fabry-Pérot cavity are clearly visible in the measured spectra, with three distinct peaks falling within the DBR stopband. The central peak is successfully positioned at the target wavelength of 4.26 µm and the resonant modes spacing is $\nu_{\mathrm{FSR}} \approx 6.5\,\mathrm{THz}$, which corresponds to an effective cavity length of $L_{eff} \approx 6\,\mu m$. This can be explained taking into account the so-called DBR penetration length. In fact, the effective number of DBR layer pairs seen by the optical wave electric field can be expressed as [148]:

$$N_{eff} \approx \frac{1}{2}\frac{n_h + n_L}{n_h - n_L} \tanh\left(2N\frac{n_h - n_L}{n_h + n_L}\right) \tag{6.20}$$

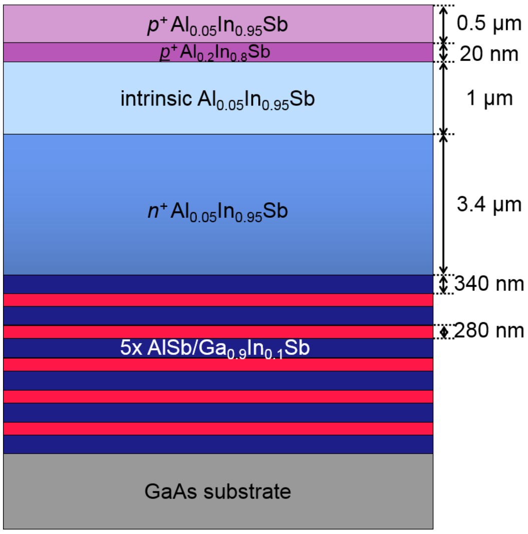

FIGURE 6.6: Schematic illustration of the MBE-grown RC-LED heterostructure with $Al_{0.05}In_{0.95}Sb$ LED active layers and a 5.5 pairs of lattice-matched $AlSb/Ga_{0.9}In_{0.1}Sb$ DBR layers located between the GaAs substrate and the lower n-type confinement layer.

As illustrated in Figure 6.3b, the phase change of the wave reflected by the DBR is zero at the Bragg wavelength and changes almost linearly with wavelength in the vicinity of it ($\lambda \approx \lambda_{Bragg}$). Therefore, it is possible to approximate the DBR mirror with an ideal metal mirror located at a distance L_{pen} from the first interface. The DBR penetration length for the reflected optical power can thus be derived as:

$$L_{pen} = \frac{1}{2} N_{eff} \left(d_H + d_L\right) \tag{6.21}$$

Consequently, the effective cavity thickness of a Fabry-Pérot cavity including a DBR mirror is given by the sum of the cavity thickness and the DBR penetration length. For the values of refractive index and thickness of the DBR layers used in this structure, the resultant DBR penetration length is $\sim 1.19\,\mu\text{m}$. Thus, the effective cavity length is:

$$L_{eff} = L_{cav} + L_{pen} \approx (4.96 + 1.19)\,\mu\text{m} = 6.1\,\mu\text{m} \tag{6.22}$$

which is in agreement with the effective cavity length calculated from the Fabry-Pérot free spectral range. This is confirmed by the excellent agreement of the mode spacing between the measured and modelled transmission spectra. The cavity has a finesse of $F = 4.15$ and a cavity quality factor of $Q \approx 46$.

The photoluminescence (PL) of the structure was investigated first. The PL was excited at room temperature with a 300 mW diode-pumped solid state laser emitting at 532 nm. The excitation beam was reflected onto the sample and the PL signal was collected with an off-axis parabolic mirror into the FTIR spectrometer. The measured PL spectra of

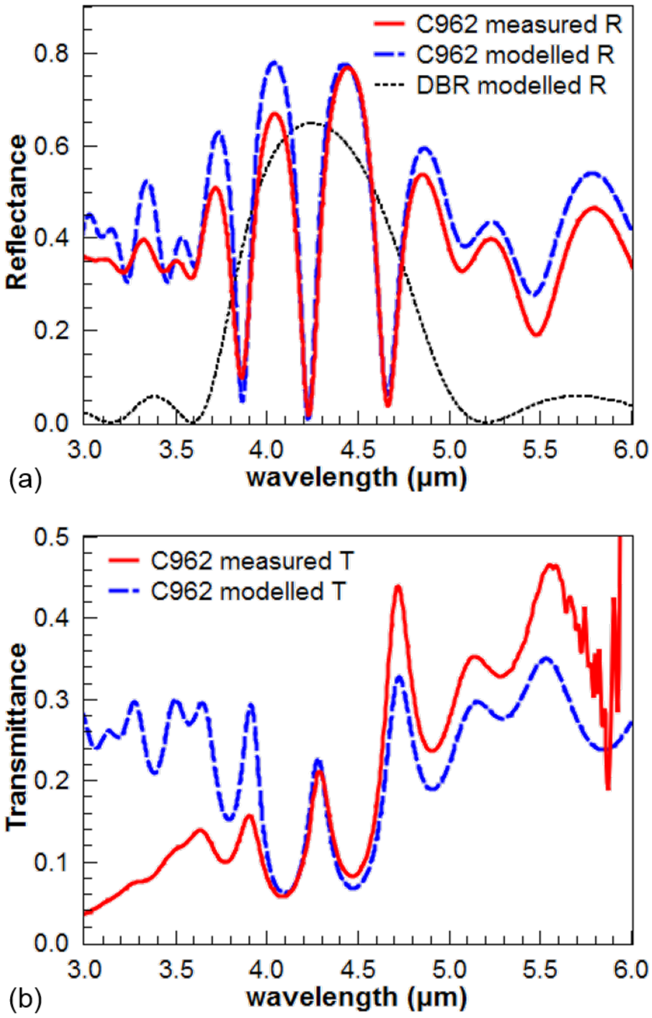

FIGURE 6.7: Measured and modelled reflectance (a) and transmittance (b) spectra for the RC-LED layer structure illustrated in Figure 6.6. The N = 5.5 AlSb/$Ga_{0.9}In_{0.1}Sb$ DBR stack has a 1.66 µm stopband centred at 4.26 µm, shown for reference in (a). The effective cavity length, given by the sum of the p-i-n $Al_{0.05}In_{0.95}Sb$ LED layer structure and the DBR penetration length, results in a Fabry-Pérot free spectral range ν_{FSR} of 6.5 THz, with three cavity modes falling within the DBR stopband.

the RC-LED structure is shown in Figure 6.8a, together with the reference spectra from an identical LED structure without the DBR mirror. The effect of the Fabry-Pérot cavity is evident with the presence of the three cavity modes peaks already observed in the reflectance and transmittance spectra. The central peak at 4.26 µm has a linewidth of about 125 nm. The ratio between the two spectra gives the emission enhancement shown in Figure 6.8b, with a maximum value of ≈ 2.5 at 4.26 µm.

Following the initial optical characterisation, electrically-pumped LED devices were processed from the same structure following the fabrication process described in Chapter 3. After patterning by photolithography, 400 µm-wide square mesas were etched by citric-acid based etching. An SEM cross section of the etched structure is shown in Figure 6.9b.

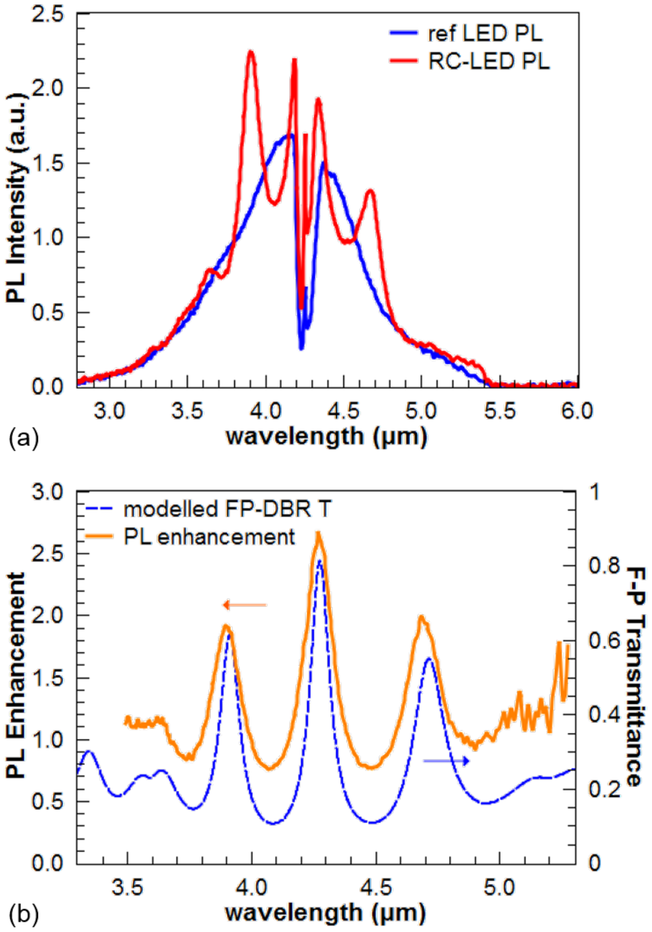

FIGURE 6.8: (a) Measured room temperature photoluminescence (PL) spectra of the RC-LED structure and a reference non-resonant LED. (b) Spectral photoluminescence enhancement showing a factor of 2.5 for the central peak at 4.26 µm. The modelled Fabry-Pérot cavity transmittance is plotted for comparison.

The etch was about 2.3 µm deep to expose the n-type contact layer. Ti/Au contacts were defined by metal deposition and lift-off.

The electroluminescence (EL) signal of the electrically-pumped RC-LED devices was measured at room temperature by a FTIR spectrometer in step-scan configuration, as described in Section 4.2.2. The devices were pulsed biased at 1 kHz, 10 % duty cycle with 100 mA peak current. Figure 6.10 shows that the resonant cavity modes can still be clearly observed in the measured EL spectra and the peak emission linewidth, determined by the cavity quality factor, is 50 % narrower compared to the reference non-resonant LED. However, no significant emission enhancement is recorded at 4.26 µm in comparison to the non-resonant LED. This can be attributed to the unoptimised position of the active region relative to the electric field distribution inside the cavity. In fact, the 1 µm-thick active region spans more than one period of the electric field oscillating inside the cavity. Therefore, as discussed in Section 6.2, assuming the radiative recombination occurs across the whole active region thickness, the antinode enhancement factor

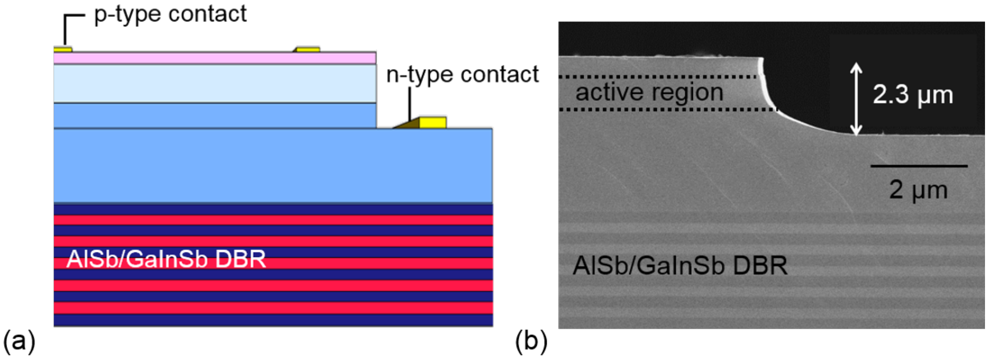

FIGURE 6.9: (a) Schematic cross-section of the fabricated electrically-pumped RC-LED. (b) SEM cross-sectional image of the RC-LED layer structure after the mesa etch step. 2.3 µm-deep square mesa are etched into the $Al_{0.05}In_{0.95}Sb$ LED layer structure in a citric acid:H_2O_2:H_2O solution, according to the process described in Section 3.3. The lattice-matched AlSb/$Ga_{0.9}In_{0.1}Sb$ DBR stack grown between the GaAs substrate and the LED active layers is left unexposed.

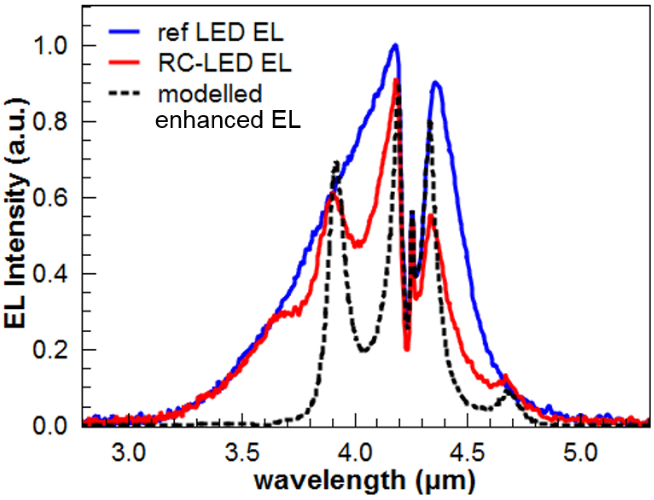

FIGURE 6.10: Measured room temperature electroluminescence (EL) spectra of the RC-LED and a reference non-resonant LED. The devices are operated in pulsed bias (1 kHz, 10 % duty cycle) at 100 mA. The expected emission spectrum (dashed line) is calculated by multiplying the reference LED emission spectrum and the modelled emission enhancement (Equation 6.7), showing good agreement with the measured EL.

would have a value close to unity ($\xi \approx 1$), resulting in no significant spectral enhancement at the resonant wavelengths. The expected RC-LED EL spectrum, approximated by the product of the EL spectra of the reference non-resonant LED and the spectral emission enhancement calculated according to Equation 6.7, is shown in Figure 6.10 for comparison with the measured one.

Table 6.1: Design parameters of the RC-LED (wafer C1060) with reduced active region and cavity thickness, illustrated in Figure 6.11.

Thickness (nm)	Layer	Repeats	Material	Doping Conc. (cm^{-3})
448	p-contact	1	$Al_{0.05}In_{0.95}Sb$	p^+ 1×10^{18}
200	active region	1	$Al_{0.05}In_{0.95}Sb$	i 2×10^{16}
2094	n-contact	1	$Al_{0.05}In_{0.95}Sb$	n^+ 1×10^{18}
340	low index	5	AlSb	undoped
280	high index	5	$Ga_{0.9}In_{0.1}Sb$	undoped
340	buffer	1	AlSb	undoped
	substrate		GaAs	

6.4.1 Cavity Design Optimisation

A reviewed cavity design was implemented in order to obtain the desired emission enhancement at the target wavelength of 4.26 µm from electrically-pumped devices. A new wafer (C1060) was grown accordingly. The main characteristic of this new cavity design is the reduction of the active region thickness and of the cavity order m_c. A number of advantages are associated with these modifications:

- The thinner active region can be conveniently placed at the antinode of the cavity electric field distribution. This increases the value of the antinode enhancement factor ξ and therefore the emission enhancement at the resonant wavelength.
- A lower cavity order m_c results in a wider emission peak linewidth, which guarantees a better overlap of the emission peak with the CO_2 absorption line.
- By reducing the cavity length, the free spectral range ν_{FSR} increases, thus reducing the intensity of the two side peaks and eventually achieving the condition of only one peak falling within the DBR stopband.

Figure 6.11 shows the schematic illustration of the cavity design and the electric field distribution in the cavity, highlighting the position of the interfaces between the different layers. The active region thickness was reduced to 200 nm and positioned at the antinode of the electric field. The total cavity thickness was reduced to 2.74 µm, which corresponds to a cavity order $m_c = 5$. The thickness of the n-type $Al_{0.05}In_{0.95}Sb$ layer was not reduced below 2 µm to guarantee the relaxation of the material to an acceptable level and, therefore, a good material quality in the LED active region. The cavity design parameters are listed in detail in Table 6.1.

The measured reflectance and transmittance spectra of the grown layer structure are shown in Figure 6.12. The spectra were normalised against the reflectance and transmittance spectra of an identical non-resonant LED structure, which allowed the elimination

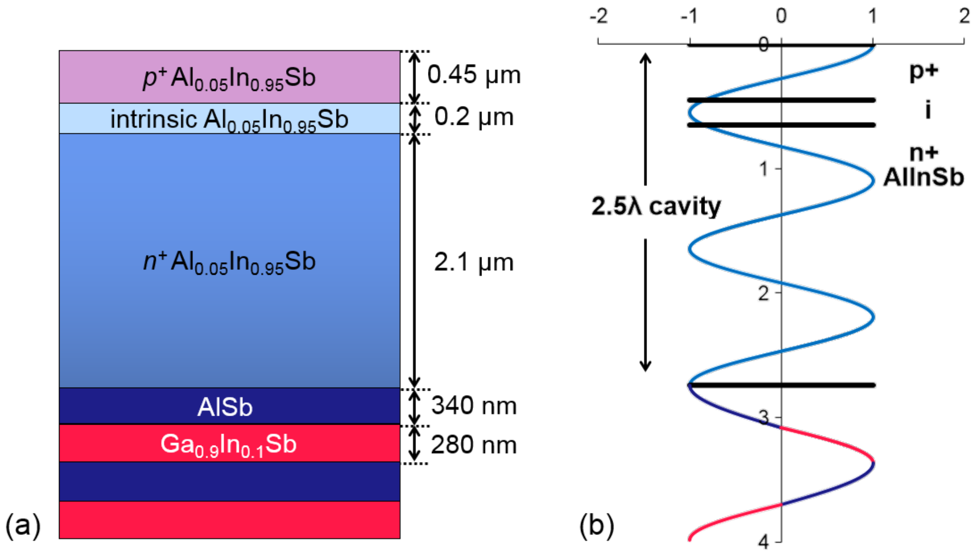

FIGURE 6.11: (a) Schematic illustration of the RC-LED heterostructure with the active region thickness reduced to 200 nm and the total cavity length reduced to 2.74 µm ($m_c = 5$). (b) Plot of the electric field in the cavity, showing the positioning of the active region at the field antinode.

of the effect of CO_2 and water vapour in the ambient air. The modelled spectra by transfer matrix method show a good agreement with the experimental data for a cavity thickness $L_{cav} = 2.78\,\mu\text{m}$.

As expected from the reduced cavity order, only one peak is present within the DBR stopband, with the side peaks sitting on the sidewalls of the DBR stopband and therefore being strongly attenuated. The resonant wavelength is found at 4.3 µm, slightly longer than the designed one, suggesting that the DBR stopband is shifted towards longer wavelengths. The cavity modes spacing is $\nu_{\text{FSR}} \approx 9.9\,\text{THz}$, which corresponds to an effective cavity length of $L_{eff} \approx 3.9\,\mu\text{m}$. This value is in good agreement with the expected effective cavity length taking into account the DBR penetration length ($L_{eff} = L_{cav} + L_{pen} \approx (2.78 + 1.19)\mu\text{m} = 3.97\,\mu\text{m}$). With a finesse of $F = 4.15$, the cavity quality factor results to be of $Q \approx 29.5$.

The photoluminescence of the layer structure was measured at room temperature and is shown in Figure 6.13. The PL emission from the RC-LED exhibits only one resonant peak corresponding to the cavity mode and shows a factor of 3 enhancement at the peak wavelength over the reference non-resonant LED. The main resonant peak has a linewidth of about 150 nm and is centred at 4.3 µm, slightly shifted towards longer wavelengths as can be seen from the CO_2 absorption feature sitting on the short wavelength side of the peak.

Electrically-pumped RC-LED devices were fabricated and the electroluminescence signal was measured at room temperature under pulsed bias conditions (1 kHz, 10 % duty cycle,

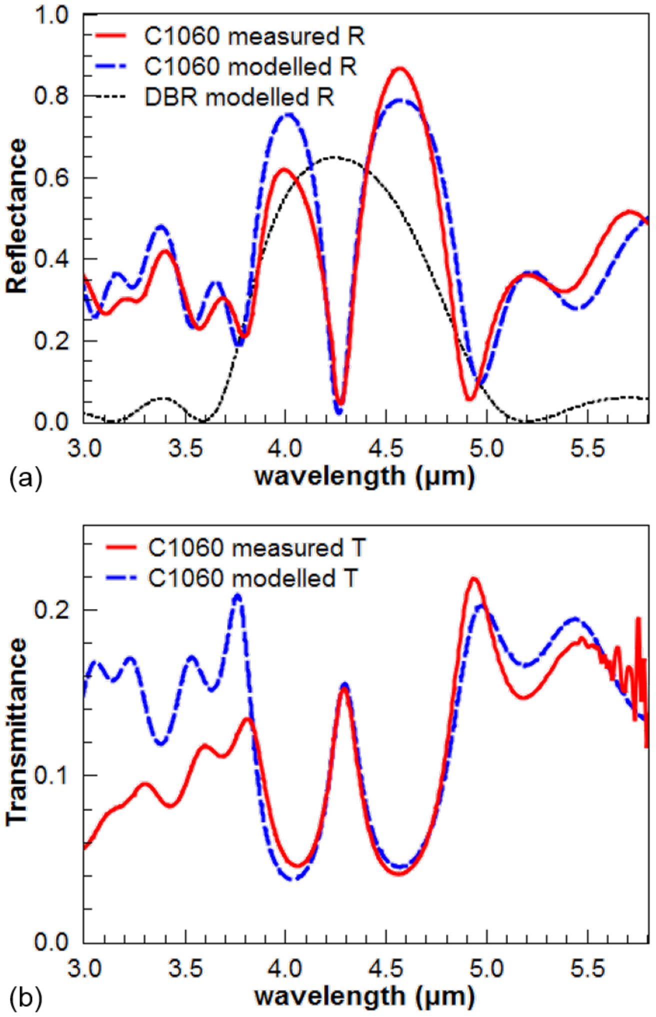

FIGURE 6.12: Measured and modelled reflectance (a) and transmittance (b) spectra for the RC-LED layer structure illustrated in Figure 6.11. The effective cavity length gives a cavity free spectral range ν_{FSR} of 9.9 THz, resulting in only one peak falling within the DBR stopband. The discrepancy in the transmittance spectra at long wavelengths is due to a variation in the relative intensity of the blackbody radiation between the measured background and sample spectra.

100 mA peak current). The EL spectra of the RC-LED and the reference non-resonant LED are shown in Figure 6.14. In contrast to what was observed from the devices on wafer C962, a strong emission enhancement at the resonant wavelength is observed from the electrically-pumped RC-LED. This is attributed to the improved cavity design and in particular to the positioning of the active region at the field antinode within the cavity. The ratio between the EL spectra of the RC-LED and the reference non-resonant LED gives an emission enhancement factor of 3 at the resonant wavelength. This value is in good agreement with the theoretical spectral emission enhancement, calculated with Equation 6.7, assuming a value of $\xi = 2$.

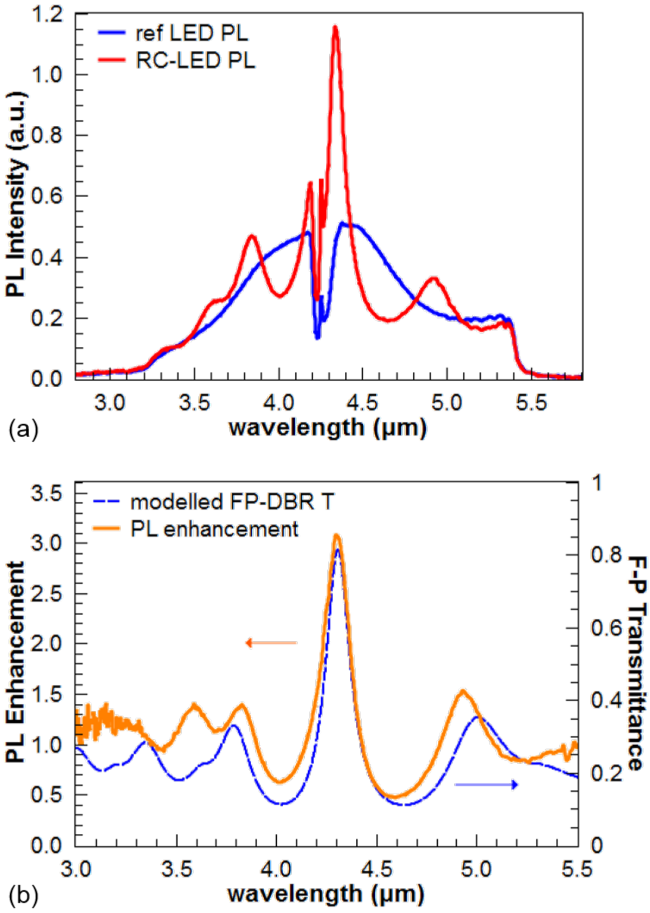

Figure 6.13: (a) Measured room temperature photoluminescence (PL) spectra of the RC-LED and a reference non-resonant LED structure with reduced layers thicknesses, according to the design parameters in Table 6.1. (b) Spectral photoluminescence enhancement showing a factor of 3 at the peak wavelength of 4.3 µm. The modelled Fabry-Pérot cavity transmittance is plotted for comparison.

As discussed in Section 6.1, one of the main advantages of a resonant-cavity LED design is the stability of the peak wavelength of emission over temperature. In fact, the resonant peak wavelength is defined by the cavity length and, therefore, shifts with temperature according to the temperature dependence of the cavity refractive index. This dependence results in a fundamental improvement over conventional non-resonant LED, for which the emission wavelength shifts according to the temperature dependence of the semiconductor material bandgap. As seen in Section 2.4, the $\mathrm{Al_xIn_{1-x}Sb}$ emission wavelength shifts to longer wavelengths with increasing temperature at a rate of -0.37 meV/K, which corresponds to 5.4 nm/K at 4.26 µm. Figure 6.15a shows the modelled normalised PL spectra of a $\mathrm{Al_{0.05}In_{0.95}Sb}$ LED over a 100 K temperature range, assuming a perfect alignment with the CO_2 absorption line at 273 K. The peak emission wavelength shifts by more than 500 nm over this temperature range, resulting in a significant variation of the signal intensity. As shown in Figure 6.16, the LED signal intensity at 4.26 µm for a standard LED can decrease to as much as 60 % of its original value over the

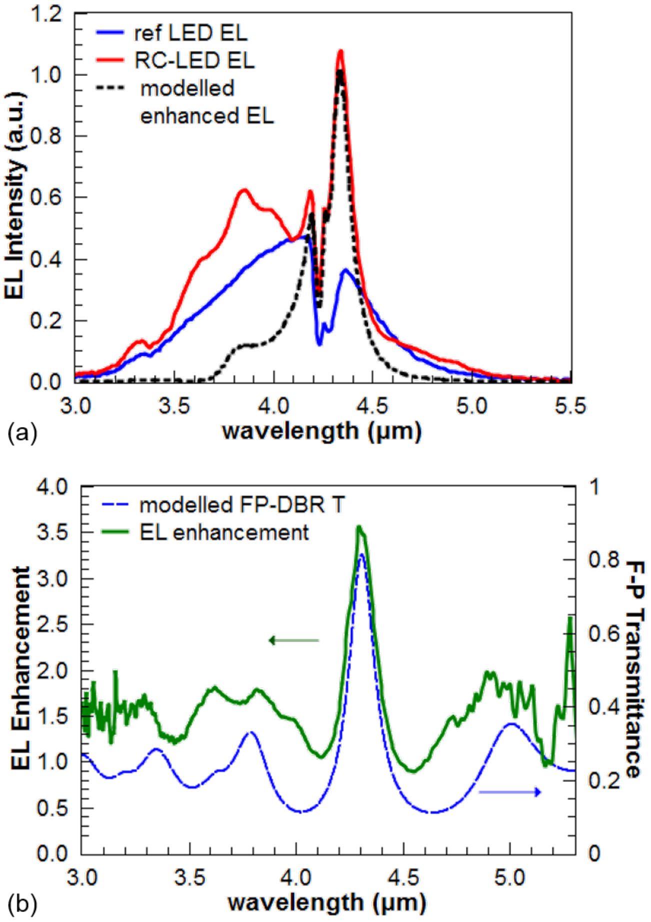

FIGURE 6.14: (a) Measured room temperature electroluminescence (EL) spectra of the RC-LED and a reference non-resonant LED. The devices are operated in pulsed bias (1 kHz, 10 %) at 100 mA peak current. The expected emission spectrum (dashed line) is calculated by multiplying the reference LED emission spectrum and the modelled emission enhancement (Equation 6.7), showing good agreement with the measured EL. (b) Spectral electroluminescence enhancement, obtained by the ratio of the measured spectra in (a), showing a factor of 3 improvement at 4.3 µm. The modelled Fabry-Pérot cavity transmittance is plotted for comparison.

100 K temperature range. This translates to a reduced sensitivity to CO_2 concentration and, therefore, affects the gas sensor performance over the range of operating temperatures. On the contrary, the peak wavelength of a RC-LED shifts with temperature according to the temperature coefficient of the cavity refractive index (for $Al_{0.05}In_{0.95}Sb$, $dn/dT \sim 4.5 \times 10^{-4}$). The reflectivity of the RC-LED layer structure was modelled by the transfer matrix method over the same 100 K temperature range, taking into account the refractive index temperature coefficient of all the layers in the structure. As shown in Figure 6.15b, the resonant peak at 4.3 µm shifts by less than 50 nm over this temperature range, at a rate of only 0.4 nm/K. This represent more than a factor of ten improvement in the emission wavelength stability with temperature, and guarantees a high sensitivity to CO_2 as the temperature varies. The normalised signal intensity at the

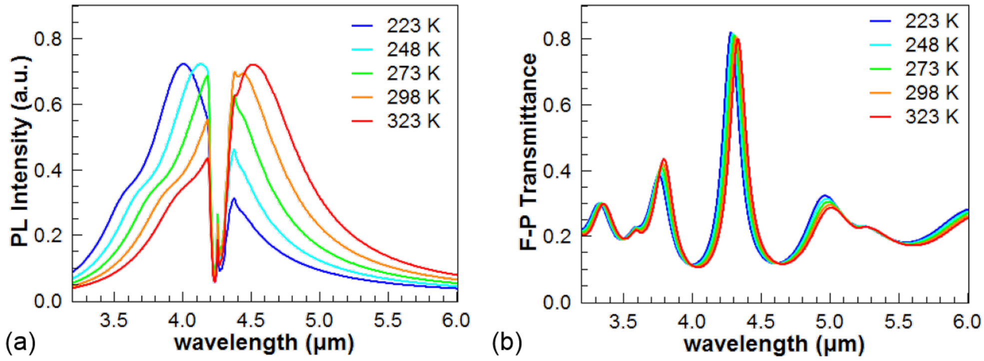

Figure 6.15: Modelled (a) photoluminescence spectra and (b) Fabry-Pérot cavity transmittance over 100 K temperature range. The PL shifts to longer wavelengths at 5.4 nm/K due to the variation of the semiconductor material bandgap with temperature. The emission wavelength of the Fabry-Pérot cavity is determined by the optical cavity length and, therefore, varies only by 0.4 nm/K in the same direction, because of the semiconductor material refractive index dependence on temperature.

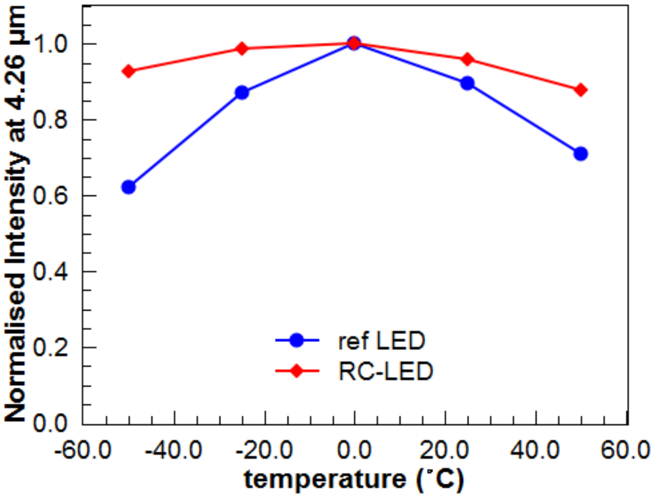

Figure 6.16: Normalised signal intensity at 4.26 µm for a non-resonant LED and a RC-LED across a 100 K temperature range. The signal intensity decreases to as much as 60 % for a non-resonant LED, while remains within 90 % of its peak value for a RC-LED. This guarantees a good spectral matching and high sensitivity to CO_2 across the whole temperature range.

resonant wavelength is plotted in Figure 6.16 as a function of temperature, showing that the CO_2 absorption line will remain aligned with the region of strong LED emission.

To summarise, the three main advantages of a resonant-cavity LED over a conventional non-resonant LED, as discussed in Section 6.1, have been demonstrated with experimental data and simulations:

1. The interference effects within the Fabry-Pérot cavity, defined by the bottom DBR mirror and the air-semiconductor interface, results in an enhancement of the light intensity emitted along the axis of the cavity at the resonant wavelengths. With

an optimised cavity design, in which a thin active region is placed at an antinode of the electric field in the cavity, a spectral enhancement of up to 3.5 times is obtained at 4.3 µm from electrically-pumped LED devices. As the LED series resistance is unchanged and the same electrical driving conditions are applied, the emission enhancement corresponds to 3.5 times improved efficiency of the LED at the target resonant wavelength.

2. The emission linewidth is determined by the cavity quality factor and therefore can be designed and tailored to match the absorption wavelength of the target gas. With a cavity finesse of ≈ 4 and an effective cavity order of 7, the peak emission linewidth is about 150 nm at full-width half-maximum (FWHM), which represent a factor of ≈ 5 narrower linewidth compared to a non-resonant LED (the emission linewidth of a non-resonant LED is $\sim 1.8kT$, which corresponds to about 680 nm at 4.3 µm). The narrower emission linewidth can contribute to dramatically improve the performance of the gas sensor. In fact, as the LED emission matches the target gas absorption line, significantly less signal is detected outside the spectral band of interest, which can generate unwanted signal and degrade the signal-to-noise ratio of the sensor. Performance simulations of the overall sensor system by GSS have confirmed that the narrower linewidth would result in a significant improvement of the sensor noise level.

3. The emission linewidth of the resonant-cavity LED is dictated by the optical cavity length. Therefore, the emission wavelength shift with temperature is determined by the temperature coefficient of the cavity refractive index and not by the energy bandgap dependence on temperature, as for a non-resonant LED. This results in a factor of 10 improvement in the emission wavelength stability with temperature, which guarantees a strong signal intensity at 4.26 µm and, therefore, a high sensitivity to the CO_2 concentration across a wide range of operating temperatures.

A design for a resonant-cavity LED emitting through the substrate was also preliminary investigated. In this configuration, the light is emitted through the DBR mirror ($R_1 = R_{DBR}$), placed between the GaAs substrate and the LED active layers. The second, highly reflective mirror, is provided by a solid layer of gold ($t_{Au} = 250\,\text{nm}$) deposited on the top surface of the LED mesa, which acts as an ideal mirror with a reflectivity $R_2 \approx 0.95$. The cavity thickness was extended by a quarter-wavelength compared to a top-emitting RC-LED to account for the π phase shift given by the metal mirror. The schematic illustration of the heterostructure design is shown in Figure 6.17. According to Equation 6.7, the spectral emission enhancement, with these values of reflectivities, is as high as 13. Additionally, the solid gold layer deposited on the top surface of the device mesa acts both as a mirror and a p-type ohmic contact, therefore overcoming the

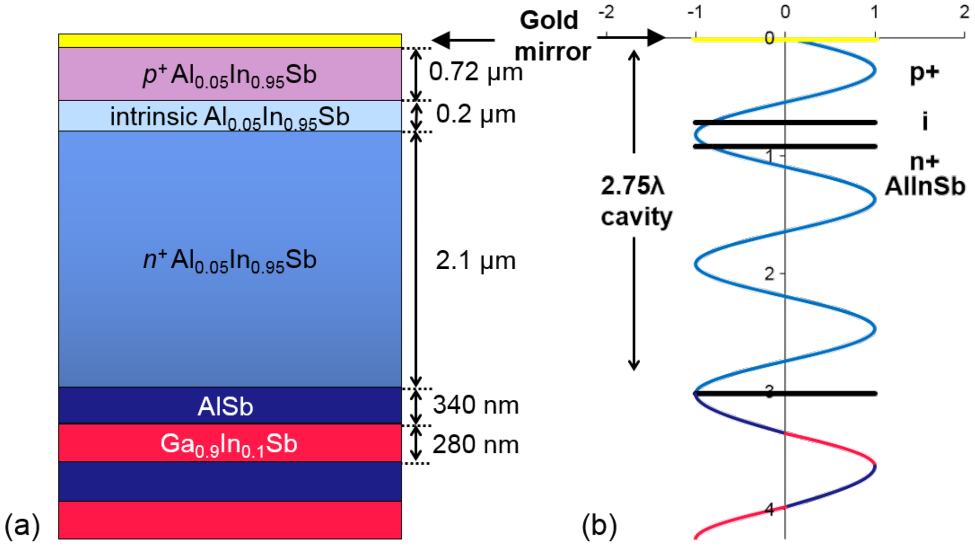

FIGURE 6.17: (a) Schematic illustration of the RC-LED heterostructure with 200 nm-thick active region and total cavity length increased to 3.02 µm to account for the phase shift introduced by the top gold mirror. (b) Plot of the electric field in the cavity, showing the positioning of the active regoin at the field antinode.

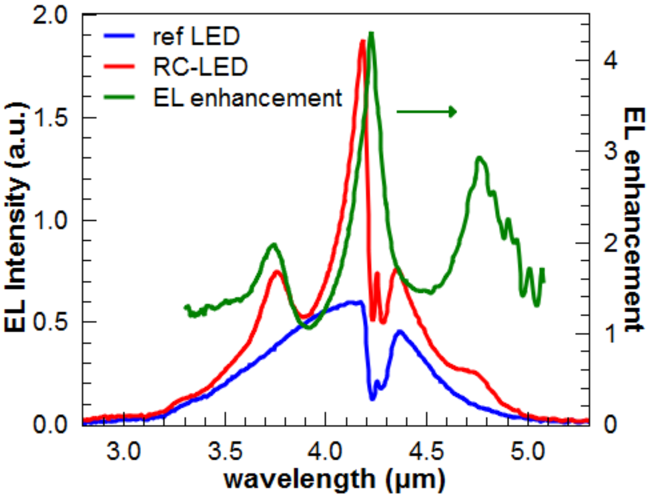

FIGURE 6.18: Measured room temperature electroluminescence (EL) spectra of the substrate-emitting RC-LED. The device is operated in pulsed bias (1 kHz, 10 %) at 100 mA peak current. The RC-LED has a solid gold top layer that acts both as the highly reflective mirror and the p-type ohmic contact. The EL signal is collected from the GaAs substrate. The emission at the resonant wavelength of 4.23 µm is enhanced by a factor of ∼ 4 compared to a reference non-resonant LED.

Gas flux	CH_4/H_2 = 6/50 sccm
ICP/RF power	400/200 W
Chamber pressure	20 mTorr
Table temperature	20 C
Wafer temperature during etching	< 100C

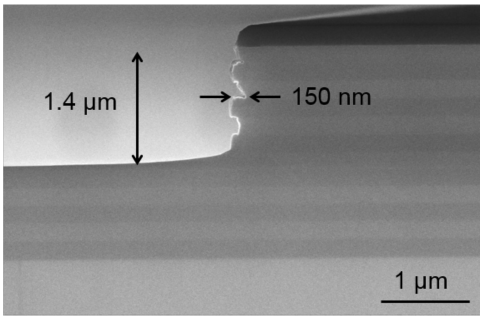

FIGURE 6.19: ICP-RIE dry etch process parameters and SEM cross-sectional image of the partially etched $AlSb/Ga_{0.9}In_{0.1}Sb$ DBR stack. The average etch rate is 93 nm/min and the undercut is limited to about 150 nm.

current spreading issue discussed in Chapter 5. The emitted light is collected from the GaAs substrate side and measured by an FTIR spectrometer. The measured electroluminescence spectra of the substrate emitting RC-LED is shown in Figure 6.18. The ratio with the EL spectra of a reference non-resonant LED results in a factor of ≈ 4 enhancement of the emission at the resonant wavelength of 4.23 μm. The fact that the obtained emission enhancement is lower than the theoretical value can be attributed to the uncertainty of the resonant conditions given by the non-ideal metal mirror and to the unpolished surface of the GaAs substrate. This approach, however, has the potential of providing even more pronounced enhancement of the LED performance.

Thanks to the successful implementation of RC-LEDs with improved spectral efficiency and narrower spectral linewidth, Gas Sensing Solutions has initiated their development as commercial sensors. As presented in Section 2.4, the production LEDs that serve as the light source of Gas Sensing Solutions' CO_2 sensors is designed as a 3-by-3 array of individual elements connected in series. Consequently, the individual LED mesa elements need to be electrically isolated. This is achieved by adding an additional etch step in the fabrication process, which completely removes the n-type material and leaves the insulating GaAs substrate exposed between the single elements. In the case of RC-LEDs, the opening of these isolation trenches between the single elements of the array would require etching through the DBR layer stack in order to reach the GaAs substrate, which adds time and complications to the fabrication process. In fact, achieving an etching of the $AlSb/Ga_{0.9}In_{0.1}Sb$ layers with a suitable profile for the subsequent fabrication steps is not trivial. In particular, due to the presence of aluminium-rich layers, the etching process with commonly used chemistries significantly slows down within the AlSb layers, thus resulting in sidewall profiles with prohibitive undercuts. Additionally, the AlSb layers undergo a rapid oxidation process if exposed to air, thus making the option of switching between different chemistries particularly impractical. The best result achieved so far was obtained with an Inductively Couple Plasma Reactive Ion Etching

TABLE 6.2: Measured resistivity values for the n-type doped $Al_{0.05}In_{0.95}Sb$, $Ga_{0.9}In_{0.1}Sb$ DBR layer and GaAs substrate.

Material	Doping Conc. (cm^{-3})	Resitivity (Ω cm)
$Al_{0.05}In_{0.95}Sb$	n-type 10^{18}	4.45×10^{-4}
$Ga_{0.9}In_{0.1}Sb$	undoped	2.25×10^{-1}
GaAs	undoped	3.25×10^{5}

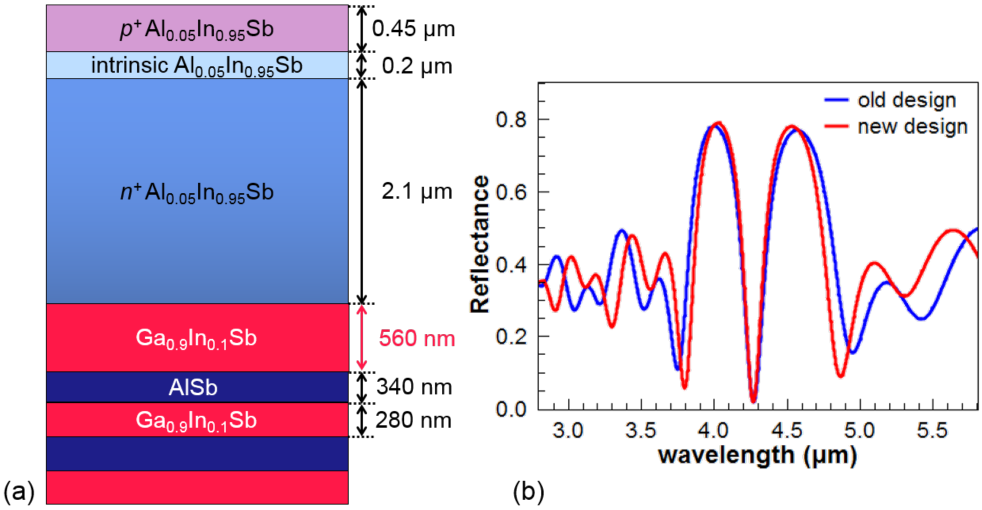

FIGURE 6.20: (a) Schematic illustration of the new proposed RC-LED heterostructure design with an additional $\lambda/2$ $Ga_{0.9}In_{0.1}Sb$ layer which can act as a non-oxidising stop-etch layer and provide electrical insulation between the individual elements of the 3-by-3 LED array. (b) Modelled reflectance spectra of the proposed RC-LED layer structure, showing no significant variation of the resonant peak. The narrower free spectral range is due to the $\lambda/2$ longer cavity.

(ICP-RIE) process and a CH_4/O_2 chemistry at low temperature. The etching parameters are indicated in Figure 6.19, together with an SEM cross-sectional image of a sample from wafer C979, in which the first 3 DBR layer pairs have been etched. The process gives smooth sample surface, a DBR average etch rate of 93 nm/min and a sidewall profile with limited undercut of 100–150 nm. The sidewall surface could be smoothed out by the deposition of a dielectric or SU-8 passivation layer before the deposition of the metal contacts.

An alternative solution comes from the high resistivity of the undoped DBR layers. In fact, GaSb is highly resistive, with an intrinsic resistivity about 10^5 higher than that of InSb at room temperature [68], making the leakage current through the GaSb buffer layer negligible. To confirm this, the measured bulk resistivities for n-type doped ($1 \times 10^{18}\,cm^{-3}$) $Al_{0.05}In_{0.95}Sb$, undoped $Ga_{0.9}In_{0.1}Sb$ and the undoped GaAs substrate are indicated in Table 6.2. The measured resistivity of the undoped $Ga_{0.9}In_{0.1}Sb$ is still more than two orders of magnitude higher than the n-type $Al_{0.05}In_{0.95}Sb$, thus providing a suitable electrical insulation between the single elements of the LED array.

An alternative DBR and RC-LED design is therefore proposed to provide a non-oxidising and insulating $Ga_{0.9}In_{0.1}Sb$ stop-etch layer. Figure 6.20a illustrates the revised layer structure, with the introduction of a half-wavelength $Ga_{0.9}In_{0.1}Sb$ layer between the DBR stack and the LED active layers. The $Ga_{0.9}In_{0.1}Sb$ layer is 560 nm thick, which is suitable thickness to act as a stop etch layer in the fabrication process used for production devices. The modelled reflectivity of the new RC-LED design is plotted in Figure 6.20b, showing the unperturbed spectra of the main resonant peak. The slightly narrower free spectral range is related to the $\lambda/2$ longer cavity.

In conclusion, the design and implementation of resonant-cavity LEDs demonstrated improved performance over non-resonant LEDs in terms of spectral efficiency and spectral purity. The investigation of substrate-emitting RC-LED suggests that an even more substantial emission enhancements, up to a factor of 10, could be achieved. With further optimisation of the layer structure tailored to the fabrication process of production devices, RC-LEDs will be exploited in commercial CO_2 gas sensors, with breakthrough improved performance in terms of spectral efficiency, spectral selectivity and temperature stability.

Chapter 7

Plasmonic-enhanced LEDs

This Chapter reports on the investigation of plasmonic patterns integration on mid-infrared LEDs for the enhancement of light extraction. The background theory of excitation and coupling to surface plasmon polaritons is reviewed and the implementation of 2D-periodic metal hole arrays on mid-infrared active devices for the enhancement of optical emission and absorption is discussed. The transmittance spectra of 2D-periodic hole arrays on a thin metal film is modelled by the Finite-Difference Time-Domain (FDTD) method as a function of the geometrical design parameters and the results are compared to the measured transmittance of fabricated test samples. The integration of metal hole arrays on AlInSb required the optimisation of the pattern definition and transfer process to achieve good uniformity and reproducibility of the designed features. Measurements of the spectral response of fully processed LED devices with 2D-periodic metal hole arrays patterned on the top surface are presented and further development work is discussed.

7.1 Optical Enhancement via Surface Plasmon Polaritons

Thanks to the rapid development of nanotechnology, techniques based on surface patterning via two-dimensional photonic crystals and surface plasmonic arrays have emerged as an appealing solution for improving the light extraction from LED devices [69, 149, 150]. Although the effectiveness of these techniques is well assessed for LEDs emitting in the visible spectral range, their integration on real devices is particularly challenging, as it requires the positioning of the active region within few nanometres from the top surface [151, 152]. In the mid-infrared region, the coupling to surface plasmon waves and the patterning of periodic structure on metal films has been extensively used for achieving high confinement of the light in the waveguide of quantum cascade lasers (QCL)

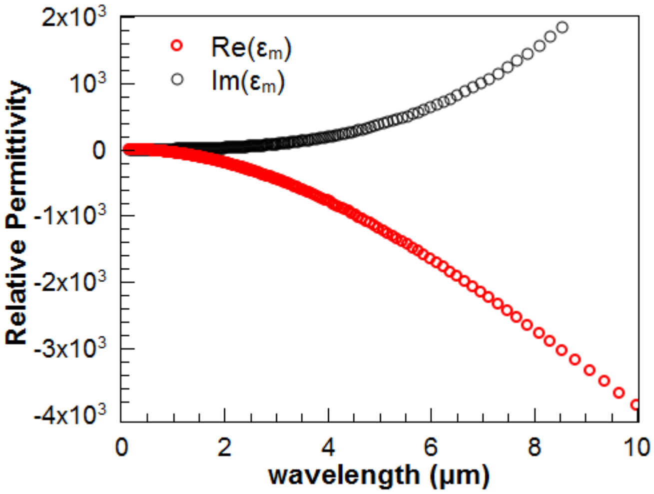

FIGURE 7.1: Real and imaginary part of gold (Au) relative permittivity up to 10 µm, calculated according to the Drude model in Equation 7.2.

and for their potential for beam shaping and steering [153–156]. Additionally, periodic metal hole arrays have been used for the realisation of passive optical filters to shape the spectral response of thermal emitters [157–159] and, more recently, to strongly enhance the light coupling to quantum-dots mid-infrared detectors [160–162]. Metal patterned surfaces have, in fact, the potential for enhancing the optical coupling and absorption thought the excitation of surface plasmon waves. Additionally, the patterned metal can act as a scattering surface, promoting the redirection of light to or from the optical device. The integration of plasmonic structure on mid-infrared optical devices is particularly interesting as the geometrical constraints are significantly relaxed and the required sub-wavelength features are in the order of 1 µm, which can be achieved with well developed fabrication techniques, such as deep-UV lithography and nano-imprinting [163, 164].

Surface plasmon polaritons (SPP) are electromagnetic modes that generates from the interaction of light and mobile surface charges at the interface between two materials with relative permittivity of opposite sign, such as a metal and a dielectric [165]. The dispersion relation between the angular frequency (ω) and the in-plane momentum ($k_{\|}$) of a SPP mode, propagating along the interface between a semi-infinite dielectric and a smooth metal, can be calculated by imposing the continuity of the tangential electric and magnetic field components across the interface, and can be expressed as [166]:

$$k_{\mathrm{SPP}} = k_0 \sqrt{\frac{\varepsilon_m \varepsilon_d}{\varepsilon_m + \varepsilon_d}} \tag{7.1}$$

where $k_0 = 2\pi/\lambda$ is the momentum in free space and ε_m and ε_d are the relative permittivities of the metal and the dielectric layer, respectively. The relative permittivity of

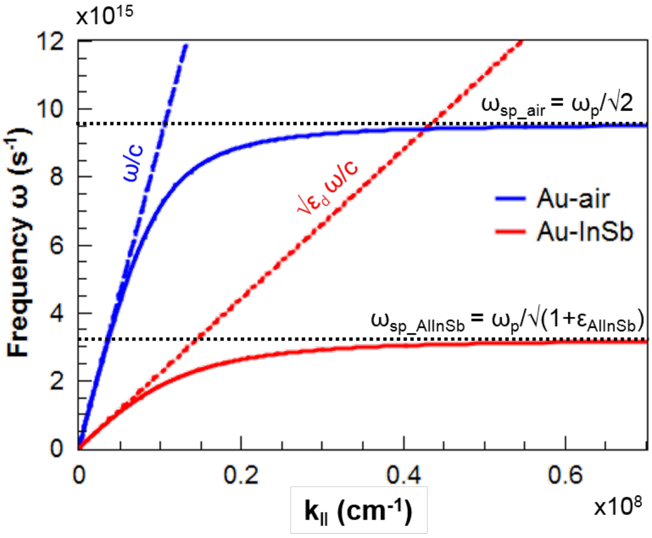

Figure 7.2: Dispersion relation of a surface plasmon mode at the Au-air and Au-AlInSb interface, according to Equation 7.1. The straight lines are the dispersion relations of photons in air and in the high index semiconductor material.

metals can be calculated according to the Drude model:

$$\varepsilon_m(\omega) = 1 - \frac{\omega_p^2}{\omega^2 - i\Gamma\omega} \tag{7.2}$$

where ω_p is the plasma frequency and Γ is the scattering rate which accounts for dissipation losses. The values of the Drude parameters for gold (Au), which is one of the most commonly used metal for plasmonic devices thanks to its physical and chemical stability, are $\omega_p = 3.39 \times 10^{15}\,\mathrm{s}^{-1}$ and $\Gamma = 9.3 \times 10^{13}\,\mathrm{s}^{-1}$. The real and imaginary part of the gold relative permittivity up to 10 µm, according to Equation 7.2, are plotted in Figure 7.1. By substituting the expression for ε_m into the dispersion relation of Equation 7.1, the SPP dispersion relation at Au-air and Au-AlInSb interfaces were calculated and their real part are plotted in Figure 7.2. The straight lines are the dispersion relations of photons in air ($k_0 = \omega/c$) and in AlInSb ($k = \sqrt{\varepsilon_{\mathrm{AlInSb}}}k_0$, with $\varepsilon_{AlInSb} = 15.2$), respectively. As the frequency increases, the in-plane momentum of the SPP mode increases, moving away from the light line and approaching an asymptotic limit. This corresponds to the surface plasmon resonant frequency ω_{SP}, which occurs when the metal and the dielectric have relative permittivities of the same magnitude, but opposite sign.

As the magnitude of the SPP momentum is always higher than the momentum of a photon in the dielectric, the SPP modes cannot be directly excited at a planar interface by incident radiation of any given frequency. Therefore, an additional momentum is needed to match the momentum of the incident optical wave to that of the SPP. This can be obtained by a metallic corrugation in the form of a periodic grating. In fact, the incident light, scattered by the periodic patterned surface, gains an additional in-plane

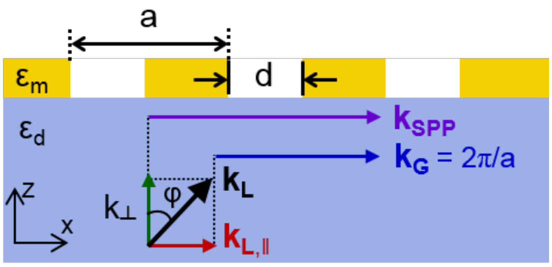

FIGURE 7.3: Schematic illustration of a periodic grating in a metal film with the wavevector diagram of the light-SPP coupling occurring thanks to the additional momentum given by the periodically patterned surface.

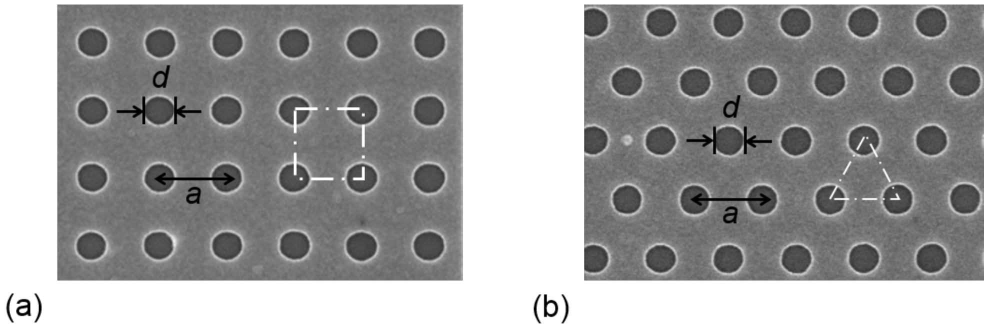

FIGURE 7.4: SEM images of two-dimensional arrays of holes in a Au film with (a) square and (b) triangular lattice fabricated in the JWNC. The array period a is 1 µm and the holes diameter is $d = 0.4 \cdot a$.

momentum multiple of the Bragg vector $k_G = 2\pi/a$, where a is the grating period. Considering the structure illustrated in Figure 7.3, with a grating patterned Au layer at the interface with a dielectric material, the matching conditions of the in-plane momentum can be written as [158]:

$$k_L + mk_G = \frac{2\pi}{\lambda_d}\sin\varphi + m\frac{2\pi}{a} = k_{\text{SPP}} \tag{7.3}$$

where $k_L = \frac{2\pi}{\lambda_d}\sin\varphi$ is the in-plane momentum of the incident light, with λ_d the wavelength in the dielectric and φ the angle of incidence, and m is an integer. Equation 7.3 can be extended to the two-dimensional case for an array of holes in a thin metal film, as the ones illustrated in Figure 7.4. The transmission spectra of such an array is characterised by resonance peaks, at the wavelengths for which the condition in Equation 7.3 is met. In case of normal incidence ($\varphi = 0$), the wavelengths at which the resonance conditions occurs can be calculated from the real part of the SPP momentum in Equation 7.1 and the condition in Equation 7.3, and are given by:

$$\lambda_{m,l} = \frac{a}{\sqrt{(m^2 + l^2)}}\sqrt{\frac{\varepsilon_m\varepsilon_d}{\varepsilon_m + \varepsilon_d}} \tag{7.4}$$

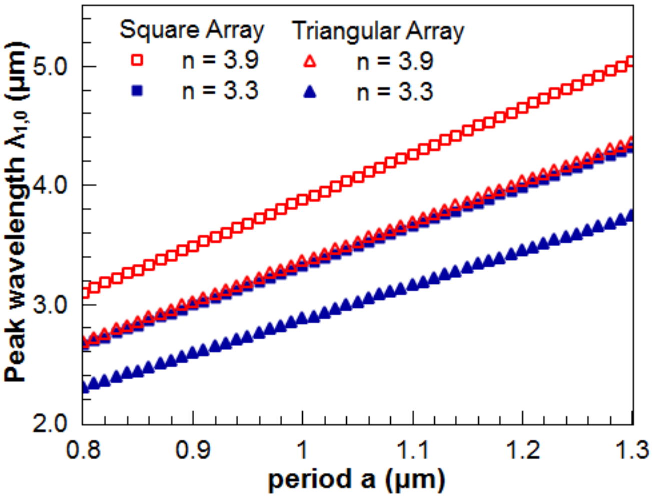

FIGURE 7.5: First order peak resonant wavelength $\lambda_{1,0}$ as a function of the array period a for both square-lattice and triangular-lattice arrays on GaAs ($n \approx 3.3$) and AlInSb ($n \approx 3.9$).

for a square-lattice array, as in Figure 7.4a, and

$$\lambda_{m,l} = \frac{a}{\sqrt{\frac{4}{3}\left(m^2 + ml + l^2\right)}}\sqrt{\frac{\varepsilon_m \varepsilon_d}{\varepsilon_m + \varepsilon_d}} \tag{7.5}$$

for a triangular-lattice array, as in Figure 7.4b, where (m, l) corresponds to the scattering order. As in the mid-infrared range $|\mathrm{Re}(\varepsilon_\mathrm{m})| \gg \varepsilon_d$, the first order resonant wavelengths $\lambda_{1,0}$ are easily defined by the array periodicity and the refractive index $n = \sqrt{\varepsilon_d}$ of the dielectric, and are plotted in Figure 7.5 for both a square-lattice and a triangular-lattice array on GaAs ($n \approx 3.3$) and AlInSb ($n \approx 3.9$). Interestingly, triangular-lattice arrays on AlInSb should give very similar resonant peak wavelengths as square-lattice arrays on GaAs.

The interest in SPPs has increased significantly after the experimental demonstration of extraordinary optical transmission (EOT) through arrays of sub-wavelength holes, with diameter $d \ll \lambda$, in thin metal films [167]. This is in contrast with what is predicted by standard aperture theory, where coupling of light through a sub-wavelength hole can only happen through evanescent waves. Even if there is still an open debate on the physical explanation of EOT [164], mainly due to the different properties of metals over different spectral regions, the main contribution to EOT from visible to mid-infrared wavelengths can be explained with the excitation of SPP modes due to the grating momentum [158, 168, 169]. Enhanced transmission and optical filters in the mid-infrared wavelength range based on structured metallic films were reported in the literature [159, 170–173], with transmission exceeding 80 % at 7.6 µm with deep sub-wavelength hole arrays ($\lambda/d \sim 6$) [168]. Two-dimensional hole arrays (2DHA) structures were

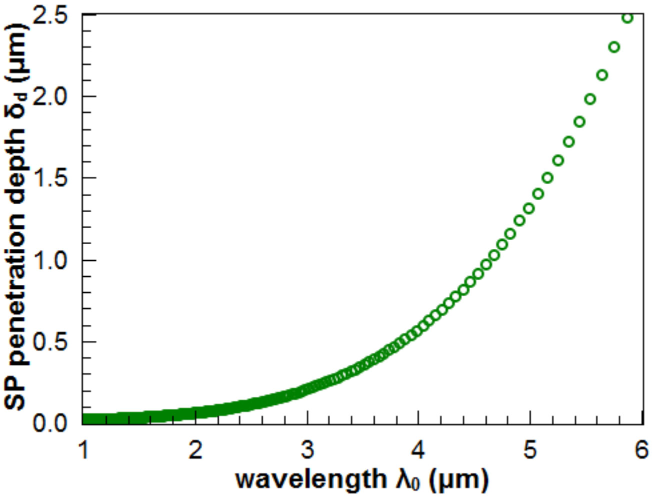

FIGURE 7.6: Penetration depth δ_d of the plasmon mode into a high-index material (AlInSb, $n \approx 3.9$) as a function of free space wavelength λ_0.

also successfully integrated on mid-infrared active devices. In particular, mid-infrared photodetectors based on InAs quantum dots (QDs) showed up to 20 times enhancement and significant narrowing of the photoresponse thanks to efficient coupling of the incident field to the surface plasmonic modes and to the strong plasmon-QDs interaction [162].

In surface plasmon enhanced optical devices, a good spatial overlap between the surface plasmonic field and the device active region is essential for an efficient coupling, as was demonstrated in case of plasmon-enhanced quantum dots infrared detectors [162, 172]. Before this, several results were reported claiming improved spectral selectivity, but only limited absorption enhancement due to the poor coupling between the plasmonic mode and the detector active region [170, 174]. This effect can be understood by considering the penetration depth of the plasmonic field into the materials that determine the interface along which the plasmonic mode propagates. Considering z the direction perpendicular to the interface, the relationship between the total momentum of light, with freespace wavevector k_0 in a material with relative permittivity ε_i, and its component along z, k_z, is given by [175]:

$$\varepsilon_i k_0^2 = k_{SPP}^2 + k_{z,i}^2 \tag{7.6}$$

where the SPP wavevector k_{SPP} is the in-plane component of the total momentum. As discussed for Figure 7.2, the SPP momentum always exceeds that of a photon propagating in the adjacent material, $k_{SPP}^2 > \varepsilon_i k_0^2$, so that the momentum component along the z direction is imaginary in both materials. Therefore, the surface plasmon electromagnetic field is confined near the metal-dielectric interface and decays exponentially with the distance from it, in both the dielectric and the metal. The field penetration depth

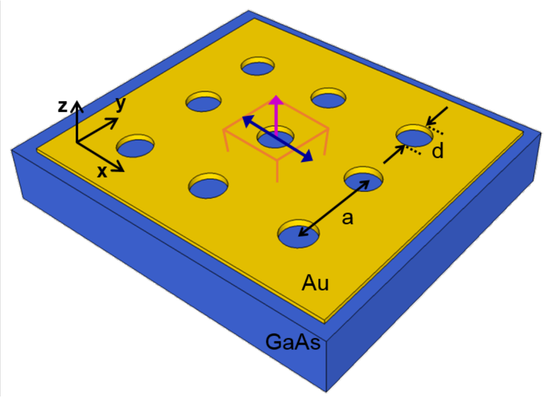

FIGURE 7.7: Schematic illustration of the structure used for the FDTD simulations with a square-lattice array of holes in a thin gold (Au) film on a GaAs substrate. The source is a plane wave incident along the z axis and the electric field is polarised along the x axis. The computational domain including a single unit cell of the array is highlighted.

in the dielectric material can be calculated by combining Equation 7.1 and 7.6 [175]:

$$\delta_d = \frac{1}{k_0}\sqrt{\left|\frac{\mathrm{Re}\left(\varepsilon_m\right)+\varepsilon_d}{\varepsilon_d^2}\right|} \tag{7.7}$$

The penetration depth into a high refractive index semiconductor, such as AlInSb, relative to the free space wavelength is plotted in Figure 7.6. The penetration depth of the plasmon mode into the dielectric is always shorter than the free space wavelength, but increases for longer wavelengths. This can be explained with the fact that the metal behaves as a better conductor at longer wavelengths and, therefore, the plasmon mode has a momentum closer to the light line and is less confined to the metal-semiconductor interface. The dependence of the penetration depth on wavelength indicates how the geometrical requirements for a good overlap between the tail of the evanescent plasmonic field and the device active region are significantly relaxed in the mid-infrared spectral region.

7.2 FDTD Modelling of 2D-periodic Metal Hole Arrays

At first, the transmittance spectra of a 2D-periodic metal hole array was modelled as a function of the different design parameters. The simulation setup is illustrated in Figure 7.7, with a square-lattice array of holes in a thin gold (Au) film on top of a GaAs substrate, which is chosen for the initial characterisation of the arrays transmittance as it is transparent at mid-infrared wavelengths and, therefore, allows direct comparison of the simulated spectra with measured transmittance of fabricated Au hole arrays.

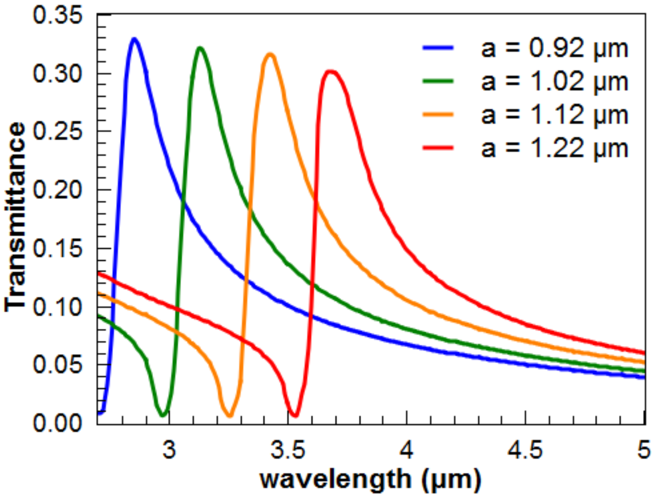

FIGURE 7.8: Simulated transmittance spectra of an array of holes in a 20 nm-thick Au film on a GaAs substrate. The periodicity is varied from 0.92 µm to 1.22 µm in steps of 100 nm, while the hole diameter is fixed at $d = 0.5 \cdot a$ (ff = 19.6 %). The peak resonance wavelength shifts linearly to longer wavelength with the increasing array period a.

The simulations were performed with the commercial software FDTD Solutions 8.9 from Lumerical [176]. The finite-difference time-domain method (FDTD) is one of the most popular numerical computational algorithms for the modelling of electromagnetics systems [177, 178]. The partial differential Maxwell's equations are approximated using finite differences in both space and time, and the temporal evolution of the electric and magnetic fields are computed at every point in space within the computation domain. One of the strengths of the FDTD method lies in its versatility, so that very diverse structures can be analysed. Additionally, being a time domain method, the response of the structure over a wide spectral range is obtained from a single simulation by using a broadband source, which substantially accelerates the analysis of spectral transfer functions.

A single unit cell of the array is modelled and symmetric boundary conditions are used to reduce the computational domain. A plane wave source centred at 4.2 µm with 2 µm bandwidth is used as a source, placed 500 nm below the metal-semiconductor interface. The computed transmittance spectra as a function of the array periodicity is shown in Figure 7.8. Periods in the range of 0.92 µm to 1.22 µm are chosen, which are expected to give peak transmission wavelengths around 4.2 µm when fabricated on AlInSb, as seen from the calculated values plotted in Figure 7.5. The gold thickness is kept constant at $t_{\mathrm{Au}} = 20$ nm and the hole diameter is scaled accordingly to $d = 0.5 \cdot a$. As expected, the spectra are characterised by a pronounced transmittance peak, which shifts linearly with the array periodicity a. The peak wavelengths are in good agreement with the analytically calculated SPP resonant wavelengths, according to Equation 7.4. As the fill factor, defined as the non-metal covered area over the array unit cell $\mathrm{ff} = \pi(d/2)^2/a^2$,

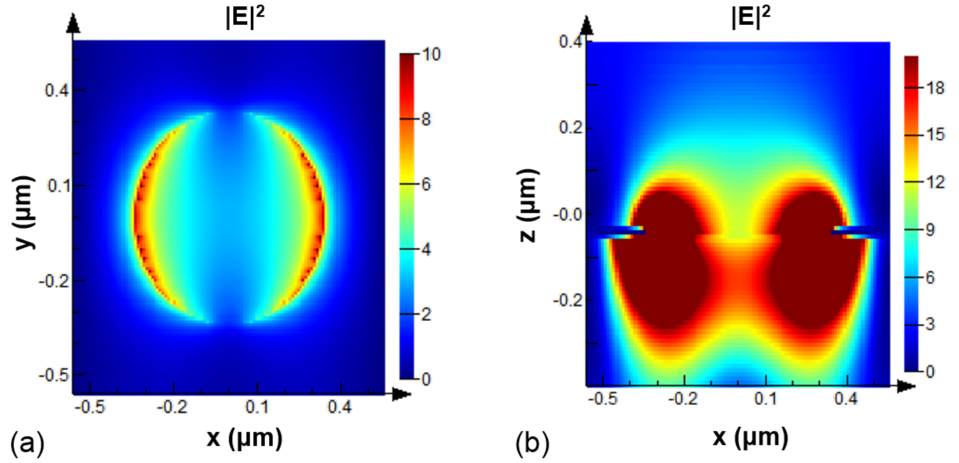

Figure 7.9: FDTD simulation results of (a) the electric field intensity at the transmitted surface of the gold and (b) the cross-sectional view of the electric field intensity on the x-z plane in the vicinity of a hole at the resonant wavelength. The intensity of the incident field is 1 V/m. The colorbar in (b) is scaled to highlight the areas in which the field intensity enhancement is at least 20.

is only 19.6 %, the higher transmittance is obtained thanks to the electric field enhancement in the proximity of the holes, as predicted by the EOT effect. Figure 7.9 shows the electric field intensity profile at the transmitted surface of the metal film in the x-y plane and at a hole cross section in the x-z plane. The colorscale of both plots has been adjusted to highlight the areas where the field intensity if at least 10 V/m and 20 V/m, respectively, which represents a significant enhancement as the incident electric field intensity is 1 V/m. In particular, Figure 7.9b highlights how the strong field intensity enhancement is found only in the first 200–300 nm from the metal-semiconductor interface. This defines the region where the active region of an active optical device has to be placed to experience the strong enhancement of the electric field caused by the interaction with the SPP mode.

Next, the effect of the metal film thickness t_{Au} is analysed. As shown in Figure 7.10, the resonant wavelength blueshifts with increasing thickness of the metallic film until it becomes almost independent of further increase above 50 nm. Finally, the effect of the hole fill factor $\mathrm{ff} = \pi(d/2)^2/a^2$ is considered, while the array period a and the metal thickness t_{Au} are fixed. As the holes become wider, the resonant wavelength redshifts and the intensity of the transmittance increases, as reported in Figure 7.11. Additionally, the bandwidth of the resonant peak becomes wider for higher fill factors, as the SPP mode is less confined within the holes. Therefore, a trade-off has to be considered between the intensity of the transmittance peak and the wavelength selectivity of the designed structure.

Following the simulation results discussed above, some conclusions can be drawn regarding the geometrical design parameters and their influence on the transmission properties

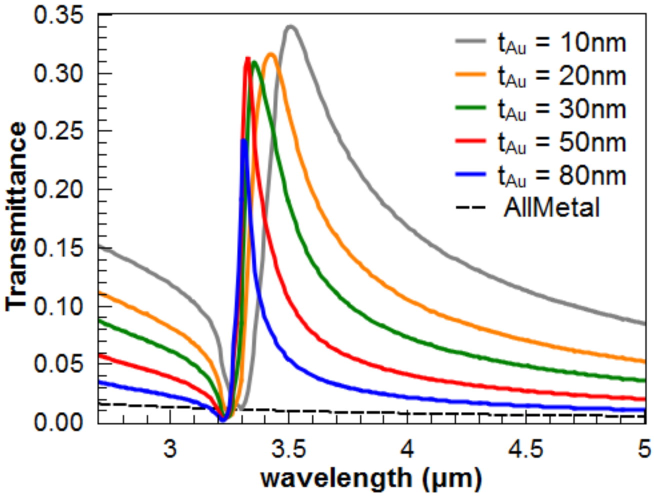

FIGURE 7.10: Simulated transmittance spectra of an array of holes, with period $a = 1.12\,\mu\mathrm{m}$ and hole diameter $d = 0.5 \cdot a$ (ff $= 19.6\,\%$), as a function of the metal film thickness t_{Au}. The peak resonant wavelength shifts to shorter wavelengths, and both the transmittance intensity and the peak bandwidth decrease with increasing metal thickness.

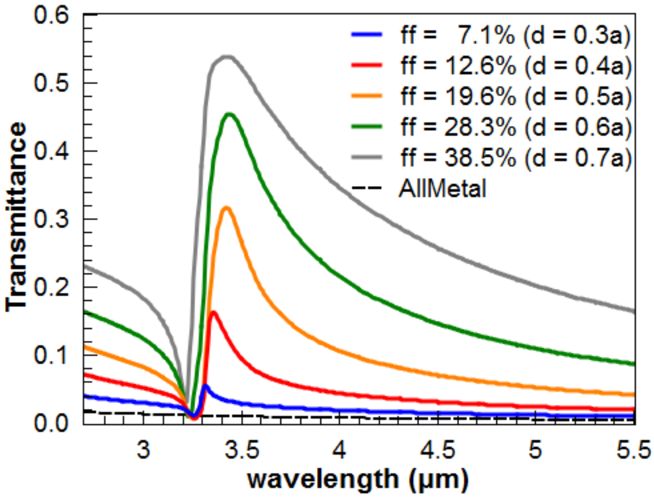

FIGURE 7.11: Simulated transmittance spectra of an array of holes in a 20 nm-thick Au film on a GaAs substrate with period $a = 1.12\,\mu\mathrm{m}$ and increasing hole diameter d. The fill factor is defined as the ratio between the non-metal covered area and the array unit cell ff $= \pi(d/2)^2/a^2$. With increasing fill factor, the peak resonant wavelength shifts to longer wavelengths, and both the transmittance intensity and the peak bandwidth increase.

of a 2D-periodic hole array patterned in a thin metal film:

- The resonant peak wavelength of the hole array structure is mainly determined by the array periodicity a and varies linearly with it. A preliminary calculation of the peak resonant wavelength can be done using the analytical expression in Equation 7.4 and 7.5. The expected periodicity to have a peak resonance at 4.26 µm on AlInSb are 1.07 µm and 1.23 µm for a square-lattice and a triangular-lattice array, respectively.
- For a fixed array periodicity, the resonant wavelength redshifts with increasing hole diameter and blueshifts with increasing metal thickness. Therefore, these two parameters must be taken into account when designing the hole array if the peak transmission needs to be aligned with the spectral response of an active optical device.
- Both the holes fill factor and the metal film thickness have to be chosen considering a trade-off between the intensity of the transmittance and the bandwidth of the resonant peak, which determines the wavelength selectivity of the grating structure.

7.3 Process optimisation for the definition of the Metal Hole Array

The first step towards the implementation of plasmonic hole array patterns on mid-infrared LEDs was the process optimisation for the pattern definition.
The lithography mask was defined by electron-beam lithography (EBL), allowing high resolution and pattern flexibility. The main feature that distinguish EBL from optical lithography is that the user-defined pattern is sequentially transferred onto an e-beam sensitive resist through a raster scan of a collimated electron beam on the surface of the sample. The EBL tool available in the JWNC is a state-of-the-art Vistec VB6-UHR-EWF 100 keV lithography tool [179], which provides 4 nm minimum spot size and 0.5 nm step resolution. A careful mask design was necessary to minimise the writing time of large hole arrays and to guarantee a good circularity of the holes.
Test patterns were fabricated on both GaAs and AlInSb samples in order to evaluate the correct e-beam exposure dose for the pattern definition and the optimal fabrication technique, while taking into account the fabrication constraints for the fabrication of devices on AlInSb, as discussed in Section 3.6.

The first tested fabrication technique was based on the deposition of a uniform gold layer onto a bare sample and its subsequent etch according to the designed hole array pattern. As the available wet etch recipes are based on strong acids that would etch the underlying AlInSb material as well, a dry etch process was tested. The fabrication steps are as follows:

- Metal deposition of a 50 nm-thick Au layer by e-beam evaporation;
- Deposition of a 200 nm-thick SiN layer by Inductively-Coupled Plasma Chemical Vapour Deposition (ICP-CVD) at room temperature;
- Spinning of positive tone e-beam resist PMMA 2010 12% for 60 seconds at 5000 rpm, giving a 550 nm-thick layer;
- E-beam exposure of the designed hole array pattern and development in 2:1 dilution of isoprophyl alcohol (IPA) and methyl isobutyl ketone (MIBK) developer at 23 °C for 45 seconds, followed by two subsequent rinse in IPA for 30 seconds each;
- Pattern transfer into the SiN layer by RIE etch in CHF_3/O_2 plasma at 20 °C for 4 minutes (Oxford Instrument Plasmalab 80 Plus etch tool [180]), followed by the PMMA resist removal in hot acetone;
- Gold etch in Ar plasma in an Oxford Instrument System 100 RIE etch tool [181], using the SiN layer as an hard mask for the pattern transfer.

The process allowed the pattern transfer with high fidelity onto the metal layer, however, due to the strong physical etch process, it resulted in a seriously damaged surface of the soft and brittle AlInSb material, as shown in Figure 7.12a.

An alternative fabrication technique is based on the metal lift-off process described in Section 3.5. Two layers of PMMA positive e-beam resist with different sensitivities are used, in order to achieve an undercut mask profile which allows an easier removal of the undesired metal. As the PMMA is a positive tone resist, the whole area around the holes has to be written by e-beam and pillars of double-layer PMMA resist are left on the surface after the development. This makes the choice of the PMMA layers thickness and the e-beam dose and development time crucial for the successful patterning of the the hole arrays. In fact, as shown in Figure 7.12b and 7.12c, a number of fabrication issues can arise when these parameters are not optimised. If the PMMA layer is too thin or the undercut profile is not pronounced, the deposited metal layer covers the sidewalls of the resist making the lift-off process unsuccessful. On the other hand, if the pattern is over-exposed, as a consequence of too high an exposure dose or too long a development time, the base of the resist pillars is reduced, making them unstable and causing them to fall off before the metal deposition. Additionally, even with optimal resist thickness and exposure dose, the resist removal process in hot acetone requires particular attention,

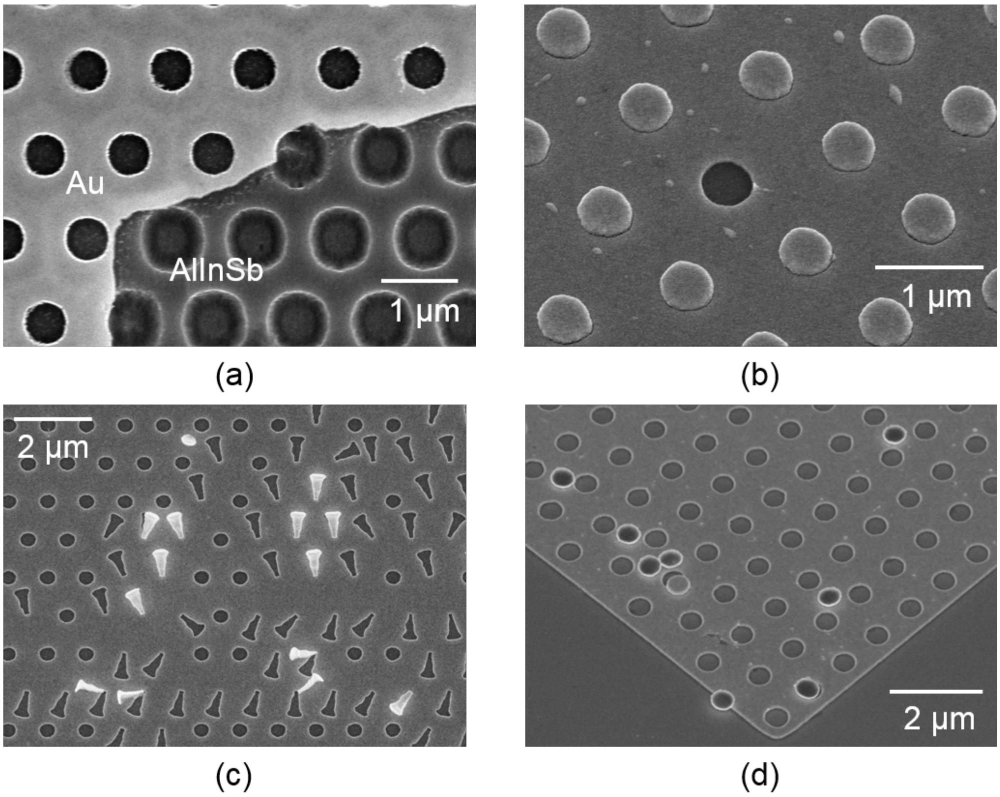

FIGURE 7.12: SEM images of unsuccessful fabrication tests of hole array patterns in thin Au layers on AlInSb: (a) holes etched into the AlInSb material after the Ar-plasma dry etch process for the removal of the unwanted Au; (b) unsuccessful lift-off process caused by the PMMA resist layer being too thin compared to the Au thickness; (c) over-exposed pattern resulting in PMMA mask pillars falling off before the metal deposition and being covered by gold; (d) re-deposition of unwanted Au disks caused by unoptimised lift-off process.

as the unwanted metal can redeposit on the pattern surface as shown in Figure 7.12d. The final developed fabrication process, that allowed the successful and reproducible patterning of metal hole arrays on both GaAs and AlInSb substrates, is described below:

- Spin the first layer of PMMA 2010 12% for 60 seconds at 5000 rpm, which gives a film thickness of about 550 nm;
- Bake on a hotplate for 5 minutes at 145 °C;
- Spin the second layer of PMMA 2041 4% for 60 seconds at 5000 rpm, which gives a film thickness of about 110 nm;
- Bake on a hotplate for 5 minutes at 145 °C;
- E-beam exposure with a dose of 540 μC/μm^2;
- Resist development in 2.5:1 dilution of IPA:MIBK at 23 °C for 45 seconds, followed by two subsequent rinse in IPA for 30 seconds each;

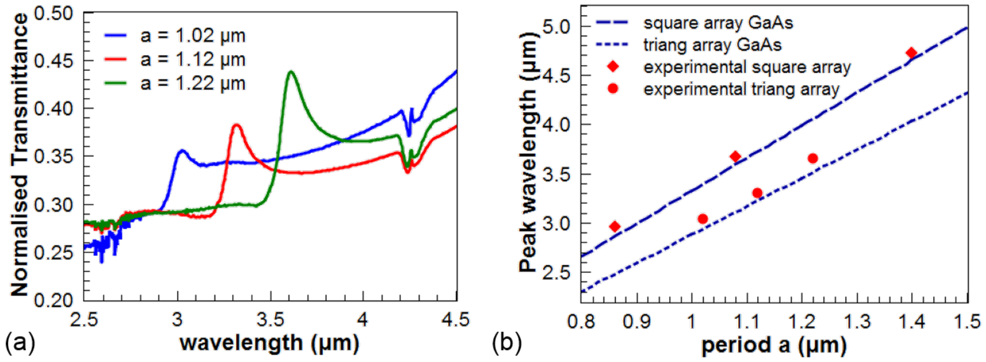

FIGURE 7.13: (a) Measured transmittance spectra of triangular-lattice hole arrays in a 20 nm-thick Au layer on a GaAs substrate. The resonant transmittance peak shifts to longer wavelengths with increasing array period a. The spectra are normalised to that of an unpatterned GaAs sample. (b) Measured and predicted peak transmittance wavelength as a function of the array period.

- Metal deposition by e-beam evaporation of Ti/Au 5 nm/50 nm. The thin layer of Ti is used to improve the adhesion of Au on the semiconductor surface.
- Lift-off in acetone at 50 °C. After the first 10 minutes, ultrasonic agitation is applied for 10 seconds to help the resist release process and the sample is turned face down to avoid redeposition of the unwanted metal. After 3 hours in acetone, the sample is rinsed in IPA and blow dried.

7.4 Characterisation of 2D-periodic Metal Hole Arrays

2D-periodic metal hole array test patterns were fabricated with varying array periods a on a GaAs substrate, transparent in the mid-infrared region. The transmission spectra were measured with a Bruker Vertex 70 FTIR spectrometer, as described in Section 4.2.1. The sample with the test patterns is illuminated perpendicularly by the non-polarised internal broadband Globar source and the transmitted light is collected with a 77 K-cooled InSb detector. To obtain the absolute transmittance, the spectra obtained from the patterned samples are normalised to that of a bare GaAs sample. The measured spectra for triangular-lattice arrays with periods of 1.02 µm, 1.12 µm and 1.22 µm are plotted in Figure 7.13a. The fill factor is designed to be nominally the same for all three patterns, and the hole diameters have been measured from SEM images to be 0.42 µm, 0.48 µm and 0.52 µm, respectively. The measured spectra show a clear transmission peak, shifting to longer wavelengths for larger array period a. The measured resonant wavelengths are 3.04 µm, 3.29 µm and 3.65 µm, respectively, and are in excellent agreement with the values calculated according to Equation 7.5 and confirmed by the FDTD modelling, within a 3 % error in the periodicity of the fabricated array.

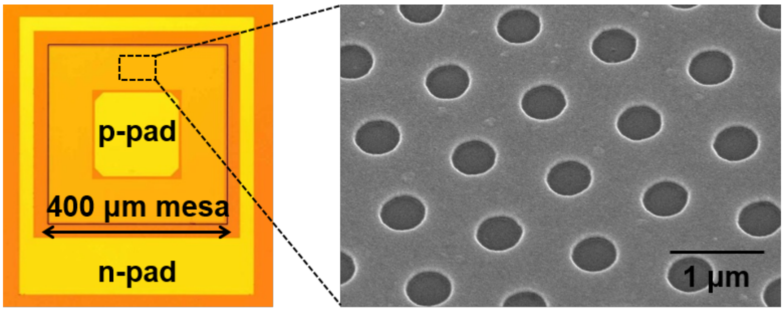

FIGURE 7.14: Optical image of a fabricated 400 µm-wide AlInSb LED with a metal hole array patterned on the top surface of the mesa structure, together with an SEM image of the triangular-lattice hole array.

Figure 7.13b shows the comparison of the measured resonant wavelengths with the theoretical values for both square-lattice and triangular-lattice hole arrays over a wide range of values. This consistency confirms a well controlled fabrication process and provides useful informations for designing plasmonic patterns with transmittance spectra aligned to the operating wavelength of mid-infrared active devices. A peak transmittance value of 45 % is recorded at 3.65 µm. Given that the non-metal covered area is only 22.3 %, this indicates a two-times stronger transmission flux compared to an unpatterned sample, which can be explained with the enhanced field intensity in the proximity of the holes, in good agreement with the modelled transmittance spectra in Figure 7.11 for similar fill factors.

Finally, 2D-periodic metal hole arrays were integrated on AlInSb LEDs. The patterns were defined as the first step on a bare AlInSb sample, according to the process discussed in Section 7.3; then, the LED were fabricated according to the standard process described in Chapter 3. The wafer used for the fabrication is a standard LED structure with a 500 nm p-type contact layer. Figure 7.14 shows an image of a complete device with a plasmonic hole array pattern covering most of the LED top surface free from the ohmic contact.

The results obtained from the transmittance measurements, validated by the FDTD modelling of a 2D-periodic metal hole array with an incident plane wave, can be considered a representative indication of the spectral response of a plasmonic-enhanced photodiode, when illuminated by a broadband source in the direction normal to the surface. For this reason, the effect of the metal hole array on the LED photocurrent signal was first evaluated. A device, with a triangular array of period $a = 1.07$ µm and hole diameter $d = 0.47$ µm, was illuminated by a Globar broadband source and the photocurrent was measured by an FTIR spectrometer. The photocurrent spectrum is plotted in Figure 7.15 and clearly shows the optical filtering effect of the patterned metal hole array, with a 30 % reduction of the spectral response when compared to a reference unpatterned device. The photocurrent peak wavelength is in good agreement with

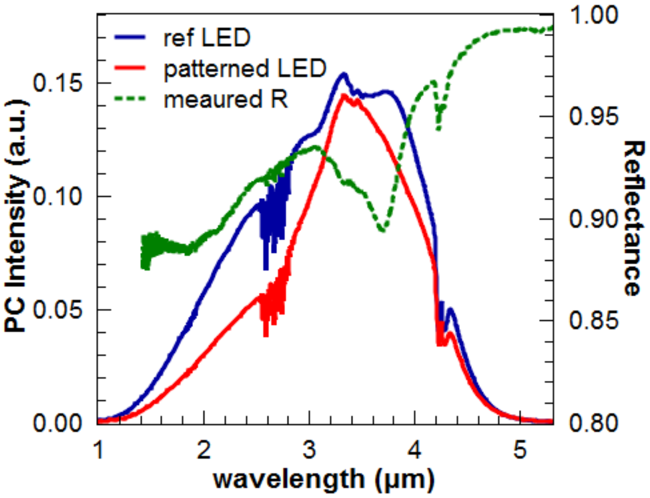

FIGURE 7.15: Measured photocurrent (PC) spectrum from an AlInSb LED, with a triangular-lattice metal hole array patterned on the top surface, when illuminated by a Globar broadband source. Compared to a reference LED, the patterned LED has a 30 % narrower bandwidth, showing the optical filtering effect of the metal hole array. The wavelength of the peak photocurrent intensity is in good agreement with the resonant wavelength expected from a triangular-lattice array of period $a = 1.07\,\mu\text{m}$, of which the measured reflectance spectrum is plotted on the right axis.

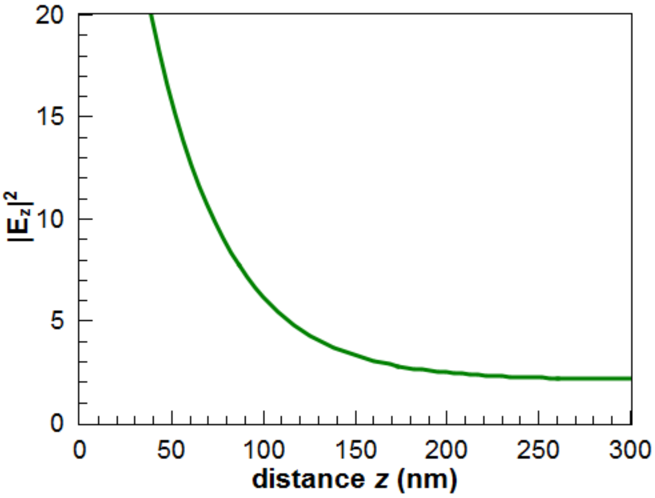

FIGURE 7.16: Simulated electric field intensity along the z direction $|E|^2$, with strong enhancement limited to 200 nm from the metal-semiconductor interface.

the reflectance spectrum of the metal hole array measured on the same device, which is shown as well in Figure 7.15 for comparison. However, no absolute spectral enhancement is observed from the device with the patterned metal hole array. This was attributed to the poor spatial matching between the LED active region and the region of field enhancement associated with the plasmonic mode at the interface with the patterned metal layer. The FDTD simulation of the electric field distribution in the proximity of the holes confirmed that the intensity in the z direction decreases exponentially with the distance from the interface, as plotted in Figure 7.16, showing that the region of strong field enhancement is limited to the first 200 nm from the metal-semiconductor interface. Therefore, the location of the device active region is essential for the efficient coupling to and from the exponential tail of the plasmonic mode. To overcome the poor spatial matching, a new wafer was designed with a p-doped contact layer only 150 nm thick. In order to compensate for the reduced thickness and avoid prohibitively high sheet resistance of the p-type contact layer, which will significantly affect the current spreading across the device area, the doping concentration was increased to $3 \times 10^{18}\,\mathrm{cm}^{-3}$. The fabrication of plasmonic patterned LED on the new wafer is currently ongoing and is expected to show a more pronounced enhancement of the spectral response at the resonant wavelength of the metallic hole array.

In case of a LED device, the optimisation of a 2D-periodic metal hole array for enhanced emission is more challenging because the photons are emitted isotropically within the device active region and, therefore, impinge on the semiconductor-interface within a range of incident angles. As a consequence, the momentum matching condition discussed in Equation 7.3 occurs for shorter wavelengths, making the patterns optimised for transmittance at normal incidence ineffective for the LED light extraction. The electroluminescence (EL) spectra from the patterned LEDs were measured at room temperature with an FTIR spectrometer as described in Section 4.2.2. The devices were biased with a square modulated signal at 10 kHz, 10 % duty cycle and 100 mA peak current. The measured spectrum from an LED with a square array of period $a = 1.07\,\mu\mathrm{m}$ and hole diameter $d = 0.47\,\mu\mathrm{m}$ is plotted in Figure 7.17, showing only marginal spectral narrowing and emission enhancement at 4.26 µm compared to a reference unpatterned LED. Despite this, it is worth noting that the majority of the top surface of the LED is covered by the metal hole array, as shown in Figure 7.14, which has a fill factor of only 16 %, suggesting a contribution from the EOT through the metal hole array.

A 3D FDTD simulation was set up to evaluate the theoretical extraction efficiency of the measured structure. The LED isotropic emission was modelled by performing a set of simulations with a dipole source swept through different locations and orientations with respect to the array square lattice [11, 182]. As large simulation volumes and a fine mesh in the z direction are required, the lateral area of the simulation domain was mainly determined by the computational time. The extraction efficiency was calculated from the power flux extracted from the structure in the vertical direction with respect to the overall power emitted from the source. The extraction efficiency enhancement as a function of wavelength is calculated by averaging the results for each dipole orientation and location, and dividing it by the results for a non-patterned LED. The modelled extraction efficiency enhancement for a square-lattice metal hole array with period $a = 1.07\,\mu\mathrm{m}$ on AlInSb is plotted in Figure 7.18, showing that the peak enhancement is found at significantly shorter wavelengths ($\lambda_{peak} \approx 3.7\,\mu\mathrm{m}$) and that

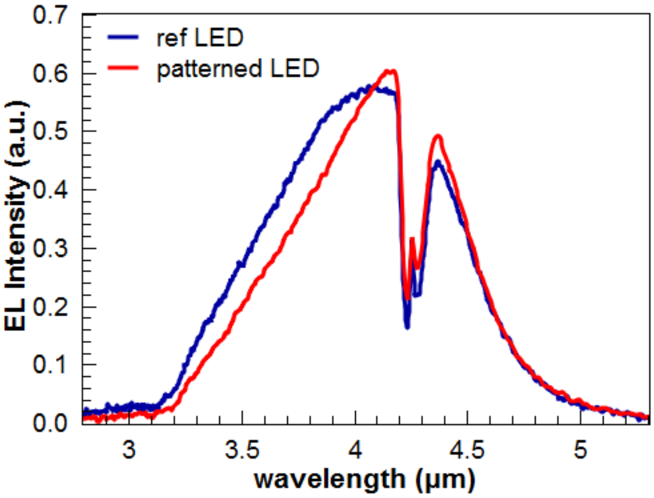

Figure 7.17: Measured electroluminescence (EL) spectrum of an AlInSb LED with a square-lattice metal hole array patterned on the top surface. The array period is $a = 1.07\,\mu\text{m}$, which is expected to give a resonant wavelength of $4.26\,\mu\text{m}$ according to Equation 7.4. Compared to a reference LED, the patterned LED shows only marginal emission enhancement and spectral narrowing.

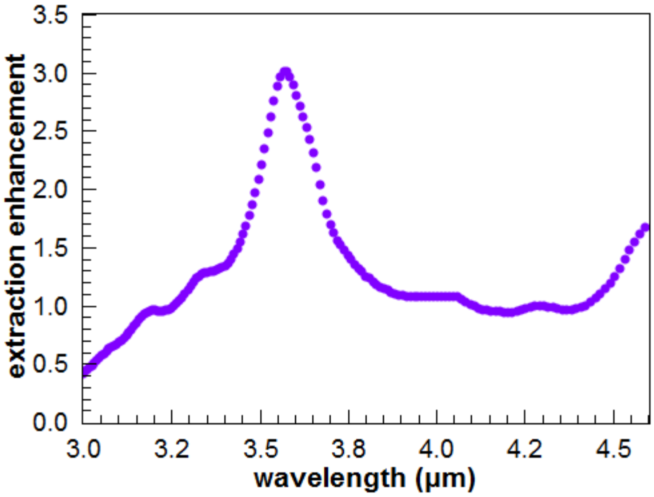

Figure 7.18: Simulated extraction emission enhancement for an AlInSb LED patterned with a square-lattice metal hole array of period $a = 1.07\,\mu\text{m}$. The peak enhancement is shifted to shorter wavelengths due to the range of incident angles of the LED isotropically emitted photons.

no enhancement is predicted at 4.26 μm. Figure 7.19 illustrates the amplitude of the transmitted electric field in the x-y plane at the wavelength of maximum enhancement, in case of both a bare AlInSb substrate and a square-lattice metal hole array.

The results of these simulations suggest that the array needs to be designed with a longer periodicity in order to obtain the predicted extraction efficiency enhancement at the target wavelength of 4.26 μm. Ultimately, an optimal array pattern could be designed with a pseudo-random distribution of array periodicity to enhance the coupling of photons emitted in a wide range of incident angles.

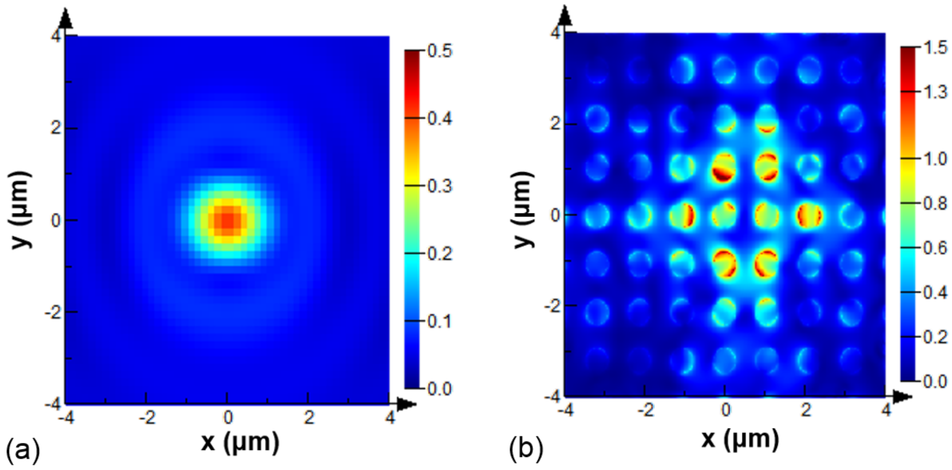

FIGURE 7.19: FDTD simulation results of the transmitted electric field in the x-y plane at the wavelength of maximum enhancement in case of (a) a bare AlInSb substrate and (b) a patterned substrate with a square-lattice metal hole array of period $a = 1.07\,\mu\text{m}$. The source is an electric dipole polarised along the x axis.

In conclusion, the integration of 2D-periodic metal hole arrays on mid-infrared active optical devices is a promising approach for the enhancement of light coupling and extraction. This technique is of particular interest at mid-infrared wavelengths, were the feature sizes and geometrical constrains for an efficient coupling design are relaxed compared to visible wavelengths. A fabrication process based on electron-beam lithography and metal lift-off was developed for the pattern definition, giving well controlled results. The analysis of the geometrical design parameters and their effect on the spectral response of the periodically patterned metal thin films was performed by Finite-Difference Time-Domain (FDTD) modelling and good agreement was found between the simulated response and the measured transmittance spectra of the fabricated patterns. The integration of 2D-periodic metal hole arrays on AlInSb LEDs confirmed their optical filtering properties, which can be beneficial for the wavelength selectivity of the target gas absorption line. However, a significant absolute absorption/emission enhancement was not observed from the patterned devices. The implementation of an optimised design with a thinner p-type contact layer and a detuned array periodicity is expected to give a stronger enhancement of the spectral performance of mid-infrared AlInSb LEDs.

Chapter 8

Conclusions and Future work

Antimonide-based light-emitting diodes (LEDs) with efficient emission in the 3–5 µm mid-infrared spectral range are a valuable technology to improve the performance of optical gas sensor. In fact, the replacement of thermal components in conventional infrared optical sensors with high performance semiconductor-based LEDs and photodiodes offers substantial advantages in terms of power consumption, response time and wavelength selectivity. The factors that still limit the performance of LEDs emitting in the mid-infrared wavelength range are the low internal efficiency, related to the dominant non-radiative recombination mechanisms in narrow bandgap semiconductors, and the ineffective out-coupling of photons generated within the high refractive index material, which sets the extraction efficiency to about 1 %.

AlInSb-based p-i-n diode heterostructures, with a thin barrier of wider bandgap material to confine the carriers in the active region and reduce the thermally generated carriers, allow room temperature operation of LEDs and photodiodes in the 3–5 µm mid-infrared spectral range. These devices are employed by Gas Sensing Solutions Ltd. in their commercial optical gas sensors for the detection of CO_2 concentration. The AlInSb LEDs have an emission spectrum centred at 4.26 µm, aligned with the CO_2 absorption lines, with a total emitted power of 6 µW and an external quantum efficiency of 3×10^{-5}.

The main objective of this project was to improve the performance of the AlInSb LEDs, achieving a higher optical output power at the target wavelength of 4.26 µm, while maintaining a low electrical input power, essential requirement for applications in portable and autonomous CO_2 optical gas sensors. For this purpose, three main approaches were investigated:

- the improvement of the diode epi-layer structure for enhanced electrical and optical performance;

- the optimisation of the LED device geometry design to achieve a uniform distribution of the bias current which leads to an efficient use of the device area for light generation;
- the integration of techniques for overcoming the intrinsic low extraction efficiency from high index semiconductor material through optical scattering, interference and resonance effects.

The direct involvement of the industrial partners in the project was fundamental to ensure that the prototype devices met the application requirements from an early stage of the research.

The main contributions of this research towards the implementation of efficient room temperature operation of mid-infrared AlInSb LEDs are highlighted in the following:

Fabrication Development. A robust and repeatable fabrication process was developed based on standard III-V semiconductor materials processing techniques, while keeping in mind the constraints related to the handling of the particularly soft and brittle AlInSb material and the relatively low temperature budget of 120–150 °C to avoid surface degradation of the processed material. A citric acid/hydrogen peroxide based wet etch recipe was characterised and optimised to achieve a reliable process characterised by:

- an etch rate of about 20 nm/min that allows a reasonable etching time for the thick epi-layer structure;
- a sloped sidewall profile suitable for subsequent fabrication steps, including passivation and metal deposition;
- a minimum selectivity to aluminium composition, to avoid re-entrant profiles at the wider bandgap barrier.

Additionally, an ICP-RIE dry etch process based on $CH_4/H_2/O_2$ plasma was investigated with promising result. An etch rate of 50 nm/min, with a smooth surface morphology and vertical sidewalls were achieved while maintaining the sample temperature below 120 °C.
Ti/Au ohmic contacts with low specific contact resistance (in the order of $1 \times 10^{-6}\,\Omega\,\mathrm{cm}^2$) were characterised on both p-type and n-type AlInSb material as a function of the doping concentration in the contact layers. The established processing guarantees repeatable electrical and optical performance of the fabricated LED devices.

Epi-layer Optimisation. Key understanding was gained on how different design parameters affects the LED electrical and optical performance. In particular, an increase of the doping concentration in the contact layers to $1 \times 10^{18}\,\mathrm{cm^{-3}}$ translated into a 1.5 times stronger emission intensity at 4.26 µm, as a result of:

- lower sheet resistance of the top p-type contact layer that has a positive effect of the bias current spreading;
- lower series resistance , which reduces the Joule heating and the associated non-radiative recombination mechanisms.

Additionally, the reduction of the active region thickness from 1 µm to 200 nm resulted in no degradation of the electrical and optical performance of the LED, while proving beneficial for the design of resonant-cavity LEDs. Moreover, the n-type contact layer was reduced from 3–3.5 µm to 2 µm. This thickness still guarantees the relaxation of the epi-grown AlInSb material to an acceptable level, as no significant variation of the surface morphology and of the LED electrical performance were observed, while significantly reducing both the growth and the etching time for production devices.

Current Crowding. Experimental results show that the current crowding effect around the top electrode can represent a significant performance limitation for top-emitting long wavelength LEDs operating at room temperature. This effects is due to the lateral injection geometry and the relatively high resistance of the p-type doped contact layer, and needs to be properly addressed when designing efficient devices. LEDs in a range of sizes and with variable electrode patterns were characterised, and the current crowding effect was demonstrated to be particularly severe for large area devices at high injection current levels. Therefore, the reduction of the LED mesa lateral dimension to 200 µm resulted in devices with a more uniform current spreading and higher emission intensity under the same electrical bias conditions. At the same time, spatial photocurrent measurements were performed to confirm the current density distribution profiles and allowed the design of an improved top-contact grid geometry that leads to a more uniform current spreading across the device area and allows a factor of three improvement of the emitted intensity from LEDs with 800 µm mesa width.

Resonant-Cavity LEDs. A Resonant-Cavity LED structure was designed and implemented with the integration of a lattice-matched $\mathrm{AlSb/Ga_{0.9}In_{0.1}Sb}$ Distributed Bragg Reflector between the substrate and the LED active layers. The resonant-cavity design is a particularly effective geometry for overcoming the low extraction efficiency of high index semiconductor LEDs. The advantage of this geometry, in fact, is twofold: the distributed Bragg reflector helps redirecting the isotropically-emitted photons towards the top surface of the device, while the cavity design adds a resonant effect that enhances the light emission at the designed resonant wavelengths. A solid methodology was implemented for the modelling of the structure spectral response and iterative designs and growth runs allowed to optimise the active region position within the cavity and the DBR mirror alignment. This resulted in the successful implementation of RC-LEDs with breakthrough performance improvement over non-resonant AlInSb LEDs, the main features being:

- A three-times enhanced emission intensity at the target wavelength of 4.26 µm;
- A five-times reduction of the full-width half-maximum of the emission spectrum compared to a non-resonant LED. The emission linewidth is determined by the cavity quality factor and can be designed to match the target CO_2 absorption line, with substantially improved noise performance of the gas sensor;
- A ten-times improved peak emission wavelength stability that guarantees high sensitivity to CO_2 across a wide range of operating temperatures.

Plasmonic-enhanced LEDs. Finally, the integration of 2D-periodic metallic hole arrays was investigated as a promising approach for the enhancement of optical extraction from AlInSb LEDs. A fabrication process based on electron-beam lithography and metal lift-off was developed for the pattern transfer on GaAs and AlInSb substrates, with well controllable and repeatable results. The effect of the geometrical design parameters of the metal hole arrays were analysed by Finite-Difference Time-Domain (FDTD) modelling and good agreement was found between the simulated response and the measured transmittance spectra of the fabricated patterns. The integration of 2D-periodic metal hole arrays on AlInSb LEDs confirmed their optical filtering properties, which can represent a significant advantage for both LEDs and photodiodes for optical gas sensing, as the spectral response can be tuned and shaped by changing the metal hole array geometrical parameters. An optimised design with a thinner p-type contact layer and a detuned array periodicity is currently under investigation to achieve a better spectral and spatial matching between the plasmonic mode and the LED active region. This would result in an enhanced optical emission intensity at the resonant wavelength, thanks to a more efficient extraction of the photons emitted above the critical angle.

The optimisation approaches and techniques developed during this work through device modelling and prototyping were transferred by the industrial partners to production devices to be tested in their final gas sensor configuration. LEDs with $1 \times 10^{18}\,\mathrm{cm}^{-3}$ doping concentration and 200 µm mesa width have already been implemented in production devices by Gas Sensing Solutions Ltd. proving excellent performance, with 2-times stronger emitted power and 50 % reduced noise across the whole temperature range of operation. Research is currently ongoing to finalise a suitable design for the transfer of the RC-LEDs configuration to mass production. The advantaged of RC-LEDs in terms of enhanced intensity at 4.26 µm, spectral narrowing of the emission spectrum and improved temperature stability can represent a disruptive progress in the performance of CO_2 optical gas sensors. This would allow Gas Sensing Solutions to expand their current market and exploit different applications that require high resolution and low noise devices.

Undoubtedly, this research project has opened up different options that can be further explored for the development of efficient AlInSb LEDs. The research activity is still ongoing, with the employment of a new Ph.D. student who will continue the current research activity. Additional funding opportunities are also being evaluated together with Gas Sensing Solutions to explore novel device geometries. The main aspects that are currently investigated and will be subject of future research activities include:

- The integration of a double heterostructure and multiple quantum wells in the LED active region to achieve higher carrier confinement and injection efficiency. The research activity is currently in progress and preliminary results have confirmed numerical simulation by showing a three-times improved emission intensity from devices with seven repetitions of $\mathrm{Ga_xIn_{1-x}Sb/Al_yGa_zIn_{1-y-z}Sb}$ quantum wells. However, further investigation is necessary to reduce the high LED series resistance and make this devices compatible for mass production.
- An optimised resonant-cavity design for an LED emitting through the substrate, which can potentially result in more than 10 times enhanced emission intensity of the designed resonant wavelength.
- The extension of the resonant-cavity LED design to other mid-infrared wavelengths. The current design, optimised for the detection of CO_2 at 4.26 µm, can be modified to give maximum emission at different wavelengths in the mid-infrared range by adjusting the aluminium composition of the LED active layers and the thickness of the DBR mirror layers. Successful results have already been achieved at 3.3 µm for CH_4 detection. Other particularly interesting wavelengths are 4.6 µm and 5.3 µm, where CO and NO have their main absorption lines, respectively.
- The further investigation of the integration of plasmonic metallic hole arrays on the top surface of mid-infrared LEDs to better understand their contribution to extraction light enhancement.
- The implementation of the investigated techniques to AlInSb-based photodiodes. In fact, similar considerations in terms of current spreading and coupling of incident radiation can be applied to the photodiode, which will benefit from an optimised

contact geometry and a resonant-cavity design for enhanced response and wavelength selectivity. This would translate into a further performance enhancement when the whole LED-photodiodes system is considered.

Bibliography

[1] J. Hodgkinson and R. P. Tatam. Optical gas sensing: a review. *IOP Publishing Measurement Science and Technology*, 72(24):4477–4479.

[2] A. Krier, M. Yin, V. Smirnov, P. Batty, P. J. Carrington, V. Solovev, and V. Sherstnev. The development of room temperature LEDs and lasers for the mid-infrared spectral range. *Physica Status Solidi (a)*, 205(1). ISSN 1862-6319.

[3] C. N. Banwell. *Fundamentals of Molecular Spectroscopy.* McGrawHill, 1983.

[4] P. T. Moseley and J. O. W. Norris. *Techniques and mechanisms in gas sensing.* Adam Hilger, 1991.

[5] E. Bakker and M. Telting-Diaz. Electrochemical Sensors. *Analytical Chemistry*, 74(12):2781–2800, 2002. doi: 10.1021/ac0202278.

[6] J. D. Ingle and S. R. Crouch. *Spectrochemical Analysis.* Prentice Hall, London, 1988.

[7] Technical specification, IRC-A1 carbon dioxide infrared sensor. Technical report, Great Notley, UK.

[8] Jane Hodgkinson, Richard Smith, Wah On Ho, John R. Saffell, and Ralph P. Tatam. Non-dispersive infra-red (NDIR) measurement of carbon dioxide at 4.2 µm in a compact and optically efficient sensor. *Sensors and Actuators B: Chemical*, 186:580 – 588, 2013. ISSN 0925-4005. doi: http://dx.doi.org/10.1016/j.snb.2013.06.006.

[9] W. T. Welfors and R. Winston. *High Collection Nonimaging Optics.* Academic Press, 1989.

[10] J. G. Crowder, S. D. Smith, A. Vass, and J. Keddie. Infrared Methods for Gas Detection. In A. Krier, editor, *Mid-infrared Semiconductor Optoelectronics.* Springer, 2006.

[11] Christopher Wiesmann. Nano-structured LEDs: Light extraction mechanisms and applications, July 2010. URL `http://epub.uni-regensburg.de/14117/`.

[12] S. D. Smith, H. R. Hardaway, and J. G. Crowder. Recent developments in the applications of mid-infrared lasers, LEDs, and other solid state sources to gas detection. volume 4651, pages 157–172, 2002. doi: 10.1117/12.467944.

[13] D. MacIsaac, G. Kanner, and G. Anderson. Basic physics of the incandescent lamp (lightbulb). *The Physics Teacher*, 37(9):520–525, 1999.

[14] J. Spannhake, O. Schulz, A. Helwig, G. Miiller, and T. Doll. Design, development and operational concept of an advanced MEMS IR source for miniaturized gas sensor systems. In *Sensors, 2005 IEEE*, 2005.

[15] Pierre Barritault, Mickael Brun, Olivier Lartigue, Jrme Willemin, Jean-Louis Ouvrier-Buffet, Stphane Pocas, and Sergio Nicoletti. Low power CO_2 NDIR sensing using a micro-bolometer detector and a micro-hotplate IR-source. *Sensors and Actuators B: Chemical*, 182(0):565 – 570, 2013. ISSN 0925-4005. doi: http://dx.doi.org/10.1016/j.snb.2013.03.048.

[16] D. L. C. Chan, M. Soljačić, and J. D. Joannopoulos. Thermal emission and design in 2D-periodic metallic photonic crystal slabs. *Opt. Express*, 14(19):8785–8796.

[17] I. Puscasu, M. Pralle, M. McNeal, J. Daly, A. Greenwald, E. Johnson, R. Biswas, and C. G. Ding. Extraordinary emission from two-dimensional plasmonic-photonic crystals. *Journal of Applied Physics*, 98(1):013531, 2005.

[18] M. P. McNeal, N. Moelders, M. U. Pralle, I. Puscasu, L. Last, W. Ho, A. C. Greenwald, J. T. Daly, E. A. Johnson, and T. George. Development of optical MEMS CO_2 sensors. volume 4815, pages 30–35, 2002. doi: 10.1117/12.482316.

[19] S. E. Alexandrov, G. A. Gavrilov, A. A. Kapralov, S. A. Karandashev, B. A. Matveev, G. Y. Sotnikova, and N. M. Stus'. Portable optoelectronic gas sensors operating in the mid-IR spectral range. volume 4680, pages 188–194, 2002. doi: 10.1117/12.454676.

[20] A. Krier, X. L. Huang, and V. V. Sherstnev. Mid-infrared Electroluminescence in LEDs based on InAs and related alloys. In A. Krier, editor, *Mid-infrared Semiconductor Optoelectronics*. Springer, 2006.

[21] M. K. Haigh, G. R. Nash, S. J. Smith, L. Buckle, M. T. Emeny, and T. Ashley. Mid-infrared $Al_xIn_{1-x}Sb$ light-emitting diodes. *Applied Physics Letters*, 90(23): 231116, 2007.

[22] C. Wiesmann, K. Bergenek, N. Linder, and U.T. Schwarz. Photonic crystal LEDs - designing light extraction. *Laser and Photonics Reviews*, 3(3). ISSN 1863-8899.

[23] J. G. Crowder, H. R. Hardaway, and C. T. Elliott. Mid-infrared gas detection using optically immersed, room-temperature, semiconductor devices. *Measurement Science and Technology*, 13(6):882.

[24] Tim Ashley, David T. Dutton, Charles T. Elliott, Neil T. Gordon, and T. J. Phillips. Optical concentrators for light-emitting diodes. volume 3289, pages 43–50, 1998. doi: 10.1117/12.305488.

[25] I. Schnitzer, E. Yablonovitch, C. Caneau, T. J. Gmitter, and A. Scherer. 30% external quantum efficiency from surface textured, thin-film light-emitting diodes. *Applied Physics Letters*, 63(16), 1993.

[26] E Hadji, J Bleuse, N Magnea, and J.L Pautrat. Resonant cavity light emitting diodes for the 3–5 µm range. *Solid-State Electronics*, 40(18):473 – 476, 1996. ISSN 0038-1101. doi: http://dx.doi.org/10.1016/0038-1101(95)00313-4. Proceedings of the Seventh International Conference on Modulated Semiconductor Structures.

[27] A. M. Green, D. G. Gevaux, C. Roberts, and C. C. Phillips. Resonant-cavity-enhanced photodetectors and LEDs in the mid-infrared. *Physica E: Low-dimensional Systems and Nanostructures*, 20(34):531 – 535, 2004. ISSN 1386-9477. doi: http://dx.doi.org/10.1016/j.physe.2003.09.004. Proceedings of the 11th International Conference on Narrow Gap Semiconductors.

[28] D. Gevaux, A. Green, C. Palmer, P. Stavrinou, C. Roberts, and C. Phillips. Resonant-cavity light-emitting diodes (RC-LEDs) and detectors for mid-IR gas-sensing applications. *IEE Proceedings - Optoelectronics*, 150, 2003. ISSN 1350-2433.

[29] I. J. Buss, G. R. Nash, J. G. Rarity, and M. J. Cryan. Finite-Difference Time-Domain Modeling of Periodic and Disordered Surface Gratings in AlInSb Light Emitting Diodes With Metallic Back-Reflectors. *Lightwave Technology, Journal of*, 28(8):1190–1200, April 2010. ISSN 0733-8724. doi: 10.1109/JLT.2010.2040803.

[30] Chandler Downs and Thomas E. Vandervelde. Progress in Infrared Photodetectors Since 2000. *Sensors*, 13(4):5054–5098, 2013.

[31] Characteristcs and use of infrared detectors. Technical report. URL `https://www.hamamatsu.com/resources/pdf/ssd/infrared_techinfo_e.pdf`.

[32] T. Ashley, C. T. Elliott, and A. T. Harker. Non-equilibrium modes of operation for infrared detectors. *Infrared Physics*, 26(5):303 – 315, 1986. ISSN 0020-0891. doi: http://dx.doi.org/10.1016/0020-0891(86)90008-4.

[33] J. G. Crowder, C. T. Elliott, and H. R. Hardaway. High performance, large area, uncooled detectors for mid-infrared wavelengths. *Electronics Letters*, 37(2):116–118, Jan 2001. ISSN 0013-5194. doi: 10.1049/el:20010072.

[34] D. J. Hall, L. Buckle, N. T. Gordon, J. Giess, J. E. Hails, J. W. Cairns, R. M. Lawrence, A. Graham, R. S. Hall, C. Maltby, and T. Ashley. High-performance long-wavelength HgCdTe infrared detectors grown on silicon substrates. *Applied Physics Letters*, 2004.

[35] Directive 2002/91/EC of the European Parliament and of the Council. Energy performance of buildings. Technical report, 2002.

[36] W. Rhodes. The EMEA and Americas Markets for Building Automation Controllers, Software and Sensors Market Research Report. Technical report, IMS Research. Wellingborough, UK, 2011.

[37] J. R. Sand. Demand-Controlled Ventilation Using CO_2 Sensors. Technical report, United States Department of Energy, Energy Efficiency and Renewable Energy, Federal Energy Management Program, 2004.

[38] US Dept of Energy. Energy Review 2009 DOE/ IEA/-0384. Technical report.

[39] N. Stafford. Future crops: The other greenhouse effect. *Nature*, 448:14–18, 2006. doi: 10.1038/448526a.

[40] R. Frodle and T. Tille. A high precision NDIR CO2 gas sensor for automotive applications. *IEEE Sens. J.*, 6:1697–1705, 2006.

[41] L Radwan. Infrared CO_2 analysis in expired air as a test of the pulmonary function. I. Evaluation of the capnographic curve. *Polish medical journal*, 6(2):403411, 1967. ISSN 0032-2938.

[42] J Zosel, W Oelner, M Decker, G Gerlach, and U Guth. The measurement of dissolved and gaseous carbon dioxide concentration. *Measurement Science and Technology*, 22(7):072001.

[43] T. Sashida, T. Saitou, and M. Egawa. Development of a carbon dioxide concentration meter using a solid electrolyte sensor. In *SICE 2002. Proceedings of the 41st SICE Annual Conference*, volume 1, pages 590–593 vol.1, Aug 2002. doi: 10.1109/SICE.2002.1195474.

[44] D R Gibson and C MacGregor. Self Powered Non-Dispersive Infra-Red CO_2 Gas Sensor. *Journal of Physics: Conference Series*, 307(1):012057.

[45] S.D. Smith, A. Vass, P. Bramley, J.G. Crowder, and C.H. Wang. Comparison of IR LED gas sensors with thermal source products. *Optoelectronics, IEE Proceedings* -, 144(5):266–270, Oct 1997. ISSN 1350-2433. doi: 10.1049/ip-opt:19971510.

[46] Desmond Gibson and Calum MacGregor. A Novel Solid State Non-Dispersive Infrared CO_2 Gas Sensor Compatible with Wireless and Portable Deployment. *Sensors*, 13(6):7079–7103, 2013.

[47] Gas Sensing Solutions Ltd., . URL `http://www.gassensing.co.uk/`.

[48] EnOcean Gmbh. Application Note AN313, Design concept for solar-powered CO_2 sensor. Technical report, 2011. URL `http://www.enocean.com/en/application-notes/ANS313`.

[49] A.A. Popov, V.V. Sherstnev, Y.P. Yakovlev, A.N. Baranov, and C. Alibert. Powerful mid-infrared light emitting diodes for pollution monitoring. *Electronics Letters*, 33(1):86–88, Jan 1997. ISSN 0013-5194. doi: 10.1049/el:19970002.

[50] T. Ashley, Elliott C. T., Gordon N. T., Hall R. S., Johnson A. D., and Pryce G. J. Uncooled InSb/$In_{1-x}Al_xSb$ mid-infrared emitter. *Applied Physics Letters*, 64 (18):2433, 1994.

[51] M. J. Pullin, H. R. Hardaway, J. D. Heber, C. C. Phillips, W. T. Yuen, R. A. Stradling, and P. Moeck. Room-temperature InAsSb strained-layer superlattice light-emitting diodes at $\lambda = 4.2\,\mu m$ with AlSb barriers for improved carrier confinement. *Applied Physics Letters*, 74(16), 1999.

[52] GR Nash, MK Haigh, HR Hardaway, L Buckle, AD Andreev, NT Gordon, SJ Smith, MT Emeny, and T Ashley. InSb/AlInSb quantum-well light-emitting diodes. *Applied Physics Letters*, 88(5), 2006.

[53] Wayne Lo and Don E. Swets. Room-temperature 4.6 µm light emitting diodes. *Applied Physics Letters*, 36(6), 1980.

[54] Fritz Weik, Gnter Steinmeyer, Jens W. Tomm, Regine Glatthaar, Uwe Vetter, Joachim Nurnus, and Armin Lambrecht. A room-temperature continuous-wave operating midinfrared light emitting device. *Journal of Applied Physics*, 99(11): 114506, 2006.

[55] Maurus Tacke. Lead-salt lasers. *Philosophical Transactions of the Royal Society of London A: Mathematical, Physical and Engineering Sciences*, 359(1780):547–566, 2001. ISSN 1364-503X. doi: 10.1098/rsta.2000.0742.

[56] P. Bouchut, G. Destefanis, J. P. Chamonal, A. Million, B. Pelliciari, and J. Piaguet. High-efficiency infrared light emitting diodes made in liquid phase epitaxy and molecular beam epitaxy HgCdTe layers. *Journal of Vacuum Science and Technology B*, 9(3), 1991.

[57] D.G. Gevaux, A.M. Green, C.C. Phillips, I. Vurgaftman, W.W. Bewley, C.L. Felix, J.R. Meyer, H. Lee, and R.U. Martinelli. 3.3 µm W quantum well light emitting diode. *Optoelectronics, IEE Proceedings* -, 150(4):351–355, Aug 2003. ISSN 1350-2433. doi: 10.1049/ip-opt:20030789.

[58] Boris A. Matveev, Nonna V. Zotova, Sergey A. Karandashev, Maxim A. Remennyi, Nikolai M. Stus', and Georgii N. Talalakin. III-V optically pumped mid-IR LEDs. volume 4278, pages 189–196, 2001. doi: 10.1117/12.426851.

[59] A Krier, V V Sherstnev, A Krier, and H H Gao. A novel LED module for the detection of H_2S at 3.8 µm. *Journal of Physics D: Applied Physics*, 33(14):1656, 2000.

[60] A Krier, H H Gao, V V Sherstnev, and Y Yakovlev. High power 4.6 µm light emitting diodes for CO detection. *Journal of Physics D: Applied Physics*, 32(24): 3117, 1999.

[61] A. Krier, M. Stone, Q. D. Zhuang, Po-Wei Liu, G. Tsai, and H. H. Lin. Mid-infrared electroluminescence at room temperature from InAsSb multi-quantum-well light-emitting diodes. *Applied Physics Letters*, 89(9):091110, 2006.

[62] B. I. Mirza, G. R. Nash, S. J. Smith, L. Buckle, S. D. Coomber, M. T. Emeny, and T. Ashley. Recombination processes in midinfrared $\mathrm{Al_xIn_{1-x}Sb}$ light-emitting diodes. *Journal of Applied Physics*, 104(6):063113, 2008.

[63] E. Fred. Schubert. *Light Emitting Diodes.* Cambridge Press, 2006.

[64] W. Shockley and W. T. Read. Statistics of the recombinations of holes and electrons. *Phys. Rev.*, 87:835–842, Sep 1952. doi: 10.1103/PhysRev.87.835.

[65] A. R. Beattie and P. T. Landsberg. Auger effect in semiconductors. *Proceedings of the Royal Society of London. Series A, Mathematical and Physical Sciences*, 249 (1256):pp. 16–29.

[66] Zoran Jakšić. *Micro and Nanophotonics for Semiconductor Infrared Detectors: Towards an Ultimate Uncooled Device.* Springer, 2014.

[67] A. R. Beattie and G. Smith. Recombination in Semiconductors by a Light Hole Auger Transition. *physica status solidi (b)*, 19(2). ISSN 1521-3951.

[68] NSM Archive - Physical Properties of Semiconductors. Ioffe Institute. URL `http://www.ioffe.rssi.ru/SVA/NSM/Semicond/`.

[69] Enhancement of light extraction from light emitting diodes. *Physics Reports*, 498 (45):189 – 241, 2011. ISSN 0370-1573. doi: http://dx.doi.org/10.1016/j.physrep.2010.11.001.

[70] Band structure of Indium Antimonide. *Journal of Physics and Chemistry of Solids*, 1(4):249 – 261, 1957. ISSN 0022-3697. doi: http://dx.doi.org/10.1016/0022-3697(57)90013-6.

[71] A R Beattie, P Scharoch, and R A Abram. Impact ionisation threshold energy surfaces for anisotropic band structures in semiconductors. *Semiconductor Science and Technology*, 4(9):715.

[72] M. Carroll, P. Blood, T. Ashley, and C.T. Elliott. Effect of intervalence band absorption on the refractive index of p-doped InSb. *Optoelectronics, IEE Proceedings -*, 147(3):157–162, Jun 2000. ISSN 1350-2433. doi: 10.1049/ip-opt:20000280.

[73] T. Ashley, A. B. Dean, C. T. Elliott, C. F. McConville, G. J. Pryce, and C. R. Whitehouse. Ambient temperature diodes and field-effect transistors in InSb/$\mathrm{In_{1-x}Al_xSb}$. *Applied Physics Letters*, 59(14), 1991.

[74] T Ashley and C T Elliott. Operation and properties of narrow-gap semiconductor devices near room temperature using non-equilibrium techniques. *Semiconductor Science and Technology*, 6(12C):C99.

[75] T Ashley, A B Dean, C T Elliott, A D Johnson, G J Pryce, A M White, and C R Whitehouse. A heterojunction minority carrier barrier for InSb devices. *Semiconductor Science and Technology*, 8(1S):S386.

[76] nextnano Gmbh. URL `http://www.nextnano.com/`.

[77] G.R. Nash, H.L. Forman, S.J. Smith, P.B. Robinson, L. Buckle, S.D. Coomber, M.T. Emeny, N.T. Gordon, and T. Ashley. Mid-Infrared $\mathrm{Al_xIn_{1-x}Sb}$ Light-Emitting Diodes and Photodiodes for Hydrocarbon Sensing. *Sensors Journal, IEEE*, 9(10):1240–1243, Oct 2009. ISSN 1530-437X. doi: 10.1109/JSEN.2009.2029815.

[78] Elias Burstein. Anomalous Optical Absorption Limit in InSb. *Phys. Rev.*, 93: 632–633, Feb 1954. doi: 10.1103/PhysRev.93.632.

[79] Harvey R. Hardaway, Tim Ashley, Louise Buckle, Martin T. Emeny, Graeme Masterton, and Graham Pryce. Optimizing Indium Aluminum Antimonide LEDs and

photodiodes for gas sensing applications. volume 5564, pages 105–112, 2004. doi: 10.1117/12.560577.

[80] C. L. Littler and D. G. Seiler. Temperature dependence of the energy gap of InSb using nonlinear optical techniques. *Applied Physics Letters*, 46(10), 1985.

[81] N. Dai, F. Brown, R. E. Doezema, S. J. Chung, K. J. Goldammer, and M. B. Santos. Determination of the concentration and temperature dependence of the fundamental energy gap in $\mathrm{Al_xIn_{1-x}Sb}$. *Applied Physics Letters*, 73(21), 1998.

[82] Compound Semiconductor Technologies Global Ltd., . URL `http://www.compoundsemi.co.uk/`.

[83] R.M Biefeld and J.D Phillips. Growth of InSb on GaAs using InAlSb buffer layers. *Journal of Crystal Growth*, 209(4):567 – 571, 2000. ISSN 0022-0248. doi: http://dx.doi.org/10.1016/S0022-0248(99)00751-4.

[84] T Sato, M Akabori, and S Yamada. High-quality highly mismatched InSb films grown on GaAs substrate via thick AlSb and $\mathrm{In_xAl_{1-x}Sb}$ step-graded buffers. *Physica E: Low-dimensional Systems and Nanostructures*, 21(24):615 – 619, 2004. ISSN 1386-9477. doi: http://dx.doi.org/10.1016/j.physe.2003.11.088. Proceedings of the Eleventh International Conference on Modulated Semiconductor Structures.

[85] X. Weng, N. G. Rudawski, P. T. Wang, R. S. Goldman, D. L. Partin, and J. Heremans. Effects of buffer layers on the structural and electronic properties of InSb films. *Journal of Applied Physics*, 97(4):043713, 2005.

[86] Shenghong Huang, Ganesh Balakrishnan, and Diana L. Huffaker. Interfacial misfit array formation for GaSb growth on GaAs. *Journal of Applied Physics*, 105(10): 103104, 2009.

[87] K.C. Nunna, Siew Li Tan, C.J. Reyner, A.R.J. Marshall, Baolai Liang, A. Jallipalli, J.P.R. David, and D.L. Huffaker. Short-Wave Infrared GaInAsSb Photodiodes Grown on GaAs Substrate by Interfacial Misfit Array Technique. *Photonics Technology Letters, IEEE*, 24(3):218–220, Feb 2012. ISSN 1041-1135. doi: 10.1109/LPT.2011.2177253.

[88] A. N. Semenov, B. Y. Meltser, V. A. Solov'Ev, T. A. Komissarova, A. A. Sitnikova, D. A. Kirylenko, A. M. Nadtochyi, T. V. Popova, P. S. Kop'Ev, and S. V. Ivanov. Features of molecular-beam epitaxy and structural properties of AlInSb-based heterostructures. *Semiconductors*, 45:1327–1333, October 2011. doi: 10.1134/S1063782611100150.

[89] James Watt Nanofabrication Centre. URL `http://www.jwnc.gla.ac.uk/`.

[90] *Mask Aligner SUSS MicroTec.* URL `http://jwnc.eng.gla.ac.uk/images/equipment/ma6.pdf`.

[91] *Shipley Microposit S1800 series photoresists.* URL `http://jwnc.eng.gla.ac.uk/pages/Process_Data_Sheets/Microposit_S1800_G2_Serie.pdf`.

[92] Gregory C. DeSalvo, Wen F. Tseng, and James Comas. Etch Rates and Selectivities of Citric Acid/Hydrogen Peroxide on GaAs , $Al_{0.3}Ga_{0.7}As$, $In_{0.2}Ga_{0.8}As$, $In_{0.53}Ga_{0.47}As$, $In_{0.52}Al_{0.48}As$, and InP. 139(3):831–835, 1992. doi: 10.1149/1.2069311.

[93] Gregory C. DeSalvo, Ron Kaspi, and Christopher A. Bozada. Citric Acid Etching of $GaAs_{1x}Sb_x$, $Al_{0.5}Ga_{0.5}Sb$, and InAs for Heterostructure Device Fabrication. 141 (12):3526–3531, 1994. doi: 10.1149/1.2059365.

[94] KowMing Chang, JiunnJye Luo, ChenDer Chiang, and Jacob KouChen Liu. Mesa etching characterization of InSb for high density image array applications. *Journal of the Chinese Institute of Engineers*, 30(1):11–16, 2007. doi: 10.1080/02533839.2007.9671226.

[95] Kelvin Nanotechnology Ltd., . URL `http://www.kelvinnanotechnology.com/`.

[96] J. Hong, E. S. Lambers, C. R. Abernathy, S. J. Pearton, R. J. Shul, and W. S. Hobson. Inductively Coupled Plasma and Electron Cyclotron Resonance Plasma Etching of an InGaAlP Compound Semiconductor System. *Critical Reviews in Solid State and Materials Sciences*, 23(4):323–396, 1998. doi: 10.1080/10408439891324202.

[97] Oxford Instruments. ICP Technology, . URL `http://www.oxfordplasma.de/technols/icp_ecr.htm`.

[98] *Oxford Instruments Plasmalab System 100 ICP180.* URL `http://jwnc.eng.gla.ac.uk/images/equipment/icp180manual94-815409.pdf`.

[99] Oxford Instruments. Inductively Coulped Plasma (ICP) Etching, . URL `http://www.oxford-instruments.com/products/etching-deposition-and-growth/plasma-etch-deposition/icp-etch`.

[100] L. Zhang, L. F. Lester, R. J. Shul, C. G. Willison, and R. P. Leavitt. Inductively Coupled Plasma etching of IIIV antimonides in BCl3/Ar and Cl2/Ar. *Journal of Vacuum Science and Technology B*, 17(3), 1999.

[101] F Frost, A Schindler, and F Bigl. Reactive ion beam etching of InSb and InAs with ultrasmooth surfaces. *Semiconductor Science and Technology*, 13(5):523.

[102] Guo-Dong Zhang, Wei-Guo Sun, Shu-Li Xu, Hong-Yan Zhao, Hong-Yi Su, and Hai-Zhen Wang. Inductively coupled plasma-reactive ion etching of InSb using CH4/H2/Ar plasma. *Journal of Vacuum Science and Technology A*, 27(4), 2009.

[103] Elena A. Plis, Maya Narayanan Kutty, and Sanjay Krishna. Passivation techniques for InAs/GaSb strained layer superlattice detectors. *Laser and Photonics Reviews*, 7(1). ISSN 1863-8899.

[104] G. Chen, B.-M. Nguyen, A. M. Hoang, E. K. Huang, S. R. Darvish, and M. Razeghi. Elimination of surface leakage in gate controlled type-II InAs/GaSb mid-infrared photodetectors. *Applied Physics Letters*, 99(18):183503, 2011.

[105] A. R. J. Marshall. *The InAs electron avalanche photodiode and the influence of thin avalanche photodiode on receiver sensitivity.* PhD thesis, Electronic and Electrical Engineering, University of Sheffield, 2009.

[106] P. J. Ker. *Development of high speed low noise InAs electron avalanche photodiodes.* PhD thesis, Electronic and Electrical Engineering, University of Sheffield, 2012.

[107] Microchem. NANO$^{\mathrm{TM}}$ *SU-8 Negative tone photoresist formulations 2-25 datasheet.*

[108] M. Shaw, D. Nawrovki, R. Hurditch, and D. Johnson. Improving the process capability of SU-8. *Microsystem Technol.*, 10(1). ISSN 0946-7076.

[109] *Plassys MEB 400s and 550s electron-beam evaporators.* URL `http://www.jwnc.gla.ac.uk/metal.html`.

[110] MicroChemicals Gmbh. *AZ 4500 Series Thick Film photoresist*, . URL `http://www.microchemicals.com/micro/az_4500_series.pdf`.

[111] MicroChemicals Gmbh. *AZ nLOF 2000 Series i-Line Photoresists*, . URL `http://www.microchemicals.com/micro/AZ_nLOF2000_bulletin.pdf`.

[112] D. K. Schroder. *Semiconductor Material and Device Characterisation.* A. John Wiley and Sons, 2006.

[113] H. S. Kim, E. Plis, A. Khoshakhlagh, S. Myers, N. Gautam, Y. D. Sharma, L. R. Dawson, S. Krishna, S. J. Lee, and S. K. Noh. Performance improvement of InAs/GaSb strained layer superlattice detectors by reducing surface leakage currents with SU-8 passivation. *Applied Physics Letters*, 96(3):033502, 2010.

[114] J.H. Klootwijk and C.E. Timmering. Merits and limitations of circular TLM structures for contact resistance determination for novel III-V HBTs. In *Microelectronic Test Structures, 2004. Proceedings. ICMTS '04. The International Conference on*, pages 247–252, March 2004. doi: 10.1109/ICMTS.2004.1309489.

[115] V. Malina, E. Hjkov, J. Zelinka, M. Dapor, and V. Micheli. Non-alloyed Ti/Au and Ti/Pt/Au ohmic contacts to p-type InGaAsP. *Thin Solid Films*, 223(1):146 – 153, 1993. ISSN 0040-6090. doi: http://dx.doi.org/10.1016/0040-6090(93)90740-G.

[116] Yoon-Suk Kim, Kerstin Hummer, and Georg Kresse. Accurate band structures and effective masses for InP, InAs, and InSb using hybrid functionals. *Phys. Rev. B*, 80:035203, Jul 2009. doi: 10.1103/PhysRevB.80.035203.

[117] P.R. Griffith and J.A. de Haseth. *Fourier Transform Infrared Spectrometry*. Wiley, New York, 1986.

[118] Werner Herres and Joern Gronholz. Understanding FT-IR data processing. *Part*, 1:352–356, 1984.

[119] Axel Donges. The coherence length of black-body radiation. *European Journal of Physics*, 19(3):245.

[120] Sadao Adachi. Band gaps and refractive indices of AlGaAsSb, GaInAsSb, and InPAsSb: Key properties for a variety of the 2–4 µm optoelectronic device applications. *Journal of Applied Physics*, 61(10), 1987.

[121] Sadao Adachi. Optical dispersion relations for GaP, GaAs, GaSb, InP, InAs, InSb, $Al_xGa_{1-x}As$, and $In_{1-x}Ga_xAs_yP_{1-y}$. *Journal of Applied Physics*, 66(12), 1989.

[122] P. P. Paskov. Refractive indices of InSb, InAs, GaSb, $InAs_xSb_{1-x}$, and $In_{1-x}Ga_xSb$: Effects of free carriers. *Journal of Applied Physics*, 81(4), 1997.

[123] V. K. Malyutenko, O. Yu. Malyutenko, A. D. Podoltsev, I. N. Kucheryavaya, B. A. Matveev, M. A. Remennyi, and N. M. Stus. Current crowding in InAsSb light-emitting diodes. *Applied Physics Letters*, 79(25), 2001.

[124] S.J. Sweeney, A.F. Phillips, A.R. Adams, E.P. O'Reilly, and P.J.A. Thijs. The effect of temperature dependent processes on the performance of 1.5 µm compressively strained InGaAs(P) MQW semiconductor diode lasers. *Photonics Technology Letters, IEEE*, 10(8):1076–1078, Aug 1998. ISSN 1041-1135. doi: 10.1109/68.701507.

[125] Hyunsoo Kim, Seong-Ju Park, Hyunsang Hwang, and Nae-Man Park. Lateral current transport path, a model for GaN-based light-emitting diodes: Applications to practical device designs. *Applied Physics Letters*, 81(7), 2002.

[126] W. B. Joyce and S. H. Wemple. Steady-state junction-current distributions in thin resistive films on semiconductor junctions. *Journal of Applied Physics*, 41(9), 1970.

[127] M. Rattier, H. Benistry, R.P. Stanley, J.-F. Carlin, R. Houdre, U. Oesterle, C. J. M. Smith, C. Weisbuch and T. F. Krauss. Toward ultrahigh-efficiency aluminium oxide microcavity light-emitting diodes: guided mode extraction by photonic crystals. *IEEE J. Selected Topics in Quant. Electron.*, 8, 2002.

[128] V K Malyutenko, A V Zinovchuk, and O Yu Malyutenko. Bandgap dependence of current crowding effect in 3–5 µm InAsSb/InAs planar light emitting devices. *Semiconductor Science and Technology*, 23(8):085004.

[129] V. K. Malyutenko, O. Yu. Malyutenko, A. Dazzi, N. Gross, and J.-M. Ortega. Heat transfer mapping in 3–5 µm planar light emitting structures. *Journal of Applied Physics*, 93(11), 2003.

[130] V. K. Malyutenko, O. Yu. Malyutenko, and A. V. Zinovchuk. Room-temperature InAsSbP/InAs light emitting diodes by liquid phase epitaxy for midinfrared (3–5 µm) dynamic scene projection. *Applied Physics Letters*, 89(20):201114, 2006.

[131] A Monakhov, A Krier, and V V Sherstnev. The effect of current crowding on the electroluminescence of inas mid-infrared light emitting diodes. *Semiconductor Science and Technology*, 19(3):480.

[132] X Guo and EF Schubert. Current crowding and optical saturation effects in GaInN/GaN light-emitting diodes grown on insulating substrates. *Applied Physics Letters*, 78(21):3337–3339, 2001.

[133] Hyunsoo Kim, Jaehee Cho, Jeong Wook Lee, Sukho Yoon, Hyungkun Kim, Cheolsoo Sone, Yongjo Park, and Tae-Yeon Seong. Measurements of current spreading length and design of GaN-based light emitting diodes. *Applied Physics Letters*, 90 (6):063510, 2007.

[134] Hyunsoo Kim, Kyoung-Kook Kim, Kwang-Ki Choi, Hyungkun Kim, June-O Song, Jaehee Cho, Kwang Hyeon Baik, Cheolsoo Sone, Yongjo Park, and Tae-Yeon Seong. Design of high-efficiency GaN-based light emitting diodes with vertical injection geometry. *Applied Physics Letters*, 91(2):023510, 2007.

[135] Hyunsoo Kim and Sung-Nam Lee. Theoretical considerations on current spreading in GaN-based light emitting diodes fabricated with top-emission geometry. 157(5): H562–H564, 2010. doi: 10.1149/1.3357271.

[136] Scott H Brewer and Stefan Franzen. Optical properties of indium tin oxide and fluorine-doped tin oxide surfaces: correlation of reflectivity, skin depth, and plasmon frequency with conductivity. *Journal of alloys and compounds*, 338(1):73–79, 2002.

[137] N. Linder. Advanced industrial design methods for leds. In *Numerical Simulation of Semiconductor Optoelectronic Devices, 2006. NUSOD '06. International Conference on*, pages 125–126, Sept 2006. doi: 10.1109/NUSOD.2006.306773.

[138] FA Kish, FM Steranka, DC DeFevere, DA Vanderwater, KG Park, CP Kuo, TD Osentowski, MJ Peanasky, JG Yu, RM Fletcher, et al. Very high-efficiency semiconductor wafer-bonded transparent-substrate (alxga1- x) 0.5 in0. 5p/gap light-emitting diodes. *Applied Physics Letters*, 64(21):2839–2841, 1994.

[139] Kanglin Xiong, Wei He, Shulong Lu, Taofei Zhou, Desheng Jiang, Rongxin Wang, Kai Qiu, Jianrong Dong, and Hui Yang. Analysis of lateral current spreading in solar cell devices by spatially-resolved electroluminescence. *Journal of Applied Physics*, 107(12):124501, 2010.

[140] N. Gross, A. Dazzi, J. M. Ortega, R. Andouart, R. Prazeres, C. Chicanne, J.-P. Goudonnet, Y. Lacroute, C. Boussard, G. Fonteneau, and S. Hocd. Infrared near-field study of a localised absorption in a thin film. *The European Physical Journal - Applied Physics*, 16:91–98, 11 2001. ISSN 1286-0050. doi: 10.1051/epjap:2001197.

[141] C. Donolato. A reciprocity theorem for charge collection. *Applied Physics Letters*, 46(3), 1985.

[142] M. R. Krames, M. Ochiai-Holcomb, G. E. Hfler, C. Carter-Coman, E. I. Chen, I.-H. Tan, P. Grillot, N. F. Gardner, H. C. Chui, J.-W. Huang, S. A. Stockman, F. A. Kish, M. G. Craford, T. S. Tan, C. P. Kocot, M. Hueschen, J. Posselt, B. Loh, G. Sasser, and D. Collins. High-power truncated-inverted-pyramid (AlxGa1x)0.5In0.5P/GaP light-emitting diodes exhibiting 50% external quantum efficiency. *Applied Physics Letters*, 75(16), 1999.

[143] E. F. Schubert, Y.H. Wang, A. Y. Cho, L.W. Tu, and G. J. Zydzik. Resonant cavity light-emitting diode. *Applied Physics Letters*, 60(8), 1992.

[144] Roel G. Baets, Danae G. Delbeke, Ronny Bockstaele, and Peter Bienstman. Resonant-cavity light-emitting diodes: a review. volume 4996, pages 74–86, 2003. doi: 10.1117/12.476588.

[145] Audrey Nelson and Andrian Kouznetsov. A 4.26 µm RCLED and a fast low-power CO2 sensor. volume 7231, pages 72310V–72310V–9, 2009. doi: 10.1117/12.809293.

[146] E.Fred Schubert, N.E.J. Hunt, Roger J. Malik, M. Micovic, and D.L. Miller. Temperature and modulation characteristics of resonant-cavity light-emitting diodes. *Lightwave Technology, Journal of*, 14(7):1721–1729, Jul 1996. ISSN 0733-8724. doi: 10.1109/50.507950.

[147] Max Born and Emil Wolf. *Principles of optics: electromagnetic theory of propagation, interference and diffraction of light.* Cambridge University Press, 1999.

[148] H Benisty, Hans De Neve, and Cl Weisbuch. Impact of planar microcavity effects on light extraction-part i: Basic concepts and analytical trends. *Quantum Electronics, IEEE Journal of*, 34(9):1612–1631, 1998.

[149] Koichi Okamoto, Isamu Niki, Alexander Shvartser, Yukio Narukawa, Takashi Mukai, and Axel Scherer. Surface-plasmon-enhanced light emitters based on InGaN quantum wells. *Nature Materials*, 3(9):601–605, 2004.

[150] William L Barnes. Light-emitting devices: turning the tables on surface plasmons. *Nature materials*, 3(9):588–589, 2004.

[151] Chu-Young Cho, Min-Ki Kwon, Sang-Jun Lee, Sang-Heon Han, Jang-Won Kang, Se-Eun Kang, Dong-Yul Lee, and Seong-Ju Park. Surface plasmon-enhanced light-emitting diodes using silver nanoparticles embedded in p-gan. *Nanotechnology*, 21(20):205201, 2010. URL `http://stacks.iop.org/0957-4484/21/i=20/a=205201`.

[152] Horng-Shyang Chen, Chia-Feng Chen, Yang Kuo, Wang-Hsien Chou, Chen-Hung Shen, Yu-Lung Jung, Yean-Woei Kiang, and C. C. Yang. Surface plasmon coupled light-emitting diode with metal protrusions into p-gan. *Applied Physics Letters*, 102(4):041108, 2013. doi: http://dx.doi.org/10.1063/1.4789995. URL `http://scitation.aip.org/content/aip/journal/apl/102/4/10.1063/1.4789995`.

[153] M. Bahriz, V. Moreau, J. Palomo, R. Colombelli, D. A. Austin, J. W. Cockburn, L. R. Wilson, A. B. Krysa, and J. S. Roberts. Room-temperature operation of 7.5m surface-plasmon quantum cascade lasers. *Applied Physics Letters*, 88(18):181103, 2006. doi: http://dx.doi.org/10.1063/1.2198016. URL `http://scitation.aip.org/content/aip/journal/apl/88/18/10.1063/1.2198016`.

[154] Gangyi Xu, Yannick Chassagneux, Raffaele Colombelli, G. Beaudoin, and I. Sagnes. Polarized single-lobed surface emission in mid-infrared, photonic-crystal, quantum-cascade lasers. *Opt. Lett.*, 35(6):859–861, Mar 2010. doi: 10.1364/OL.35.000859. URL `http://ol.osa.org/abstract.cfm?URI=ol-35-6-859`.

[155] J.-P. Tetienne, A. Bousseksou, D. Costantini, R. Colombelli, A. Babuty, I. Moldovan-Doyen, Y. De Wilde, C. Sirtori, G. Beaudoin, L. Largeau, O. Mauguin, and I. Sagnes. Injection of midinfrared surface plasmon polaritons with an integrated device. *Applied Physics Letters*, 97(21):211110, 2010. doi: http://dx.doi.org/10.1063/1.3519985. URL `http://scitation.aip.org/content/aip/journal/apl/97/21/10.1063/1.3519985`.

[156] A. Babuty, A. Bousseksou, J.-P. Tetienne, I. Moldovan Doyen, C. Sirtori, G. Beaudoin, I. Sagnes, Y. De Wilde, and R. Colombelli. Semiconductor surface plasmon sources. *Phys. Rev. Lett.*, 104:226806, Jun 2010. doi: 10.1103/PhysRevLett.104.226806. URL `http://link.aps.org/doi/10.1103/PhysRevLett.104.226806`.

[157] Y.-H. Ye and Jia-Yu Zhang. Middle-infrared transmission enhancement through periodically perforated metal films. *Applied Physics Letters*, 84(16), 2004.

[158] R Ortuño, C García-Meca, FJ Rodríguez-Fortuño, A Håkansson, A Griol, J Hurtado, JA Ayucar, L Bellieres, PJ Rodríguez, F López-Royo, et al. Midinfrared filters based on extraordinary optical transmission through subwavelength structured gold films. *Journal of Applied Physics*, 106(12):124313, 2009.

[159] Reyhaneh Soltanmoradi, Qin Wang, Min Qiu, and Jan Y Andersson. Transmission of infrared radiation through metallic photonic crystal structures. *Photonics Journal, IEEE*, 5(5):4500608–4500608, 2013.

[160] P. Martyniuk, J. Antoszewski, M. Martyniuk, L. Faraone, and A. Rogalski. New concepts in infrared photodetector designs. *Applied Physics Reviews*, 1(4):041102, 2014.

[161] Pierre Berini. Surface plasmon photodetectors and their applications. *Laser and Photonics Reviews*, 8(2). ISSN 1863-8899.

[162] Rajeev V. Shenoi, Shawn-Yu Lin, Sanjay Krishna, and Danhong Huang. Order-of-magnitude enhancement of intersubband photoresponse in a plasmonic quantum dot system. *Opt. Lett.*, 39(15):4454–4457, Aug 2014.

[163] Ross Stanley. Plasmonics in the mid-infrared. *Nature Photonics*, 6(7):409–411, 2012.

[164] S. Law, V. Podolskiy, and D. Wasserman. Towards nano-scale photonics with micro-scale photons: the opportunities and challenges of mid-infrared plasmonics. *Nanophotonics*, 2:103–130, April 2013. doi: 10.1515/nanoph-2012-0027.

[165] Heinz Raether. *Surface plasmons on smooth surfaces.* Springer, 1988.

[166] H. F. Ghaemi, Tineke Thio, D. E. Grupp, T. W. Ebbesen, and H. J. Lezec. Surface plasmons enhance optical transmission through subwavelength holes. *Phys. Rev. B*, 58:6779–6782, Sep 1998. doi: 10.1103/PhysRevB.58.6779.

[167] Thomas W Ebbesen, HJ Lezec, HF Ghaemi, Tineke Thio, and PA Wolff. Extraordinary optical transmission through sub-wavelength hole arrays. *Nature*, 391 (6668):667–669, 1998.

[168] John Chun-Chieh Chang, Zu-Po Yang, Danhong Huang, D. A. Cardimona, and Shawn-Yu Lin. Strong light concentration at the subwavelength scale by a metallic hole-array structure. *Opt. Lett.*, 34(1):106–108, Jan 2009.

[169] MS Shishodia and AG Unil Perera. Heterojunction plasmonic midinfrared detectors. *Journal of Applied Physics*, 109(4):043108–043108, 2011.

[170] Jessie Rosenberg, Rajeev V Shenoi, Thomas E Vandervelde, Sanjay Krishna, and Oskar Painter. A multispectral and polarization-selective surface-plasmon resonant midinfrared detector. *Applied Physics Letters*, 95(16):161101, 2009.

[171] Jessie Rosenberg, Rajeev V. Shenoi, Sanjay Krishna, and Oskar Painter. Design of plasmonic photonic crystal resonant cavities for polarization sensitive infrared photodetectors. *Opt. Express*, 18(4):3672–3686, Feb 2010.

[172] Chun-Chieh Chang, Yagya D. Sharma, Yong-Sung Kim, Jim A. Bur, Rajeev V. Shenoi, Sanjay Krishna, Danhong Huang, and Shawn-Yu Lin. A surface plasmon enhanced infrared photodetector based on InAs quantum dots. *Nano Letters*, 10 (5):1704–1709, 2010. doi: 10.1021/nl100081j.

[173] Surface plasmon enhanced IR absorption: Design and experiment. *Photonics and Nanostructures - Fundamentals and Applications*, 9(1):95 – 100, 2011. ISSN 1569-4410. doi: http://dx.doi.org/10.1016/j.photonics.2010.12.002.

[174] Sang Jun Lee, Zahyun Ku, Ajit Barve, John Montoya, Woo-Yong Jang, SRJ Brueck, Mani Sundaram, Axel Reisinger, Sanjay Krishna, and Sam Kyu Noh. A monolithically integrated plasmonic infrared quantum dot camera. *Nature communications*, 2:286, 2011.

[175] William L Barnes. Surface plasmon-polariton length scales: a route to subwavelength optics. *Journal of Optics A: Pure and Applied Optics*, 8(4):S87, 2006.

[176] Lumerical Solutions Inc. FDTD Solutions. URL `https://www.lumerical.com/tcad-products/fdtd/`.

[177] Allen Taflove, Susan C Hagness, et al. Computational electrodynamics: the finite-difference time-domain method. *Norwood, 2nd Edition, MA: Artech House, l995*, 1995.

[178] John B Schneider. Understanding the finite-difference time-domain method. *School of electrical engineering and computer science Washington State University.–URL: http://www. Eecs. Wsu. Edu/˜ schneidj/ufdtd/(request data: 29.11. 2012)*, 2010.

[179] Vistec Electron Beam GmbH. *Vistec VB6 UHR EWF electron beam lithography tool.* URL `http://www.vistec-semi.com/`.

[180] *Oxford Instruments Plasmalab 80 Plus.* URL `http://www.oxfordplasma.de/systems/80plus.htm`.

[181] *Oxford Instruments Plasmalab System 100.* URL `http://www.oxfordplasma.de/systems/100ll.htm`.

[182] H. Greiner and J. Pond. Simulation of light extraction from oleds with fdtd solutions, Sept 2006. URL `http://docs.lumerical.com/en/poster_sim_light_extraction_OLEDS.pdf`.